eman ta zabal zazu

Universidad del País Vasco

Euskal Herriko Unibertsitatea

Magnetization reversal behavior of ferromagnetic thin films and nano-structures

Olatz Idigoras Lertxundi

-Phd Thesis-

Supervisor: Dr. Andreas Berger

2013

Olatz Idigoras Lertxundi

Supervisor: Dr. Andreas Berger

Donostia-San Sebastian (2013)

Laburpena

Teknologiaren eskaria gailuen miniaturizaziori dagokionez etengabea da, non gailu hauen artean sistema ferromagnetikoen miniaturizazioak ere garrantzi handia duen hainbat aplikazio teknikori begira, esaterako, disko gogorren eta ausazko atzipenezko memoria magnetikoen (MRAM) industriaren alorrean. Bereziki, teknologia garaikidearen hobekuntza zein teknologia berrien garapena, propietate magnetikoen oinarrizko ezagutzan eta material magnetiko berrien ikerkuntzan datza. Teknologiaren etengabeko eskaerak eta teknologia hau oinarri duen fisikaren ezagutzaren beharrak, nanogeruza fin eta nanoegituren magnetizazioaren alderanzketa ikerkuntza gai aktibo bilakatu dute azken hamarkadetan. Hala ere, ikerkuntzak esparru honetan lorpen handiak egin dituen arren, oraindik erantzunik gabeko hainbat galdera aurki daitezke, besteak beste, ea ze eragin daukaten sisteman lokalki egindako aldaketa fisikoek magnetizazioaren alderanzketa kolektiboan edo nola eragin dezaketen kanpo parametroek alderanzketaren dinamikan. Bestalde, sistema ferromagnetikoen miniaturizaziorako, beharrezkoa da desio diren propietateak dituzten nanoegituren fabrikaziorako modu eraginkorrak bilatzea eta hobetzea, zein nanoegitura hauen propietate magnetikoak xehetasun eta prezisio handiz karakterizatu ahal izatea.

Tesi honen helburu orokorra nanogeruza finen eta nanoegituren magnetizazioaren alderanzketa prozesuaren gaineko ezagutza hobe bat lortzean datza. Gai honi dagozkion efektu desberdinak xehetasun handiz ikertzen dira, esaterako, ezohiko magnetizazioaren alderazketa eta fase trantsizio dinamikoa.

Tesia kapitulu desberdinetan dago banatuta, non lehenengo kapituluan tesiaren helburuak azaltzen diren. Bigarren kapituluak, magnetismoari eta magnetizazioaren alderanzketari buruzko oinarrizko ezagutza laburbiltzen du. Atal honetan sistema ferromagnetikoen energia ekarpen garrantzitsuenak deskribatzen

dira, eta hauetan oinarrituz sistema sinpleenen magnetizatioaren alderazketaren prozesua xehetasunez azaltzen da. Kapitulu honetan magnetizazioaren alderanzketaren dinamika ere deskribatzen da.

Tesian zehar erabili diren teknika esperimentalak hirugarren kapituluan deskribatzen dira. Tesi honetan azaltzen diren nanogeruza fin guztiak, "sputtering" izeneko teknika erabiliz hazi dira (ikusi 3.1.1.1. atala). Teknika honekin baliatuz propietate fisiko zehatzak dituzten nanogeruzak hazi dira, besteak beste, maila handiko kristal egitura duten nanogeruzak. Nanoegituren fabrikazioa, aldiz, litografia teknika desberdinekin lortu daitekeen arren, tesi honetan landutako fokatutako elektroi sortaren bidez eragindako deposizio (*focused electron beam induced deposition*, FEBID) teknikak (3.1.2.2.) eta fokatutako ioi sortaren (*focused ion beam*, FIB) bidezko fabrikazio teknikak (3.1.2.1.) abantaila esanguratsuak aurkezten dituzte besteekin alderatuz. Fokatutako elektroi sortaren bidez eragindako deposizio teknikari dagokionez, pausu bakarreko fabrikazio teknika izateaz gain, hiru dimentsiotako egitura konplexuak fabrikatzeko ahalmenak balio anitzeko teknikan bihurtzen du. Bestalde, fokatutako ioi sortari esker, posible da aurrez hazitako nanogeruzetan, nanoegiturak sortzea inongo erretxin edo produktu kimikorik erabili gabe.

Kapitulu honetan propietate fisikoak, eta bereziki magnetikoak, karakterizatzeko erabili diren tekniken deskribapen bat ere egiten da. Propietate fisikoak neurtzeko, besteak beste X-izpien difrakzio eta islapen neurketak gauzatu dira (3.2.1. atala). Neurketa hauei esker nanogeruzen kristal egitura zein lodiera karakterizatu daiteke. Bestalde, indar atomikoko mikroskopioa (*atomic force microscope*, AFM) ere erabili da (3.2.2. atala), gainazalaren topografia neurtzeko eskala nanometrikoan.

Propietate magnetikoei dagokionez, Kerr efektu magneto-optikoan oinarritzen diren, laser bidezko neurketa aparailua (3.3.1.2. atala) eta mikroskopioa (3.3.1.3. atala) erabili dira alde batetik eta laginen bibrazioan oinarritzen diren bi magnetometro bestetik (3.3.1.1. eta 3.3.1.2. atalak).

Magnetizazioaren alderanzketan aldaketa lokalek duten eraginaren gaineko ikerketa laugarren kapituluan deskribatzen da. Lan honetan kristalografiaren antolamenduak, aleazioaren konposizioak eta geruzen lodierak kobaltozko eta kobalto aleazioetako nanogeruzen magnetizazioaren alderanzketan duten eragina aztertu da.

Horretarako, lehenik erreferentzi bezala antolamendu kristalografiko maila handiko 30 nm-ko kobalto geruza duen lagina hazi da. Lagin hauetan antolamendu maila handiko kristal egitura zehatza lortu ahal izateko, hain zuzen ere (10$\underline{1}$0) kristal egitura duen kobaltozko nanogeruza lortzeko, laginak epitaxialki hazi dira horretarako egokiak diren azpigeruzak erabiliz. Antolamendu kristalografiko hau erakusten duten laginek geruzaren planoan definituta dagoen ardatz bakarreko anisotropia magnetikoa erakusten dute. Hori horrela izanik, sistema ferromagmetiko hauen magnetizazioaren alderanzketan parte hartzen duten energia ekarpen desberdinak errez banatu eta aztertu daitezke, honek sistema hau erreferentzia-lagin bezala aukeratzea justifikatzen duelarik. Ondorioz, magnetizazio alderanzketan parte hartzen duten energia ekarpenak bereizteko ahalmenak, sisteman lokalki eginiko aldaketak magnetizazioaren alderanzketa prozesuan duen eraginaren ikerketa zehatzagoa burutu daiteke. Antolamendu kristalinoak propietate magnetikoetan duen eragina aztertzeko asmoz, prozesu epitaxiala partzialki eten da (4.1. atala), antolamendu maila desberdineko kobalto laginak lortuz. Laginen izaera kristalinoa degradatzen den heinean anisotropia maila magnetikoa gutxitzen dela behatu da, magnetizazioaren alderazketa prozesuan, erreferentzia laginetan ez bezala, dominio magnetikoak azaltzen direlarik. Magnetizazio dominioen existentzia modu sinple eta eraginkor baten analizatzeko, dominioen irudikapen metodo berri bat garatu da, Kerr efektu magneto-optikoan oinarritzen den mikroskopian oinarrituz (B. apendizea).

Honez gain, maila handiko antolamendu kristalografikoa duten kobalto-rutenio aleazioz osatutako 30 nm-ko nanogeruzak hazi dira (4.2. atala). Hazitako laginetan rutenioaren kontzentrazio aldatu da, rutenio gutxiko aleazioetatik, %30-erainoko rutenio kopurua duten nanogeruzataraino. Kobalto-rutenio nanogeruza hauek ere epitaxialki hazi dira, (10$\underline{1}$0) kristal egiturarekin, non horretarako, lortu nahi den rutenio kontzentrazio mailarekin aldatzen den azpigeruza espezifiko berri bat txertatu den geruza-sekuentzia epitaxialean. Rutenioa 4d trantsizio metala izanik, jakina da 4d trantsizio metalak 3d trantsizio metalekin nahasten diren kasuetan materialek propietate magnetiko erakargarriak erakusten dituztela. Tesi honetan hazi diren kobalto-rutenio laginen propietate magnetikoei dagokionez, saturazio magnetizazioaren eta Curie tenperaturaren murrizketa lineal bat aurkitu da, aleaziozko nanogeruzetan rutenioaren kontzentrazioa igo den heinean. Lehenengo

ordenako anisotropia konstanteari dagokionez, ordea, jarrera ez monotono bat aurkitu da, non tarteko rutenioaren kontzentrazioentzat anisotropia konstantearen balioak handiagoak diren. Aleazio hauen propietate magnetiko berriak, besteak beste, anisotropiaren energiaren konstante altuak eta Curie temperatura baxuak, izatean datza, gaur egungo disko gogorren industriarako erakargarriak direnak.

Magnetizazioaren alderazketan ze eragin duen aztertu den azken aldagaia, nanogeruzen lodiera da (4.3. atala). Nanogeruzen propietate magnetikoek hauen lodierarekiko duten menpekotasuna handia izan daiteke. Adibidez, jakina da nanogeruza oso finetan gainazaleko anisotropiaren eragina beste energia ekarpenei gainjartzerainokoa izan daitekeela, kasu askotan magnetizazioaren ardatz errazaren norabidea guztiz aldatzeraino. Bestalde, epitaxialki hazitako laginetan, hasierako geruzek oinarriarekiko duten kristal egitura desberdintasuna dela eta jasaten duten tentsioa gradualki desagertu daiteke geruzaren lodiera handitzen den heinean. Ondorioz, ikerketa honetan ikusi den bezala, 100 eta 150 nm-ko lodierako kobaltozko laginetan, propietate magnetikoak ez dira geruzan zehar uniformeak eta magnetizazioaren alderanzketa bi jauzi edo guztiz korrelatu gabeko prozesu baten bitartez gauzatzen da. Propietate berdinak dituzten lagin finagoentzat ordea magnetizazioaren alderanzketa korrelazio osoz eta jauzi bakarrean ematen da.

Bosgarren kapituluan, partzialki desantolatutako laginetan aurkitu den ezohiko anomalia aztertu da. Lagin hauetan, baldintza jakin batzuetan ohiko magnetizazio alderanzketaren erakusle den histeresia agertzen bada ere, kanpoko eremu magnetikoa ardatz zailean aplikatzen denean, ezohiko magnetizazioaren alderanzketa neurtu daiteke (5-1. irudia). Kerr efektuan oinarritzen den mikroskopio bitartez egin diren neurketen (5-4. irudia) zein planteatu den eredu teoriko baten bitartez (5-2. ekuazioa), ardatz zailean gertatzen den ezohiko magnetizazioaren alderanzketaren jatorria, lerrokatu gabeko anisotropia energia ekarpenearen eta akoplamendu magnetikoaren energia ekarpenaren arteko lehiaketan dagoela aurkitu da, lehiaketaren ondorioz sistema egoera frustratu batean aurkitzen delarik.

Ezohiko magnetizazioaren alderanzketa hau ulertzeko kontsideratu dezagun, bi ale magnetiko dituen sistema bat, ale bien arteko ardatz errazak angelu jakin baten bitartez desbideratuta daudelarik. Kanpo eremu magnetikoa batezbesteko ardatz zailean aplikatuz gero, honen indarra txikitzean, ale bakoitzaren magnetizazioak

hurbilen daukan ardatz errezerantz alderanzten hasiko da. Aldi berean, ordea, bi aleen arteko akoplamendu energia bi magnetizazioak norabide berdinean mantentzen saiatuko da, eta energía ekarpenen lehiaketa honek bi aleen magnetizazioen guraize bezelako egoera bat utziko du, ezohiko magnetizazioaren alderanzketari bide emanez (5-8. irudia (a)). Ezohiko efektu hau aurrez beste lan batzutan neurtu ahal izan bazuten ere, orain arte ez zuen inork azalpen zehatzik eman bere jatorriaren inguruan.

Seigarren kapituluan, fase trantsizio dinamikoan egin den ikerketa azaltzen da. Sistema magnetiko batean maiztasun handiko eremu magnetiko bat aplikatzean, sisteman dauden momentu magnetikoak ez dira kanpo eremu magnetiko honi jarraitzeko gai, beraien erlaxazio denbora aplikatutako eremua baino geldoago den kasuetan. Ondorioz ez da magnetizazioren alderanzketarik gauzatzen eta periodo ziklo baten batez besteko magnetizazioa balorea, Q, ez da zero. Aurrez egindako lan teorikoei esker jakina da Q parametroak bigarren ordenako fase trantsizio dinamiko bat erakusten duela, kanpo eremuaren maiztasunarekiko ordena parametroaren papera jokatzen duelarik. Hemen aurkezten den lan honetan denboran zehar konstante den kanpo eremu magnetikoaren osagai gainjarriak fase trantsizio dinamikoan duen garrantzia aztertu da teorikoki eta esperimentalki kobaltozko laginetan. Teorikoki zein esperimentalki ikusi denez, denboran konstante den eremu magnetikoaren osagai hau ordena parametroaren, Q-ren, eremu konjokatua da.

Azken kapituluak, zazpigarrenak hain zuzen ere, nanoegituren fabrikazioa eta hauen propietate magnetikoei buruzko ikerketa laburbiltzen du. Lehenik eta behin, Kerr efektu magneto-optikoan oinarritzen den mikroskopiak, argiaren uhin-luzera baino txikiagoak diren nanoegiturak neurtzeko duen gaitasuna ikertu da (7.1. atala). Mikroskopio optikoa hornitzen duen bereizmen handiko kameraz eta aztertu nahi den interes gunea hautatzeko aukera ematen duen softwareaz baliatuz, bereizmen limitea baino txikiagoak diren nanoegituren magnetizazioaren alderazketa neurtzea posible dela erakusten da tesi honetan. Hau frogatzeko kobaltozko nanohariak fokatutako elektroi sorta bidezko deposizio teknikarekin fabrikatu dira, non zabalera txikiena duen haria 30 nm-koa den (7.2. atala). Ondoren, hari hauen magnetizazioaren alderanzketa Kerr efektu magneto optikoan oinarritzen den mikroskopioaren bitartez neurtu da, 30 nm-ko hariarentzat ziklo bakarreko neurketan seinale-zarata erlazio esanguratsua, 4.1 baliokoa, lortu delarik.

Kapitulu honetan ere fokatutako ioi sortaren bidez kobalto-platino geruzatan nanoegiturak sortzeko modu eraginkor bat erakutsi da (7.3. atala). Kobalto-platino geruzen propietate magnetikoak oso sentikorrak dira egituraren edozein aldaketa txikietara eta ondorioz ondo ez fokatutako ioekin desio ez diren aldaketak utzi daitezke nanoegituran bertan. Lan honetan titanio nitrurozko (TiN) maskara bat erabiliz, hasierako propietate magnetikoak mantentzen duten 100 nm-ko tamaina laterala duten nanoegiturak fabrikatzeko aukera erakusten da.

Abstract

In general terms, this thesis studies the magnetization reversal behaviour of ferromagnetic thin films and nano-structures. In one core part of the thesis, the influence of crystallographic alignment, materials composition and thickness onto the magnetic properties of Co and Co alloy thin films has been studied in detail. Hereby, an epitaxially grown 30 nm thick (10$\underline{1}$0) Co thin film, which has in-plane uniaxial magnetic anisotropy, has been utilized as a reference structure due to its simple and well-understood behaviour. In order to modify the crystallographic alignment in a continuous and controlled fashion, a method to interrupt the epitaxy has been developed and applied. The magnetic properties of these crystallographically modified samples have been analysed by magneto-optical Kerr effect magnetometry and microscopy. Hereby, it was observed that while in samples with good crystallographic alignment the magnetization reversal is still simple and dominated by uniform magnetization states, non-uniform intermediate stable or meta-stable states emerge in the case of sufficiently disordered samples, even though macroscopic uniaxial anisotropy is still maintained. Furthermore, in samples with partial crystallographic alignment, an anomaly has been found, in which conventional hard axis behaviour disappears in a very narrow range of applied field directions. In such samples, a frustrated magnetic state occurs when the magnetic field is applied along the hard axis, which arises from the competition between ferromagnetic exchange and locally misaligned uniaxial anisotropies of adjacent grains. The existence of such a frustrated state along the nominal hard axis has been theoretically explained in the framework of a two-grain model and has been experimentally corroborated by microscopic imaging. As a function of thickness, epitaxial Co films exhibit a slight variation of their magnetization properties, which is triggered by and consistent with a crystallographic strain release upon increasing the film thickness.

For the study of magnetic alloys, CoRu films of different compositions have also been grown epitaxially with (10$\underline{1}$0) crystallographic orientation. Hereby, it has been necessary to modify the epitaxial growth sequence and incorporate an individualized template for each magnetic alloy concentration, in order to fabricate alloy films of comparable crystal quality. For the so-prepared samples, key magnetic properties have been measured, such as, Curie temperature, saturation magnetization and anisotropy constants as a function of composition. It has been found that the magneto-crystalline anisotropy constant shows a complex and non-monotonous behaviour as a function of Ru content in the alloy, while saturation magnetization and Curie temperature show a more expected monotonic decrease with Ru concentration.

In addition to the material oriented studies, Co-films have also been utilized to experimentally investigate the dynamic phase transition and specifically, the influence of a constant bias field onto the phase diagram and phase stability. These experimental studies have been furthermore complemented by theoretical calculations based upon the Kinetic Ising model in mean field approximation. Also here, the role of the constant bias field has been analysed, which was identified as the conjugated field of the dynamic order parameter.

Finally, the benefits that the magneto-optical Kerr effect microscope offers for the study of individual structures, even nano-scale structures, has been demonstrated and analysed. Specifically, single cycle hysteresis loop measurements of 30 nm wide Co wires, fabricated by means of focused electron beam induced deposited, have been demonstrated. Also, 100 nm wide wires of only 0.8 nm Co layer thickness (as part of a Pt/Co/Pt-trilayer structure) have been measured with the Kerr microscope with excellent signal to noise ratio, allowing the distinction of uniform vs. non-uniform reversal. These specific Pt/Co/Pt nanostructures have been successfully fabricated, maintaining their original perpendicular anisotropy, by means of focussed ion beam induced layer intermixing. For this purpose, a special TiN hard mask had to be developed, which acts as a sacrificial layer, and opens up a new and promising pathway for directly nano-structuring multilayer materials by means of focused ion beam exposure without damaging their magnetic properties in a wide surface area.

List of abbreviations

AC: Alternating Current
AR: Area Ratio (illuminated magnetic area versus total area)
AFM: Atomic Force Microscope
BLS: Brillouin Light Scattering
DC: Direct Current
EA: Easy Axis
EDX: Energy-Dispersive X-ray spectroscopy
FEBID: Focused Electron Beam Induced Deposition
FIB: Focused Ion Beam
FM: FerroMagnetic
FWHM: Full Width at Half Maximum
HA: Hard Axis
HF: HydroFluoric acid
LLG: Landau Lifshitz Gilbert
MD: Multi-Domain
MFT: Mean Field Theory
MO: Magneto-Optical
MOKE: Magneto-Optical Kerr Effect
MRAM: Magnetic Random Access Memories
OR: Orientation Ratio
PM: ParaMagnetic
PSSW: Perpendicular Standing Spin Wave
RF: Radio Frequency
RMS: Root Mean Square
ROI: Region Of Interest
SD: Single-Domain
S/N: Signal to Noise ratio
SE: Secondary Electrons
SEM: Scanning Electron Microscope
SQUID: Superconducting Quantum Interference Devices
SW: Stoner-Wohlfarth
TEM: Transmission Electron Microscope
XRD: X-Ray Diffraction
UHV: Ultra High Vacuum
VSM: Vibrating Sample Magnetometry

List of variables[a]

$\Delta\Omega$	full width at half maximum in rocking curve measurements
$\Delta I/I_0$	magneto-optical signal
$(\Delta I/I_0)_{sw}$	magneto-optical signal of sub-wavelength structures
α	magnetization angle with respect to the EA
α_N	magnetization angle with respect to the surface normal
α_G	Gilbert damping constant
β	external applied field angle with respect to the EA
β_c	critical exponent of the DPT present in Q ($P \rightarrow P_c$)
γ	gyromagnetic ratio
δ	magnetization angle with respect to the applied field direction
δ_c	critical exponent of the DPT present in Q ($P = P_c$, $H_b \rightarrow 0$)
ε	dielectric constant
$\tilde{\varepsilon}$	dielectric tensor
ε_K	Magneto-Optical Kerr effect ellipticity
η	dimensionless applied field frequency
θ	X-ray detector angle respect to the surface plane
θ_K	Magneto-Optical Kerr effect rotation
τ	relaxation time of the magnetization
φ	rotation angle with respect to surface normal in XRD measurements
ω	X-ray incidence angle respect to the surface plane
ω_c	smallest misalignment angle between anisotropy axes in the two-grain model for the HA anomaly to emerge
ω_H	frequency of the external applied oscillatory field
ω_k	misalignment angle between anisotropy axes in the two-grain model
A_{maq}	illuminated magnetic area in MOKE microscopy
A_{nomaq}	illuminated non-magnetic area in MOKE microscopy
D_i	ion dose used in FIB fabrication processes
d	distance between atomic planes in a crystal
E	free energy per unit volume
E_{2q}	free energy of a two-grain model with misaligned anisotropy axes
E_{ex}	free energy contribution of the exchange interaction per unit volume
E_k	free energy contribution of the magneto-crystalline anisotropy per unit volume
E_s	magnetostatic free energy per unit volume
E_s	free energy contribution of the surface anisotropy per unit volume
E_{sw}	Stoner Wohlfarth free energy per unit volume

[a] Variables are not listed here if they occur only in the immediate context of a statement.

E_z	Zeeman free energy per unit volume
H	externally applied field
H_b	constant applied field (bias field)
H_{eff}	effective field
H_c	coercive field
H_k	anisotropy field
H_{cl}	closure field
H_0	amplitude of external oscillatory applied field with frequency ω_H
H_s	magnetostatic field
H_{swi}	switching field
I	detected light (incl. X-ray) intensity
$J_{i,j}$	exchange interaction constant between i-th and j-th spins defined as energy per unit volume
J	macroscopic exchange interaction constant defined as energy per unit volume
J_g	effective inter grain exchange interaction constant defined as energy
k	running index of discretization steps in DPT calculations
K	total number of discretization steps in DPT calculations
K_i	*i*-th order magneto-crystalline anisotropy constant defined as energy per unit volume
K_s	surface magneto-crystalline anisotropy constant defined as energy per unit area
m_a	magnetic moment per lattice site
m	magnetization normalized to the saturation magnetization
M	magnetization defined as the magnetic moment per unit volume
M_r	remanent magnetization defined as the remanent magnetic moment per unit volume
M'_{rea}	extracted remanent magnetization (M) along the EA
M'_{ha}	extracted remanent magnetization (M) along the HA
M_0	reference magnetization defined as the reference magnetic moment per unit volume
M_s	saturation magnetization defined as the saturation magnetic moment per unit volume
N	number of magnetic moments
NN	number of nearest neighbours
p	parallel linearly polarized light with respect to the plane of incidence
P	applied field period, $P = 2\pi/\omega_H$
P_c	critical applied field period
Q	cycle-averaged magnetization
Q_v	Voigt constant of magneto-optical effects
r_{pp}, r_{sp}, r_{ps}, r_{ss}	Fresnel reflections coefficients
s	perpendicular linearly polarized light with respect to the plane of incidence
S	spin operator
S_k	X-ray scattering wave vector
T	temperature
t	time
t_{hk}	thickness

T_C	Curie temperature
T_R	room temperature
t_{Co}	Co layer thickness
t_{ox}	SiO_2 interlayer thickness
V	volume of the magnetic system
x	ruthenium concentration in $Co_{1-x}Ru_x$ alloy
y	ruthenium concentration in $Cr_{1-y}Ru_y$ alloy

1. Scope of this thesis

Technological advances today are demanding the ever increasing integration and further miniaturization of devices[1–3], especially in the electronics sector.[1,3] Among such devices, ferromagnetic systems have important technological relevance, primarily in the data storage industry.[4,5] Specifically here, the improvement of current technologies and the viability of new technologies depend on a fundamental understanding of magnetic properties and require the search and investigation of new magnetic materials, structures and properties at nano-scale dimensions. For example, in hard disks media technology[4,6] or magnetic random access memories (MRAMs)[7], data storage relies on a precise control of local magnetization reversal pattern and processes in order to achieve ever higher data capacities and faster data storage and read-out speeds. The continuous demands of technology and the need to understand the fundamental physics upon which this technology is based have made the study of magnetization reversal in thin films and nanostructures a core area of active research during the last several decades[8–12]. However, despite all these works, there are still many open questions, which need to be addressed, such as the precise understanding of how local variations of magnetic properties may affect the collective magnetization reversal and how external parameters can change the dynamics of the reversal, for instance. On the other hand, in order to miniaturize ferromagnetic systems, it is essential to find efficient pathways of fabricating such structures with the desired properties and to be able to characterize their magnetic properties with sufficient detail and precision.

Overall, this thesis aims to achieve a better understanding of magnetization reversal processes in thin films and nanostructures and studies in detail different

effects that are related to this very subject, such as, anomalous magnetization reversal and the dynamic phase transition.

The thesis is organized as follows. In Chapter 2, basic aspects of ferromagnetism and magnetization reversal are reviewed. In Chapter 3, the experimental techniques used within the framework of this thesis are introduced. Chapter 4 describes the studies carried out for the analysis of magnetization reversal in thin films when different intrinsic properties are changed, such as the crystallographic structure and quality, the composition of the ferromagnetic alloy or the film thickness. Overall, the study has been focused on Co and Co-alloy thin films with uniaxial magneto-crystalline anisotropy. Here, the motivation to study how magnetization reversal properties change upon crystallographic structure modifications comes from a severe lack of understanding in how far crystallographic disorder affects the details of magnetization reversal, especially in the range of low and modest disorder. In contrast to this low disorder regime, highly disordered or completely disordered materials have been studied extensively in the past[13,14], as well as highly ordered epitaxial single crystal thin films[15,16]. On the other hand the study of Co alloys, specifically, the CoRu alloy series and its composition effect onto different magnetic properties, has been motivated by the interesting as well as useful properties that alloys containing ferromagnetic 3d transition metals and 4d or 5d transition metals exhibit.[17–20] The specific choice of investigating the CoRu alloy series in detail was made because up to now the magnetic properties of CoRu alloy thin films have remained largely unexplored, despite their technological relevance[21–24]. Furthermore, the thickness dependence of magnetic properties and magnetization reversal has been studied for epitaxially grown Co thin films, in order to identify the thickness regime where simple magnetization reversal behaviour can be expected and crystal ordering and composition effects onto magnetization reversal can be easily identified. In Chapter 5, a detailed study of an anomalous magnetization reversal in thin films with modest crystallographic disorder levels is described. This unusual magnetization reversal only emerges in a narrow range of the applied field angles and previous works were not able to explain this effect due to a lack of precise control of the crystallographic order in thin films[25–31].

Chapter 6 discusses how external characteristics may affect the magnetization reversal. Specifically, when changing certain characteristics of the externally applied field, such as the frequency or applied field amplitude, ferromagnetic systems may not be able to reverse its magnetization anymore and instead exhibit a dynamic state sequence that defines a dynamically ordered non-equilibrium phase. The main motivation of analysing the dynamic phase and the associated dynamic phase transition, is to understand the underlying physical principles that determine such dynamic phenomena, such as the question of existence and nature of a possible conjugate field to the order parameter[32,33], for instance.

The study of magnetization reversal in Co based nanostructures is described in Chapter 7, where in addition to their efficient fabrication, a method to characterize their individual properties is shown. This chapter has two objectives: one is to explore the ability of magneto-optical Kerr microscopy to be sensitive to magnetic signals arising from nanostructures well below the optical resolution limit and the second is to find effective ways of fabricating nanostructures in promising magnetic materials systems, such as Co or Co/Pt-multilayers, whose properties are very sensitive to fabrication induced secondary effects.

2. Ferromagnetism and magnetization reversal

2.1. Ferromagnetism and its energy contributions

In ferromagnetic materials neighbouring magnetic moments are aligned along the same direction, at least on sufficiently short length scales, so that the net moment density per atom adds up to a non-vanishing macroscopic magnetization. As a result, such ferromagnetic materials exhibit a spontaneous net magnetization even in the absence of an externally applied magnetic field below a characteristic temperature[b], which is called Curie temperature (T_C)[34,35]. The spontaneous net magnetization of ferromagnetic materials exhibits a power law behaviour in the vicinity of the Curie temperature, above which these materials cease to have a spontaneous magnetization, and instead convert into a paramagnetic state. Specifically the spontaneous net magnetization exhibits a second order phase transition as a function of temperature near T_C (schematic shown in fig. 2-1)[35,sect.6.2.]. The existence of this spontaneous

[b] There are also so called ferrimagnetic materials, that present a spontaneous net magnetization but are not considered ferromagnetic materials. They are formed by different sub-lattices with opposite magnetic moments of unequal size, so that they also add up to a macroscopic net magnetization.

magnetization and phase transition was described by the Weiss molecular field postulate already in 1907.[35]

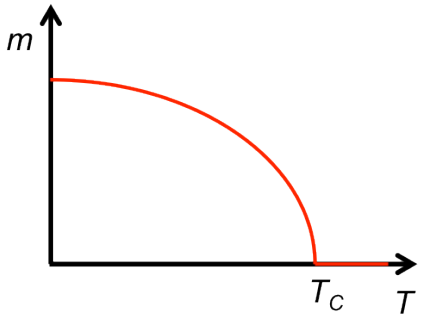

Figure 2-1: Schematic of the second order phase transition that the spontaneous magnetization of a ferromagnet exhibits when the sample temperature approaches the Curie temperature.

The origin of the ferromagnetic state is the exchange interaction[35,sect.4.2.]. In solids the electron orbitals of neighbouring atoms overlap, leading to an interaction of electrons by interatomic exchange coupling. Specifically, the exchange interaction is a quantum mechanical effect that arises from the combination of electrostatic interaction between electrons on nearby atoms, namely Coulomb repulsion and the necessity to satisfy the Pauli exclusion principle, which requires fermion symmetry properties from the combined spatial and spin parts of the electronic wave function. The energies of a 2 electrons system can then be expressed by their relative spin orientation, so that one can replace the overall electron Hamiltonian by an effective spin interaction. The extension of this pair-wise spin interaction to multi-electron systems is the Heisenberg model, which is given as

$$E_{ex} = -\frac{1}{2}\sum_{i,j} J_{ij}\hat{S}_i \cdot \hat{S}_j \qquad (2\text{-}1),$$

where $\hat{S}_i$ and $\hat{S}_j$ are dimensionless spin operators of the appropriate size of *i*-th and *j*-th electrons and J_{ij} is the exchange constant between them, i.e. the strength of the exchange interaction, which has units of energy per unit volume. In conjunction with equation (2-1), the exchange constant J_{ij} will be positive for ferromagnetic materials, which implies that the spins of the corresponding electrons prefer to align parallel to each other. In case of a negative exchange constant, the favourable state is that, in which the adjacent spins are aligned in an antiparallel way, which is the case for

antiferromagnetic materials. Generally, the exchange interaction is the strongest relevant interaction within a ferromagnetic system.

In ferromagnetic 3d transition metals, like Co, Fe or Ni, the itinerant electrons are the main cause of the net magnetic moment in solids and one needs to describe ferromagnetism within the framework of the energy band model of electrons. As a consequence of the Coulomb repulsion and the kinetic energy of electrons, the bands with opposite spin may exhibit a shift in between each other, known as the exchange split, which gives rise to a non-vanishing magnetic moment. This spontaneous ferromagnetism, due to a band splitting is commonly described by the Stoner criterion.[35,sect.7.3]

In the description so far we have considered that the magnetization is completely isotropic. For instance, in the Heisenberg Hamiltonian, energy levels do not depend on the absolute spatial direction of the spins. However, in ferromagnetic systems, spins or magnetic moments may have preferential orientations, which results in a spatial anisotropy of the total energy. A common source of anisotropy is the magnetocrystalline anisotropy[36,sect.5.2.]. This is caused by a combination of spin-orbit coupling and the crystallographic field. The spin-orbit interaction arises due to coupling of the orbital moment, resulting from the motion of the electron around the nucleus and the spin angular momentum. Specifically it can be expressed it terms of a scalar product of the orbital and spin angular momentum. On the other hand, the crystal lattice has certain symmetries and these symmetries are reflected in the electron orbitals due to the attractive or repulsive interactions exerted on them by the electric field created by all nearby ions. At least, this is the case for the orbitals that are involved in the chemical bond of the solid. As a consequence, the spin-orbit coupling will lead to an energy contribution that reflects the symmetry of the crystal lattice and causes the fact that spin orientations along certain crystallographic orientations are energetically favourable. Depending on the crystal symmetry, the magneto-crystalline anisotropy can be uniaxial, biaxial, cubic, etc. Also, it can be very weak, so that it can be considered effectively absent. Systems, which do not exhibit any preferential orientation, are the so-called magnetically isotropic systems.

Anisotropy free energies can be written as phenomenological expressions, which are actually power series expansions of the magnetization orientation that take

into account the crystal symmetry. Specifically, the dependence of the free energy as a function of the magnetization orientation is given by equation (2-2) for a system with hexagonal close packed (hcp) crystallographic structure, which is one particular case of uniaxial symmetry [36 sect. 5.2.2]:

$$E_k = K_0 + K_1 \sin^2 \alpha + K_2 \sin^4 \alpha + higher\ order\ terms$$

(2-2)[c].

Here, K_0, K_1, and K_2 are anisotropy constants of different order and their dimension is given in energy per unit volume. α is the angle between the magnetization and the anisotropy axis. Considering that in an hcp crystallographic structure the anisotropy axis is along the *c* axis, α denotes the angle between the magnetization and *c* axis. Higher order anisotropy terms can be included in the series expansion beyond the terms shown in eq. (2-2). In these higher order terms, the azimuthal orientation in the basal plane of the hcp lattice come to place as well. Nevertheless, the values of the K_i are generally rapidly decreasing with their order, making the series expansion of equation (2-2) useful in the first place and in fact, it is usually possible to truncate the expression after $\sin^2 \alpha$ in many cases. Moreover, when calculating the magnetization direction, the K_0 anisotropy constant can be also neglected, since it does not vary with the magnetization direction and it does not contribute to the location of the energy minima in terms of the magnetization orientation. In case, only the first order anisotropy constant is relevant, eq. 2-2 simplifies to

$$E_k = K_1 \sin^2 \alpha$$

(2-3),

so that the anisotropy energy has two minima at α = 0º and α = 180º along the anisotropy axis for $K_1 > 0$. This type of anisotropy is known as easy-axis (EA) magneto-crystalline anisotropy and in this case the orientation where it is hard to magnetize is known as the hard axis (HA). In contrast, for $K_1 < 0$ the anisotropy energy has one minimum at α = 90º, which corresponds physically to the entire plane perpendicular to the magneto-crystalline anisotropy axis. In this case, there is no

[c] Despite the fact that the equation (2-2) has the drawback of not being an orthogonal or orthonormal expansion, this is the most commonly used form. Therefore, it will be used in this thesis as well.

preferable axis, but instead there is a preferable plane known as easy plane magnetocrystalline anisotropy.

For a complete description of the energy of a ferromagnetic material one needs to take into account also the magnetostatic interaction. In ferromagnetic bodies each magnetic moment represents a magnetic dipole and the dipole-to-dipole interaction gives rise to a magnetostatic energy. Correspondingly, the magnetostatic energy describes the interaction of the magnetic field created by the magnetization distribution of the sample itself and the actual magnetization[35,sect.6.7.4.]. For a system with *N* magnetic moments it is given by

$$E_s = -\frac{M_s}{2N}\sum_{i}^{N} \hat{m}_{a_i} \cdot \vec{H}_{s(i)}$$

(2-4)[d],

where $\hat{m}_{a_i}$ is the atomistic lattice magnetic moment's unit vector, $\vec{H}_{s(i)}$ is the stray field vector or magnetostatic field vector at $\hat{m}_{a_i}$ and M_s is the saturation magnetization. The magnetostatic energy is also known as demagnetization energy, because it has the tendency to cause domain states (see sect. 2.2.) and thus the net demagnetization of a ferromagnetic body. Under special circumstances, specifically when the magnetization is uniform inside a sample, the magnetostatic energy takes the form of an effective anisotropy and it can be considered as a part of the anisotropy energy, which is known as a shape anisotropy.

There are also other possible energy contributions, specifically ones that originate from the coupling of the magnetic degrees of freedom to other aspects of the solid, such as for instance the magneto-elastic coupling energy[36,sect.5.3.2.]. The magneto-elastic coupling energy denotes a change in the preferred direction of the magnetization due to an applied stress or vice versa, when the relative position of the magnetization with respect to the lattice changes, the system may spontaneously deform its shape to minimize its joint magnetic and elastic energies. However, in the physical systems that are considered in this thesis the magnetoelastic effects can be

[d] The prefactor 1/2 in eq. (2-4) appears because the magnetostatic energy is a self-energy and one needs to avoid double counting because each magnetic moment contributes as a field source and as a moment.

treated as effective anisotropy effect, so that they can be described within the framework of the anisotropy energy discussed above.

When an external field is applied to a ferromagnetic body, the magnetic moments inside the body try to align with this external field, which is described by another energy term. The energy term arising from the interaction between the magnetic moments inside the system and the external field is called Zeeman energy[34,sect. 2.5.3.] and is given as

$$E_z = -\frac{M_s}{N}\sum_i^N \hat{m}_{a_i} \cdot \vec{H}$$

(2-5),

where $\vec{H}$ is the externally applied field vector.

Overall, the total free energy of a ferromagnetic body with *N* magnetic moments and uniaxial magnetocrystalline anisotropy can be given by,

$$\begin{aligned} E &= E_{ex} + E_k + E_d + E_z \\ &= -\frac{J}{2N}\sum_i^N \sum_{j\neq i}^{NN} \hat{m}_{a_i} \cdot \hat{m}_{a_j} \\ &\quad + \frac{K_1}{N}\sum_i^N \sin^2 \alpha_i - \frac{M_s}{2\mathrm{N}}\sum_i^N \hat{m}_{a_i} \cdot \vec{H}_{s(i)} - \frac{M_s}{N}\sum_i^N \hat{m}_{a_i} \cdot \vec{H} \end{aligned}$$

(2-6)

where *J* is the exchange coupling constant and $\hat{m}_{a_i}$and $\hat{m}_{a_j}$ are the unit vectors of atomistic lattice magnetic moments, where *i* denotes each magnetic moment in the system going from 1 to *N* and *j* represents each of the nearest neighbours, *NN,* of *i*. K_1 is the magnetocrystalline anisotropy constant[e], α is the angle between the magnetization and the anisotropy axis, M_s is the saturation magnetization, $\vec{H}_{s(i)}$ is the magnetostatic field, originating from the magnetization distribution itself and $\vec{H}$ is the applied field. Generally, it is not possible to find simple solutions for $\hat{m}_{a_i}$that minimize the above energy expression, because the different energy contributions are typically not minimized by the same magnetization distribution. Moreover the long-

[e] Higher order terms have been neglected here.

range non-linear character of the magnetostatic interaction makes it even more difficult to find a solution of the problem.

2.2. Magnetization reversal processes

Magnetization reversal refers to the complete process of magnetization inversion from positive magnetic saturation to negative magnetic saturation or vice versa, which commonly occurs when sweeping an external applied field with sufficient strength and low frequency to align the magnetization uniformly with the field direction[36]. If the external applied field is swept back and forth the projection of the magnetization along the field typically shows a hysteretic behaviour (fig. 2-2), whose hysteretic part results from the fact that the system can populate multiple local free energy minima for a certain field range (see sect. 2.2.1.1.).

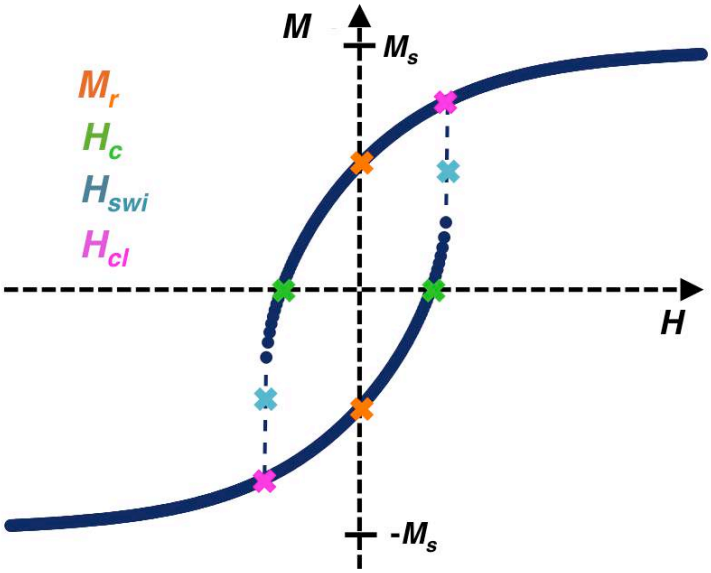

Figure 2-2: Simulated *M*(*H*) hysteresis loop using the SW model (sect. 2.2.1.1) at an applied field angle of 60º away from the *EA*. Orange crosses represent the remanent magnetization values, green crosses the coercive field points, blue crosses the switching field and pink crosses the closure field.

Figure 2-2 shows an example of a hysteresis loop, where the magnetization projection along the applied field axis versus the applied field strength is shown. If initially a strong positive external field is applied, the magnetization will align or nearly align with the external field, thus exhibiting a magnetization value close to

saturation M_s[f]. When decreasing the applied field from positive values towards zero, the magnetization still shows a positive value at zero applied field, which is called remanence or remanent magnetization M_r (orange crosses in fig. 2-2). Indeed, a negative field is needed to bring the magnetization state towards zero. This necessary field to have zero magnetization is known as the coercive field H_c (green crosses in fig. 2-2), and it gives an account of the hardness of the magnetic material. Upon reversal of the applied field to the opposite direction, the magnetization might switch, presenting a discontinuous jump in the M (H) dependence (dashed lines in fig. 2-2). The field where this discontinuous jump occurs is called the switching field (H_{swi}) (blue crosses in fig. 2-2). For even higher applied fields, M (H) becomes a single-valued function and the minimum field at which such a single-valued relation is reached, is known as the closure field (H_{cl})[g] (pink crosses in fig. 2-2)[14].

M(H) hysteresis loops and magnetization reversal have been some of the most enduring symbols of ferromagnetic materials. However, except for a few cases, it is not possible to predict macroscopic M(H)-curves of arbitrarily shaped ferromagnets in a quantitative manner. Overall, the hysteresis loop shape and magnetization reversal processes are related to the rather complex landscape of the free energy. As a consequence of this complexity, the magnetization reversal can proceed by different paths and thus the hysteresis loop shape is difficult to predict. In the following the main mechanisms that may show up in magnetization reversal are classified and described.

Coherent rotation

The coherent rotation[36,chapt.8] process can be described by a single magnetization vector, which rotates continuously as the result of a competition between anisotropy energy and the Zeeman energy when their directions are not collinear. Fig. 2-3 shows an example of the schematics of coherent magnetization

[f] In the case of a system showing uniaxial anisotropy, in order to completely saturate the system the field needs to be applied along the anisotropy axis or perpendicular to it. For any other arbitrary orientation, the magnetization only approaches asymptotically the saturation as the field strength is increased, since the torque on the magnetization itself exerted by the anisotropy interaction does not allow the magnetization to align completely with the external field.

[g] Many times the closure field coincides with the switching field, as in this case.

rotation[h]. In this case illustrated here, the field is applied 80° away from the *EA*, β = 80°. Here, β is given by the angle between the applied field and the EA. For sufficiently large applied field, the magnetization will be almost aligned with the externally applied field, thus α will be close to 80°. Upon a decrease of the external applied field strength, the torque created by it, will decrease and the torque created by the anisotropy field will become more and more significant, rotating the magnetization towards the EA, until it becomes completely aligned with it for $H = 0$.

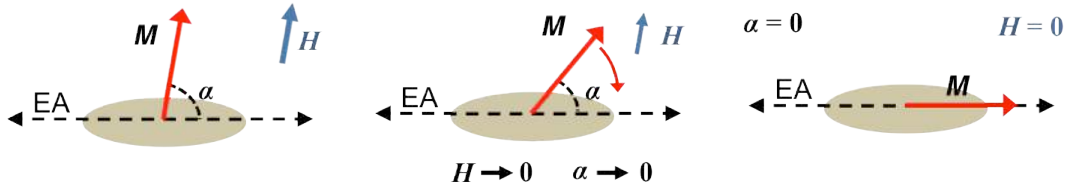

Figure 2-3: Schematic of the coherent rotation mechanism as result of a magnetic field of varying strength applied 80° away from the EA.

This magnetization reversal mechanism is reversible, so that if the external field is applied again in the initial direction, the magnetization will rotate back through the same configurations for same applied field strengths.

Magnetization switching

The magnetization switching arises from the magnetization jumping from a local energy minimum to a global energy minimum at a certain applied field strength and represents a discontinuity in M (H) dependence.

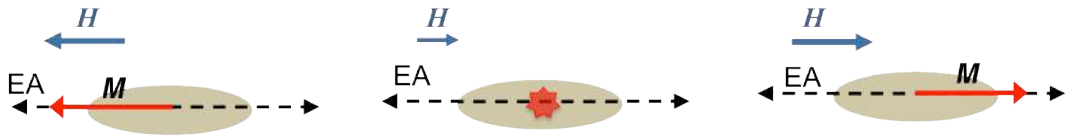

Figure 2-4: Schematic of the magnetization switching mechanism for applied field along the EA.

This causes the magnetization to orientate with the global energy minimum without passing through intermediate orientations. A schematic of the magnetization switching mechanism can be observed in fig. 2-4 (from left to right). Initially

[h] This is the simplest case of rotation, where a uniform magnetization state is considered. However rotation can also happen in non-uniform magnetization states or in a non-uniform manner. Moreover, there exist more types of rotation, apart from the coherent rotation, such as, curling rotation or buckling rotation [34,sect.7.3.].

magnetization is aligned with the external applied field and at certain opposite applied field strength, the magnetization will change abruptly its direction.

This magnetization reversal mechanism is irreversible, namely if the external field is applied again in the initial direction, magnetization will not switch back through the same steps for the same applied field strengths. This is a consequence of the free energy having multiple minima and therefore disallowing the system to achieve thermal equilibrium up to a certain applied field value. If the system would be in thermal equilibrium throughout the whole applied field process, no hysteresis should occur.

Similar discontinuous jump processes happen also locally in macroscopic samples, which are the origin of the so-called Barkhausen noise[36,sect.9.3.].

Domain formation

If the only energy terms present in ferromagnetic systems were the exchange and anisotropy energy, then all magnetic moments would be always aligned in the same direction. At short distances exchange dominates and yields to parallel alignment of the magnetization. Anisotropy has the additional effect of favouring the alignment along certain preferred directions. However, Weiss discovered in 1907 that in ferromagnetic bodies different regions with different magnetization orientations coexist, which could result in a vanishing net magnetization as a macroscopic sample average. In this case, the magnetization is aligned in nearby regions, while this ordering is lost for longer distances within the systems. The regions of alignment, in which the magnetization is uniform, are called domains[36,chapt. 7] and different domains are separated by regions, in which the magnetic moments rotate coherently, known as domain walls. Domains exist because the magnetostatic energy in large-scale systems strongly favours the formation of magnetization configurations, for which the net magnetization is close to zero.

Figure 2-5 shows the process of domain formation. In fig. 2-5 (a) a system is considered, in which a uniform magnetization aligns with its EA, so that anisotropy energy and the exchange energy are minimized. However this configuration results in a large stray field, which increases the magnetostatic energy contribution. Therefore, in order to keep the magnetostatic energy as low as possible, one might lower the stray field by the formation of several antiparallel domains (fig. 2-5 (b)). However,

the misalignment of the moments within the required domain walls leads to an energy cost due to exchange interaction and anisotropy. A further decrease of the magnetostatic energy can be achieved due to the formation of boundary domains (fig. 2-5 (c)). In this case, however, the exchange and anisotropy energies are increased even further. Overall, domain formations may be expected until the energy required to establish a domain wall is greater than the reduction in magneto-static energy in the entire domain pattern.

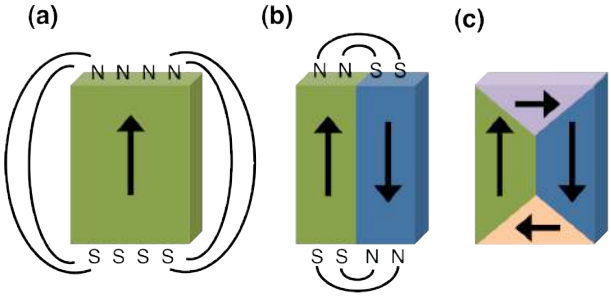

Figure 2-5: Domain formation due to magnetostatic energy. (a) shows a uniform magnetization state with large stray fields, (b) show an antiparallel bi-domain magnetization state with smaller stray fields and (c) shows so-called Landau domain structure, in which closure domains are formed.

A possible formation of domains during magnetization reversal is the outcome of a competition of the exchange energy, anisotropy energy, the magnetostatic energy and Zeeman energy. As the total energy depends on the sample shape, size and its relation to the easy axis, the occurrence of domain formation is closely related to the geometrical features and internal structure of the system.[37]

2.2.1. Magnetization reversal in confined structures

Confined systems or more specifically nanoscale structures have at least one dimension in the nanometre range. Many intrinsic magnetic properties may differ appreciable from bulk material at this scale, such as for instance, Curie temperature or anisotropy.[12,38,39] Moreover, in systems with reduced dimensions, the magnetostatic energy minimization due to domain creation, usually does not overcome the increase in exchange energy caused by domain wall formation. Thus along the reduced direction single domain magnetic configurations are usually more favourable as a consequence of such spatial confinement. In conventional magnetic materials the single-domain limit along the reduced direction depends on the specific material parameters. However, usually this limit is somewhere below the micrometre scale.

For instance, the theoretical limit to have a single domain state in hcp Co spherical systems is around 26 nm in diameter size[40,sect.2.1.].

2.2.1.1. Stoner Wohlfarth model

One of the most relevant simplified cases of magnetization reversal is the so-called Stoner Wohlfarth (SW) model[41], which represents an approximative description for particles with uniform magnetization. This model is especially relevant for small particles, where spatially non-uniform states can be ignored in all directions[i]. In this case, the energy is given by the sum of exchange energy, anisotropy energy and Zeeman energy, in which case the total anisotropy energy may be a combination of magnetocrystalline and shape anisotropy energy. The simplest case to consider hereby is a uniaxial magnetic anisotropy, which is also the most appropriate model to describe most of the samples shown in this thesis. If one assumes only the first order (K_1) anisotropy constant, the SW model free energy is given by

$$E_{SW} = E_{ex} + K_1 \sin^2 \alpha - MH\cos(\alpha - \beta) \qquad (2\text{-}7)^{j}$$

where α is the angle between the magnetization and the anisotropy EA and β is the angle between the field direction and the anisotropy EA. In the SW model, the typically very large exchange energy (E_{ex}) can be ignored because it does not have any angular dependence following the condition of a uniform magnetic state, meaning that the exchange energy is always minimized independent from the magnetization vector orientation. Additionally, equation 2-7 assumes that the magnetization vector is restricted into the plane that is created by the field vector and the EA, so that the azimuthal component can be ignored. Even though, this is not the most general

[i] In single domain systems, the system is too small to allow for stable multiple domain states, but it might nonetheless allow for possible modest deviations from uniformity, such as bending of the magnetization orientation at the interfaces. In contrast, in particles with uniform magnetization the magnetization is collinear along the entire system, without any deviation from it. As one makes particles smaller, first the single domain condition is fulfilled and only at even smaller dimensions the (nearly) uniform state condition can be satisfied.

[j] The uniform state is not related to the simple anisotropy term here and one can consider more complex anisotropies (even misaligned shape and magneto-crystalline anisotropies together).

magnetization orientation geometry, it is the lowest energy for M.[k] Figure 2-6 shows the schematic of the model, considering a uniaxial system, namely eq. (2-7).

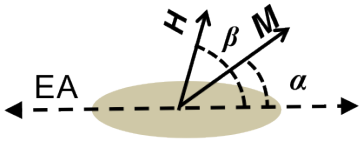

Figure 2-6: Representation of the SW model described by eq. 2-7.

Figures 2-7 (a)-(c) show calculated free energy profile colour maps of eq. (2-7), as a function of the applied field H normalized to the anisotropy field H_K and the angle between the magnetization and the EA, α. The H_K value for the uniaxial SW model, in which only the first anisotropy constant is considered, is equal to $2K_1/M_s$. Specifically figures 2-7 (a)-(c) show $E(H/H_K, \alpha)$ colour-coded maps for applied fields along the EA (fig. 2-7 (a)), 45° away from the EA (fig. 2-7 (b)) and along the HA (fig. 2-7 (c)). Figures 2-7 (d)-(f) show the respective hysteresis loops, namely the projection of the magnetization along the applied field direction normalized to the saturation magnetization as a function of H/H_K. Within the $E(H/H_K, \alpha)$ colour maps, the black dots guided by dashed lines represent the anticipated path that the magnetization vector will take for applied fields going from positive to negative saturation states, if the magnetization vector will follow always the nearest local minimum. In the case of the applied field along the EA ($\beta = 0°$) one can observes that the magnetization sits always along the EA, namely at $\alpha = 0°$ or $\alpha = 180°$. When a strong enough positive field is applied, the magnetization lies in the only existing energy minimum ($\alpha = 0°$), which is the global minimum and which coincides with the applied field direction and EA. Upon the removal of the external applied field, i.e. $H/H_K = 0$, two equal energy minima appear at $\alpha = 0°$ and $\alpha = 180°$. However, if there are no thermal excitation or tunnelling processes feasible, the magnetization only populates one energy minimum at this point, which is the same energy minimum in which it was located previously. Therefore the magnetization state in each moment will be determined by the field and system history. Thus, in this case the magnetization will lie at $\alpha = 0°$. When a negative external magnetic field is applied

[k] In order to calculate effects that include thermal excitations, one needs to take all magnetization degrees of freedom into consideration.

subsequently, i.e. a field is applied at the 180° orientation, the energy minimum at α = 0°, in which the system lies, moves up in energy, thus becoming a local minimum only while the other one at α = 180° is further reduced in its position, and therefore represents the absolute minimum. At a certain negative field strength (for applied fields along the anisotropy axis, this value is equal to H_K), the local minimum in which the system has been located up to now disappears, so that the magnetization switches to the global minimum at α = 180° in a discontinuous jump (represented by the dashed line in fig. (2-7) (a)).

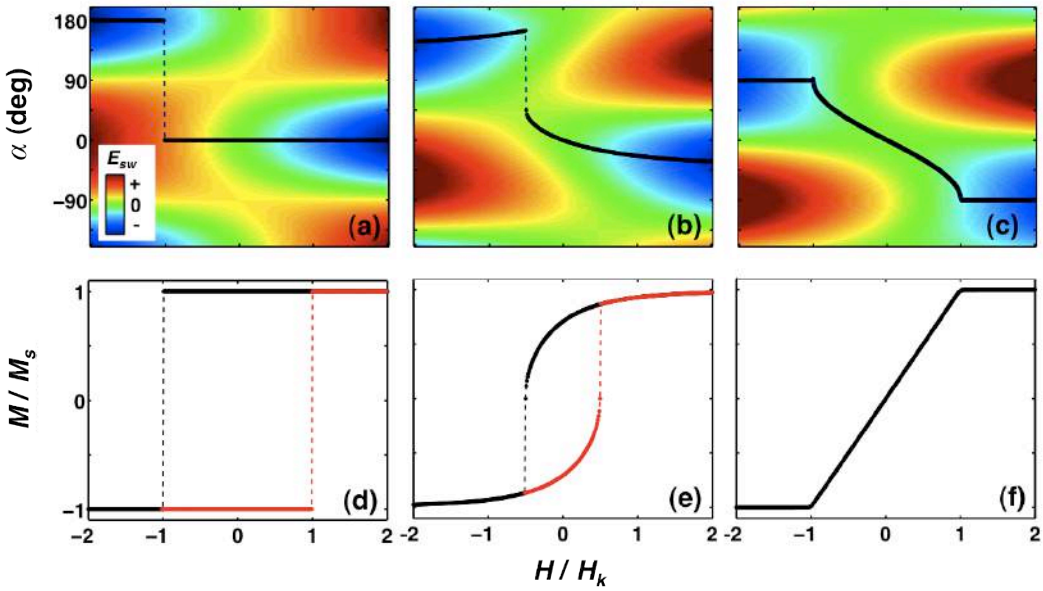

Figure 2-7: SW model representation; (a)-(c) free energy profile colour maps calculated by using eq. (2-7) as a function of applied field normalized to the anisotropy field and the magnetization angle with respect to the EA. Specifically (a) shows the free energy profile for an applied field along the EA, (b) for an applied field 45° away from the EA and (c) for an applied field along the HA. Black dots guided by dashed lines on top of the colour maps represent the magnetization position, which is given by the nearest local energy minimum for applied fields from positive to negative saturation. (d)-(f) show hysteresis loops for the applied field along the EA (d), for an applied field 45° away from the EA and (e) for the applied field along the HA (f). In (d)-(f) black colour indicates the *M*(*H*) branch for an applied field going from positive to negative saturation and red colour indicates the *M*(*H*) branch for an applied field going from negative to positive saturation.

For even higher positive applied field values the system will occupy the only minimum that exists. If one considers now that the applied field is swept from negative saturation to positive saturation, the magnetization will stay at α = 180° up to the field strength, at which this minimum disappears, namely up to an applied field equal to $H_K = 2K/M_s$. This behaviour is represented by square hysteresis loops, where the magnetization takes values of M_s or $-M_s$ only (fig. 2-7 (d)) and it shows an abrupt magnetization reversal at $\pm H_K$.

When the magnetic field is applied in directions other than along the EA, such as β = -45°, for instance, the position of the energy minimum rotates towards to the EA (fig. 2-7 (b)) upon reducing the external magnetic field. This rotation is represented by a continuous reduction of the absolute magnetization value in the hysteresis loop, which only means a decrease of the projection of the magnetization along the applied field direction (fig. 2-7 (e)). Also in this geometry, the occupied energy minimum disappears, i.e. is destabilized, at a certain field strength of opposite sign, so that the magnetization will switch to the global minimum exhibiting in a discontinuous $M(H)$ jump. For even higher reverse fields this global energy minimum will move towards the applied field direction, i.e. in this case towards α = 135°. This rotation is also visible in the hysteresis loop, where the absolute value of the magnetization increases towards M_s after the magnetization switch (fig. 2-7 (e)). For applied fields along the HA (β = 90°) the magnetization lies always in one of the two equivalent global minima, which move their positions upon applied field changes (fig. 2-7 (c)). In this case the magnetization reversal does not undergo any switching and correspondingly, there is no hysteretic behaviour (fig. 2-7(f)).

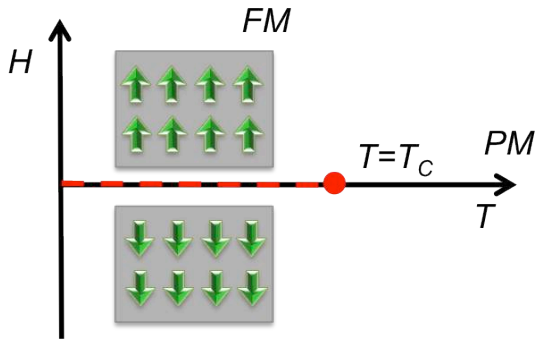

Figure 2-8: Schematic of the phase diagram of a ferromagnet as a function of temperature and externally applied field.

The discontinuous jump in M (H) dependence is related to the first order phase transition that ferromagnetic systems undergo at zero field. Figure 2-8 show a phase diagram of the magnetization as a function of temperature and externally applied field. As described in connection with fig. 2-1, the magnetization undergoes a second order phase transition as a function of temperature, for which the critical temperature above which the ferromagnetic system (FM) exhibits a paramagnetic state (PM) is known as Curie temperature (T_C). If one analyses now the magnetization as a function of an externally applied field below T_C, the magnetization undergoes a

first order phase transition, where for positive applied fields, the magnetization is positive and for negative applied fields, the magnetization is negative (as shown in fig. 2-8). However, there exists a field range, in which multiple energy minima can be populated (as seen in fig. 2-7), which is called the coexistence region and it is this coexistence region that is the origin of hysteresis. For the SW model, this is a bistability region, because only two (meta)stable states exist.

2.2.1.2. Thin films

In thin films, the magnetization will try to orient within the film plane in order to minimize the demagnetizing field, at least if the magneto-crystalline anisotropy is not large enough to overcome this effect. If one considers uniform magnetization states only, one can give the magnetostatic energy for thin films as follows,

$$E_s = 2\pi M_s^2 \cos^2 \alpha_N \qquad (2\text{-}8),$$

where α_N is the angle between the film normal and the volume averaged magnetization vector M[42].

If one considers a material with out-of-plane uniaxial magneto-crystalline anisotropy, for which the second and higher order anisotropy constants can be ignored, the total magnetostatic and magneto-crystalline energy will be given by

$$E_{s+k} = (2\pi M_s^2 - K_1) \cos^2 \alpha_N \qquad (2\text{-}9),$$

which has the form of an effective anisotropy[l]. In case, the magneto-crystalline anisotropy constant K_1 is larger than $2\pi M_s$, a uniform magnetization state would be energetically minimized by aligning along the surface normal, while otherwise it will be more favourable for magnetic moments to lie in the plane of the film. Even though eq. 2-9 is a good guideline for the classification of in-plane and out-of-plane oriented magnetic films, especially in the ultrathin film limit, the actual behaviour can be slightly different and more complicated due to domain formation.

[l] Please note that the anisotropy energy, specifically $K_1 \sin^2 \alpha_N$ can be transformed to $K_1 - K_1 \cos^2 \alpha_N$ where the first term is ignored in the energy minimization, since it is constant and does not vary with the magnetization angle, just as in the case of K_0 in eq. 2-2.

Furthermore, ultra-thin films exhibit another anisotropy. It is the so-called surface anisotropy[34, sect. 8.2.2.], caused by the fact that the symmetry of the electron orbitals is broken at the surface or interface, resulting in an additional anisotropy related to the crystal surface structure. Typically the surface anisotropy energy is written in the form of

$$E_{sf} = \frac{2K_s}{t_{hk}} \sin^2 \alpha$$

(2-10),

if one considers the surface contribution as being factored into a film thickness averaged volume contribution. In extremely thin films, where t_{hk} is very small, the surface anisotropy can dominate the total anisotropy. For example, Co films of a few monolayer thicknesses, grown on top of a Pt layer, can have an effective anisotropy that is so strong that it overcomes the shape anisotropy and results in a magnetization state along the surface normal[43] (see chapter 7).

However, as mentioned before, for thicker films the total anisotropy including the shape effect generally results in an in-plane magnetization due to the magnetostatic or demagnetizing field. Nevertheless, as the thickness increases even further for samples with out-of-plane magneto-crystalline anisotropy, it might be energetically favourable to form stripe domains, which have a local magnetization component out-of-plane.[44]

Most of the thin film systems shown in this thesis have a thickness of 30 nm, i.e. a thickness that it is not significantly affected by the surface anisotropy and, furthermore they are designed to exhibit a uniaxial magneto-crystalline anisotropy with the easy axis in the plane of the film. Thus, considering strong demagnetization and in-plane magneto-crystalline anisotropies, the film magnetization can be restricted to in-plane orientations only. Although in this case in-plane demagnetization fields still exist, they are very small, so that one has a good justification to neglect them. Under this assumption, thin films should behave quite similar to the SW-model described earlier. For applied fields along the EA, the reversal would take place for a field strength corresponding to $H = 2K_1/M_s$, at least if the material is completely homogeneous and without defects and if one neglects the possible overcoming of the energy barrier due to thermal fluctuations. However, in

real thin films, defects will be always present, as well as thermal noise, leading to thermal activation and locally reduced anisotropy values and therefore to a modified reversal behaviour, especially lower switching field thresholds. When this local switching field is reached, a reversed domain will nucleate locally and subsequently, this reversed domain will expand throughout the sample and cause a complete reversal of the film if the applied field is large enough to overcome the domain wall propagation barrier.

For an applied field away from the EA, the magnetization reversal is usually initiated by coherent rotation as in the case of the SW model, up to the point where a switching process or multiple switching processes are triggered, which usually also proceed by domain nucleation and propagation.

For samples, which do not exhibit very precise crystalline alignment and correspondingly strong uniaxial in-plane magneto-crystalline anisotropy, the magnetization reversal will be even more complex as described in sect. 4.1.3., where complex meta-stable multi-domain states are being formed.

2.2.1.3. One dimensional nanostructures

The term one dimensional nanostructures refers to systems that are confined to the nanometric scale in two directions, such as nanowires. Therefore, these structures are able to form domains only along the third direction, if at all. In such one dimensionally elongated structures, the demagnetization field has the tendency to align the magnetization along the long axis in order to decrease the stray fields in the case of small magneto-crystalline anisotropy and without an external field being applied. Therefore, in this case nanowires and related structures will exhibit a large shape anisotropy, which has to be taken into account in the magnetization reversal process. In cases of nanostructures with magneto-crystalline anisotropy or surface anisotropy, as in the case of Co/Pt multilayer structures studied in sect 7.3., the overall energy landscape becomes more complicated due to the possible shape and surface anisotropy competition.

2.3. Dynamic aspects of magnetization reversal

Up to now the magnetization reversal has been discussed based upon energy minimization, assuming that the system always follows a succession of energy minima states. However, under these considerations two important aspects that may influence the reversal process have been omitted, namely how the system will approach the equilibrium upon changing external parameters such as the applied field strength and how the magnetization will react to rapidly time-varying fields. In the discussions above, it has been considered that the applied magnetic field variations are much slower than the relaxation time of the system, and that the magnetization is able to follow the externally applied field, when it is energetically favourable. Moreover in the static picture based on the SW model, the model predicts a jump of the magnetization state at the switching field, H_{si}, but it does not explain at all how this jump proceeds and how the energy is dissipated from the system. Correspondingly, the discussion about nucleation domains and domain wall propagation is a qualitative, empirical picture, which cannot be fully understood by energy minimization alone.

In order to explain properly how the system approaches the equilibrium state one needs to take into account the dynamics of the magnetic system with a proper description of the temporal evolution of the magnetization. One approach to describe these dynamic aspects is by means of the Landau Lifshitz Gilbert (LLG) equation [36,sect. 6.2.3.], which gives an equation of motion for the magnetization in an effective field, which incorporates the energetics of the system and includes a damping effect that allows to dissipate the energy. Indeed, without energy dissipation, the discontinuous jump in the magnetization state could not happen, since the magnetic system needs to transfer the energy somehow out of the magnetic sub-system in order to fall into the next energy minimum. The LLG equation is briefly discussed in the following. It is known that any local magnetic moment[m] M carries a corresponding angular momentum and since the torque exerted by the field is equal to the rate of change of the angular momentum, one can write

[m] Here, local means a volume element small enough so that it can be assumed to be well represented by a uniform magnetization. Hereby, the magnetization value M in the grain is given by its mean field value.

$$\frac{d\vec{M}}{dt} = \gamma\vec{M} \times \vec{H}_{eff}$$

(2-11),

where γ is the gyromagnetic ratio, which relates the magnetic moment to its angular momentum. $\vec{M}$ is the local magnetic moment vector and H_{eff} is an effective field that is defined at each point inside the ferromagnetic body, and which contains the externally applied field, the magnetostatic field and contributions arising from exchange and anisotropy energy, referred to as exchange field and anisotropy field. Specifically the effective field can be expressed as[36,sect. 6.2.1.]

$$\vec{H}_{eff} = -\frac{\partial E}{\partial \vec{M}}$$

(2-12).[n]

Equation (2-11) describes a motion of precession that the magnetic moment follows around the direction of the effective field. However, this description is applicable only to magnetic moments that do not dissipate energy out from the magnetic system. In this case, if the magnetization is not initially in an equilibrium state, it will start precessing around the effective field axis and it will never approach equilibrium (fig. 2-9 (a)), because eq. 2-11 describes a purely gyroscopic effect with no dissipation mechanism.

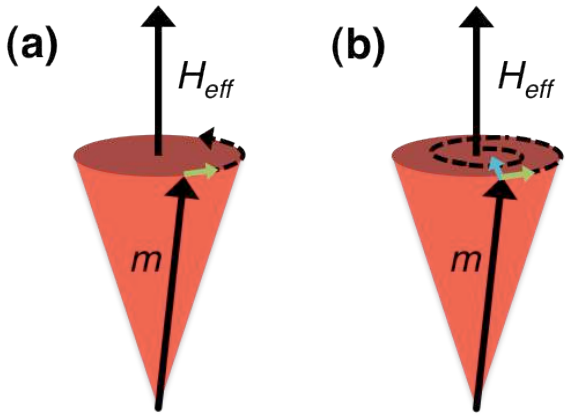

Figure 2-9: Schematics of the motion of a magnetic moment. (a) shows the un-damped precessional motion and (b) shows a damped precessional motion.

[n] Equation (2-11) and (2-12) can be local equations valid at every point inside a macroscopic body.

One way of including the energy dissipation is by introducing a damping or magnetic relaxation term. A phenomenological description that contains such damping is given by

$$\frac{d\vec{M}}{dt} = \gamma\vec{M}\times\vec{H}_{eff(i)} - \frac{\gamma\alpha_G}{M_s}\vec{M}\times\frac{d\vec{M}}{dt}$$

(2-13),

where α_G is the Gilbert damping constant. Equation (2-13) is known as the Landau-Lifshitz-Gilbert (LLG) equation and allows the description of how the magnetization evolves with time under an effective field by gradually removing energy from the magnetic sub-system (fig. 2-9 (b)).

Even if there are a few examples where the LLG can be solved in closed form, so that one can explore the complete dynamic evolution, for most sample geometries and situations, however, one has to resort to a numerical solution, which limits the accessible time frame. Also, the magnetostatic interaction is a limitation, because it has long-range character and thus requires most of the computational resources. Therefore, unfortunately numerical solutions of the LLG equation are limited to short time scales only.

For longer time windows, one can model the dynamics of ferromagnetic systems by means of Monte Carlo methods using different types of Hamiltonians. The Monte Carlo method is a stochastic technique to estimate the magnetic population using a probability distribution. It has been traditionally used to describe thermal equilibrium effects[45,46]. However, because the starting state can be randomly chosen, states away from equilibrium can be selected and their dynamic evolutions can be followed[47,48]. Correspondingly, non-equilibrium phenomena and their dynamics can be studied as well, when the external control parameters are varied faster than the system can approach equilibrium within the Monte Carlo computational framework.

In order to simplify the calculation of magnetization dynamics even further, other methods are being used. For instance, one common form to get an approximate solution is the mean field approximation[49]. The mean field approach consists in suppressing magnetization fluctuations terms. In its most common form, it assumes

that all magnetic moments in the system feel an identical field produced by all their neighbours[o]. While the accuracy of such a mean field approximation might vary, it generally allows for a closed form or simple numerical solution that enables the study of the phase space in great detail and with high numerical precision, even though it is only a solution of this approximate (mean-field) problem[p].

[o] Nevertheless, one can use the mean field approach to perform calculation without the need for translational invariance, as is the case shown in ref. 170.

[p] Actually, the LLG is in a sense a mean field solution, because the entire interaction Hamiltonian is expressed as an effective field, a mean field. The difference here to more conventional mean field solutions is that due to the fact that the dynamics is expressively solved here, temporal fluctuations are not suppressed. However, fluctuations within each volume element are ignored or approximated by an average local magnetization, which is a (mean-field like) expectation value.

3. Experimental techniques

This chapter describes different experimental techniques that have been used during the thesis. The chapter is divided into three different sections, with the fabrication section focusing on techniques that have been used to fabricate magnetic samples, either thin films or nanostructures. Hereby, special attention is given to thin film growth and especially to the sputter deposition technique, which has been used for high quality magnetic sample growth. Section two describes techniques used for structural characterization of magnetic samples, mainly focusing in the X-ray diffractometry and reflectivity. This techniques permit a detailed crystallographic characterization and thickness calibration of the thin films previously deposited by sputter deposition system, with their results being key ingredients for correlating the crystallographic structure effects to magnetic properties. Finally, the techniques that have been used to characterize the magnetic properties are discussed in the magnetic characterization section. Among these techniques, special consideration is given to the Magneto-Optical Kerr Effect (MOKE) technique, which has been an essential component in several studies, such as, in the microscopic magnetic property analysis in Co thin films performed by MOKE microscopy as well as dynamic phase studies carried out by MOKE magnetometry.

3.1. Fabrication

3.1.1. Thin film growth

Thin films can be deposited onto a substrate by means of different techniques, such as for instance atomic layer deposition, e-beam or thermal evaporation and sputtering. Most of these techniques can be grouped into two types of deposition processes, physical vapour deposition processes and the chemical vapour deposition processes[50]. In this thesis, the sputter deposition technique has been used in order to grow thin films, which falls into the physical vapour deposition class. In this technique, the process starts with the creation of atoms or species of the desired material, which subsequently travel through a combination of plasma and gas pressure until they reach the substrate and condensate on it. Hereby, the actual growth sequence can show a wide variety of phenomena, depending on the deposited species and the substrate, their tendency to form alloys, the substrate temperature and the kinetic aspects of the growth that determine, how much time the growth front region is given to explore the relevant energy landscape. In the absence of interface alloying, one can classify different growth modes on purely energetic considerations. In this case, the growth can proceed by layer-by-layer film growth (Frank- van der Merwe growth mode), three dimensional nuclei or island formation (Volmer-Weber growth mode) or by a combination of both (Stranski-Kranstanov growth mode), depending on the specific surface energies of the materials involved.[51,sect.2.1.]. This classification scheme of the growth sequence, however, is based on equilibrium states and thus is limited to cases where the growth kinetics is not crucially important.

Except under special conditions, deposited thin films usually exhibit a polycrystalline structure due to different crystallographic orientation or orientations of each growth nucleus. Such polycrystalline thin films can display overall random crystallography, due to statistical randomness or they can show preferential orientations, i.e. a crystallographic texture. A crystallographic texture can appear for instance as a consequence of the different surface energies that different crystal orientations have.

Nonetheless, one can obtain highly crystalline films by epitaxial growth[51,sect.2.1.]. Epitaxy means that the crystallographic order of a film is being

determined by that of the substrate as a result of sufficient matching between both along the interface. In general, single crystalline substrates are needed in order to get single crystalline deposited layers. Furthermore, in order to achieve epitaxial growth, it is necessary that both materials, substrate and deposited layer, are crystallographically compatible. This can also be achieved by the use of intermediate layers of other materials to tune the initial crystallographic alignment towards the desired one. However, there are other conditions that may cause epitaxy to fail despite having a good match between the substrate and the deposited material. For instance, if one wants to grow a particular orientation of a specific surface which is not stable, even by itself, then it is generally difficult if not outright impossible to grow such an orientation, even if a perfect lattice match condition with a suitable substrate or intermediate layer exists. Also, substrate and film can have a tendency to form alloys due to a surface reaction, which then might interrupt the otherwise perfect epitaxial relation. Furthermore, in order to have epitaxial growth, clean and smooth substrate surfaces are needed, which can generally only be achieved under ultra high vacuum conditions.

Epitaxial growth technology enables the preparation on thin films of extremely good crystalline quality and with the desired crystallographic order. This fact is interesting for many technological and fundamental aspects, since many physical properties, such as, electronic, optical and magnetic properties, depend on the crystalline quality and even on specific crystalline orientations.

In this thesis, thin films of varying crystalline quality have been grown by means of actively modifying the epitaxial substrate-film relation using an ultra high vacuum (UHV) sputter deposition system.

3.1.1.1. Sputter deposition

Sputtering is a physical vapour deposition method that is widely used in thin film fabrication due to its robustness, i.e. stable operation and deposition conditions[51], which is also one of the reasons for using this technique in this thesis. It works by introducing a suitable pressure of a suitable gas, usually the chemically inert argon (Ar), into a vacuum chamber, where a self-contained Ar^+ plasma is created upon charging an electrode electrically (DC sputtering). The electrode is the target material

that is going to be sputtered. The process of sputtering itself consists in the erosion of the target material by the positively charged Ar^+ ions from the plasma. This happens, because the positively charged ions are accelerated into the negatively charged target, i.e. the cathode, so that they strike with enough kinetic energy to dislodge atoms from it. These target atoms move then ballistically away from the target (as long as the pressure in the chamber is not too high) into all directions including towards the substrate, where one intends to deposit them for the purpose of growing a film. A schematic of the process is shown in fig. 3-1.

The main reason to use a plasma is, that it continuously produces an ion flow itself, so there is no need for an external ion gun. This enables one to make the sputter deposition setup efficient and compact. Moreover, it offers the possibility to control the ions flux that is eroding the deposition material at the target in an easy and efficient way. Also, there are especially efficient designs that allow for a high ion flux based upon this overall design. Furthermore, the plasma erosion of the target does not depend on the vapour pressure of the material and thus it is especially suitable for alloy deposition or for very high melting temperature materials.

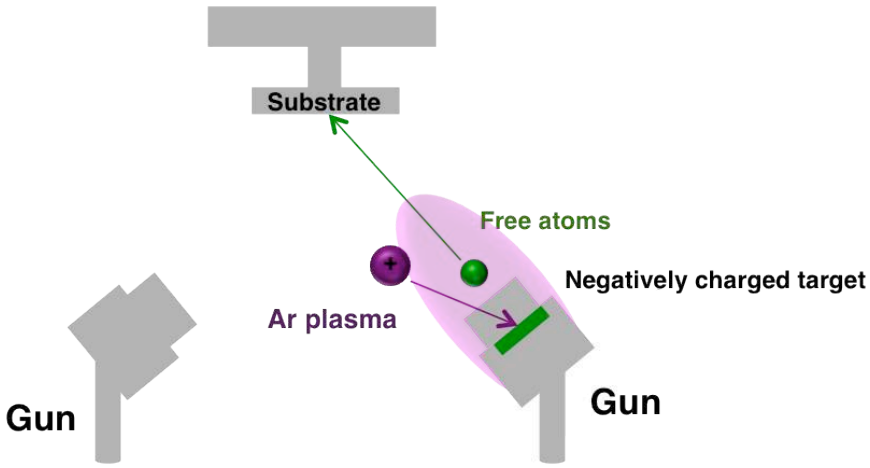

Figure 3-1: Schematic of the sputtering process by an Ar plasma.

The conventionally used sputtering technique is magnetron sputtering. It consists of a crosswise magnetic field over the cathode, which traps the electrons in orbits created by the magnetic field and thus enhance the probability to ionize neutral Ar atoms, resulting in high ion fluxes and consequently higher deposition rates. Moreover, the possibility of lower Ar pressure to create high plasma densities allows one to work at lower sputtering pressures and in consequence the sputtered particles

suffers less collisions on their way to the substrate, resulting in yet higher deposition rates. This magnetic field is obtained by placing hard magnets behind the target or cathode. Different designs of magnetrons exist in order to get the best efficiency and compatibility for different target materials[52]. However in all of them, the magnets are arranged in such a way that one pole is positioned at the central axis of the target and the second pole is formed by a ring of magnets around the outer edge of the target. The first available design was the balanced one, where all the magnetic flux created from outer magnets is compensated by the central magnet. In this configuration the plasma is confined to the close vicinity of the target and the ion and electron bombardment onto the substrate is minimal, i.e. a feature that makes this design especially useful for temperature or radiation sensitive substrates. However, in some cases an ion or electrons bombardment during growth can improve the film properties[53], a scenario that can be obtained by using the unbalanced magnetron configuration. In this configuration the magnetic flux of the inside magnets is not fully compensated by the outside ring magnets and some magnetic field lines extend towards the substrate. This results in a significant plasma density in the vicinity of the substrate and thus, a considerably increase of the ion bombardment onto the substrate.

While supplying a direct current (DC) is sufficient for metal targets in order to control its surface potential, given that all charges arriving from ion bombardment are removed by a simple current flow, this is not possible for insulating substrates and instead, the top surface of the target would become positively charged. In order to avoid this, one needs to remove the positive charging in a different fashion for insulating target materials. This is accomplished by supplying instead of DC power and alternating radio frequency (RF) power[51,sect.4.2.2.]. Hereby, positively charged Ar ions bombard the target during negative half cycle, causing sputtering. However, the bombarding ions charge the target surface positively by emission of electrons from it and by adding the ion charge directly. This charge is neutralized during positive half cycle where electron bombardment neutralizes the target. Consequently the sputtering process occurs only during the first half cycle, so that in RF sputtering the deposition rates are generally lower or even substantially lower than in DC sputtering.

Another mode of the sputtering deposition technique is reactive sputtering[51,sect.4.3.2.]. It consists of introducing a reactive gas into the chamber while

sputtering in order to achieve a reaction between the sputtered atoms and the reactive gas. This technique is usually applied to grow oxide and nitrides films, such as Al-oxide and Ti-nitride. Varying the relative pressures of the inert and reactive gases and the applied power of the sputtered material one can control the stoichiometry of the deposited film. Also, it should be mentioned that the sputtering technique allows the growth of thin film alloy materials by sputtering simultaneously from multiple targets using multiple guns.

The sputter deposition system used in this work is an ATC series UHV sputtering system from AJA International, Inc. Company. It has two chambers, both equipped with turbo-molecular pumps. One is a load lock chamber that is used to introduce substrates to the main chamber without breaking the vacuum condition within the main chamber and the main chamber itself, where the sputter deposition and other processing is done (see fig. 3-2 (a)). In the main chamber, there are 7 sputter guns, which are the containers for the target material and which are equipped with magnetrons for plasma generation and confinement. Therefore, this system allows to place 7 different targets in the main chamber and gives the possibility to grow a sequence of layers made from of up to 7 different materials without breaking vacuum. The guns are equipped with shutters that can be opened for deposition (fig. 3-2 (b) shows the inside picture of the main chamber where the 7 guns are visible, one of which having an open shutter).

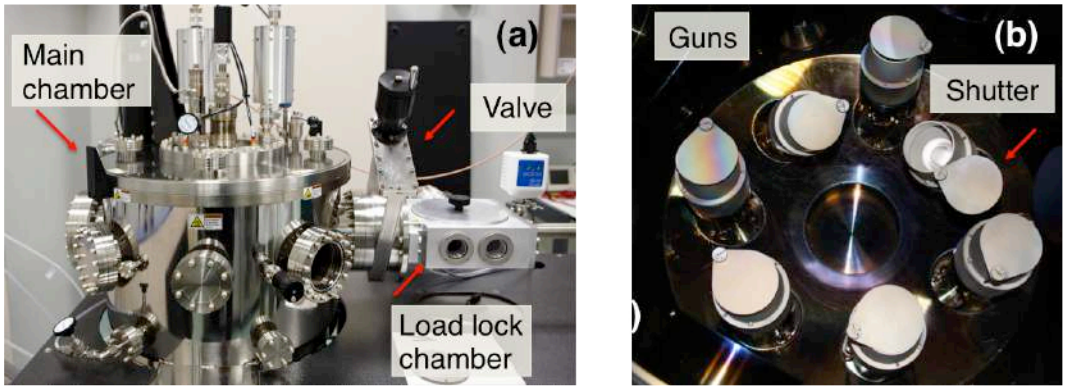

Figure 3-2: UHV sputter deposition system from AJA. (a) Outside view of the main chamber and load lock chamber. (b) Inside view of the main chamber.

In all guns, the magnetron configuration can be adjusted from unbalanced configuration (fig 3-3 (a)) to balanced configuration, which is used for especially sensitive substrates (fig. 3-3 (c)), and it can be furthermore made compatible with

magnetic targets (fig. 3-3 (b)). The balanced configuration helps the magnetic field saturate and overcome the shunting effect of magnetic target materials, thus allowing the magnetron sputter deposition of high permeability targets.

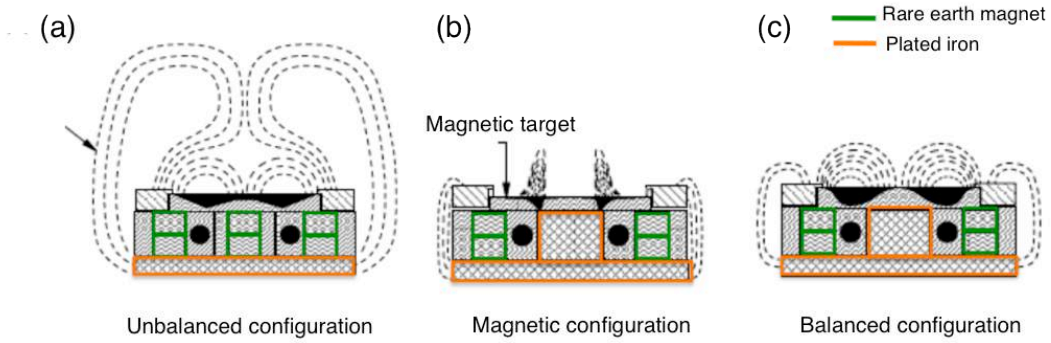

Figure 3-3: Drawing of possible magnetron configuration in the AJA UHV sputter deposition system ATC series (provided by AJA International, Inc) (a) unbalanced configuration, (b) magnetic configuration and (c) balanced configuration.

In total, the system has 2 RF and 4 to DC power supplies, so that it allows the simultaneous depositions or co-deposition of up to 6 materials for alloying purposes. The 7 sputter guns are all compatible with DC and RF power supplies. All sputter guns can be tilted to point towards the sample holder, where the substrate is placed and by this arrangement single or multiple guns are aligned to point to a common focal in the vicinity of the substrate (see schematics in fig. 3-1). This configuration allows the minimization of the time between subsequent layer deposition processes because there is no need to re-position the substrate or the guns for each deposition. Also, this geometry gives complete freedom to easily grow alloys of any number of materials in any ratio with precise control. Furthermore, during the depositions one can rotate the substrate holder, capable to hold samples of up to 4 inches in diameter, in order to achieve high uniformity. A thickness uniformity of 1 nm over a 4 inch wafer for 80 nm thick SiO_2 films has been measured, where the SiO_2 has been deposited by RF sputtering. For 20 nm thick DC sputtered Ni films, a uniformity better than 1 nm has been measured, also over 4 inch wafer test samples. Usually, the substrates used in this thesis have been around ten times smaller than these full-size wafers, which have been used in the uniformity tests. Consequently, the thickness uniformity in samples presented here is even better than these test results indicate.

Specifically, the uniformity is generally better than the precision, with which one can measure the thickness by means of X-ray reflectometry presented in section 3.2.1.

While different sputter pressures have been utilized for the film growth, here only the results for samples grown with the same pressure, namely 3 mTorr, are being presented for comparability reasons. This pressure is low enough to ensure high deposition rates and good vacuum condition but high enough to ensure a stable plasma. In order to control the sputtering pressure in the main chamber the system has a gate valve between the turbo pump and chamber that is controlled automatically. This valve allows controlling the sputtering pressure with a resolution of $1x10^{-4}$ Torr for the usual sputtering pressure ($3x10^{-3}$ Torr), so that the actual sputter pressure during a deposition sequence is very stable, typically better than ±4%.

The argon gas that has been used is 99.99% pure and the flow has been kept constant at 20 standard cubic centimetres per minute during the depositions. In addition, the system has two more inlets for oxygen and nitrogen, which are used for reactive sputtering.

The sputter system has the option to heat the substrate up to 850 °C during material deposition or after it, by means of two lamps placed on top of the substrate holder. The system achieves a temperature uniformity of better than ±1% over the entire substrate holder (4 inches of diameter). Furthermore, the temperature controller reaches a temperature stability of better than ± 2 °C for temperatures above 200 °C.

In order to characterize the deposition rate of a material, deposition time calibration samples have been made for every target material, which have then been analysed by measuring the thickness with high accuracy via X-ray reflectivity, (sect. 3.2.1.) [q]. Figure 3-4 shows the measured thickness as a function of deposition time for Co using a sputtering power of 40 W and Fe using a sputtering power of 35 W. All the data points for same material and different deposition time fall onto a single line (fig. 3-4 red dashed line) within the experimental error. These results indicate that the

[q] The system allows also to calculate the deposition rate by a quartz crystal monitor (SIGMA SQM-160), which was used to obtain an approximate deposition rate prior to calibration sample growth. This quartz crystal monitor allows deposition rate calibration of many different materials. The crystal monitor calibration error has been found to vary from material to material, overall being less than 10%.

deposition rate maintains constant for different deposition times and that opening and closing of the shutter does not affect the precision in any relevant way. This is consistent with the fact that opening and closing of the shutter takes only about half a second while the entire deposition is typically much longer. The deposition rate is given by slope of the least-squares linear fit (fig. 3-4 red dashed line) to the data.

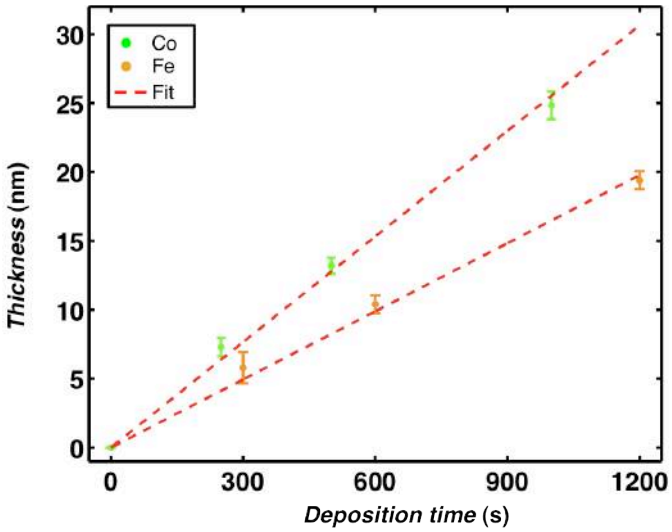

Figure 3-4: Deposited film thickness as a function of the deposition time, measured by X-ray reflectivity for Co (green dots) and Fe (orange dots). The red dashed lines show the linear least squares fits to the two data sets.

Furthermore, it has been verified that the deposition rate is linearly proportional to the deposition power at least for all the key material utilized in this thesis, as well as several few others, such as, Co, Ru, Cr, Ni, Pt, Ag and Pd. Figure 3-5 shows an example for Co (green dots) and Ru (blue dots), where all the thickness measurements have been done by X-ray reflectivity (sect. 3.2.1.) on calibration samples using a deposition time of 300 s. Here, the film thickness is shown versus sputtering power. Dashed red lines show the linear fits to the thickness data.[r] This linear dependency of the thickness, i.e. deposition rate, versus the sputtering power is important for precise alloy fabrication with different concentrations (as shown in sect. 4.2) by means of co-deposition from 2 or more guns simultaneously, since it allows for the efficient interpolation of deposition rates. Different concentration alloys are

[r] According to figures 3-4 and 3-5 the deposition time dependency is more robust to create different thickness layers than the power variation method. Therefore, whenever possible the sample series were prepared by deposition time variation.

obtained by adjusting the sputtering power to obtain the desired ratio between the deposition rates of the different elements in the alloy film. The sputter powers used for samples in this thesis vary between 50 W and 250 W. At lower sputtering powers, P < 50 W, the plasma is not always stable and at high powers, P > 250 W, the deposition rate may be too high to obtain films with good quality. Also, at high powers there exists the risk to overheat the target. So when a concentration difference of materials in the alloy is high, such as in the case of $Co_{0.95}Ru_{0.05,}$ and too high or too low powers would be needed to obtain this concentration, it is necessary to limit the flow of the low concentration material. In order to do so, the shutter of the material with lower concentration is opened and closed at short intervals during the alloy deposition. Hereby, the number of opening and closing and the time in each state is optimized to achieve a compromise between obtaining a good concentration uniformity along the alloy growth direction, i.e. avoid multilayering, and the suppression of any shutter opening/closing time influence. Therefore, one should open/close the shutter as many times as possible but avoid that each open or close state is too short.

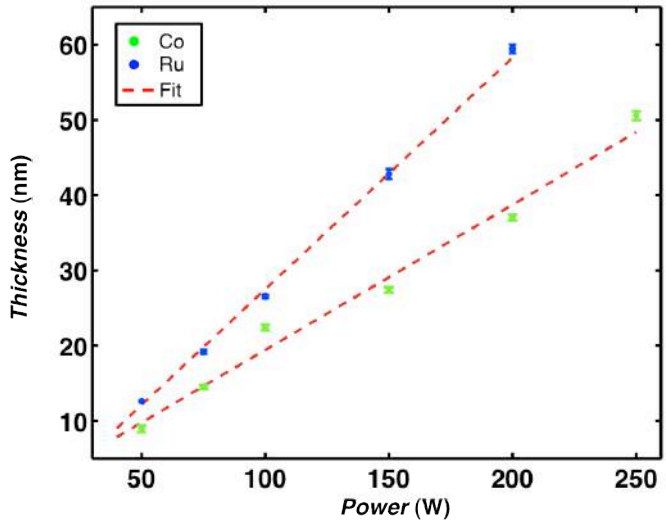

Figure 3-5: Deposited film thickness as a function of sputtering power, measured by X-ray reflectivity for Co (green dots) and Ru (blue dots). The red dashed lines show the linear least squares fits to the two data sets.

As mentioned above, the ATC series UHV sputter system is equipped with a load-lock chamber (see fig. 3-2(a)) apart from the main chamber. Using a load-lock has two major advantages, throughput and film quality. With the main chamber at a base vacuum of around 10^{-8} Torr, samples can be introduced via the low volume load-

lock and processing can begin within 10 minutes after substrate introduction, while if the main chamber were to be vented every time for substrate introduction, it would take at least 15 hours before achieving suitable vacuum conditions. The other advantage is film quality. If the deposition chamber vacuum is not optimal before beginning a deposition process, there is more residual water vapour present, which breaks down in the plasma and results in unwanted oxygen and hydrogen incorporation into the film chemistry. In order to transfer samples from the load lock chamber to the main chamber the system has a magnetic arm and both chambers are separated by a mechanical valve that can be opened and closed manually. The main chamber is only opened to replace targets or for system maintenance. Every time that the chamber is opened, all targets are cleaned by presputtering at low power (40 W) for at least 30 min.

All processing steps that are involved in the sputtering process can be controlled remotely by a commercial software called PHASE II, and it is furthermore possible to pre-program entire multilayer deposition sequences.

3.1.2. Nanostructure fabrication

3.1.2.1. Focused ion beam (FIB) nano-fabrication

FIB nano-fabrication is in essence locally confined material removal by sputtering, usually of previously deposited thin films[54,55]. The confinement of the ion beam is possible due to liquid metal ion sources that are punctual emitters with a narrow emission area and high brightness[54,sect.1.3.]. Usually, Ga^+ ion sources are being used[54,sect.1.3.], because Ga has a low melting temperature and a relatively low vapour pressure. In general, the technique allows the removal of material with nanometre scale precision at well-localized sites by milling of small holes. Consequently, by scanning the beam in a predefined pattern over the sample, precise machining of complex structures can be obtained.

At a predefined beam energy, the milling volume (μm^3) amongst other parameters is dependent on the milled material itself (fig. 7-8) and proportional to the ion dose, which depends mostly on the ion beam current, pitch size and the exposure time[55]. The ion exposure time is defined by the dwell time, i.e. time for which the ion

beam is kept at each particular point, and the number of passes of the beam over the various points. The pitch size is defined as the distance between two subsequently irradiated points. If one considers to increase the ion beam current in order to decrease the milling time for a fixed dose, one needs to the take into account that the lateral resolution is better for smaller currents. On the other hand, the energy transfer from the ion beam to the specimen should be higher than the atom binding energy in order to sputter atoms from the target material.

One of the main utilizations of FIB nano-structuring is the creation of thin lamella for transmission electron microscopy[54]. Due to the well control milling capacity of the FIB, it is possible to create thin enough lamellas that are transparent to an electron beam in the exact desired placed of a given sample.

3.1.2.2. Focused electron beam induced deposition (FEBID)

FEBID is based on the electron-induced dissociation of a molecular precursor gas into volatile and non-volatile components[56,57]. The non-volatile components deposit then onto a surface, where secondary electrons (SE) are generated. The secondary electrons have the right energy to dissociate precursor molecules, while the cross-sections of the high-energy primary electrons are very small[57]. Therefore, the deposit shape is determined by the SE emission pattern, which is of course related to the primary electron pattern. A schematic of this process is shown in fig. 3-6. The precursor gas is injected into the system by a gas injector (fig. 3-6 (a)). During local irradiation by the focused electron beam, secondary electrons generated in the substrate dissociate the precursor molecules into volatile and non-volatile components (fig. 3-6 (b)) and as a result, the non-volatile component gets deposited onto the surface (fig. 3-6 (c)).

There are many parameters that may affect the final deposition, such as the electron beam conditions, namely energy and current, which determines the final electron emission sites and thus the final lateral resolution of the deposit. Moreover, the electron beam energy and beam current play also an important role for the purity of the deposit[58]. Other processing parameters that mainly affect the final shape and purity of the deposition are the dwell time, the pitch size, the number of repetition for

which the writing pattern is done, the water vapour, pressure in the chamber and the precursor flux.[58,59]

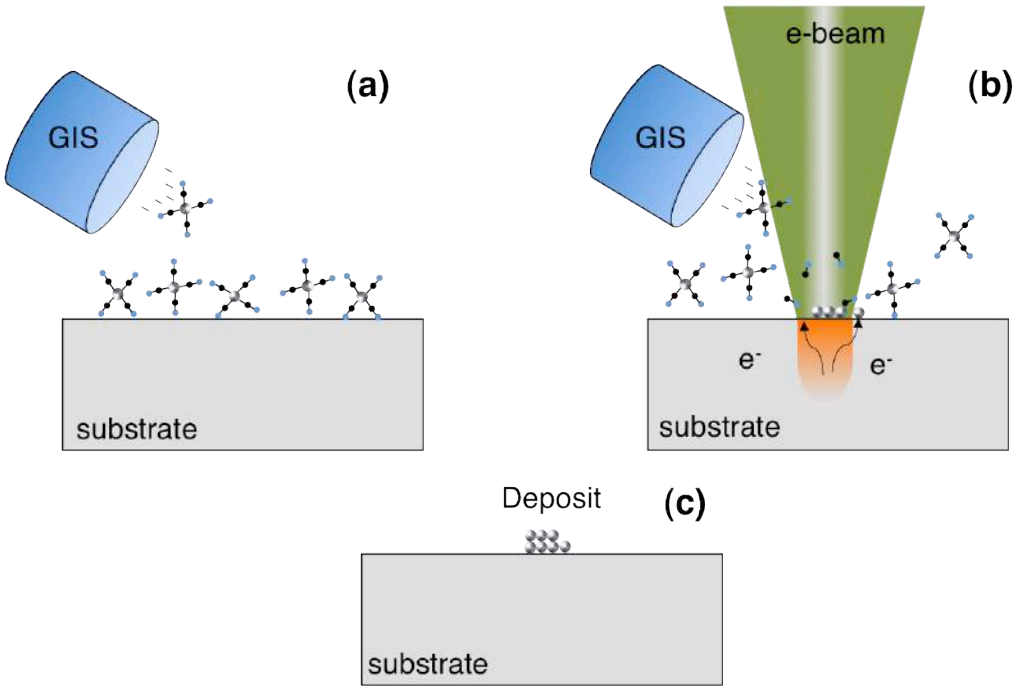

Figure 3-6: (Courtesy of Dr. E. Nikulina) schematic of the focused electron beam induced deposition process: (a) precursor gas is injected, (b) secondary electrons dissociate the precursor molecules and (c) the non-volatile compounds will form a deposit.

The key attractive feature of FEBID apart from being a one-step fabrication process is the possibility to grow 3-dimensional complex nanostructures[60]. Moreover, nano-fabrication of lateral dimensions below 1 nm has been demonstrated in Tungsten dots using this technique[61]. It also allows for the deposition of different ferromagnetic materials, such as for instance Fe, where deposits up to 70 at. % of metal content have been achieved[62,63]. In the case of Ni, the achieved purity is much lower, only around 40 at. %[64]. However most of the work done using FEBID for ferromagnetic materials has been done on Co [59,60,65–67], where purities of to 95 at. % have been achieved as well as final deposits with lateral sizes down to 30 nm[59].

3.1.2.3. Helios NanoLab 600 DualBeam system

The Helios NanoLab 600 DualBeam is a commercial instrument from FEI Company and it combines a focused electron beam with a focused ion beam in a high vacuum chamber. Figure 3-7 (a) shows a photograph of the entire system, while (b)

shows a photograph taken inside the vacuum chamber, where electron and ion beam columns and the gas injection system's needles (GIS) are visible.

The system has two ion columns, one Ar^+ column whose energy can be varied from 0.2 kV to 2 kV and a high-performance Ga^+ column whose beam energy can be varied from 1 kV to 30 kV. In this work, only the Ga^+ column has been used. Using the Ga^+ column at high beam energies, such as 30 kV and 1 pA beam current, one can achieve a milling resolution of approximately 10 nm. However, as described in chapter 7, the beam is not perfectly sharp and it has rather wide tails that might influence considerably the surroundings of the narrow focal area. In this thesis, the effect that this tail causes onto magnetic properties at different ion doses has been studied by fabricating differently sized nanostructures from Co/Pt-multilayer films with and without protective layer (chap. 7).

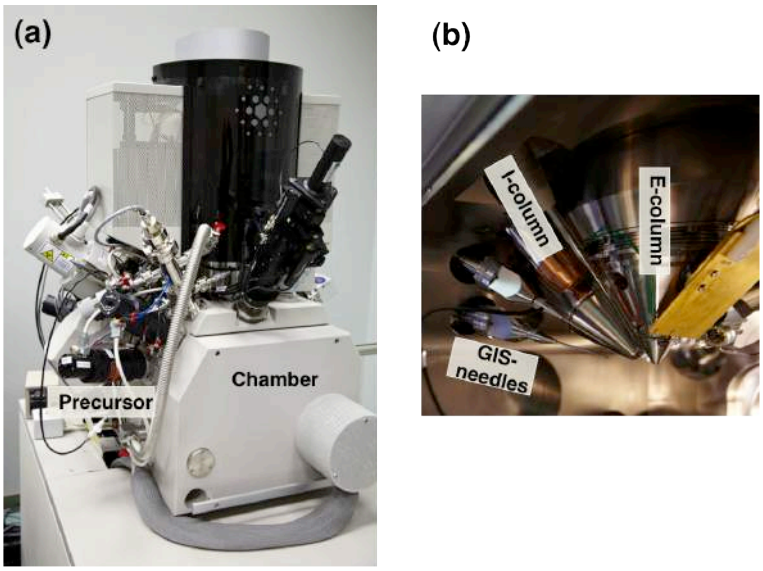

Figure 3-7: Photographs of the Helios Nano Lab DualBeam: (a) of the entire system and (b) of chamber interior.

The electron beam energy can vary from 0.2 kV to 30 kV and it can be used to image with a lateral resolution better than 0.7 nm at 30 kV in scanning transmission electron microscopy mode and with a resolution of 1 nm in scanning electron microscopy mode. In FEBID operation, the primary energy beam spot also has an about 1 nm resolution. The Helios NanoLab DualBeam system at CICnanoGUNE is equipped with 3 gas injectors (two of them visible in fig. 3-7) and 3 precursor reservoirs, where precursor gases for Pt, Co and SiO_2 deposition are stored. The precursor gas injection system consists of a reservoir, which is coupled to a fine

capillary, whose open end can be brought into close proximity of the substrate surface, on which the electron beam is focused. In this thesis, only Co nanostructure deposition has been performed since the work is focused on the analysis of magnetic properties of thin films and nanostructures. For the Co nanostructure fabrication, dicobalt optacarbonyl $Co_2(CO)_8$ has been used as a precursor. As mentioned before, the deposition parameters and beam conditions affect the final properties of the structure, such as in the lateral resolution and purity, in a very sensitive way. Thus, to be able to fabricate functional magnetic nanostructures, all deposition condition, such as beam energy and beam current, have been optimized first, a task that has been carried out by Dr. E. Nikulina from the Electron Microscopy group at CIC nanoGUNE[58].

All the structures shown in this thesis are fabricated using a beam current of 2.7 nA and varying the beam energy in order to achieve the desired lateral dimensions. At this beam current the purity of Co is higher than 80 at. %, measured by Energy Dispersive X-ray spectroscopy (EDX). The dwell time has been always the same, namely 1µs, which has been found by Dr. E. Nikulina to be a good value to obtain high purity structures, and the pitch size has been chosen to be 5 nm, which ensured good thickness uniformity along the structure. The deposition time is given by number of passes, which has been varied in order to fabricate structures of different thicknesses. Figure 3-8 shows examples of Co zigzag structures fabricated by FEBID with beam conditions of 2.7 nA and 25 kV.

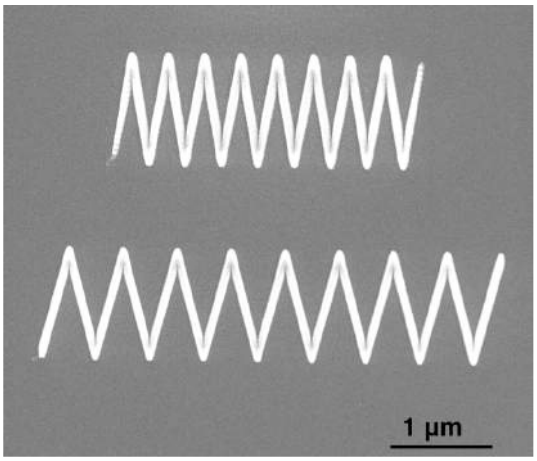

Figure 3-8: FEBID zigzag Co nanostructures.

3.2. Structural characterization

3.2.1. X-ray diffractometry and reflectivity

X-ray diffraction techniques consist of exposing a material to X-ray waves so that if the material has a crystalline structure (fig. 3-9 (b)), i.e. is composed of regularly spaced atoms, the scattered X-rays waves from these atoms will interfere constructively and destructively in certain spatial directions producing an spatially varying intensity diffraction pattern[68,69]. The diffracted pattern is then characteristic for the specific crystalline structure of the material. Thus, it allows materials characterization and identification of atomic lattices in a non-destructive way. The reason for using X-rays for the analysis of the interatomic distances and not other electromagnetic waves, is the fact that their wavelengths, approximately 0.5-2.5 Å, are similar to the inter-atomic distances in solids, which is relevant according to Bragg's law (eq. 3-1).

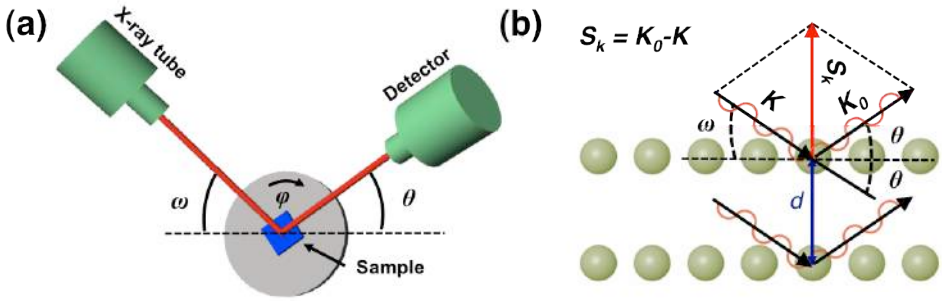

Figure 3-9: Schematic of X-ray diffraction: (a) perspective image of the different angles in the X-ray diffraction experiment, (b) schematic illustration of wave interference in crystallographic structures.

According to the Bragg's law only at certain angles θ from the surface plane (see schematics of X-ray angles in fig. 3-9 (a)) a constructive interference happens, namely when

$$n\lambda = 2d\,sin(\theta) \qquad (3\text{-}1),$$

where d denotes distance between adjacent atomic planes, λ is the X-ray wavelength and n is an integer that gives the interference order. Thus, collecting the intensity at the detector as a function of the 2θ angle, an intensity spectrum can be collected. In

this spectrum the peaks give the angular position where constructive interference happens and thus the distance between planes, which are normal to scattering vector, S_k (see fig. 3-9 (b)). The scattering vector is given by the difference of the incoming wave vector and scattered wave vector. The angle in between the incidence wave vector and surface plane is referred as ω (see fig. 3-9 (a)). Upon scanning ω-2θ, one can compare the obtained diffracted spectrum to a database that has diffracted spectra for crystal structures for many materials compiled, which enables one to identify the crystalline order in the sample. Using this database each diffracted peak can be described by a Miller index[68,chapt.2], which denotes the crystallographic plane that satisfies Bragg's law.

When ω equals θ (case shown in fig. 3-9 (b)), this distance, d, denotes the spacing between adjacent planes that are perpendicular to the surface and the corresponding measurement is called θ-2θ diffraction measurement[69,sect.1.2.]. This type of measurement is the primary method used to characterize the crystallographic quality of the thin films in this thesis.

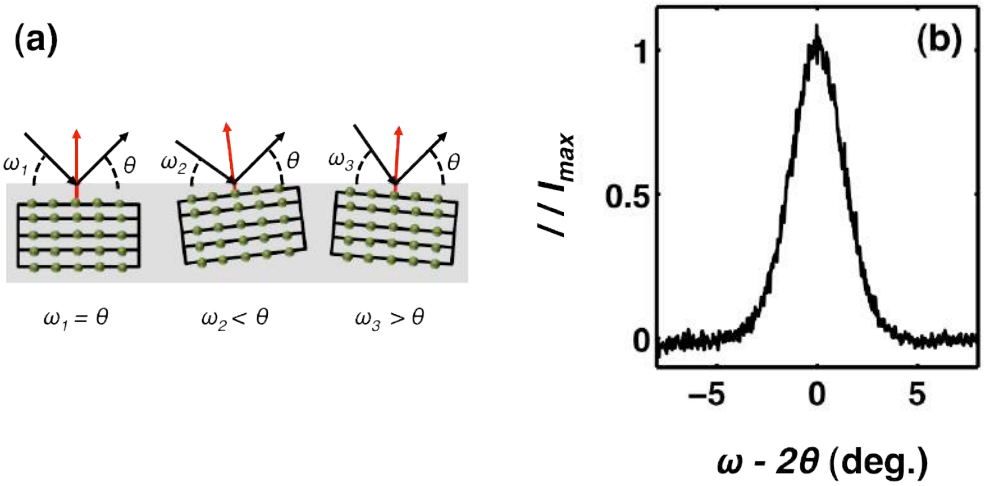

Figure 3-10: (a) Schematics of X-ray diffraction in samples with slightly out-of-plane tilted crystal grains, which results in a distribution of scattered waves. Consequently, the Bragg condition is fulfilled for different incoming angles ω. (b) Rocking curve measurement performed for the Co (10$\underline{1}$0) diffracted plane in an epitaxially grown thin film.

In order to perform a detailed analysis of the crystallographic quality of the samples grown in this thesis, also rocking curve measurements and φ[s] scans have been performed. A rocking curve measurement is done by fixing the detector at

[s] As one can observe in the schematic of the X-ray experiment (fig. 3-9 (a)), φ corresponds to rotation angles with respect to the axis normal to the surface plane.

specific angle 2θ, where the diffracted Bragg peak under investigation emerges, while scanning the incident beam angle (ω) around θ. From the width of the diffracted peak in the rocking curve, one can determine the out of plane spread of crystalline grains (fig. 3-10 (a))[69,sect5.5.3.]. Figure 3-10 (b) shows an example of a rocking curve measurement for a Co-film at the (10$\underline{1}$0) diffracted peak. The full width at half maximum (FWHM) of this rocking curve measurement is 3.13° ± 0.02º.

Even though θ-2θ scans and rocking curve measurements are crucial for the crystallographic structure characterization of crystalline samples, these two measurements do not take into account possible azimuthal orientation misalignment. In order to characterize this, one can perform φ scan[69,sect.5.6.1.], which consists of scanning φ and measuring the diffracted intensity in a certain crystallographic peak.

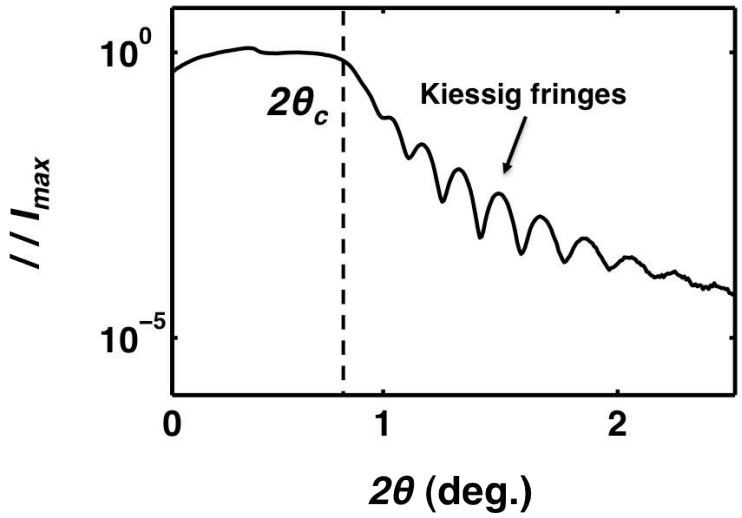

Figure 3-11: X-ray reflectivity measurement on a 41 ± 1 nm thick Ag film.

In order to calibrate the thickness of thin films, the aforementioned X-ray reflectivity measurements have been performed. In this technique, one measures the interferences pattern, generated by reflected waves from top and bottom interface of a thin film. Analogous to the Bragg condition, constructive and destructive intensity pattern occur, known as a Kiessig fringes, from which one can extract the thickness of thin films[69,sect.4.5.]. In this technique, the X-ray incident beam angle and the detector angles are scanned at grazing incidence angles and they are symmetrically moved, i.e. ω *is* equals θ. An example of a reflectivity measurement of a sputtered Ag film with a nominal thickness of 40 ± 2 nm can be seen in fig. 3-11. $2\theta_c$ is the critical angle, above which the X-ray can penetrate the sample, and which can be calculated by

Snell's law using the refractive index of the material under study. From the distance between the Kiessig fringes, a thickness of 41 ± 1 nm has been obtained for the film here. This sample has been grown by using a previously calibrated deposition rate, so that the small error in between the nominal and real thickness verifies the very good reproducibility of the thickness of films fabricated by the ATC series UHV sputter system.

In order to characterize the crystallinity and thickness of thin film samples fabricated by sputter deposition, a commercial X-ray diffraction system from PANalytical (X'Pert PRO PANalytical X-ray diffractometer) has been used (fig. 3-12). This system is equipped with a very precise and reproducible ω-2θ goniometer with an angular precision of 0.00001°. The anode material used to create the X-ray beam is copper, so that all measurements presented here are done with Cu K_α radiation (λ = 0.154 nm). The K_β radiation is removed in the incident beam by means of a hybrid monochromator[68,69], which at the same time collimates the beam and allows high-resolution measurements. The X-ray detector uses PIXcel technology, which is solid-state detector[69instrumental_box_7] that comprises more than 65.000 pixels and is generally more efficient than traditional detectors.

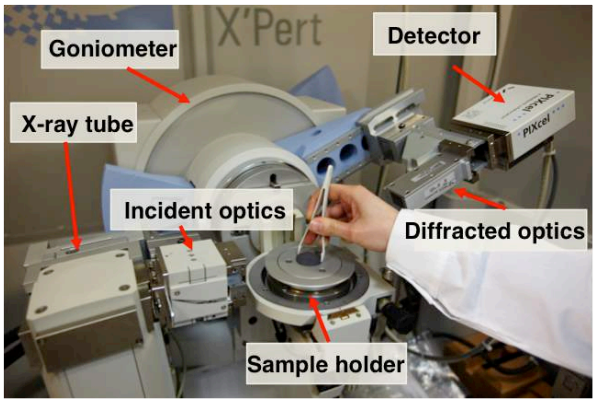

Figure 3-12:Photograph of the X'Pert PRO PANalytical X-ray diffractometer

3.2.2. Atomic force microscopy

The atomic force microscopy (AFM) technique is based on a cantilever with a sharp tip at the end. When this sharp tip is close enough to a surface, the attractive and repulsive forces between the tip and the surface deflects the cantilever.[70] So, if one now follows the point of deflection onset in the tip-sample approach as a function of lateral tip position, the topography of a surface can be measured. The deflection is

measured by reflecting a laser beam from the cantilever onto a four segments photodetector and by calculating the difference in reflected intensity between the segments of the photodector. In order to scan the cantilever along the surface a piezoelectric actuator is used. In general, there are different ways of performing AFM measurements, contact mode, non-contact mode and tapping mode.

The measurements in the thesis have been performed in tapping mode. Here, the cantilever oscillates with relatively large amplitude, so that it comes into contact with the sample. The forces acting on the cantilever cause the amplitude of this oscillation to decrease, as the tip gets closer to the sample. One then operates the AFM in such a way that the distance between sample tip and surface is kept constant in order to maintain always the same oscillation amplitude. The voltage that is applied to the piezo to raise or to lower the cantilever in order to keep the distance constant is then measured as a signal as one scans the tip laterally over the sample surface. This technique allows quite high resolution without damaging the sample.

The atomic force microscope at CIC nanoGUNE (5500 Agilent AFM microscope) is a high-resolution microscope for topographic characterizations with a lateral resolution down to 2 nm. A vertical resolution of 0.5 nm can be achieved using ultrahigh-resolution tips having a tip radius of approximately 1 nm. However in this work standard tips from AppNano have been used with a tip radius of 6 nm, which allows a lateral resolution of around 10 nm. The lateral single frame scan range of this Agilent AFM can be up to 100 x 100 μm^2 with 5120 x 5120 data points per image.

3.3. Magnetic characterization

3.3.1. Magneto-Optical Kerr Effect (MOKE)

The Magneto-Optical Kerr Effect (MOKE) describes the magnetization induced changes to reflected light by a magnetic material that do not occur in a non-magnetic material. The physics of the Kerr effect is fundamentally the same as for the Faraday effect except that the Kerr effect refers to reflected light while the Faraday effect is the corresponding light polarization change in transmitted light.

The common observation of both effects is a polarization change when *s* or *p* linearly polarized light[t] is transmitted or reflected from a magnetic surface. The polarization change can be represented by a rotation of the polarization plane and an ellipticity change[u]. Fig. 3-13 shows the example how linearly polarized light with *s* polarization becomes elliptically polarized light with ellipticity ε_K and rotation θ_K when it is reflected from a magnetic surface. ε_K and θ_K are dependent on the magnetic state of the sample.

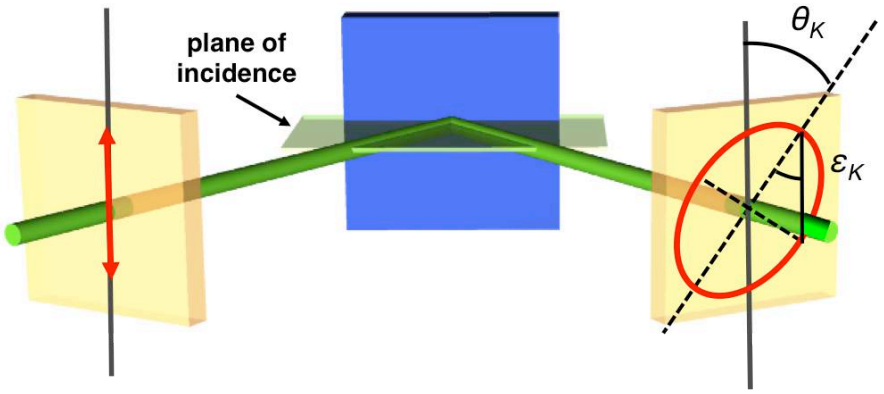

Figure 3-13:Magneto-optical Kerr effect. Linearly polarized light with *s* polarization reflected from magnetic surface results in elliptically polarized light with rotation θ_K and ellipticity ε_K.

A linearly polarized light consists in a superposition of two circularly polarized lights (left and right circularly polarized light) of equal intensity. In classical physics if one considers that a linearly polarized light reflects from a magnetic medium, the Lorentz force acting on the electrons due to the static magnetic induction present in a ferromagnet will affect left circularly polarized light and right circularly polarized light in different ways. This will result in a net polarization effect, which is the Kerr effect[71–74].

From a macroscopic point of view, the rotation and the ellipticity of the polarization plane are described as arising from different indices of refraction for the two circularly polarized modes. In order to quantitatively describe magneto-optical

[t] *s* and *p* are the orthogonal orientations of linearly polarized light with respect to the plane of incidence (see fig. 3-13), respectively having an electric field vector perpendicular or parallel to the plane of incidence.

[u] While this is true for longitudinal and polar effects (see sect. 3.3.1.1.), the transverse effect does not cause a polarization change for incoming *s* and *p* polarization lights. Instead it causes an intensity change in *p* polarization and no effect for pure *s* polarization.

(MO) effects, one needs to solve the electromagnetic wave equation in magnetic materials, i.e. for the non-trivial dielectric tensor of a magnetic medium[71], which is composed by a symmetric and an antisymmetric part. If one assumes an otherwise optically isotropic material and uses the correct choice of the coordinate system, the symmetric part consists only of equal diagonal elements and does not directly contribute to the MO effects. In this case the dielectric tensor of a magnetic material is given by,

$$\tilde{\varepsilon} = \varepsilon \begin{pmatrix} 1 & -iQ_v m_z & iQ_v m_y \\ iQ_v m_z & 1 & -iQ_v m_x \\ -iQ_v m_y & iQ_v m_x & 1 \end{pmatrix}$$

(3-2)

where ε is the conventional dielectric constant, Q_v is the Voigt constant or the magneto-optical coupling constant and the normalized magnetization vector is given by $m = (m_x, m_y, m_z)$.

In a simplest case,[v] the two normal modes of the dielectric tensor corresponds to the left-circularly and right-circularly polarized lights, which have refractive indices of

$$n_{L,R} = n\left(1 \pm 1/2Q\, \vec{m} \cdot \hat{k}\right)$$

(3-3),

where $\hat{k}$ represents the light propagation direction. The difference in the refractive index leads to the magnetically induced change in light polarization.

Just as in conventional reflective optics or ellipsometry one can calculate the reflection matrix of the structure including the magnetization dependent terms. Hereby, one can describe the reflection of a planar sample by the Fresnel reflection matrix[71,73]

$$R = \begin{pmatrix} r_{pp} & r_{ps} \\ r_{sp} & r_{ss} \end{pmatrix}$$

(3-4),

[v] This is valid only for pure polar effects (see sect. 3.3.1.1.), for general reflection condition and arbitrary magnetization states, solutions of the wave equation can be found in refs. 72,74.

where r_{pp}, r_{sp}, r_{ps} and r_{ss} are the Fresnel reflections coefficients which are derived from the electromagnetic boundary condition of a planar wave on a planar interface. For otherwise optically isotropic materials, the r_{sp} and r_{ps} terms are magnetically induced reflection coefficients, that couple *p* and *s* polarized light [w]. By measuring the Kerr ellipticity and rotation using the appropriate optical tools, one can infer the r_{ps} and r_{sp} to r_{ss} and r_{pp} ratios respectively, considering

$$\phi^S = \theta_K^S + i\varepsilon_K^S = \frac{r_{ps}}{r_{ss}}$$

$$\phi^P = \theta_K^P + i\varepsilon_K^P = \frac{r_{sp}}{r_{pp}}$$

(3-5),

and thus extract the relative magnetization changes[x] in the sample while varying the externally applied field. The MOKE effect, commonly given by ε_K and θ_K, depends among other quantities on the incidence angle and wavelength and usually is on the order of hundredth of a degree[75]. Despite this rather small size, it is possible to measure the magnetization reversal by means of MOKE with very good sensitivity, because r_{sp} and r_{ps} invert with the sign of the magnetization, thus allowing for a very sensitive difference measurement.

3.3.1.1. MOKE fundamentals

There is a generally used classification scheme of MOKE geometries, where each geometry refers to one of the three components of the overall magnetization vector[71].

Longitudinal geometry describes the magnetization component that is parallel to both, the plane of incidence and the sample surface. Linearly *s* or *p* polarized incoming light becomes elliptically polarized light with a rotated axis upon reflection. The Kerr rotation θ_K and ellipticity ε_K induced by this magnetization component are linearly related to the in plane magnetization component that is parallel to the direction of the applied field.

[w] The exact expression for the Fresnel reflection coefficients for the bulk case and the thin film limit can be found in refs. 71 and 73 respectively.

[x] As mentioned before, this is valid only for longitudinal and polar geometry (see sect. 3.3.1.1.).

In the polar configuration, the effect of the magnetization vector that is perpendicular to the sample surface is described. This configuration is similar to the longitudinal MOKE configuration, in that the polar-MOKE induced ellipticity ε_K and the rotation θ_K of the reflected beam are proportional to the out of plane magnetization component. This configuration has been used to measure the magnetization reversal in Co/Pt multilayers (studied in chap. 7), since they exhibit a perpendicular anisotropy.

Lastly in the transverse MOKE, one considers the magnetization parallel to the sample surface and perpendicular to the plane of incidence. Instead of measuring a polarization change of the reflected light, in this case one typically measures an intensity change of the reflected light in *p* polarization.

For this work, only longitudinal and polar configurations of the MOKE have been used.

3.3.1.2. MOKE magnetometry setup

The MOKE magnetometry setup used in this thesis, is a home built setup and it can be adjusted to measure all three of the above described MOKE configurations, i.e. longitudinal, polar and transverse MOKE. In fig. 3-14, a schematic of the setup for longitudinal MOKE geometry can be seen, which has been used to performed macroscopic magnetic characterizations of thin films (sect. 4.1.2.), including the studies of the dynamically ordered phase in thin Co films (sect. 6.2.). For these measurements, the setup has been equipped with a polarization stabilized diode laser of 532 nm wavelength (green laser), which already emits linearly polarized light.

Considering the relatively high power output of this laser and the highly reflective surfaces of the here investigated film samples, it has been necessary to limit its power by an attenuator in order to avoid saturation of the detectors. The attenuator as can be seen in fig. 3-14 is placed right in front of the laser and it reduces the laser power to 3-4 mW on the sample surface. Behind the attenuator, a linear polarizer is used to obtain light with an even higher degree of polarization.

After the laser light is reflected from a magnetic sample, it is converted into elliptically polarized light with a rotated axis. In order to measure the magnetization in the sample one can measure the magnetically induced ellipticity or rotation.

Depending on the material and optical conditions, such as the incidence angle and wavelength it is more appropriate to measure one or the other property. In this thesis, the MOKE ellipticity has been measured.

The reflected elliptically polarized light can be considered as being composed by two perpendiculars and out of phase linear polarizations, E_0 coming from the ordinary non-magnetic reflection of the incident light and E_M arising from the magneto-optical effects. However, due to the fact that the magnetically induced ellipticity and rotation are small effects (few hundredth of adegree[75]), they result in vastly different values for E_0 and E_M, which can be difficult to measure with high accuracy by the same type of detector due to linearity and saturation limitations. In order to enhance the ellipticity of the laser light a quarter wavelength retarder has been used, which creates elliptically polarized light with a major axis of E_0+E_M and a minor axis of E_0-E_M. After the retarder a Wollaston cube beam splitter in combination with a differential photodiode with on-chip amplifier has been used to separate the light into two orthogonal components and extract intensity variations created by the MOKE ellipticity ε_K from them.

One can describe the path that the light follows in the setup mathematically by using Jones matrices (see appendix A), from which the intensity difference measured (I) by the differential photodiode is given as

$$I = 4Im\left[r_{pp}r_{sp}^{*}\right]$$

(3-6)[y].

Considering that the r_{sp} is proportional to the magnetization component that is parallel to the applied field, one can extract the magnetization component along the longitudinal field and thus measure the hysteresis loops of that component.

Inside the MOKE setup, the sample is mounted onto a holder that can be rotated around the surface normal of the sample with a precision of 0.5° from 0° to 360° for the purpose of studying the angular dependence of magnetic properties. The field is applied horizontally, and thus in the plane of incidence. For this, an electromagnet is utilized that can generate up to 3000 Oe field strength at the sample. In the dynamically ordered phase experiment (sect. 6.2.), it has been necessary to

[y] In equation 5-6, *Im* denotes imaginary part, while r_{sp}^{*} is the complex conjugate of r_{sp}.

generate an extremely precise AC field amplitude, as well as, a predefined constant field (bias field) with minimal variations, which has been continuously monitored by a hall probe placed near the sample. Additionally, it has been necessary to apply the AC field at high and easily variable frequencies. In order to achieve these specifications, a special magnet with sintered Ferrite core has been used, for which the root mean square (rms) noise level of the AC field amplitude and the DC field bias has been determined to be only 0.022 Oe or less in all experiments.

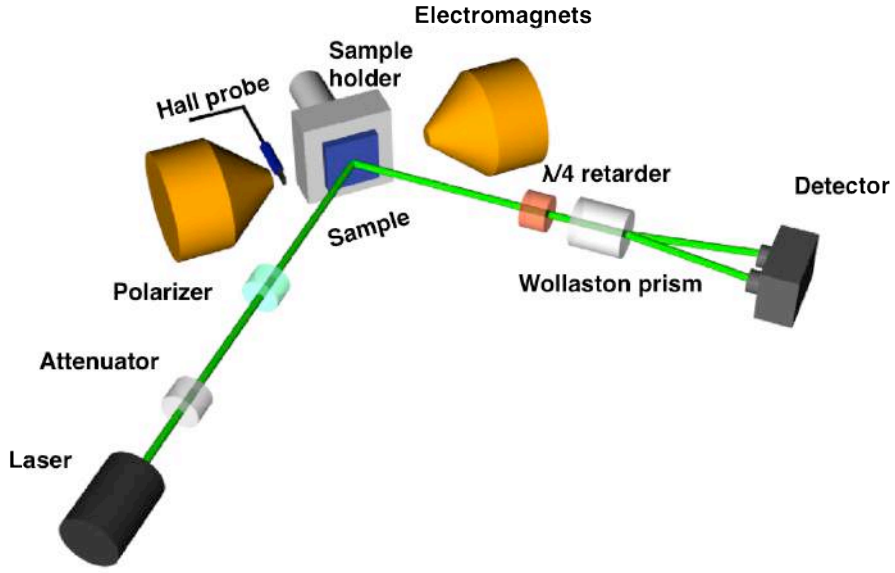

Figure 3-14: Schematic drawing of the MOKE magnetometry setup.

Overall, this longitudinal MOKE setup enabled the measurement of a 30 nm Co-film saturation signal with a signal-to-noise ratio of 48.2 in 30 µsec, thus allowing high performance single-shot measurements of complete hysteresis loops with frequencies of up to 1.7 kHz.

3.3.1.3. MOKE microscopy

In order to analyse the microscopic magnetization structure, one can use a magneto-optical imaging technique, called MOKE microscope. It is based on the Kerr effect, just as described above and it allows for non-invasive microscopic characterizations of magnetic states and properties.

In the MOKE microscope, the measuring principle is similar to the MOKE setup. Initially, light emitted from a lamp is converted into a linearly polarized beam and passes through an adjustable slit aperture. This adjustable silt aperture gives the

possibility to regulate the incidence angle of the light onto the sample, e.g. by placing the aperture in the centre the light impinges onto the sample along the surface normal. Therefore, by guiding the light with the slits to impinge onto the sample at a certain angles and by applying the external field in the appropriate direction, one is able to choose between different MOKE sensitivities, namely longitudinal, transverse and polar sensitivity. Afterwards the light passes through a polarizer, which polarizes it linearly, it is directed towards to the sample by reflection in a beam splitter and it is subsequently focused by an objective lens.

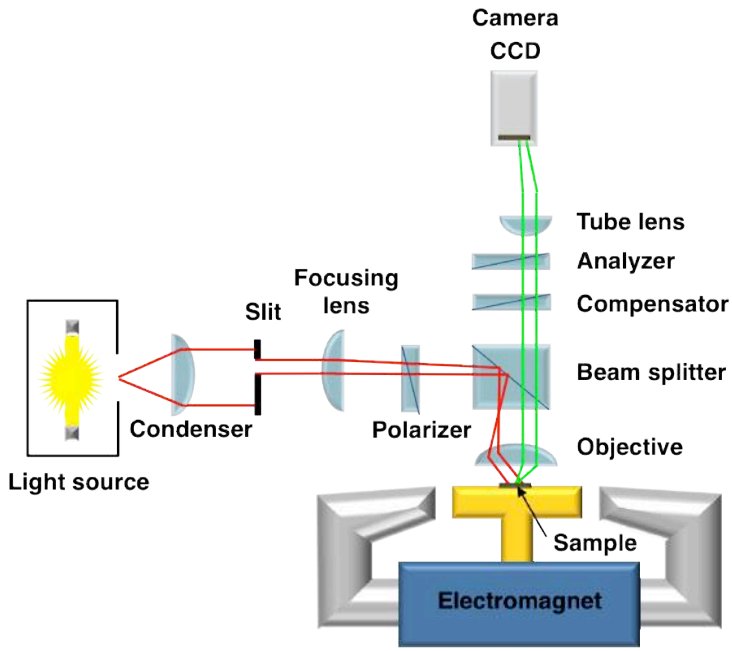

Figure 3-15: Schematic of the magneto-optical Kerr effect microscope setup.

After reflection the light is captured by the objective and then passes through the beam splitter again, which transmits the light to the optics to extract the Kerr signal. The operation principle to extract the Kerr effect signal is slightly different here in comparison the MOKE magnetometry setup, since instead of Wollaston prism there is combination of compensator and analyser being used here. These elements enable a light intensity contrast between the different polarization states corresponding to the different local magnetization states of the sample[76].

The compensator is a variable quarter wave plate, which is used to convert the elliptically polarized light into linearly polarized light, transforming the ε_K information into a polarization rotation[76]. The analyser is oriented nearly perpendicular to the incident beam polarizer. As a result the component that

maintains the initial polarization after the reflection is attenuated while the component created by the magneto-optical effects (ε_K converted to polarization rotation in the compensator) is transmitted. The intensity image that passes the analyser is then recorded by a CCD-camera. In order to obtain only the magnetic signal, the microscope operation software allows for the possibility to remove the non-magnetic background by means of a simple background subtraction at every point locally, i.e. for every pixel on the CCD-camera that records the microscope image. This is a crucial aspect because it allows to remove the topographic signals that can have a polarization signature and retain only polarization changes arising from magnetization variations.

Our EVICO@ Kerr microscope allows (schematics shown in fig. 3-15) the measurement of local $M(H)$ curves and domain imaging[76,77] with an optical microscopy resolution limit of approximately 500 nm. In order to be able to image different size domains the microscope is equipped with objective lenses that cover the magnification range from 5 x up to 100 x. Moreover the system is equipped with an auxiliary magnification changer, known as optovar, that allows the amplifications of 1 x, 1.25 x, 1.6 x, 2 x and 4 x. Thus, by using a 100 x objective lens and a microscope amplification of 4 x, one can obtain a magnification of 400 x.

The electromagnet allows the generation of in-plane fields up to 5000 Oe and out-of-plane fields up to 400 Oe. In order to study the angular field dependence of the microscopic magnetic properties, it is possible to rotate the sample in steps of 1º.

Even though the microscope has been recently equipped by different wavelength LEDs, in this thesis a highly stable and intense Xenon white lamp with a power of 75 W has been used as a light source.

Figure 3-16 (a) shows a domain structure measured by the here describe MOKE microscope for a Co film. The image size is 90 µm x 70 µm. Different grey scales in the image represent different magnetization orientations. Hysteresis loop measurements in the Kerr microscope consist in the analysis of intensity variations as a function of the externally applied field. As default, the intensity variation analysis is done considering the entire image. However, the software gives also the possibility to follow the signal of any subsection of the CCD array by selecting any arbitrary shape area (region of interest, ROI) (fig. 3-16 (b)). By doing so, one can analyse hysteresis

loops of small areas by selecting only a few pixels in the region of interest. As we will see in chap. 7, this makes it possible to measure magnetization reversal of only 30 nm wide individual wires, i.e. wires far smaller than the diffraction limit. This is possible, because the microscope allows one to minimize the intensity coming from the non-magnetic sample part. Even though this approach is still limited by optical resolution, the signal to noise performance of the illumination system, polarization optics, and the CCD camera system is so good, that it allows to measure signals that come from only a small fraction of the analysed surface area. So, overall it is the combination of minimizing the analysed non-magnetic surface area that enters the signal path plus the excellent sensitivity of the detection system overall, that make the MOKE microscope presented hereby sensible to signals arising from structures with sizes well below the wavelength (sect. 7.1).

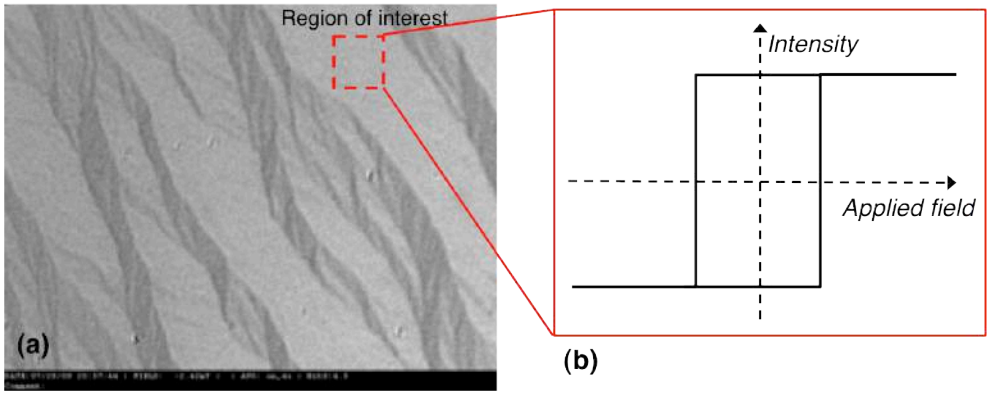

Figure 3-16: Magneto-optical Kerr effect microscope measurement capabilities. (a) magnetic domain images taken for a Co thin films by means of the MOKE microscope, red dashed line shows the capability of the system to select a region of interest and measure the hysteresis loop only in this area. (b) schematic of a hysteresis loop that corresponds only to the selected region of interest.

3.3.2. Macroscopic magnetometry

3.3.2.1. Vibrating sample magnetometry

Vibrating sample magnetometry (VSM) is based upon placing a magnetic sample inside one set of coils, known as the detection or signal pick-up coils and by vibrating the sample in order to measure its magnetization[78]. Specifically, the flux change caused by a moving magnetic sample generates an induced voltage in the

pick-up coils that is proportional to the total magnetic moment of the sample[z]. The relation between the voltage and magnetic moment is calibrated by means of a reference sample. Thus by measuring this voltage one can measure the absolute total moment of a magnetic sample. Usually VSM systems are also equipped with an electromagnetic coil in order to generate an external field and thus enable measurements of the magnetization as a function of the applied field.

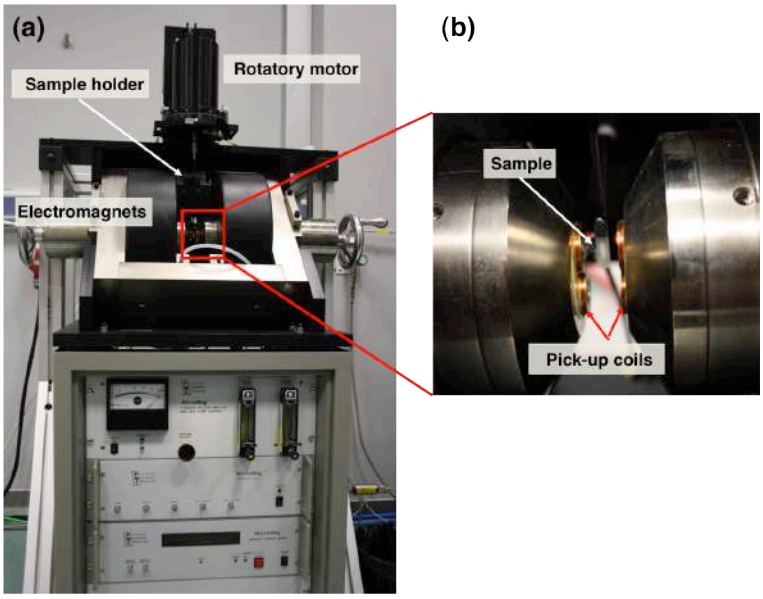

Figure 3-17: Photographs of the MicroMagTM Model 3900 VSM System, from Pricenton Measurements Corporation: (a) entire system and (b) sample area.

The VSM used in thesis is a commercial instrument, namely the MicroMagTM Model 3900 VSM System from Pricenton Measurements Corporation. This instrument is a high sensitivity instrument, which can measure signals down to 0.5 μemu at 1 second per point. In order to place the sample (limited to sizes smaller than 8 x 8 mm^2) in the proper and calibrated position between the coils, the system has linear translation stages that permit the movement along the three Cartesian axes. Moreover, the system allows an automatic rotation of the sample about the axis that is perpendicular the applied field. This option permits an automatic characterization of

[z] Afterwards one can normalize the total magnetization to the magnetic volume in order to get the magnetization per volume. In this thesis, only thin film samples have been measured by VSM. For arbitrarily shaped substrates, the sample volume normalization of the magnetization has been done in the following way: by weighting the substrates, one can determine the sample area since the density and the thickness of the substrate are known. Once the sample area is known it is easy to calculate the volume, since the sample thickness of the magnetic layer is measured precisely by means of X-ray reflectometry.

the angular dependence of the magnetometry measurements, which has been done in order to extract different magnetic properties, such the magnetic anisotropy constants and the saturation magnetization for Co and Co alloy thin films (sects. 4.2.2. and 4.3.2.).

The gap in between the electromagnet poles is adjustable and at a minimum gap width of 1.27 cm, the maximum achievable applied field is 2.1 x 10^4 Oe. Furthermore, the system is equipped with a furnace, which works under continuous flow of helium in a temperature range of 100 °C and 800 °C.

3.3.2.2. Superconducting Quantum Interfence Devices - Vibrating sample magnetometry

Superconducting Quantum Interference Devices - Vibrating sample magnetometry (SQUID-VSM) is based on the same principle as the VSM but with superconducting pick up coils and a superconducting quantum interference device as the flux detector, which leads to a better magnetic signal sensitivity. The SQUID-VSM at CIC nanoGUNE is a commercial system, the MPSM SQUID VSM EverCool system from Quatum Design. It offers a magnetic sensitivity better than 10^{-8} emu with only 4 seconds of data averaging at zero applied field. Moreover, it can apply magnetic fields up to 7 x 10^4 Oe with a step resolution of 0.05 Oe[79]. The system also allows cooling the sample from room temperature down to 2 K by means of an integrated liquid Helium system, which is equipped with a recirculation compressor system and a 70 litre dewar, so that the cooling system is self contained (“closed loop”) and virtually eliminates helium losses.

For the here presented work, this system has been used primarily for the characterization of the Curie temperatures of thin film samples, as discussed in sect. 4.2.2.

4. Uniaxial Co and Co-alloy thin films

As mentioned before, Cobalt is a one of the 3d ferromagnets together with Fe and Ni. In these materials the origin of the magnetic moment arises from the incomplete 3d orbitals. In particular, Cobalt has 7 electrons in the 3d orbitals per atom, a fact that leads to 3 vacancies or three uncompensated spins in the atomic electron configuration. Co, like Fe and Ni, is an itinerant ferromagnet or band structure ferromagnet, and the net magnetic moment of bulk Co is given by the overlapping outermost orbitals, i.e. the 3d orbitals with 7 electrons on them and the 4s orbital with 2 electrons, which results in a magnetic moment of 1.72 μ_B.[80] Bulk Co exhibits ferromagnetism until its Curie temperature of T_C = 1115 ºC and it has a saturation magnetization of 1422 emu/cm^3 at room temperature.[80] However, these values may vary in thin films. Hereby, one generally finds that while M_s is usually quite robust except for the ultrathin film limit, T_C might vary more substantially and in a much larger range of film thickness[38,39].

Regarding its crystallographic structure, bulk Co exhibits a hexagonal close packed (hcp) phase at temperatures below 415 ºC, while above this temperature, it presents a stable face centred cubic (fcc) phase.[81] Nonetheless, as mentioned before in

sect. 3.1.1., in thin films one can change the energy balance, so that specific crystallographic structures can be stabilized. This section of the thesis is focused on Co and Co based alloy thin films, which have been grown epitaxially in the hcp crystallographic phase. In the hcp crystallographic phase, the magnetic easy axis is along the *c* axis of the crystallographic structure and thus, it exhibits uniaxial symmetry[36]. This specific feature, together with the relatively high coercive field exhibited by hcp Co and Co-alloys, makes hcp Co-alloys the exclusively used materials for hard disk drive recording media applications during the past decades.

In general, Co is a widely used material in technology applications, such as, in Giant Magneto-Resistant or Tunnel Magneto-Resistant read heads for magnetic storage devices[82]. Furthermore, within the same technological application, the recording layer of hard disk drives is a Co based thin film alloy[6], namely CoCrPtB and it is being used in a mixture together with oxide materials, such as Ti-oxide, Ta-oxide or Si-oxide that make up most of the grain boundaries in the finished disks. These materials exhibit high anisotropy, a characteristic that is essential for information storage stability and it can be fabricated as ultrasmall grain material, a fact that makes today's high storage capacity possible. Besides its use in hard disk media, Co thin film alloys are used broadly in technology going from catalysts[83] to Lithium based batteries[84].

As a result of the importance of the ferromagnetic and ferromagnetic alloy thin films for different technological applications, their fundamental properties, such as the magnetization reversal has been a key focus area of active research during several decades[8–12]. However, despite of the vast amount of studies, many aspects are still not well understood because magnetization reversal is a collective phenomenon[36], just like ferromagnetism itself, but in addition it is also very strongly influenced by local property variations[85–87], which can be structural or compositional in nature.

This chapter intends to develop a better insight into this aspect and therefore it is focused on understanding how the crystallographic order, composition or thickness may affect the magnetic properties on Co and Co-alloy thin films. As a starting reference system, 30 nm thick single crystal Co thin film samples with hcp structure and (10$\bar{1}$0) surface orientation have been chosen. This system exhibits an in-plane

uniaxial magneto-crystalline easy axis. The selection of the system has been based on the idea of utilizing a film type, in which the different energy contributions to the magnetization reversal are easily identifiable[15,34]. Therefore, magnetization properties and related magnetization reversal should be simple and variations in the intrinsic properties of the system may cause clearly classifiable modifications in the reversal. The reference sample thickness of 30 nm has been chosen because it is small enough to avoid any multi domain states in the direction of the surface normal, so that analysing the surface magnetization is sufficient to analyse the complete domain structure. On the other hand, 30 nm is of the order of the skin depth for optical wavelengths, so that magneto-optics as one of the key magnetic characterization tools used in this thesis is especially efficient and produces bulk like signal levels for these thin film samples.

4.1. From epitaxial to weakly textured Co thin films

Concerning structural changes and their effect on magnetization reversal, up to now the vast majority of studies has been focused on thin film systems, in which the long-range crystalline order is either very high[15,16], very low[13,14] or on samples with specific structural imperfections[88]. However, none of these works performed a comprehensive study of the crystallographic quality effect onto magnetization reversal, since none of them was based on a systematic change of the crystallographic order in samples with otherwise identical characteristics.

Magnetization reversal processes in both extreme cases, i.e. in thin films with high crystal quality and thus very long correlation lengths of the reversal and in thin films with low crystallographic coherence are well understood. In many cases, they can be described and predicted with high accuracy[13–16,89,90]. However, the intermediate range of partial magnetization reversal correlation is far less understood and the difficulty of fabricating partially disordered materials in a continuous and reproducible fashion limits the well-defined experimental accessibility of this range. Therefore, this part of the thesis work has been intended to make a step towards the experimental characterization and understanding of magnetization reversal in partially disordered thin films. Specifically, it will be analysed how a continuous decrease of the long-range crystalline order affects on the magnetization reversal

correlation. This approach has the advantage that one can easily define a reference point, namely epitaxial single crystal films, such as the reference (10$\underline{1}$0) Co thin film and consider them as the starting point, from which the crystallography is being modified.

4.1.1. Crystallographic and structural properties

For the epitaxial growth of the reference samples, namely (10$\underline{1}$0) Co thin films, the work done by Yang et al.[91] has been followed and their recipe has been adapted to achieve optimum sample growth conditions in the ATC series UHV sputter deposition system (sect. 3.1.1.1.). The overall growth sequence of the system is shown in fig. 4-1. As substrates, Si wafers with (110) orientation have been used, which exhibits uniaxial surface symmetry. Prior to deposition, each wafer has been cleaned in an ultrasonic bath first with acetone to remove large particles and organic residues. Afterwards, poly-isopropanol has been used to remove the acetone and finally the wafer has been rinsed in deionised water. The native oxide of the wafers has been then removed by using a wet hydrofluoric acid (HF) chemical etch, which has been monitored by means of ellipsometric measurements. In this work a solution of 2.5% HF in deionised water has been used at room temperature for 5 minutes, after which the substrate has been immediately transferred into the UHV sputter system.

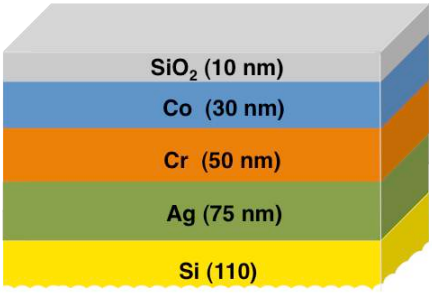

Figure 4-1: Schematic of the layer sequence for epitaxial Co (10$\underline{1}$0) growth with in plane uniaxial anisotropy.

On top of the so-prepared Si (110) single crystal wafers, 75 nm of Ag and 50 nm of Cr layers have been deposited to facilitate the desired epitaxial growth of the Co layer. Both, Ag and Cr, have been grown by DC magnetron sputtering at a power of 40 W and 100 W, respectively, achieving deposition rates of 0.124 ± 0.003 nm/s and 0.053 ± 0.002 nm/s in the sputter system. Subsequently, Co films of 30 nm thicknesses have been deposited by DC magnetron sputtering onto this template layer

sequence, using a power of 100 W for a deposition rate of 0.043 ± 0.002 nm/s. On top of Co, 10 nm of SiO_2 have been RF sputtered at 300 W to prevent the Co from oxidizing or otherwise deteriorating under ambient conditions. All layers have been grown at a room temperature using an Ar-gas sputter pressure of 3 mTorr and an Ar gas flow of 20 standard cubic centimetres per minute. All individual deposition rates have been determined by X-ray reflectivity measurements on test sample thickness series for each material as explained in sect 3.2.1. prior to fabricating the actual samples.

The epitaxial relationships between the layers of the above described system can be seen in figs. 4-2 (a)-(c) based on their respective bulk lattices. Si exhibits a face-centred diamond cubic crystal structure with a unit cell of two atoms and with a length of 0.543 nm, so that the Si (110) crystallographic plane results in a rectangular cell with dimensions of 0.768 nm x 0.543 nm as indicated in fig. 4-2 (a). On the other hand, Ag has a face centred cubic (fcc) crystallographic structure with a unit cell length of 0.409 nm, resulting in the Ag (110) crystallographic orientation having a rectangular unit cell with dimensions 0.578 nm x 0.409 nm (fig. 4-2 (a)). Therefore, a 2x4 Ag (110) [001] supercell mesh of dimensions 1.156 nm x 1.636 nm matches almost perfectly to the 1.152 nm x 1.629 nm size of half a 3 x 3 Si (110) [001] supercell mesh. Between them, the mismatch is only 0.4% in the Si (110)[001]/Ag (110)[001] direction, while in the Si (110)[1$\underline{1}$0]/Ag (110)[1$\underline{1}$0] direction it is 0.35 % (fig. 4-2 (a)), so that good epitaxy of this particular Ag-surface orientation should be feasible. The subsequently grown Cr with its body centred cubic (bcc) crystallographic structure fits well with (211) [0$\underline{1}$1] surface orientation onto Ag (110) [001] as can be seen in fig. 4-2 (b) having a mismatch of only -0.25% in Ag (110)[001]/Cr (211)[0$\underline{1}$1] direction, even though this creates a not insubstantial mismatch in the Ag (110)[1$\underline{1}$0]/Cr (211)[$\underline{1}$11] direction, namely -13.5%. However, as corroborated by X-ray diffractometer measurements later on (fig. 4-3) this considerable mismatch in one direction does not prohibit the epitaxial growth of the (211) Cr orientation onto the Ag (110) template layer. Finally, the Cr (211) surface provides an excellent template for Co with hexagonal close packed (hcp) crystallographic structure and a (10$\underline{1}$0) surface plane orientation, aligning the [0001] direction along the [1$\underline{1}$0] direction of the Cr (211) surface, causing a mismatch of

only -0.5% in this specific direction (fig. 4-2 (c)). In the Cr (211)[$\underline{1}$11]/Co (10$\underline{1}$0)[1010] direction, the mismatch is only 0.4%. In this specific Co-film crystallography and orientation, the hcp c-axis, which is also the magneto-crystalline bulk easy axis, is in the film plane and given that the films have near bulk crystallography and are sufficiently thick, the *c*-axis is expected to be the magnetic EA as was previously observed in ref. 91.

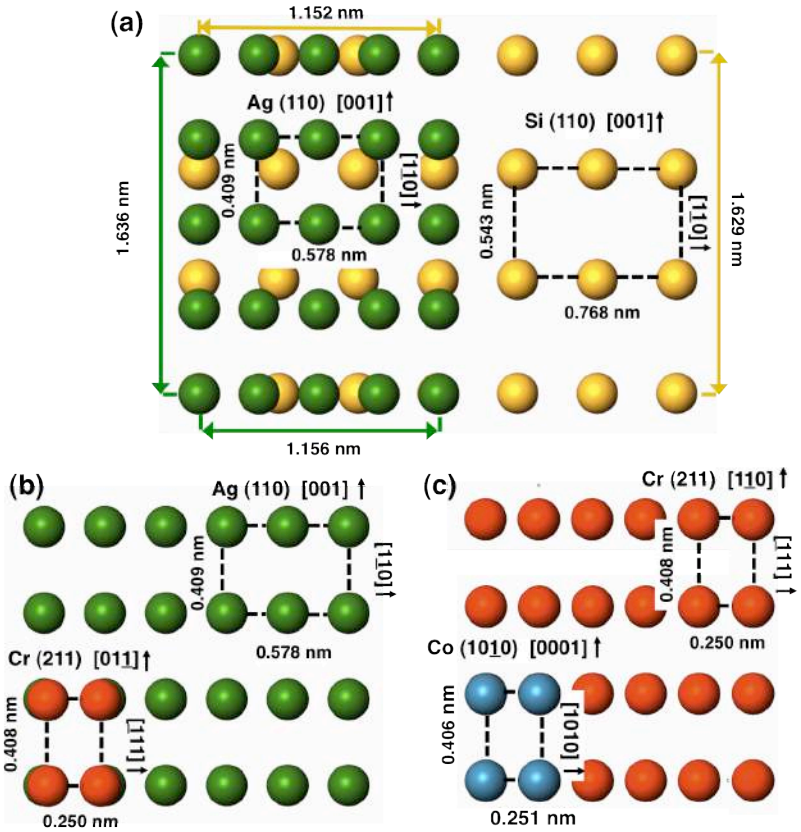

Figure 4-2: display of the epitaxial relations between subsequent layers in the stacking sequence Si(110)[001]/Ag(110)[001]/Cr(211)[0$\underline{1}$1]/Co(10$\underline{1}$0)[0001] by means of their respective crystallographic surface unit cells. (a) shows the epitaxy relation of Si(110)[001]/Ag(110)[001], (b) of Ag(110)[001]/Cr(211)[0$\underline{1}$1] and (c) of Cr(211)[0$\underline{1}$1]/Co(10$\underline{1}$0)[0001].

In order to characterize the crystallographic structure of the so-prepared Co films, X-ray diffractometry measurements have been performed, primarily in the θ-2θ mode. Figure 4-3 shows a typical θ-2θ X-ray diffraction (XRD) measurement for an epitaxial sample, namely for the reference sample type, i.e. a 30 nm Co (10$\underline{1}$0) film. One can observe only the Si (220), Ag (220), Cr (211), Co (10$\underline{1}$0) and Co (20$\underline{2}$0) diffraction peaks, corroborating the epitaxial nature of the sample. For Co, apart from a narrow first order diffracted peak, which corresponds to (10$\underline{1}$0), a higher order

diffraction is also visible, namely the (20$\underline{2}$0)-peak, which is a sign of the good crystallographic quality of the so-grown Co film. The (20$\underline{2}$0) diffracted peak would not be visible or even further reduced if the epitaxy were poor. The SiO_2 overlayer grows amorphously and, thus, it does not show any diffracted peak in the XRD measurements.

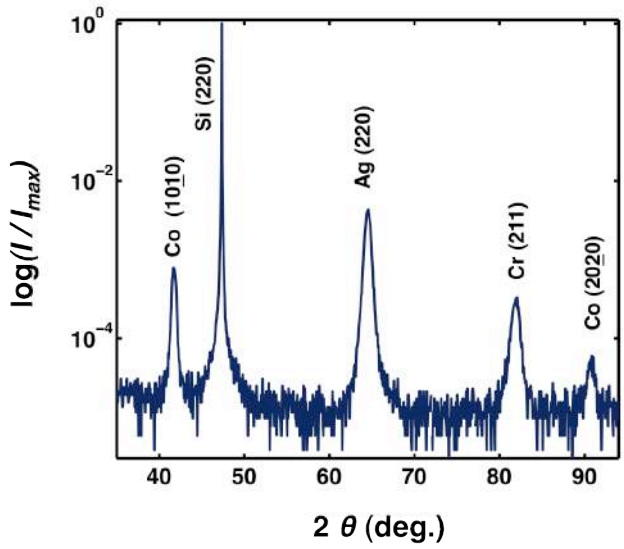

Figure 4-3: X-ray θ-2θ diffraction measurement for the epitaxially grown Co(10$\underline{1}$0) reference sample type.

Using the above described epitaxial reference sequence as a starting point, a series of samples with continuously tuned crystallographic order going from high quality epitaxial samples to samples with very limited crystallographic alignment have been grown by partially interrupting the epitaxy. In order to achieve this partial interruption of the epitaxy, a SiO_2 interlayer has been deposited directly onto the HF etched Si substrate (fig. 4-4). It is known that SiO_2 layers deposited onto Si grow amorphously[92]. The SiO_2 interlayer has been grown by RF magnetron sputtering in the same UHV sputter deposition system at low plasma power in order to achieve precise thickness control. For this purpose, a deposition power of 60 W and an Ar pressure of 3 mTorr have been chosen. Under these conditions the deposition rate of SiO_2 is very low, only $0.0110 \pm 6 \times 10^{-4}$ nm/s, so that it opens up a substantial experimental window in terms of deposition time even for the growth of very thin films. Thus, it allows one to conduct a precise and reproducible study of partial epitaxy suppression. In this work results for samples with SiO_2 interlayer thickness, t_{ox}, of 0 nm, 0.11 nm, 0.132 nm, 0.154 nm, 0.165 nm, 0.275 nm, 0.33 nm, 0.385 and

0.55 nm are presented. However, the samples with low t_{ox} are primarily discussed here because they present the t_{ox}-range, in which the epitaxial growth and the magnetic properties are affected in the most relevant way.

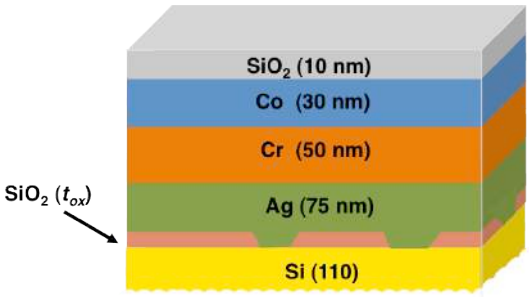

Figure 4-4: Schematic of the layer sequence for partially interrupted epitaxial Co (10$\underline{1}$0) film growth.

Figure 4-5 shows θ-2θ XRD measurements for three samples with t_{ox} = 0.11 nm as green line, t_{ox} = 0.132 nm as red line and t_{ox} = 0.154 nm as yellow line. In order to have a clear comparison in between the samples and with the full epitaxy case, the X-ray diffraction spectrum for the reference sample or which is equivalent, for t_{ox} = 0 nm has been included (blue line) here as well.

For the sample with t_{ox} = 0.11 nm, one can observe in addition to the peaks that correspond to the epitaxial growth sequence, a small peak that corresponds to the Ag (111) crystallographic orientation (2 θ = 37.9°), showing that already the Ag-film is not single crystalline anymore. Consequently, the diffracted Cr (211) peak as well as the Co (10$\underline{1}$0) peak intensities decrease, which is a sign of their reduced crystallographic quality. Additionally, the second order diffracted peak of the Co (10$\underline{1}$0) plane, namely the (20$\underline{2}$0) peak, which is clearly visible for the epitaxial sample, is barely visible for the t_{ox} = 0.11 nm sample. By increasing t_{ox} further, one can observe that the (110) crystallographic texture of the Ag layer decreases continuously and new peaks appear arising from other crystallographic orientations, such as, (200) and (311). In these two samples, namely samples with t_{ox} = 0.132 nm and t_{ox} = 0.154 nm, the crystallographic quality of Co and Cr decreases even further and the Co (20$\underline{2}$0) peak disappears completely. However, despite of the decrease of (110) Ag texture in these samples, the intensity ratio in between the Ag (220) and (111) peak does yet indicate random orientation. Thus, even though the epitaxial peaks are reduced, they are still more prominent than in a sample with randomly

oriented crystal grains. For polycrystalline Ag with random grain orientations, the (111) peak has 4.50 times the intensity of the Ag (220) peak.[93] Here, however, the Ag (220) peak intensity is still higher than the intensity for the Ag (111) peak, which means that these samples have a very substantial degree of (110) texture. Given that a predominant Ag (110) texture does not grow on a completely random template layer, the texture observed in fig. 4-5 must be the result of a still existing partial epitaxy, which cannot be fully suppressed by the only 0.154 nm thick Si-oxide. So one can conclude that these samples with different amount of t_{ox}, have different degrees of epitaxy induced texture.

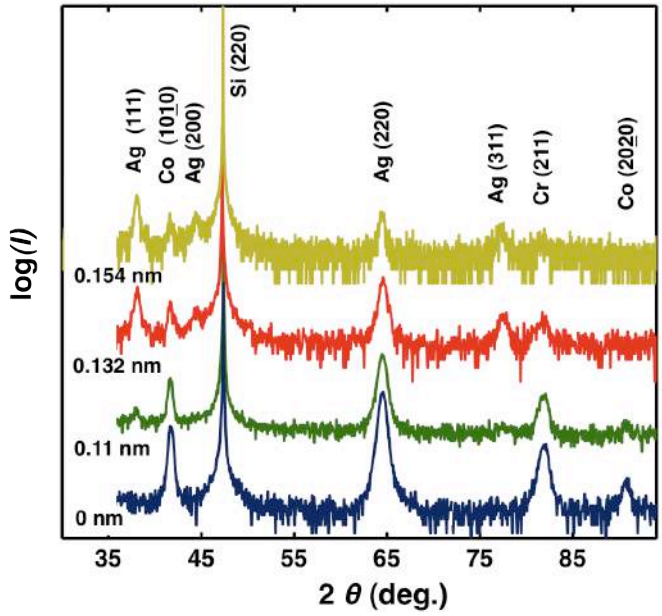

Figure 4-5: X-ray θ-2θ diffraction measurements for the epitaxial Co(10$\bar{1}$0) reference sample with t_{ox}=0 nm (blue line) and partially epitaxial Co (10$\bar{1}$0) samples, where t_{ox} = 0.11 nm (green line), t_{ox} = 0.132 nm (red line) and t_{ox} = 0.154 nm (yellow line)

The partial epitaxy nature of these Co films and the increased suppression of epitaxy by increasing t_{ox} can be seen clearly in fig. 4-6. Upon increasing the Si-oxide interlayer thickness, the ratio between the Ag (111) and Ag (220) peak intensities increases, i.e. a gradual decrease of Ag (110) texture (fig. 4-6) is observed as more and more of the Si-substrate surface is being covered by the Si-oxide interlayer. Therefore, as the SiO_2 interlayer is introduced, one interrupts the epitaxy and gradually changes the template from a pure Ag (110) single crystal layer towards a randomly oriented polycrystalline Ag layer. As one modifies the Ag crystallographic structure, the crystallographic orientations of the subsequently grown Cr and Co films

are also altered in a similar fashion, resulting in the gradual disappearance of the epitaxial Cr and Co XRD peaks.[aa]

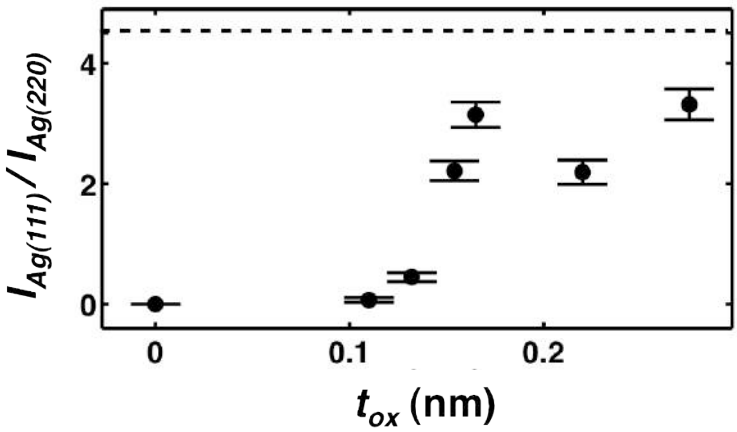

Figure 4-6: Ratio between X-ray peak intensities arising from the (111) and (220) Ag crystallographic planes as a function of t_{ox}. The dashed line represents the $I_{Ag(111)}/I_{Ag(220)}$ ratio for randomly oriented polycrystalline samples.

Consistent with the previously shown XRD results, a continuous increase of the Co (10$\underline{1}$0) peak width has been found upon increasing the Si-oxide interlayer thickness, measured as the full width at half maximum in rocking curve measurements ($\Delta\Omega_{Co}$) (fig. 4-7 green squares), which is a measure of the out-of-plane spread of the Co (10$\underline{1}$0) crystallographic plane as explained in sect. 3.2.1. While for the reference sample with t_{ox} = 0 nm, the $\Delta\ \Omega_{Co}$ is 3.13° ± 0.02º, a value comparable to others obtained for other epitaxially grown metal films[94], the sample with t_{ox} = 1.32 nm for instance exhibits a $\Delta\ \Omega_{Co}$ of 5.61° ± 0.10. As t_{ox} is increased further $\Delta\ \Omega_{Co}$ increases as well, indicating a continued decrease of crystallographic alignment.

In order to measure the azimuthal crystallographic spread in these Co layer as a function of t_{ox}, φ scans have been measured on the Co (10$\underline{1}$1) pole by means of the X-ray diffractometer (sect. 3.2.1). Figure 4-8 shows this type of measurement for samples with t_{ox} = 0 nm (blue), t_{ox} = 0.11 nm (green) and t_{ox} =0.132 nm (red) normalized to the maximum intensity in each measurements. In all of the samples, two diffraction peaks that are 180° apart from each other can be observed, thus indicating two fold symmetry and corresponding azimuthal crystalline orientations[91].

[aa] The reason of not seeing Cr and Co diffracted peaks arising from other crystallographic structure as t_{ox} increases, is the low signal to noise ratio. In order to characterize polycrystalline samples, it is usually better to perform grazing incidence X-ray diffraction measurements[69,chapt.4].

In addition, one can observe from these measurements that the width of the diffracted peak increases as t_{ox} increases, which is the result of the crystalline azimuthal spread, a fact that is consistent with all the previously shown structural measurements (fig. 4-5, fig. 4-6 and fig. 4-7).

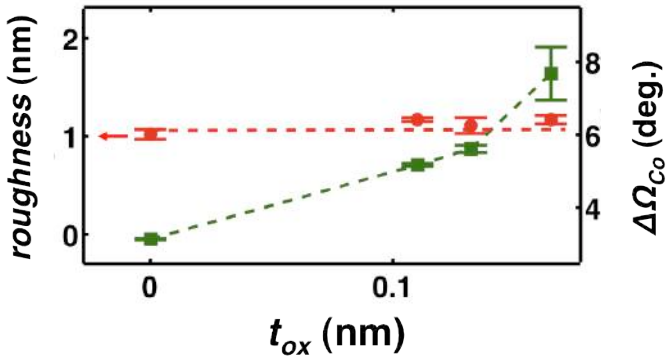

Figure 4-7: Structural properties of the Co film sample series as a function of t_{ox}. The root mean square surface roughness is represented by red dots. The full width at half maximum of the rocking curve measured for the Co (10$\bar{1}$0) diffracted peak as a function of t_{ox} is represented by green squares. The dashed and solid lines guides to the eyes.

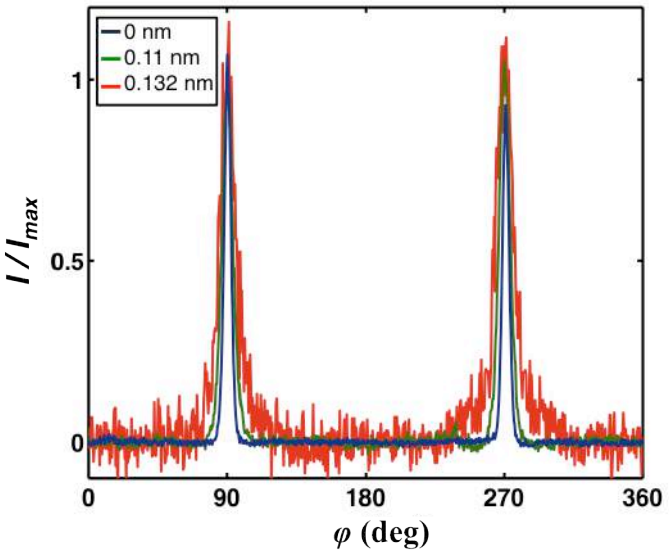

Figure 4-8: φ scan of X-ray diffraction measurements on the Co (10$\bar{1}$1) peak for samples with t_{ox} = 0nm (blue), t_{ox} = 0.11 nm (green) and t_{ox} = 0.132 nm (red).

In order to verify, that the structural changes observed in these Co samples with different t_{ox} are clearly dominated by a change in crystallographic grain alignment and not due to topographical changes, the root mean square (RMS) surface roughness has also been measured for all samples by atomic force microscopy (AFM). Here, one cannot observe any significant change in film roughness upon

introducing the Si-oxide interlayer (fig. 4-7 red circles). All samples show RMS roughness at a nearly identical level of 1.1 nm (shown by dashed red line).

4.1.2. Macroscopic magnetic properties

After obtaining samples with continuously tuned crystallographic order in the vicinity of epitaxial single crystal films and after characterizing their structural properties in detail, their macroscopic magnetic properties have been analysed. For this purpose, the previously described home built magneto-optical Kerr effect (MOKE) setup has been used. The incident light has been *p* polarized and the magnetic response of the sample has been measured by the MOKE induced ellipticity of the reflected light.

Figure 4-9 shows several hysteresis loops measured at room temperature for the fully epitaxial or reference sample (figs. 4-9 (a)-(c)) and partially epitaxial samples with t_{ox} = 0.132 nm (figs. 4-9 (d)-(f)) and t_{ox} = 0.154 nm (figs. 4-9 (g)-(i)) at different applied field angles with respect to the samples' easy axes (EA). Specifically, figures 4-9 (a), (d) and (g) display hysteresis loops for the applied field being oriented along the EA (β = 0°), figures 4-9 (b), (e) and (h) at β = 40° and figures 4-9 (c), (f) and (i) at β = 60°. In each case, the sample magnetization (M) is normalized to a reference magnetization M_0, which is the magnetization value at the maximum applied field, namely H = 1800 Oe[bb].

Along the EA, all the three samples (t_{ox} = 0 nm, t_{ox} = 0.132 nm and t_{ox} = 0.154 nm) show very similar behaviour with high remanent magnetization and a sample size avalanche magnetization reversal[cc] (figs. 4-9 (a), (d) and (g)). However despite these similarities one can also observe differences. For instance, the samples with t_{ox} = 0.132 nm and t_{ox} = 0.154 nm (figs. 4-9 (d) and (g)) exhibit a bending of the

[bb] The main reason to use M_0 instead of the saturation magnetization value (M_s) for the normalization is the fact that M_s is a somewhat elusive experimental quantity, because only along the easy or the hard axis can one actually achieves $M = M_s$. For all other directions, this is not possible and one would have to extrapolated the data to estimate M_s in these directions. So, given that the specific value of M_s is not particularly relevant here, M_0 has been used as a reliable experimental magnetization value for the data normalization.

[cc] Sample size avalanche magnetization reversal denotes that all the magnetic moments within the system switch together producing a magnetization reversal of the entire sample within a single field step.

hysteresis loops just before the avalanche reversal point is reached, an effect that is absent or at least far weaker in the epitaxial sample. Moreover this bending is a bit more pronounced for the t_{ox} = 0.154 nm sample, i.e. the one with a higher degree of structural disorder. Such a bending of the hysteresis loop is caused by the fact that with only partial epitaxy, the entire film is no longer a single crystal and the anisotropy axes of different grains are not fully aligned anymore. Thus, even for field orientations along the nominal EA, some magnetization rotation is occurring and becomes most visible just prior to the correlated magnetization reversal switch. This misalignment of the easy axes is more pronounced as the t_{ox} increases, i.e. as the epitaxy decreases, resulting in a more evident bending of the EA hysteresis loop for the sample with t_{ox} = 0.154 nm than for the t_{ox} = 0.132 nm sample. As the external field is applied away from the EA, i.e. for β = 40° (figs. 4-9 (b) (e) and (h)) and β = 60° (figs. 4-9 (c), (f) and (i)), the hysteresis loops change gradually for all samples. But even though the three samples exhibit a clear angular dependence and a clear transition from easy axis to hard axis behaviour, the variation of hysteresis loops as a function of β differs between them. For instance, at β = 60° the reversal of the fully epitaxial sample is still dominated by an abrupt magnetization switch (fig. 4-9 (c)), while for the partially epitaxial samples (figs. 4-9 (f) and (i)), the hysteresis loops shows a far bigger bending and a much smaller magnetization switch or no visible magnetization switch at all in the case of the t_{ox} = 0.154 nm sample.

From the difference in hysteresis loop bending towards saturation magnetization at β = 40° and β = 60° at high applied fields, one can observe a clear decrease of susceptibility with crystallographic disorder, a feature that indicates a decrease of the effective magneto-crystalline anisotropy.

In order to achieve a more detailed characterization of the angular dependence of the magnetization reversal in these Co films with different degrees of epitaxy, hysteresis loops have been measured as a function of β in steps of 5° or even 0.5° in the vicinity of the HA. From these hysteresis loop measurements the remanent magnetization values, $M_{r,}$ have been extracted.

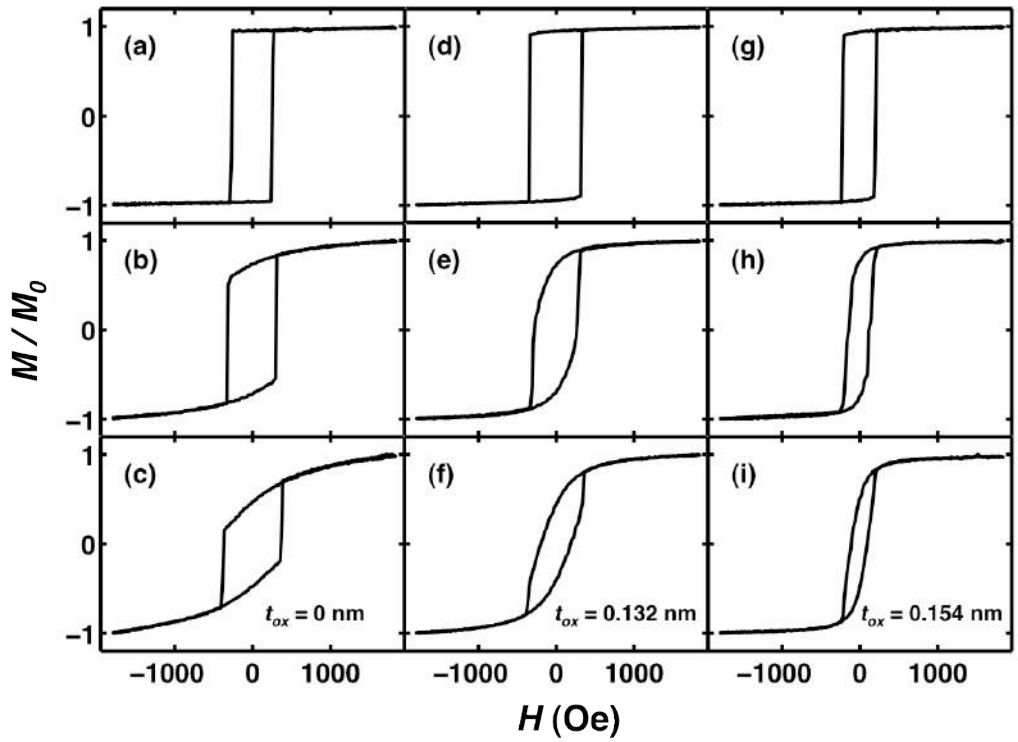

Figure 4-9: Hysteresis loops measured for Co (10$\bar{1}$0) samples with different SiO_2 interlayer thickness: (a)-(c) for t_{ox} = 0 nm, (d)-(f) for t_{ox} = 0.132 nm and (g)-(i) for t_{ox} = 0.154 nm. (a), (d), (g) show hysteresis loops for an applied field along the EA, (b), (e) and (h) show hysteresis loops for an applied field 40° away from the EA and (c), (f) and (i) show hysteresis loops for an applied field 60° away from the EA.

Figures 4-10 (a)-(f) show as solid black lines the experimentally determined remanent magnetization values as a function of β for 6 different samples, representing different t_{ox} and thus different degrees of crystallographic alignment. The remanent magnetization value for each β, is calculated by averaging the absolute values of the positive and negative remanent magnetization over 20 loops, which have been measured under identical conditions. Similar to the hysteresis loops shown in fig. 4-9, one observes a strong angular dependence of M_r/M_0 for all samples with a periodicity of 180°, which is the signature of uniaxial anisotropy. One can also appreciate from this series of curves that the angular dependence becomes slightly less pronounced as t_{ox} increases.

In the case of the fully epitaxial reference sample and for t_{ox} = 0.11 nm, the remanent magnetization is almost exactly 1 along the EA (β = 0°) and its value decreases in sinusoidal way as one goes further away from the EA towards the HA (β = 90°), where M_r vanishes as expected. This behaviour agrees very well with the ideal case of the rotation of the coherent magnetic state, which is shown as a dot-dashed

red line in all figs. 4-10 (a)-(f), and which simply describes the absolute value of a sinusoidal variation of the magnetization projection onto the rotating field axis[dd].

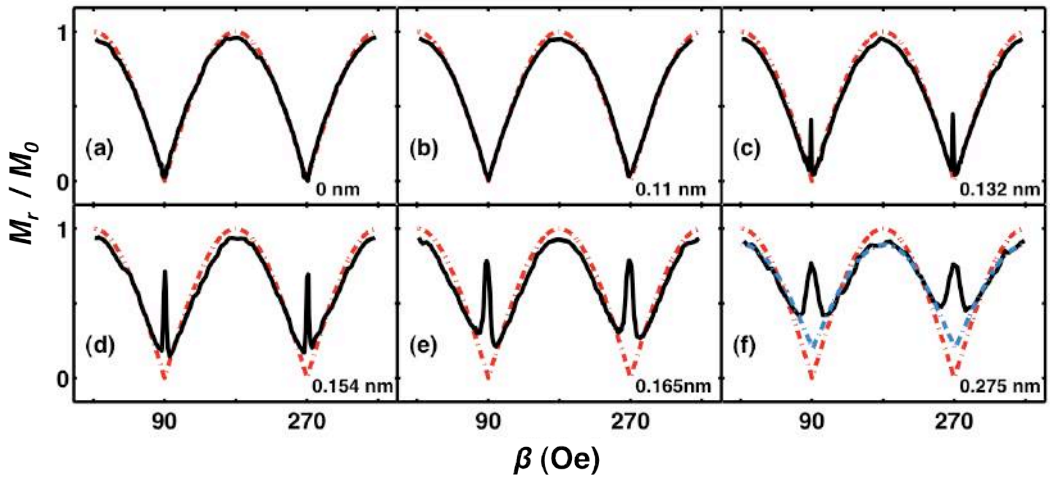

Figure 4-10: Measured M_r/M_0 values for (10$\underline{1}$0) Co samples with different crystallographic order corresponding to a deposited SiO_2 interlayer thickness of 0 nm (a), 0.11 nm (b), 0.132 nm (c), 0.154 nm (c), 0.165 nm (e) and 0.275 nm (f) (black lines). The red dashed lines display perfect uniaxial anisotropy behaviour, where M_r/M_0 is given by the uniform magnetic state projection onto the applied field axis, and the blue dashed line in (f) shows the least squares fit of the M_r/M_0 data by using an adapted model (eq. 4-1) for imperfect uniaxial anisotropy.

For samples with higher disorder, i.e. t_{ox} = 0.132 nm, 0.154 nm, 0.165 nm and 0.275 nm (figs. 4-10 (c)-(f)), one still observes a clear variation of M_r/M_0 as a function of β, and even though the M_r/M_0 values along the EA are no longer equal to 1 they still exhibit high values of 0.85 and above. Also, for most of the β range, the angular dependence of M_r seems only moderately or even minimally affected, as if the decrease in crystalline alignment had little influence onto the remanent magnetization states. However for applied field orientations near the HA, the behaviour is drastically changed in a non-trivial fashion. Instead of a vanishing or only small remanence value, as expected for simple uniaxial samples, one observes a steep increase of the M_r/M_0 values along the nominal HA upon decreasing the crystalline alignment, i.e. as one moves from sample to sample. The second aspect that is very unusual, is the fact that this high HA remanence is limited to the immediate vicinity of the HA itself, resulting in very sharp M_r-peaks in figs. 4-10 (c)-(f). This unusual behaviour, i.e. the peak-like increase of M_r/M_0 near the HA, is discussed in more detail in chapter 5.

[dd] This behaviour is identical to the well-known and previously described SW-model (sect. 2.2.1.1.), which is also based on uniform magnetization states.

In order to quantify the partial or imperfect uniaxial anisotropy in these Co samples with different crystallographic order, the orientation ratio has been determined. The orientation ratio is the ratio between the remanent magnetization in the EA (M_{rea}) versus the HA (M_{rha}) and it is widely used in industrial applications of magnetism to classify the goodness of materials[95,96]. Although, the orientation ratio determination is usually based on a two point measurement only (M_{rea} and M_{rha}), this is not appropriate here due to the HA anomaly. Thus, all experimental M_r/M_0 data in the entire field orientation range (β) have been utilized for the determination of the orientation ratio. Using an adapted formula for the projection of the magnetization onto the applied field axis, the extrapolated EA (M'_{rea}) and HA (M'_{rha}) magnetization values have been defined and subsequently the orientation ratio has been calculated. Hereby, the normalized M_r at different applied field angles is assumed to follow,

$$\frac{M_r}{M_0}(\beta) = b + a|cos(\beta)| \qquad (4\text{-}1),$$

where b and a are parameters that describe the degree of uniaxial alignment. This equation is capable of describing the full sample spectrum from perfect uniaxial alignment to isotropic samples by changing the b and a parameters. For the perfect coherent magnetization rotation case with uniaxial anisotropy, $b = 0$ and $a = 1$, which are the dot-dashed red lines in figs. 4-10 (a)-(f). On the other hand, for isotropic samples, the a factor is 0 and b takes a finite value between 0 and 1, depending on the specific angular independent M_r/M_0 value of the samples.

Least-squares fits to eq. 4-1 have been performed for the experimental M_r/M_0 data of all Co samples, with one example being shown in figure 4-10 (f) as a blue dashed line. The least-squares fits agree very well with all experimental data, except of course, in the vicinity of the nominal HA for the samples with t_{ox}= 0.132 nm, 0.154 nm, 0.165 nm and 0.275 nm. Here, the HA anomaly appears, which cannot be described by the simple sinusoidal functional form of eq. 4-1.

From the fit parameters of equation 4-1, i.e. a and b, the magnetic orientation ratio (OR) has been calculated, which is given as the ratio of the projected remanent magnetizations in the EA (M'_{rea}) and HA (M'_{rha}):

$$\mathrm{OR} = \frac{M'_{rea}}{M'_{rha}} = \frac{a+b}{b}$$

(4-2).

For fully epitaxial samples as well as for the t_{ox} = 0.11 nm sample, OR values are extremely high, consistent with the high level of crystallographic alignment in these samples. As the t_{ox} increases, OR value decreases (fig. 4-11 (a)). However, only for samples with t_{ox} = 0.33 nm or higher, OR is nearly equal to 1, indicating isotropic or nearly isotropic behaviour. For intermediate t_{ox} values a continuous decrease of uniaxial magnetic anisotropy upon increasing t_{ox} can be very well observed.

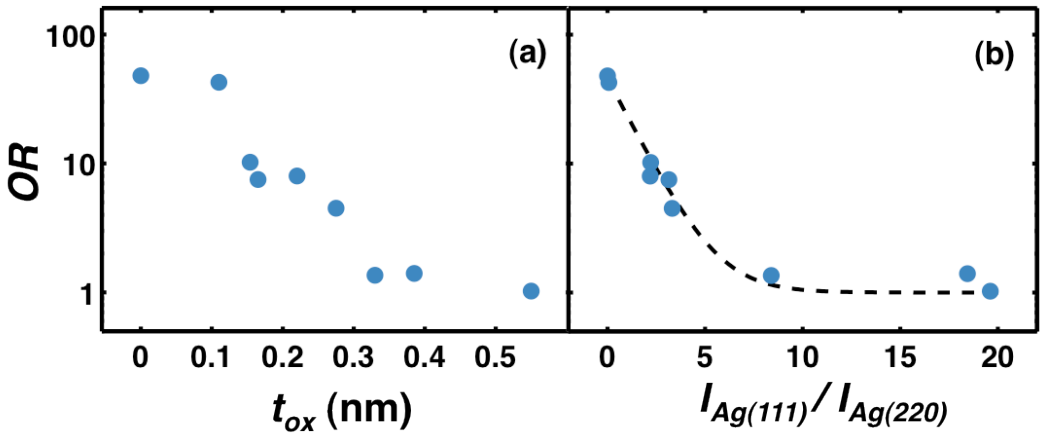

Figure 4-11: (a) shows the orientation ratio value as function of t_{ox} and (b) shows the orientation ratio as a function of the ratio between the Ag (111) and Ag (220) diffracted peaks intensity for the Co film sample series with partial epitaxy.

Figure 4-11 (b) shows the same extrapolated OR values as a function of the XRD peak ratio $(I_{Ag(111)}/I_{Ag(220)})$. This plot shows very clearly that the magnetic anisotropy alignment in the Co-films is fully correlated with the degree of (110) texture in the Ag-template layers. This is, of course not a surprising result, because it is the (110) Ag texture that enables the growth and the alignment of the Co (10$\underline{1}$0) surface orientation. Thus, as the (110) Ag texture decreases the crystalline quality of Co (10$\underline{1}$0) decreases and the uniaxial magneto-crystalline behaviour becomes weaker until it disappears completely. Figure 4-11 demonstrates clearly, that the methodology of partially interrupting the epitaxy of an otherwise uniaxial thin film allows for the introduction of crystalline misalignment that affects the magnetic anisotropy alignment in a well-controlled and continuous manner.

4.1.3. Magnetic multidomain existence analysis

While much of the previous discussion has been focused on the macroscopic magnetic property dependence on the crystallographic alignment, in this section the attention turns to microscopic magnetization reversal features. As mentioned before, ideal uniaxial systems exhibit two key processes, magnetization rotation and magnetization switching, with both of them being dependent on the magnetic field strength and orientation. For extended ferromagnets, such as the here analysed thin film samples, the magnetization reversal typically is triggered by a locally activated nucleation process due to almost always present defects as well as thermal noise when the externally applied field is along the EA. Both aspects lead to the effect that observed switching fields are generally far lower than the anisotropy field, which is the anticipated switching field within the SW-model for T = 0 K. Subsequent to the initial nucleation, domain walls propagate rapidly, so that well-ordered samples go through a succession of transient domain states that are neither stable nor metastable [97,98]. For applied fields away from the EA, the magnetization reversal is given by a combination of domain nucleation and its rapid expansion together with a coherent rotation that arises from the competition between the Zeeman energy and the anisotropy energy. This means that on the quasi-static time scale, ideal ferromagnetic films with uniaxial in-plane anisotropy are characterized by uniform magnetization states throughout their reversal process. Thus, with the introduction of crystallographic misalignment, the biggest qualitative change in magnetization reversal is the possible occurrence of static domain states. Therefore, the following microscopic investigation is focused on exactly this key aspect of magnetization reversal in films with varying crystallographic alignment, namely the existence of static and thus meta-stable reversal domains.

To study the existence of reversal domains, detailed MOKE microscopy studies have been performed at room temperature as a function of the magnetic field angle and strength for the above-discussed Co film samples of different crystallographic quality. For this purpose, the previously described MOKE microscopy system has been used (sect. 3.3.1.3.) in longitudinal geometry, so that it is sensitive to the magnetization component that is parallel to the externally applied field. As mentioned before, this microscopy system allows for the study of the

angular field dependence of the magnetic properties and hence specifically of the resulting domain pattern thanks to a sample stage that allows for a precise rotation around the surface normal.

In order to address the relevant scientific question at hand, which in this study is the existence of stable or meta-stable magnetization reversal domains, magnetization states throughout an entire magnetization reversal sequence have been imaged. By doing so one acquires a vast amount of data, i.e. a series of MOKE microscopy images that lead to a complete video sequence for each magnetization reversal geometry. Therefore, in order to extract the most relevant information, it is sensible to compact the data by devising a representation scheme, which enables an easy and automated identification of the existence of multidomain states. For this reason, a new representation method has been developed, which consists in taking the magnetization reversal video sequence generated by all MOKE images and by analysing the magnetization distribution to extract the range of domain existence. The representation method is described in detail in appendix B.

Figure 4-12 shows the multidomain existence ranges during magnetization reversal as a function of different applied field angles and strength, i.e. measurements that are analogous to the angular dependence of the upper branch of conventional hysteresis loops, for 6 of the uniaxial thin film Co-samples with varying degree of crystallographic alignment. These domain existence data as a function of H and β have been extracted from the MOKE microscopy measurements using the methodology described in appendix B. Hereby, black indicates a single domain state, while other colours reveal the existence of multidomain states. While the epitaxial reference sample in fig. 4-12 (a) does not show any static multidomain state as expected, the samples with sufficiently large SiO_2 interlayers and correspondingly reduced crystallographic order show clearly visible existence regimes of multidomain states in figs. 4-12 (c)-(f). Moreover, by comparing all the individual figures it is clear that the multidomain existence range increases with increased crystallographic disorder.

In the case of the t_{ox} = 0.11 nm sample, shown in fig. 4-12 (b), multidomain states appear for only one measured field strength for a few of the applied field angles. Thus, domain state existence cannot be seen as fully stable here. Instead, the

specific domain observation here is a consequence of imaging transient, but rather slowly changing, domain states in the exact moment, at which a domain wall moves through the sample area that has been imaged by the MOKE microscope. This interpretation is consistent with the fact that the appearing pattern of domain wall stability is not reproducible, but changes in between measurement runs in a statistical manner.[99]

For the samples with t_{ox} = 0.132 nm and t_{ox} = 0.154 nm, multidomain structures appear already for measurements near the EA. However, this existence only manifests itself at few applied field strength values, consistent with the fact that in the EA itself domains are less likely to occur. As β is increased up to around 50°, the existence range of these multidomain states increases. For even larger values of β, no static domains are observed in either sample, meaning that the reversal appears to be dominated again by uniform magnetization states[ee].

For samples with higher crystallographic misalignment, i.e. t_{ox} = 0.165 nm and t_{ox} = 0.275 nm, the multidomain reversal states become even more relevant but also here, the field range, in which non-uniform states appear, decreases for angles near the nominal EA and HA.

On top of all maps in fig. 4-12, green lines show the measured angular dependence of the coercive field H_c that has been extracted from MOKE hysteresis loop measurements. The H_c curve for the fully epitaxial reference sample, as well as for the sample with t_{ox} = 0.11 nm, show an initial increase of H_c with β until around 65°, after which it decreases for even larger magnetic field angles. This type of shape has been previously observed in highly ordered uniaxial samples[98]. It indicates two different mechanisms for reaching a zero magnetization component state along the field axis. For applied fields near the EA, i.e. β < 65°, H_c is dominated by the switching field as one observes in figs. 4-12 (a) and (b), even if the reversal process may start by a coherent rotation. However, for applied fields near the HA, i.e. β > 65°, zero magnetization is achieved by means of the coherent rotation process before

[ee] Here, one has to be aware that the contrast that is measured by the MOKE microscope is reduced for these field angles, which also explains the changing contrast for the multidomain representation as one moves from low β to high β in all these measurements.

a switch actually occurs at even larger reverse fields. Thus, a distinct change in the H_c vs. beta behaviour occurs at this intermediate field angle.

For samples with higher crystallographic misalignment, the coercive field vs. applied field angle dependence is very different. One can see a decrease of H_c with β for the samples with $t_{ox} \geq 0.132$ nm and this effect is becoming more pronounced as the disorder increases. It is worthwhile to notice that this qualitative change in behaviour happens at the same disorder level, at which stable reversal domains begin to occur. However the effects might not be so closely related as this correlation suggests, since H_c and domain existence do not coincide for high β in samples with $t_{ox} = 0.132$ nm figs. 4-12 (c) and $t_{ox} = 0.154$ nm (d).

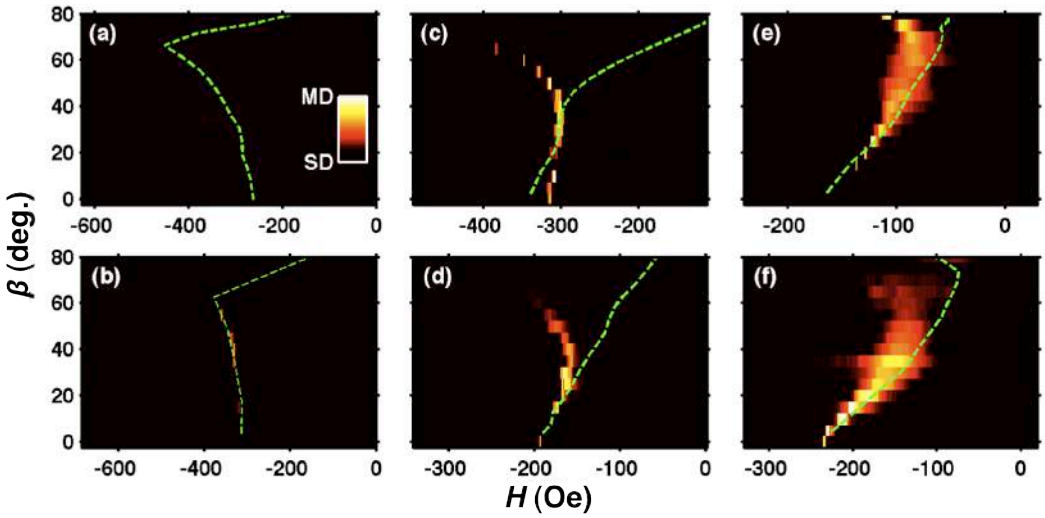

Figure 4-12: Domain state existence maps for the magnetization reversal of in-plane uniaxial Co-films with different degree of crystallographic order: (a) fully epitaxial (10$\underline{1}$0) Co film, and partially epitaxial films with a deposited SiO_2 interlayer thickness of (b) 0.11 nm, (c) 0.132 nm, (d) 0.154 nm (e) 0.165 nm and (f) 0.275 nm. Also shown as a green dashed line in every plot, is the angular dependence of the coercive field, which has been extracted from MOKE hysteresis loop measurements. All maps use the same colour scheme, which is displayed in (a): black corresponds to full magnetic uniformity or a single domain (SD) state, while other colours correspond to the existence of magnetic non-uniformities, i.e. multiple domain states (MD).

For the samples with $t_{ox} = 0.132$ nm and $t_{ox} = 0.154$ nm, H_c overlaps with the domain existence range up to applied field angles of around 40° and 30° respectively, indicating that the reversal processes at H_c are dominated by domain processes. However, as the field angle increases further, the H_c line separates from the domain stability range, which is still existent. This simply means that for $\beta > 40°$ for sample with $t_{ox} = 0.132$ nm and $\beta > 30°$ for sample with $t_{ox} = 0.154$ nm the processes at H_c are dominated by magnetization rotation, whereas domain generation occurs only for

larger field values near the completion of the magnetization reversal process. It is worthwhile to notice that this phenomenon appears closer to the EA, as the disorder level increases in the sample. For samples with t_{ox} = 0 nm and t_{ox} = 0.11 nm, H_c is dominated by coherent rotation for $\beta > 65°$, while for samples with t_{ox} = 0.132 nm and t_{ox} = 0.132 nm, this happens already for $\beta > 40°$ and $\beta > 30°$, respectively.

For films with even higher grain misalignment, such as the samples with t_{ox} = 0.165 nm and t_{ox} = 0.275 nm, the angular dependence of H_c traces the domain existence range closely over most, if not the entire field orientation range. This means that for high disorder levels, domain states control most of the magnetization reversal process, so that also the behaviour near the coercive field is dominated by intermediate domain states, almost or entirely independent from the magnetic field orientation, even though these types of films still exhibit very clear uniaxial magnetic anisotropy.

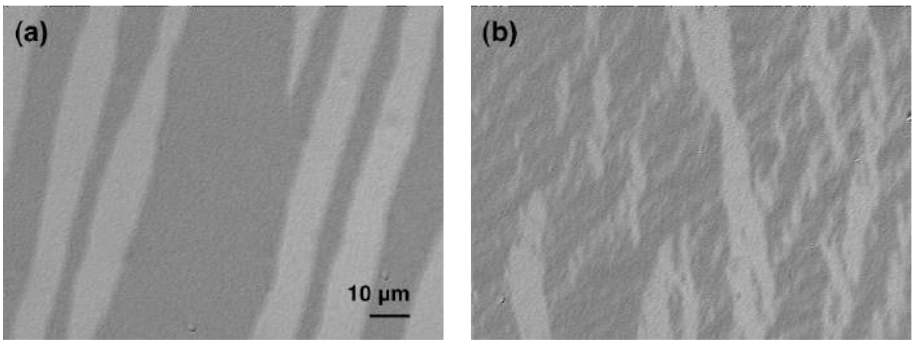

Figure 4-13: Domain structures, imaged by Kerr effect microscopy, for samples with t_{ox} = 0.132 nm (a) and t_{ox} = 0.165 nm (b) in the vicinity of the coercive field during the magnetization reversal process.

This magnetization reversal difference between lower disorder samples, such as the t_{ox} = 0.132 nm and 0.154 nm Co-layers, and higher disorder samples, such as the t_{ox} = 0.165 nm and 0.275 nm films, is also reflected in the actual shape of the non-uniform or magnetic domain states. Figure 4-13 shows domain images taken at β = 30° for the t_{ox} = 0.132 nm (a) and t_{ox} = 0.165 nm (b) samples in comparison. For samples with higher disorder, i.e. fig. 4-13 (b), the magnetization correlation length is decreased and correspondingly, smaller size domains appear forming ripple like structures, in contrast to the t_{ox} = 0.132 nm sample, shown in fig. 4-13 (a), where well defined and bigger domains are generated that furthermore exhibit only two possible magnetization values. On the other hand, no apparent difference in the domain shape

has been found between domain states generated near $H = H_c$ for small β and generated at $H > H_c$ for high values of β for the slightly disordered samples, i.e. t_{ox} = 0.132 nm or t_{ox} = 0.154 nm.

4.2. Co-Ru alloy thin films

As mentioned already, the investigation of magnetic alloys is a crucial aspect of the evolving fundamental understanding of ferromagnetism, as well as its technological application in numerous fields[100]. This is driven by the interest in achieving a broadly applicable scientific description of the physics of ferromagnetism and ferromagnetic materials as well as the need to optimize key magnetic properties such a saturation magnetization, Curie temperature, magneto-crystalline anisotropy, etc. for specific purposes. In particular, alloys between 3d ferromagnets and 4d or 5d transition metals have attracted vast attention, because theoretical and experimental studies suggest that in a ferromagnetic environment they are easily spin polarized by neighbouring 3d atoms, such as Fe and Co[17,19,20] and that their addition to alloys generates interesting magnetic properties such as large magneto-crystalline anisotropy[17]. It is for this very reason, that all magnetic hard disk drive storage is based today on Pt-containing Co-alloys[4,6,101]. Among the 4d transition metals Ru has recently attracted some wider attention due to its physical properties and it has had a prominent role in magnetics technology, primarily as interlayer coupling material. Since the discovery of oscillating interlayer exchange coupling in Ru by Parkin and co-workers[102], Ru has been used for exactly this purpose in magnetic read sensors[103], anti-ferromagnetically coupled recording media[104] and for high performance soft magnetic underlayers for perpendicular magnetic recording[6]. Despite this most significant technological relevance, the vast amount of studies has been limited to ferromagnet/Ru bilayer or multilayer systems [102,105–107], so that rather little is known about the magnetic properties of CoRu alloys[108–116] and even less on epitaxially grown CoRu alloy films[108–110]. In references 112 and 114, the authors report on the chemical synthesis of CoRu alloy nanoparticles, they analysed their crystallographic phases and they show that they exhibit a ferromagnetic state by means of hysteresis loop measurements. CoRu alloys deposited as thin films have been studied in references 108–110, 115 and 116 but these works focused mainly on crystallographic

phase characterization[115], chemical ordering[108–110] and basic magnetic characterization[108–110,116]. Also, a detailed analysis of the atomistic origin of the polarization in Ru atoms within ferromagnetic alloys has been reported[113]. However, none of these CoRu alloy studies shows a complete investigation of detailed magnetic properties in crystalline CoRu alloys, such as, magnetic anisotropy, magnetic saturation values or T_C as a function of alloy concentration.

Considering that CoRu alloys are fairly unexplored compounds and given that CoRu alloy studies are a most suitable extension of the above Co-film work, epitaxial CoRu alloy films have been fabricated. In addition, other different Co alloys, such as, CoCr and CoCrNi, have been also grown, but their properties have been not analysed in detail, so that they are not described here.

In this section, detailed studies on the structural and magnetic properties of $Co_{1-x}Ru_x$ alloys grown epitaxially at room temperature with (10$\underline{1}$0) crystallographic orientation are described.

4.2.1. Crystallographic and structural properties

$Co_{1-x}Ru_x$ (10$\underline{1}$0) alloy thin film samples have been grown by using the previously described UHV sputter deposition system. Here, x is the atomic concentration of Ru in the alloy. As an initial attempt to grow epitaxial 30 nm $Co_{1-x}Ru_x$ alloy thin films with (10$\underline{1}$0) crystallographic structure, the same layer sequence as for the epitaxial Co reference sample (sect. 4.1.1. fig. 4.1) has been used, namely Si (110) as the substrate/75 nm Ag/50 nm Cr/30 nm $Co_{1-x}Ru_x$. However, using this underlayer structure for $Co_{1-x}Ru_x$-alloys with $x = 0.3$[ff], the obtained crystallographic quality of the resulting (10$\underline{1}$0) CoRu-alloy film is poor. Figure 4-14 shows an XRD-measurement of such a sample, specifically a $Co_{0.70}Ru_{0.30}$ alloy film ($x = 0.30$). Even though a (10$\underline{1}$0) diffraction peak can be observed at $2\theta = 40.4°$ for the CoRu alloy layer, its comparatively low peak intensity manifests low crystallographic quality. This substantially decreased growth quality is, of course, not too surprising because the excellent lattice matching conditions in between the bcc Cr (211) and the hcp Co

[ff] At least this is true for $x = 0.3$, which was the initially tested alloy concentration, using Si (110) as substrate/75 nm Ag/50 nm Cr/30 nm $Co_{1-x}Ru_x$, layer sequence. For lower x, the crystallographic quality might be different with this layer sequence.

(10$\underline{1}$0) lattice planes do not hold for CoRu-alloys with substantial Ru-content due to the larger size of the Ru atom. The hexagonal lattice parameters for bulk Ru are a = 2.705 Å and c = 4.282 Å, while the constants for bulk Co are 2.51 Å and 4.06 Å, respectively. Correspondingly, this results in significantly larger lattice spacing in CoRu-crystals than pure Co[114].

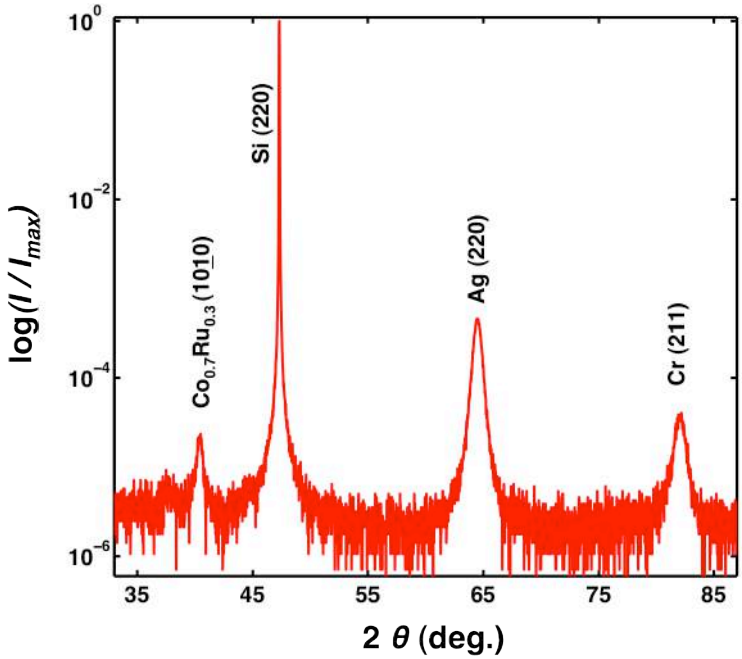

Figure 4-14: θ-2θ X-ray diffraction spectra for a 30 nm thick (10$\underline{1}$0) $Co_{0.7}Ru_{0.3}$ sample grown by using the Si substrate/75 nm Ag /50 nm Cr underlayer sequence.

In order to overcome low crystallographic quality of these (10$\underline{1}$0) CoRu-alloy films, the epitaxial underlayer sequence has been altered to achieve better lattice matching conditions. Specifically, a $Cr_{1-y}Ru_y$ intermediate layer has been introduced by splitting the initially 50 nm thick Cr underlayer into two layers, namely a 25 nm thick film of pure Cr that is deposited onto the Ag and a subsequently deposited 25 nm film made from an appropriate $Cr_{1-y}Ru_y$ alloy. Hereby, the atomic concentration of Ru in CrRu alloy is represented by y. The corresponding layer sequence is shown in fig. 4-15. Just as in the case of the magnetic CoRu-alloy, the lattice constant of the Cr underlayer increases by introducing Ru [117], and this produces a better template for the magnetic CoRu alloy if the CrRu-alloy underlayer is sufficiently thick to relax its lateral lattice spacing. However, one needs to be careful with CrRu alloy selection since too much Ru in the CrRu-alloy may result in a breakdown of the epitaxy already at the Cr to CrRu interface.

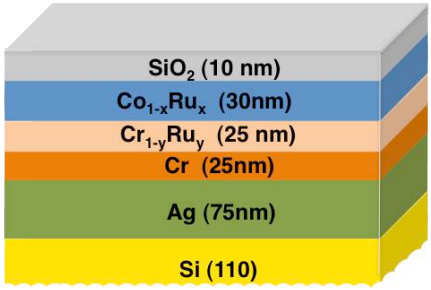

Figure 4-15: Schematic of layers sequence for epitaxial $Co_{1-x}Ru_x$ ($10\underline{1}0$) growth.

In order to achieve the best epitaxial growth conditions, one needs to find the optimal $Cr_{1-y}Ru_y$ stoichiometry for every composition of the magnetic $Co_{1-x}Ru_x$ alloy. Upon conducting a detailed study of the epitaxial growth, I has been able to conclude that having a ratio of 1.2 in between the Ru content in the magnetic $Co_{1-x}Ru_x$ alloy and $Cr_{1-y}Ru_y$ underlayer material results in excellent growth conditions and an optimized crystallographic quality for the respective film thicknesses that have been explored here. One example for the high quality of the so achieved epitaxial growth is shown in fig. 4-16, where the XRD-data for a $Co_{0.70}Ru_{0.30}$ sample grown onto a $Cr_{0.75}Ru_{0.25}$ underlayer can be seen. Also, a diffracted peak arising from $Cr_{0.75}Ru_{0.25}$ layer with (211) crystallographic orientation can be observed at slightly lower angles than the diffracted peak from the (211) Cr layer. This shift to lower angles demonstrates the increase of the lattice constant of the Cr layer by alloying it with Ru. For the $Co_{0.70}Ru_{0.30}$ film itself, an intense ($10\underline{1}0$) diffracted peak is visible, that is about equal in quality to the previously discussed and well established pure Co ($10\underline{1}0$) reference film (fig. 4-3). Just as for pure Co, the higher order diffracted peak for the $Co_{0.70}Ru_{0.30}$ ($10\underline{1}0$) crystallographic orientation is also visible.

Upon establishing the high epitaxial quality of this growth sequence, i.e. Si substrate (110)/Ag 75nm (110)/Cr 25 nm (211)/$Cr_{1-y}Ru_y$ 25 nm (211)/$Co_{1-x}Ru_x$ 30 nm ($10\underline{1}0$)/ SiO_2 10 nm amorphous overcoat for environmental protection (fig. 4-15), 7 different Co_xRu_{1-x} alloy films have been grown with x = 0, 0.05, 0.10, 0.15, 0.20, 0.25 and 0.30 and the correspondingly optimized Cr_yRu_{1-y} underlayer stoichiometry, so that a x/y-ratio of 1.2 has been preserved.

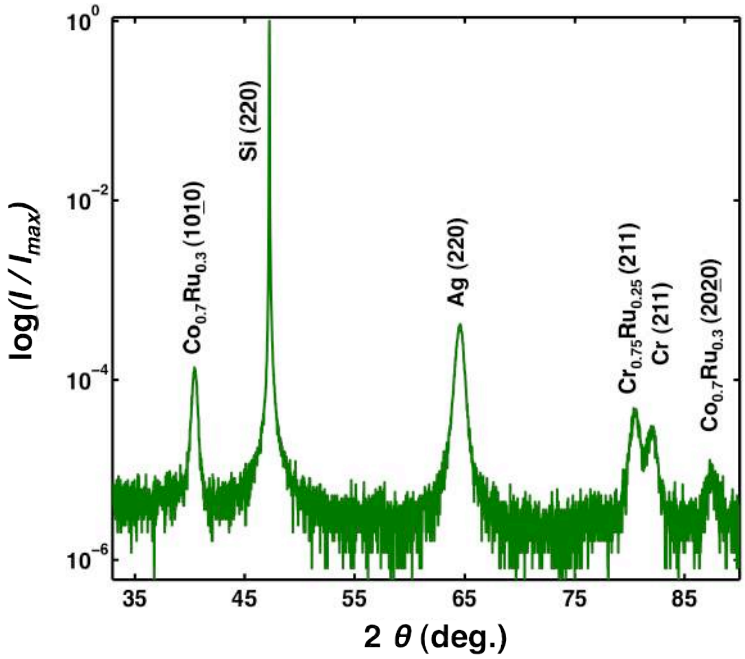

Figure 4-16: θ-2θ X-ray diffraction spectra for a 30 nm thick (10$\underline{1}$0) $Co_{0.70}Ru_{0.30}$ sample, grown by using the Si substrate/75 nm Ag /25 nm Cr/25 nm $Cr_{0.75}Ru_{0.25}$ underlayer sequence.

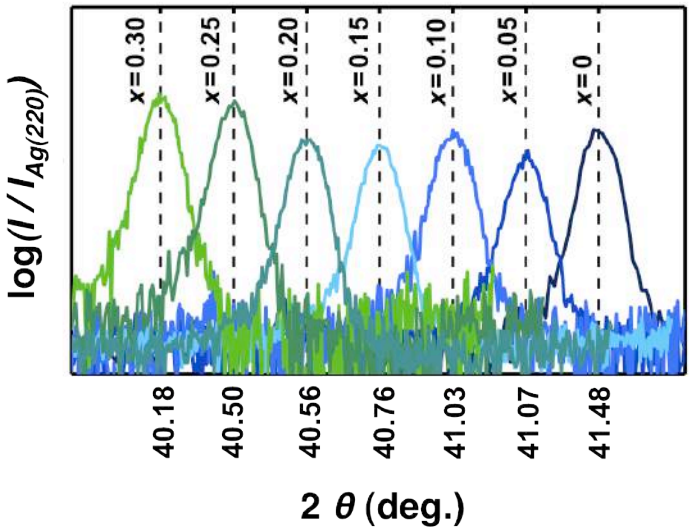

Figure 4-17: $Co_{100-x}Ru_x$ (10$\underline{1}$0) crystallographic XRD-peaks normalized to the corresponding Ag (220) peak intensity of the each individual sample for $Co_{1-x}Ru_x$ films with different Ru concentration (x values indicated).

Figure 4-17 shows the Co_xRu_{1-x} (10$\underline{1}$0) X-ray diffraction peaks for the entire set of samples, normalized to the Ag (220) peak intensity of each individual sample, which defines, as observed before, the initial epitaxial quality of the growth sequence. For clarity, the angular references points are shifted to have equidistance space in between the different Co_xRu_{1-x} (10$\underline{1}$0) diffracted peaks in the plot. As one can see

from the data, the different $Co_{1-x}Ru_x$ (10$\underline{1}$0) peaks are all very similar in their height and width, verifying the fact that one can achieve equally good crystallographic quality for the series of $Co_{1-x}Ru_x$ (10$\underline{1}$0) epitaxial films in the entire stoichiometry range investigated here with the newly devised underlayer structure, that includes an intermediate $Cr_{1-y}Ru_y$ underlayer of appropriately adapted and *x*-dependent *y*. Thus, one can now study how the composition affects the magnetic properties of $Co_{1-x}Ru_x$ epitaxial films, given that uniform crystallographic sample quality has been established.

4.2.2. Macroscopic magnetic properties

Here, the macroscopic magnetic characterization has been carried out by means of VSM measurements using the 3900VSM from Princeton Measurement Corporation, described in section 3.3.2.1. Figure 4-18 shows nine hysteresis loops measured at three different applied field angles for $Co_{0.9}Ru_{0.1}$ (figs. 4-18 (a)-(c)), $Co_{0.85}Ru_{0.15}$ (figs. 4-18 (d)-(f)) and $Co_{0.8}Ru_{0.20}$ (figs. 4-18 (g)-(i)) thin films at room temperature. (a), (d) and (g) show hysteresis loops for applied fields along the EA, (b), (e) and (h) for applied fields 40° away from the EA and (c), (f) and (i) for applied fields 60° away from the EA[gg].

A pronounced angular dependent change of the hysteresis loop shape is visible for all three CoRu alloys shown here. While for applied fields along the EA all samples exhibit a square shape hysteresis loop, for applied fields away from the EA, i.e. β = 40° and β = 60°, the magnetization reverses initially via coherent rotation followed by a sample size magnetization switch. This behaviour is fundamentally identical to the epitaxial reference sample of pure Co shown in section 4.1.2 (figs. 4-9 (a)-(c)). Despite these similarities, please, note that for high applied field strength and β = 60°, the magnetization shows quite different slopes for the different samples. While for $Co_{0.9}Ru_{0.1}$ the magnetization does not change much for field values higher than 2500 Oe, the $Co_{0.75}Ru_{0.15}$ and $Co_{0.80}Ru_{0.20}$ samples still show considerable M/M_0 vs. H slope, i.e. susceptibility in this field range. This difference might be indicative

[gg] Hereby M_0 is the magnetization value measured at applied fields of 5000 Oe.

of the alloy dependent magneto-crystalline anisotropy, which has been analysed in a quantitative manner below.

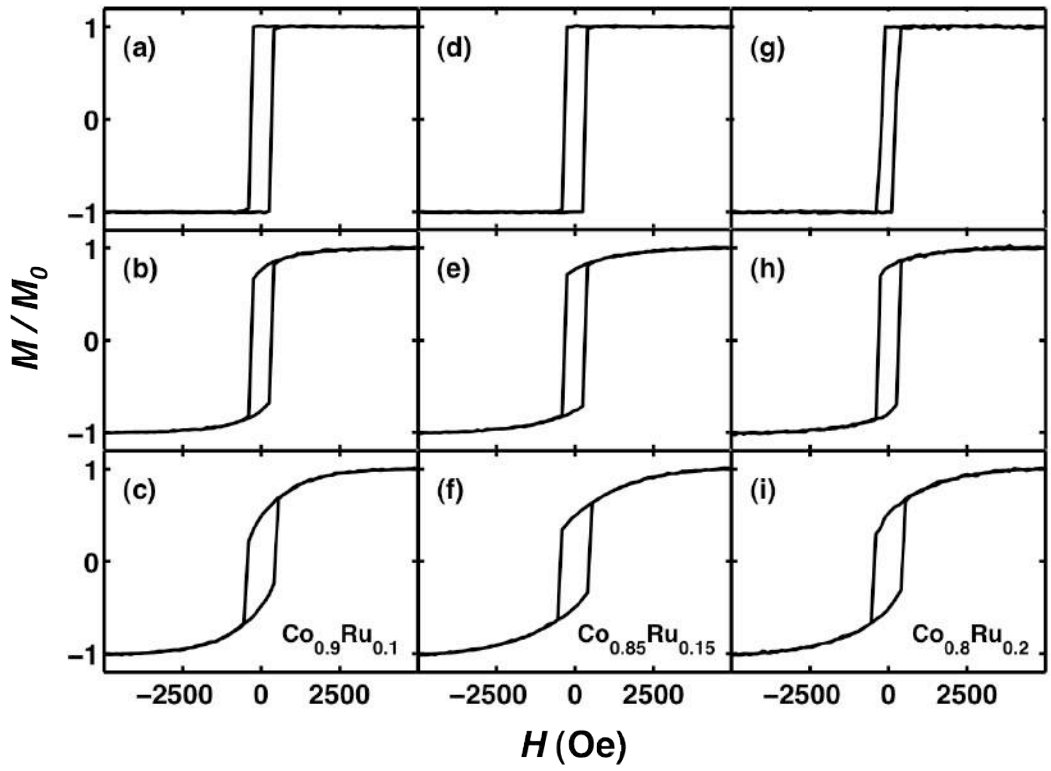

Figure 4-18: Hysteresis loops measured for (10$\underline{1}$0) $Co_{1-x}Ru_x$ alloy thin films of different Ru concentration (x): (a)-(c) for x = 0.1, (d)-(f) for x = 0.15 and (g)-(i) for x = 0.2. (a), (d), (g) show hysteresis loops for applied fields along the EA, (b), (e) and (h) show hysteresis loops for applied fields 40° away from the EA and (c), (f) and (i) show hysteresis loops for applied fields 60° away from the EA.

Just as in the case of the pure Co-films, the full angular dependence of the hysteresis loops have been measured in steps of 5° and from these hysteresis loop measurements, the remanent magnetization M_r values have been extracted.

Figure 4-19 shows the measured M_r/M_0 dependence from the applied field angle (solid black curves) for $Co_{1-x}Ru_x$ samples with x = 0, 0.05, 0.1, 0.15, 0.2 and 0.25 extracted from individual hysteresis loop measurements. In all cases, a 180° of periodicity is observed, which is the sign of uniaxial anisotropy. The dashed red lines represent the uniform magnetic state projection onto the applied fields axis for perfect uniaxial symmetry at zero temperature. For almost all compositions a nearly perfect match between the measured data and the ideal uniaxial anisotropy behaviour is observed, with OR values higher than 20, except for the $Co_{0.75}Ru_{0.25}$ sample, for which the match is not so good as one can clearly see in fig. 4-19 (f). Here, the OR value is decreased to 5.2.

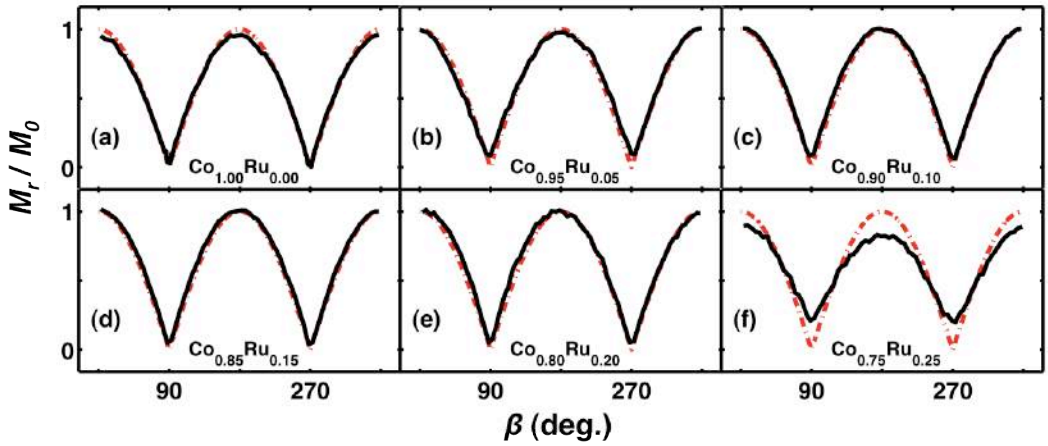

Figure 4-19: Measured M_r/M_0 values for ((10$\bar{1}$0) $Co_{1-x}Ru_x$ alloy thin films of varying Ru concentration (x), (a) x= 0, (b) x = 0.05, (c) x = 0.1, (d) x= 0.15, (e) x =0.2 and (f) x = 0.25. The red dashed line displays the perfect uniaxial anisotropy behaviour, where M_r/M_0 is given by the uniform magnetic state projection onto the applied field axis.

Figure 4-20 shows normalized magnetization M/M_s[hh] colour-coded maps as a function of the in-plane applied field angle β with respect to the easy axis, and the field strength H for samples with x = 0, 0.05, 0.10, 0.15, 0.20 and 0.25 measured at room temperature. At every field orientation angle, the magnetization has been measured starting from saturation (H = 5 kOe) down to remanence. These $M(H)$-data set have been obtained by measuring from β = 0° to β = 360° using a step size of 5°. At high fields and near the EA, i.e. β = 0° and β = 180°, M/M_s is equal to 1 (value represented by brown colour), while at low fields near the hard axis (β = 90° and β = 270°), M/M_s approaches vanishing values shown by the blue colour. All M/M_s (H,β)-maps show a clear 180º periodicity verifying the already seen uniaxial magnetic behaviour. Moreover, the experimental M/M_s (H,β)-maps illustrate clearly that straightforward magnetization saturation happens only along the EA and the HA and that it cannot be achieved fully along any other direction, thus mimicking the perfect textbook behaviour of the SW model (sect. 2.2.1.1.). Furthermore, it is evident from the experimental data that the overall features vary from sample to sample due to the change in alloy composition. In order to quantify the variation of the magnetic properties, specifically the anisotropy constants as a function of Ru concentration, least-squares fits have been performed of the M (H,β) data using the previously explained total free energy per volume (E) of a uniformly magnetized system with

[hh] Here, M_s has been calculated by least-squares fitting the whole M (H,β) maps as described below.

uniaxial anisotropy, where

$$E = -\vec{H}M_s\hat{m} - K_1'(\hat{m}\cdot\hat{n})^2 - K_2'(\hat{m}\cdot\hat{n})^4 \qquad (4\text{-}3).$$

Hereby $\vec{H}$ is the applied field vector and M_s represents the saturation magnetization, whose direction is given by the unit vector, $\hat{m}$. K_1' and K_2' represent first and second order magneto-crystalline anisotropy constants with the easy axis orientation given by the unit vector $\hat{n}$. Due to the assumption of uniform magnetic states only, the exchange energy does not appear expressively, because it is not orientation dependent and thus it can be ignored in the energy minimization. The first term in equation (4-3) is the Zeeman energy, which describes the interaction between the externally applied field vector $\vec{H}$ and magnetization vector $M_s\hat{m}$. If one restricts the magnetization to in-plane orientations only due to the strong demagnetizing effects along the surface normal, the free energy can be re-written as

$$E = -HM_s[cos(\alpha-\beta)] + K_1[sin^2(\alpha)] + K_2[sin^4(\alpha)] \qquad (4\text{-}4),$$

where the first and second order anisotropy constants are given as $K_1 = K_1' - 2K_2'$ and $K_2 = -K_2'$. Moreover, energy terms $-K_1'$ and $-K_2'$ have been omitted from the energy expression because they do not have any orientation dependence, and are therefore not relevant in the energy minimization analysis. The angle between the applied field and the magnetization is given by α-β, where α denotes angle of the magnetic field direction with respect to the EA. Hereby, H is given in units of Oe, M_s in units of emu/cm^3 and K_1 and K_2 in units of energy per volume, namely erg/cm^3. In order to fit the experimental $M(H,\beta)$ data maps, the angle of magnetization direction with respect to the easy axis (α) has been determined numerically calculating the local minimum according to eq. (4-4) starting from saturation and following the closest energy minimum for decreasing field amplitudes H down to zero for each applied field angle β. Each complete $M(H,\beta)$ map has been fitted simultaneously using only 3 free fitting parameters, namely M_s, K_1 and K_2. Figures 4-20 (g)-(l) show the corresponding results normalized to M_s side-by-side with the experimental data. Comparing both, an excellent agreement for all samples has been found with typical R^2 values of 0.96.

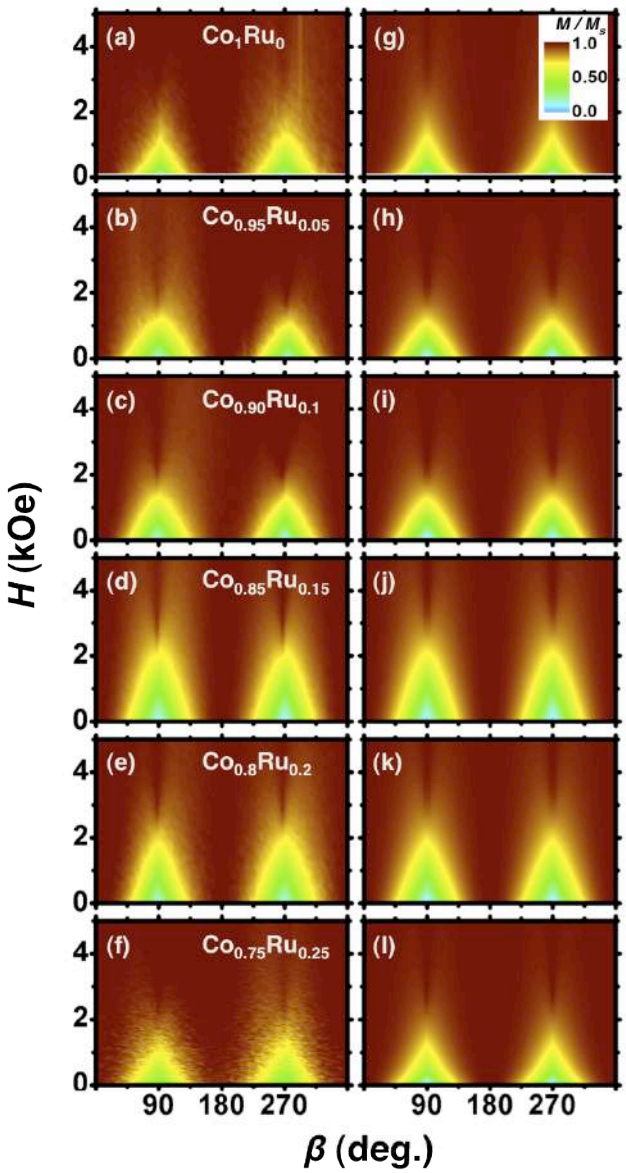

Figure 4-20: In-plane angular dependence of the magnetization value as a function of applied field angle and applied field strength for epitaxial (10$\underline{1}$0) $Co_{1-x}Ru_x$ samples with x = 0, 0.05, 0.10, 0.15, 0.20, 0.25. The data are displayed as colour-maps in (a)-(f) and are normalized to the saturation magnetization M_s.(g)-(l) show the corresponding least-squares fits of the data determined by only 3 free parameters for each map, specifically K_1, K_2 and M_s.

The extracted saturation magnetization M_s values are shown in fig. 4-21 (a) as a function of Ru concentration. Note that these M_s values correspond to the room temperature values. For pure Co, i.e. x = 0, M_s is identical to the bulk Co M_s[80] within the experimental error and also very similar to previously shown values for uniaxial Co films[15]. As expected, M_s decreases upon introducing Ru into the alloy and does so in an almost linear fashion with the Ru content.

The dependencies of K_1 and K_2 on the Ru-concentration are plotted in figure 4-21 (b)[ii]. For K_1 a clear non-monotonic behaviour can be observed. For pure Co the K_1 is 0.417 ± 0.14 x 10^6 erg/cm^3. When Ru is introduced into the lattice, K_1 decreases down to 0.28 ± 0.05 x 10^6 erg/cm^3 for only 5% of Ru, but surprisingly the value of K_1 then starts to increase again as additional Ru is incorporated into the alloy. For a Ru content of 20% and higher, K_1 values decrease again, thus making the alloy dependence of the anisotropy non-monotonic and non-trivial. While the value of K_2 is higher than K_1 for the pure Co sample, it decreases to rather small values upon introducing even only 5 % Ru into the alloy, and it stays at these low values for all other Ru-concentrations. It is hereby worthwhile to emphasize that despite the reduction in M_s, the sample with 15% Ru exhibit an increased K_1-value, so that the conventionally defined anisotropy field $H_{K1} = K_1 / 2M_s$ actually gets enhanced substantially beyond the pure Co-value, a fact that is clearly visible in fig. 4-20, where the cone-shaped HA structures are far larger for the 15% Ru-sample than for the pure Co-film.

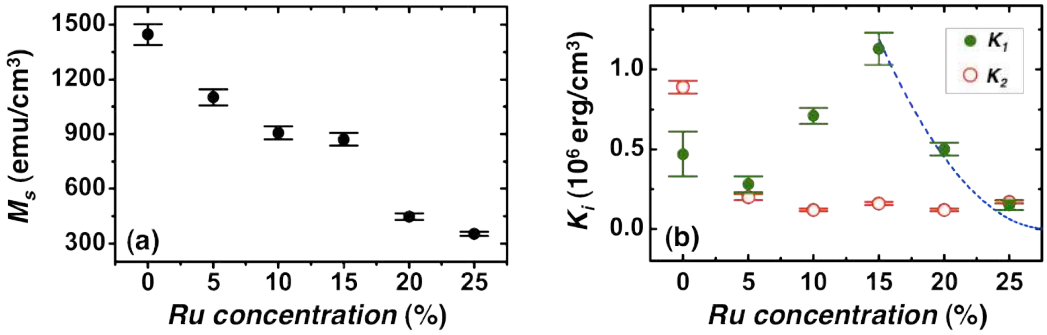

Figure 4-21: Experimentally determined magnetic materials properties for epitaxial (10$\underline{1}$0) $Co_{1-x}Ru_x$ alloy films as a function of the Ru-concentration: (a) saturation magnetization M_s and (b) first and second order uniaxial magneto-crystalline anisotropy constants, K_1 (green solid dots) and K_2 (red open circles). The dashed blue line in (b) represents the expected decrease of K_1 due to purely thermal effects that originate from the concentration dependent decrease of the Curie temperature given by eq. 4-7.

I have also estimated the Curie temperatures (T_C) of the samples from M vs. T measurements, made with the SQUID-VSM[jj]. For this purpose, the magnetic

[ii] Note that K_1 and K_2 are room temperature values.

[jj] There are two reasons why T_c has not been measured directly. One is that there were no instruments available that could measure at high enough temperature, at least for samples with x = 0 and x =0.05. The second and more important reason is that at high temperatures, the structural properties of the sample may change substantially, for example by annealing or even alloying and consequently the magnetic properties would irreversibly modified.

moments of all samples have been measured along the EA for temperatures from 300 K down to 5 K using a low bias field. As an example, figure 4-22 show the *M* vs. *T* measurements (black dots) performed for the $Co_{0.85}Ru_{0.15}$ sample.

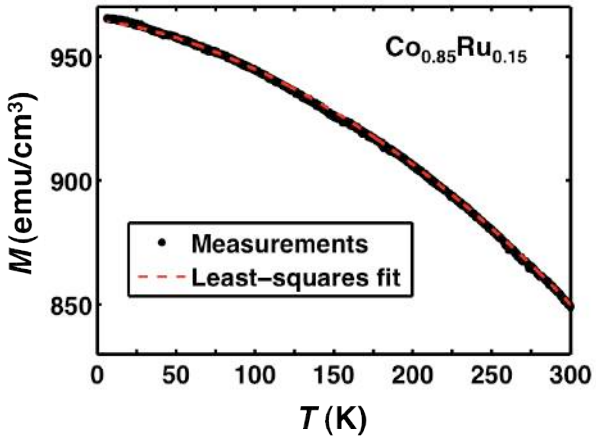

Figure 4-22: Magnetization versus temperature measured along the EA for a 30 nm thick $Co_{0.85}Ru_{0.15}$ film (black dots). The dashed red line represents the least squares fit of the data to equation 4-5.

In order to extrapolate T_C, an approximate interpolation formula for $M(T)$ has been used, which was described and tested in ref. 118 and assumes

$$M(T) = M_s(0)\left[1 - s\left(\frac{T}{T_C}\right)^{3/2} - (1-s)\left(\frac{T}{T_C}\right)^{5/2}\right]^{1/3} \qquad (4\text{-}5)$$

for the temperature dependent magnetization $M(T)$ for all temperatures below T_C. By fitting this equation to the experimental data, one can estimate the Curie temperature as one of the fitting parameters, with s and M_s being the other fit parameters of the interpolation formula. Hereby, the s parameter defines the overall shape of the M vs. T curve. A least-squares fit using eq. 4-5 for the M vs. T data measured for $Co_{0.85}Ru_{0.15}$ can be seen in fig. 4-22 as a red line, matching the experimental data extremely well.

The extracted T_C values using equation 4-5 for all Ru concentrations of the alloys studied here are shown in fig. 4-23. The T_C value of $Co_{0.70}Ru_{0.30}$ is represented by an open circle because it has been directly measured, rather than merely extrapolated. The larger uncertainty for the T_C values at low Ru content arises from the fact that the extrapolation is done far outside the measured temperature range in this case, and thus one has to consider the associated systematic errors. Similar to the

Ru-concentration dependence of M_s, an almost linear decrease in T_C is observed as the Ru-content increases in the alloy.

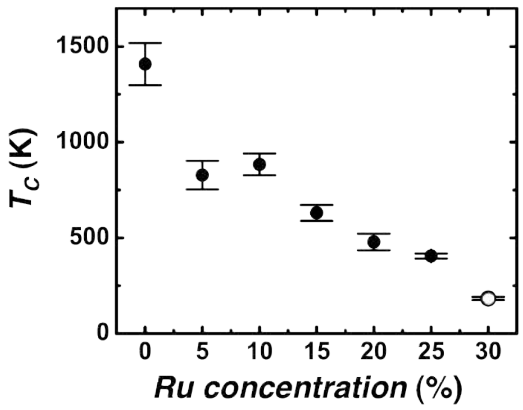

Figure 4-23: Experimentally determined Curie temperatures (T_C) for epitaxial (10$\underline{1}$0) $Co_{1-x}Ru_x$ alloy films as a function of the Ru-concentration. The open symbol for 30% of Ru indicates the direct measurement of T_C in contrast to the extrapolated T_C values, which are shown as solid circles.

On the other hand, the effect of Ru onto magneto-crystalline anisotropies can be very substantial, since the Ru atoms can become polarized due to a hybridization of the 5p orbitals of Ru with the 3d orbital of Co as proposed in ref. 113. The spin-orbit coupling constant for Ru atoms is around 0.150 ± 0.014eV[119], while for Co and other 3d transition metals it is around 50 meV[120], which is furthermore strongly reduced due to the crystal field. As consequence, even a modest spin polarization of Ru atoms can change the spin orbit coupling and thus the magneto-crystalline anisotropy constant very substantially, if it is introduced into an alloy together with Co. However such atomistic considerations are generally not reliable in metallic solids, because the relevant orbitals are hybridized in the solid state and thus will cause non-trivial alloy related changes. The non-monotonous Ru concentration dependence of the anisotropy as observed here is likely to be one example of this complexity. Indeed, other studies suggest that even an oscillating compositional dependence of the anisotropy may arise from a competition between the lattice constant and the strength of spin-orbit coupling[121,122]. One can also not exclude the possibility of ordered alloy formation at certain ratios of concentration, which form lower symmetry lattice structures and thus possibly higher anisotropy values, as previously observed on CoPt and FePt alloys[18]. However, the ordered alloy formation is not very probable here, because it has been shown to occur only at deposition temperatures between 500 K and 700 K, for which long range ordered $Co_{1-x}Ru_x$ alloys

with hcp crystallographic structure were observed for $0.125<x<0.25$[109,110].

However, what can be understood from fundamental principles is the K_1 decrease for high Ru content that one finds in fig. 4-21 (b). Hereby, one has to keep in mind that the K_i are defined via the order parameter orientation dependence of the free energy (eq. 4-4). Thus, all K_i have to approach zero as the alloy's T_C approaches the measurement temperature T, which is room temperature T_R here. The Callen-Callen theory[123,124], which has been shown to be valid for several magnetic alloys over an extended temperature range,[125], predicts for temperatures near T_C that the first order uniaxial anisotropy term follows

$$K_1(T) = \kappa_1(0)\left(\frac{M_s(T)}{M_s(0)}\right)^2$$

(4-6)

where $M_s(0)$ is the saturation magnetization at 0 K and the prefactor $\kappa_1(0)$ is a quantity that is proportional to the zero temperature anisotropy constant $K_1(0)$. Considering that M_s at room temperature is approximately linear dependent from the Ru concentration x (fig. 4-21 (a)), and furthermore assuming for simplicity that in the alloy concentration range, in which T_C approaches room temperature T_R the electronic state of the system and thus $K_1(0)$ and $M_s(0)$ values do not change, one can derive

$$K_1(x \to 0.28^-, T = T_R) = \zeta \frac{\kappa_1(T=0)}{\left(M_s(T=0)\right)^2}(0.28 - x)^2$$

(4-7),[kk]

as the approximate boundary condition that describes the reduction of $K_1(x)$ for the $Co_{1-x}Ru_x$ alloy series in the vicinity of x = 0.28, for which T_C approaches the measurement temperature T_R. Hereby, ζ is a pre-factor that describes the x-dependence of M_s for $T = T_R$. Equation 4-7 describes the effect on K_1 that exclusively arises from thermal excitation occurring in the vicinity of T_C. From figure 4-21 (b), where eq. 4-7 is displayed as a dashed line, one can observe that the K_1 values for high Ru concentrations follow the expected behavior quite well despite the rather substantial approximations and simplifications being made in the derivation of eq. 4-

[kk] Equation (4-7) is valid for $x < 0.28$, while $K_1 = 0$ for $x > 0.28$.

7. Therefore, one can conclude that despite its apparent oscillating behavior there are only two clear regimes of K_1 as a function of the Ru concentration (fig. 4-21 (b)). For low Ru concentrations, K_1 goes down sharply, but for concentrations > 5%, K_1 increases again strongly. The room temperature K_1 then decreases again as $T_C(x)$ approaches the measurement temperature T_R, exclusively or predominantly due to thermodynamic effects.

4.3. Thickness dependence of Co thin films

As mentioned before (sect. 2.2.1.2.), it is well known that the thickness plays an important role in thin ferromagnetic films. For instance, in ultrathin films the overall anisotropy can be dominated by surface anisotropy. However, for thicker films, the total anisotropy including the shape anisotropy may result in an in-plane magnetization state due to the magnetostatic anisotropy contribution.

In the thickness range investigated here, the surface to volume ratio is rather small, so that no strong thickness dependence of the magnetic properties is expected. It might nonetheless be present. One of the main reasons for this is the possible crystallographic strain variation along the film thickness. Thus, otherwise identically prepared and similar films of different thickness may have different strain values and therefore they might show thickness dependent magnetic properties.

In this section, it is discussed how thickness may affect the magnetic properties of the epitaxially grown (10$\underline{1}$0) Co samples with in plane uniaxial magnetic anisotropy. The main purpose of this thickness dependence study is to investigate how sensitive the magnetic properties are with respect to the film thickness and thus, how representative the previous studies of Co-films and Co-alloy films are, which have been all done at 30 nm thickness.

4.3.1. Crystallographic and structural properties

Epitaxial (10$\underline{1}$0) Co samples with 15 nm, 50 nm, 100 nm and 150 nm thicknesses have been grown, using the same growth sequence as for the reference sample, namely the 30 nm (10$\underline{1}$0) Co thin film. Figure 4-24 shows the layer growth sequence, in which the Co thickness (t_{Co}) has been varied.

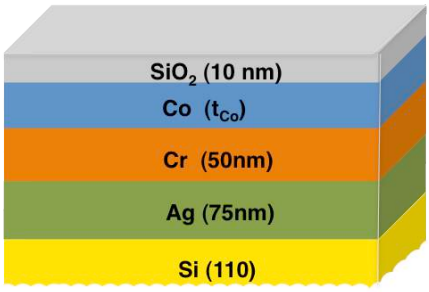

Figure 4-24: Schematic of the layer sequence for epitaxial Co (10$\underline{1}$0) growth with varying thicknesses.

The X-ray θ-2θ diffraction measurements of these (10$\underline{1}$0) Co samples with different thickness display only those diffraction peaks that arise from the intended epitaxial layer sequence, namely the (220) peak for Ag layer, the (211) peak for the Cr layer and for Co, the (10$\underline{1}$0) plane, for which second order diffracted peak (20$\underline{2}$0) is also visible (fig. 4-25). As expected the diffraction peak intensity for Co (10$\underline{1}$0) and (20$\underline{2}$0) increases as the Co layer becomes thicker, simply due to the larger amount of epitaxially ordered Co material. From these X-ray spectra, one can conclude that the Co epitaxy and thus the crystallographic quality are nearly independent from the film thickness. Even for the thinnest film studied here, i.e. t_{Co} = 15 nm, the X-ray diffraction spectrum shows good Co crystal quality with (10$\underline{1}$0) orientation.

However, upon carefully analysing the angular position of the Co (10$\underline{1}$0) diffracted peak as a function of t_{Co} (see fig. 4-26), a continuous increase towards to higher 2θ angles is found as t_{Co} increases. This increase indicates that in small thicknesses the Co layer is under strain, which is partially being released as the thickness increases, hereby approaching the bulk Co lattice parameter values[II]. For bulk Co, according to the reference 126, the diffracted peak for the (10$\underline{1}$0) plane appears at 2θ equal to 41.56°, which is identical within the margin of error with the (10$\underline{1}$0) Co peak for the t_{Co} = 150 nm sample (2θ = 41.55 ± 0.1°).

[II] Please note that in order to be sure that this angular displacement was not due to a systematic error in the measurements, the position of the Ag (220) diffracted peak has been also analysed as a function of t_{Co}. In this analysis no variation of the angular position as a function of t_{Co} has been observed.

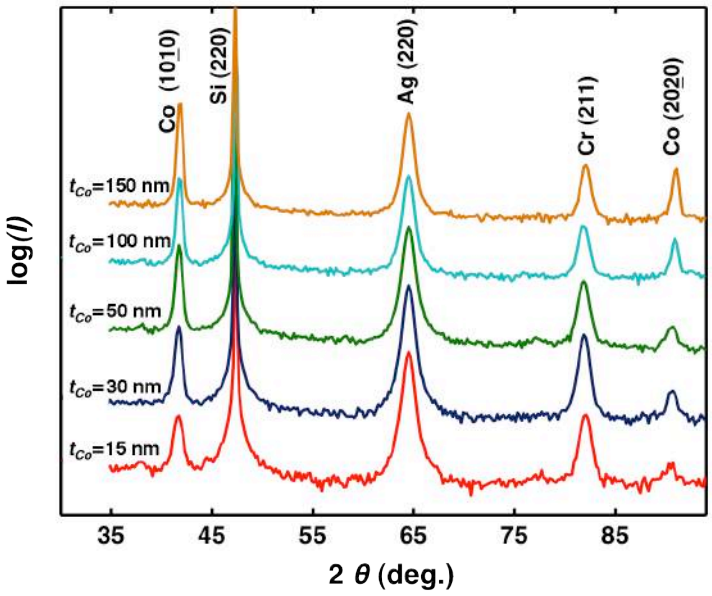

Figure 4-25: θ-2θ X-ray diffraction spectra for (10$\bar{1}$0) oriented Co film samples of different thicknesses: 15 nm (red line), 30 nm (blue line), 50 nm (green line), 100 nm (turquoise line) and 150 nm (yellow line).

In order to confirm that the thickness does not have any substantial crystallographic effect along the azimuthal orientation, φ scans have been performed with the X-ray diffractometer for these Co samples. Hereby, no apparent broadening of the diffracted peaks has been observed. Therefore, one can conclude that despite the strain release, the thickness does not affect the azimuthal order of the crystal structure in these Co films.

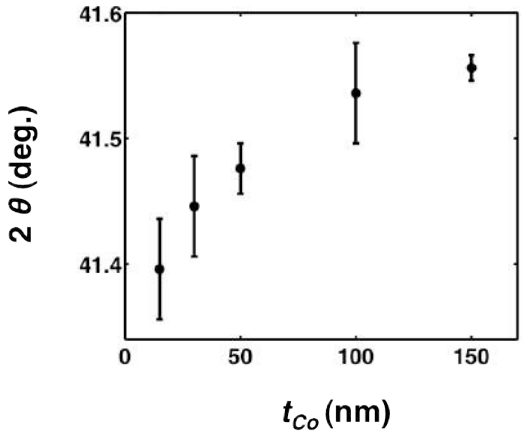

Figure 4-26: 2θ position for Co (10$\bar{1}$0) diffracted peak as a function of t_{Co}.

4.3.2. Macroscopic magnetic properties

Macroscopic magnetic measurements for these samples with varying Co-layer thickness have been carried out by VSM at room temperature. Figure 4-27 show nine

hysteresis loops measured for samples with t_{Co} equal to 15 nm (figs. 4-27 (a)-(c)), equal to 100 nm (figs. 4-27 (d)-(f)) and equal to 150 nm (fig. 4-27 (g)-(i)) at different applied field angles. Figs. 4-27 (a), (d) and (g) display hysteresis loops along the EA, figs. 4-27 (b), (e) and (h) show hysteresis loops 40° away from the EA and (c), (f) and (i) hysteresis loops 60° away from the EA. Besides the slightly poorer signal-to-noise ratio in the hysteresis loop measurements for the 15 nm thick Co film due the reduced magnetic volume (figs. 4-27 (a)-(c)), one can clearly observe that their shape is really similar to the 30 nm reference sample for all applied field angles. While for external applied fields along the EA (fig. 4-27 (a)), a square hysteresis loop is visible, for applied field angles away from EA, i.e. β = 40° (fig. 4-27 (b)) and β = 60° (fig. 4-27 (c)), the hysteresis loops show a gradual bending followed by single switch.

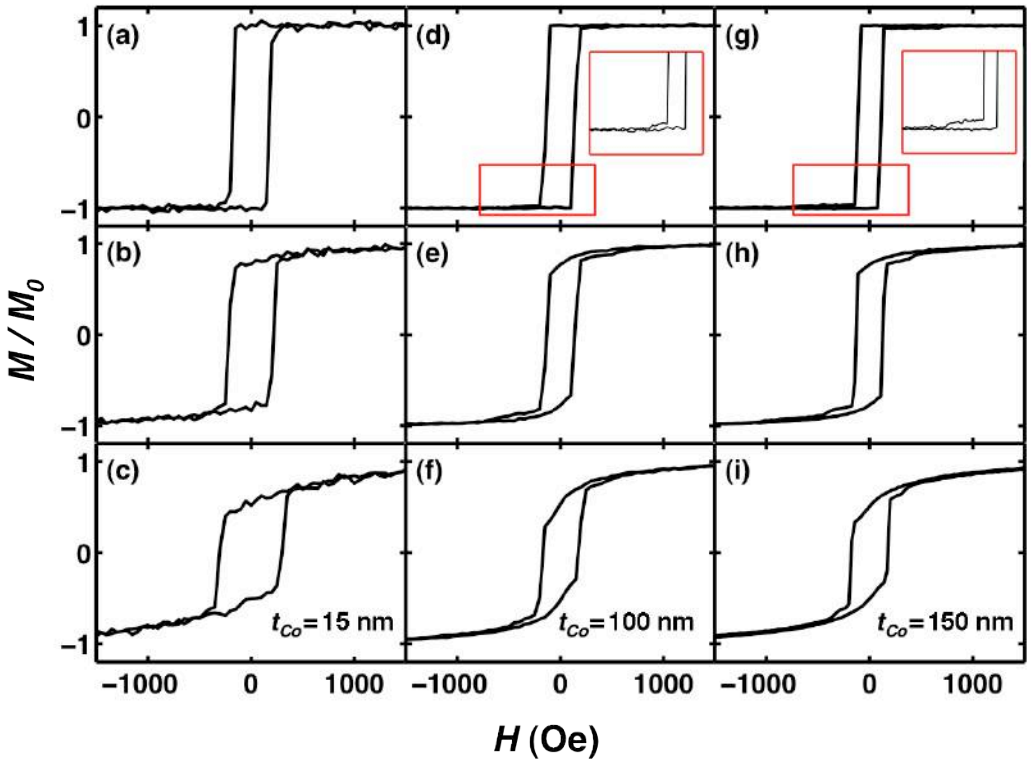

Figure 4-27: Hysteresis loops measured for (10$\underline{1}$0) Co thin films of varying thicknesses (t_{Co}): (a)-(c) for t_{Co} = 15 nm, (d)-(f) for t_{Co} = 100 nm and (g)-(i) for t_{Co} = 150 nm. (a), (d), (g) show hysteresis loops for applied fields along the EA, (b), (e) and (h) show hysteresis loops for applied fields 40° away from the EA and (c), (f) and (i) show hysteresis loops for applied fields 60° away from the EA. The inset figures in (d) and (g) show a zoom of the hysteresis loop areas, in which the second jumps appear during the reversal.

For thicker epitaxial Co films, i.e. the t_{Co} = 100 nm (figs. 4-27 (d)-(f)) and t_{Co} = 150 nm (figs. 4-27 (g)-(i)) samples, the hysteresis loops show a square shape for the applied field along the EA (figs. 4-27 (d) and (i)) as well as a reversal that proceeds

by a bending of the hysteresis loop plus an irreversible sample switch for applied field away from the EA (figs. 4-27 (e)-(f) and (h)-(i)). In addition, however, they show an unusual second switch at higher applied field values for all applied field angles. For applied fields along the EA, the inset figures show a zoom in the vicinity of the area where the second jump occurs. Comparing this second jump for both samples, one can observe that the effect is more pronounced for the thicker sample, where the jump corresponds to a larger fraction of the total magnetization. Therefore, this effect appears to be correlated with the thickness of the Co layer. Moreover, a decrease of the coercive field can be observed upon increasing the Co thickness.

Figure 4-28 shows experimental M_r/M_0 values as a function of applied field angle β for (10$\underline{1}$0) Co samples, in which t_{Co} is 15 nm (fig. 4-28 (a)), 50 nm (fig. 4-28 (b)), 100 nm (fig. 4-28 (c)) and 150 nm (fig. 4-28 (d)). As in previous studies, the M_r/M_0 values have been extracted from angular dependent hysteresis loop measurements performed for field orientation steps of 5°. All samples show uniaxial magnetic anisotropy with a clear 180° periodicity for the M_r/M_0 angular dependence. While for thinner samples, i.e. t_{Co} = 15 nm and t_{Co} = 50 nm, the M_r/M_0 angular dependence exhibits almost perfect uniaxial anisotropy behaviour (red dashed lines in fig. 4-28), the M_r/M_0 angular dependence deviates from this perfect behaviour near the HA in thicker Co samples, i.e. for t_{Co} = 100 nm and t_{Co} = 150 nm. In order to quantify the discrepancy from perfect uniaxial behaviour, OR values using equation 4-2 have been calculated. While the t_{Co} = 15 nm and 50 nm samples show OR values higher than 20, the t_{Co} = 100 nm and 150 nm samples present OR values of only 9.5 and 10.6, respectively. The decrease of the OR value as well as the occurrence of a second jump in the reversal as the film thickness increases could possibly arise from the strain release as a function of thickness. This strain release, as the magnetic reversal measurements indicate (see fig. 4.27), might induce a depth dependent variation of the magneto-crystalline anisotropy. Then, one would have a lower anisotropy in one part of the sample and a higher anisotropy in another. Considering that domain walls in Co are approximately 100 nm wide, it appears feasible that non-uniform and depth-dependent reversal could occur in thicker samples, which might also cause more complicated magnetization reversal paths, and in turn explain the features observed in fig. 4.27 for t_{Co} =100 nm and 150 nm.

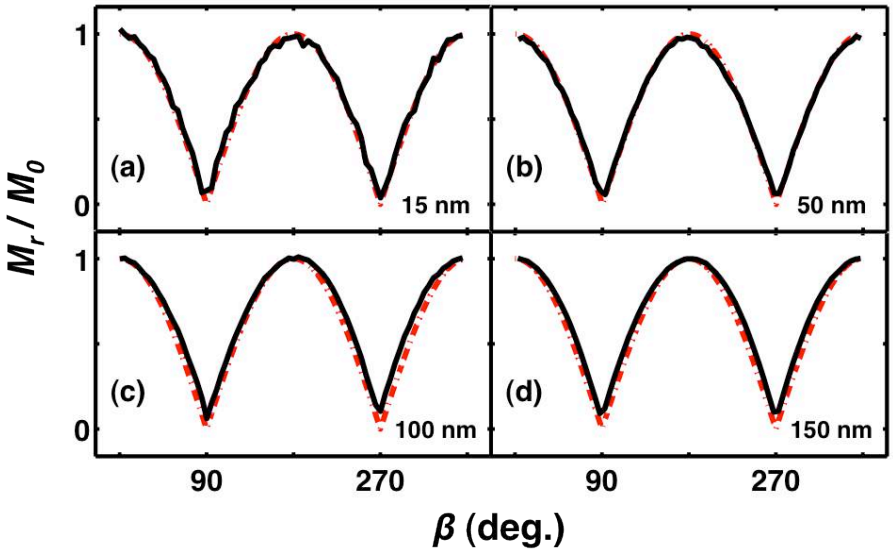

Figure 4-28: Measured M_r/M_0 values as a function of field orientation for (10$\bar{1}$0) Co thin films with varying thicknesses (t_{Co}): (a) for t_{Co} = 15 nm, (b) for t_{Co} = 50 nm, (c) for t_{Co} = 100 nm and (d) for t_{Co} = 150 nm. The red dashed line displays the perfect uniaxial anisotropic behaviour, for which M_r/M_0 is given by the uniform magnetic state projection onto the applied field axis.

M/M_s data for these samples have been analysed in the entire angular range of applied fields at room temperature. Figure 4-29 show the colour coded M/M_s (H,β) maps that correspond to samples with t_{Co} = 15 nm (fig. 4-29 (a)), 50 nm (fig. 4-29 (b)), 100 nm (fig. 4-29 (c)) and 150 nm (fig. 4-29 (d)). Also here, the brown colour indicates M/M_s equal to 1 and the blue colour represents vanishing M/M_s values. All samples show the same type of cone shape near the *HA*, just as the CoRu alloy samples. However, one can observe that the cone structure gets smaller as the Co thickness increases.

By least-squares fits of the measured M (H,β) data to the free energy equation 4-4, M_s, K_1 and K_2 have been extracted for each t_{Co}. Even though a reasonable agreement between the fits and the measured M (H,β) data has been found for all the samples, the R^2 values clearly indicate larger discrepancies for samples with thicker Co layer. While for samples with t_{Co} = 15 nm and 50 nm the R^2 is better than 0.95, in is only in the range of 0.89-0.92 for the t_{Co} = 100 nm and t_{Co} = 150 nm samples. This is consistent with the previously seen results in figs. 4-26 and 4-27, in that the thick Co samples do not show anymore a perfectly uniform magnetization reversal behaviour. Therefore, one can not expected the exceptionally good fit quality for the M (H,β) maps to be maintained here, given that the analysis is based on a uniform magnetic state model. Figures 4-29 (a)-(d) show measured M (H,β) maps already

normalized to the M_s and figures 4-29 (e)-(h) show fitted M (H,β) maps, also normalized to M_s.

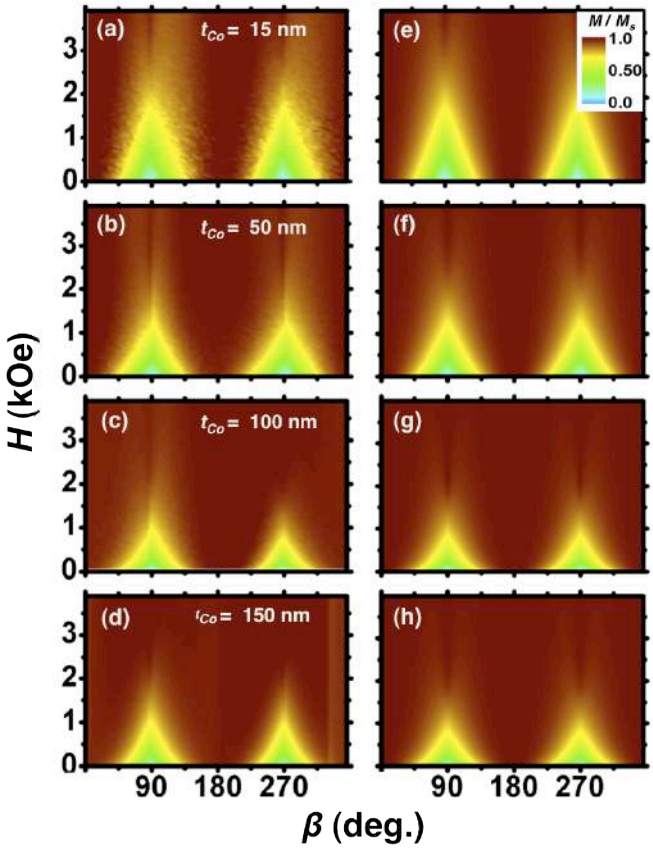

Figure 4-29: In-plane angular dependence of the magnetization value as a function of applied field angle and applied field strength for epitaxial (10$\underline{1}$0) Co samples with different thickness t_{Co} = 15, 50, 100 and 150 nm. The data displayed as colour-maps in (a)-(d) are normalized to the saturation magnetization M_s, which is extracted from least-squares fitting of the data to eq. 4-4. (e)-(h) show the corresponding least-squares fits of the data determined by only 3 free parameters, namely K_1, K_2 and M_s.

The extracted room temperature M_s values are displayed in fig. 4-30 (a) and as expected an almost constant value of M_s is observed that is identical with the magnetization saturation value of bulk Co, M_s = 1422 emu/cm^3 within the error[80]. The slightly smaller value for the 15 nm Co could arise from an only 0.5 nm thick intermixing layer at both film interfaces. Given that such an intermixing layer will be independent from the film thickness, it would impact the M_s estimate of thinner samples far more than thicker films. The overall M_s error estimates, on the other hand, stay constant independent from the film thickness because the absolute error is dominated by the sample area error, which is not correlated with the sample thickness.

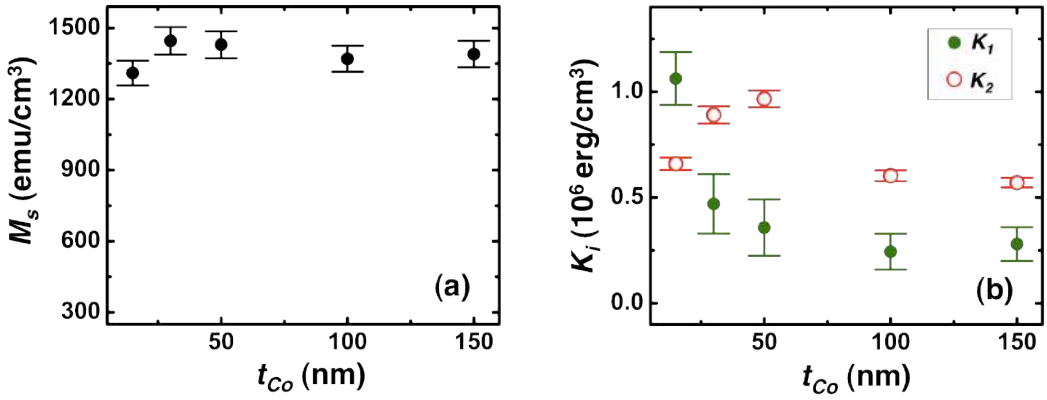

Figure 4-30: Experimentally determined magnetic materials properties for epitaxial (10$\underline{1}$0) Co films as a function of the Co thickness (t_{Co}): (a) saturation magnetization M_s and (b) first and second order anisotropy constants K_1 (green solid dots) and K_2 (red open circles).

The resulting anisotropy constants, K_1 and K_2, can be seen in fig. 4-30 (b). Consistent with the decrease of the cone area in the experimental $M/M_s\,(H,\beta)$ maps (figs. 4-28 (b)-(d)), a visible decrease of the K_1 can be observed for thicker samples. As discussed before, this decrease arises most likely from the strain release with thickness [mm]. Concerning the second order anisotropy, K_2, a non-monotonous behaviour is observed. While an increase of K_2 is observed for samples with $t_{Co} < 100$ nm, K_2 decreases for samples with larger thickness of the Co layer, i.e. samples for which a second jump in the magnetization reversal has been observed and the reversal ceases to be following simple uniform magnetic behaviour.

Overall one can conclude that while epitaxial films with different film thickness can be consistently prepared with single crystal quality, the associated magnetic properties change slightly with thickness due to a growth induced strain release. Especially above a threshold thickness of approximately 100 nm, this can lead to non-uniform magnetization reversal processes. On the other hand, figure 4-30 shows that very thin films, such as 15 nm or less may show strongly enhanced anisotropy values due to strain or surface effects, so that magnetization reversal might show a strong thickness dependence in terms of coercive field or other key quantities, even though one is exclusively in a uniform magnetization state regime. Therefore, the 30 nm film thickness chosen for most of the samples in this thesis is indeed a

[mm] Note also that the fits for the samples with 100 nm and 150 nm Co thickness do not show a perfect agreement with the data, a fact that may introduce a systematic error in the anisotropy estimates for these two samples.

good compromise to allow for a robust study of the previously investigated effects, because this thickness produces a sufficiently high magnetic signal and is well below the thickness threshold, where non-uniform magnetization reversal processes are to be expected for epitaxial films, which in turn would make a quantitative data analysis more difficult if not outright impossible.

4.4. Conclusions

In this chapter, magnetic thin films have been studied for the purpose of investigating the crystallography influence onto magnetic properties in slightly disordered film, where deviations from perfect uniform behaviour first occur as well as perform a concentration dependent study of the magnetic properties of epitaxial CoRu alloy films. The study has been utilizing primarily 30 nm thick films, which has been corroborated to be a very suitable thickness for the analysis of the previously mentioned effects. However, certain aspects remain unresolved. For instance, it would be interesting to support by means of a vector or depth resolved magnetometry that there is a thickness dependence anisotropy variation as the thickness increases in Co layers.

Due to the achievement of a continuous and reproducible tuning of the crystallographic order, a detailed analysis of the magnetic property dependence from the crystalline order has been possible. This study that covers key knowledge gaps of previous works, which also correlated magnetic properties with crystallographic order, but which lacked the very good control of the crystallographic tenability that was devised and utilized here.

Furthermore, one can envision that the CoRu alloy work done here opens a pathway to grow epitaxial CoRu and related alloys with high crystalline quality at low temperatures, that combine low Curie temperature values and high magneto-crystalline anisotropy. However, the non-monotonous anisotropy behaviour as a function of alloy composition will require more theoretical and experimental studies to achieve a broad-based understanding for this alloy series specifically and for related types of magnetic alloys in general.

5. Hard axis anomaly

In section 4.1.2., it has been observed that in samples with reduced crystallographic order, the remanent magnetization exhibits an unusual increase when the external field is applied along the HA. This chapter is focused on the study of this anomalous behaviour in detail.

Signatures of anomalies in the magnetization reversal process near the magnetic hard axis have been previously observed by several groups[25–31]. However, in these previous works no detailed investigation was done that made it possible to correlate the anomalous behaviour to the details of crystallographic order, mainly due to a lack of sufficient control of crystal quality. Thus, the origin of these anomalies could not be accurately studied. In reference 25, the authors made an experimental observation of the anomaly by detecting a hard axis hysteretic behaviour while applying biased circular field cycles. This paper also describes a method of measuring the applied field angular range, in which the HA anomaly appears, the so-called

dispersion angle. However, the paper and the in it described methodology do not allow any other quantitative observation, such as, the shape and overall height of the anomalous magnetization, and furthermore there is no correlation with sample preparation or crystalline quality reported. In the works by Scheurer et al.[27] and Hamrle et al. [30], an increase of the coercive field was reported when the field was applied along the HA in biaxial magneto-crystalline anisotropy systems, specifically bcc Fe thin films[27] and Co-based Heusler alloy thin films[30]. Also in these works, the anomalous behaviour was associated to the crystallographic misalignment of adjacent grains without investigating how this misalignment may affect this anomalous phenomenon in a quantitative or even qualitative manner. Hamrle and co-workers[30] found stripe domain structure formation with 90º domain walls when the magnetization was reversed for fields applied along the HA. However, the overall complex magnetic reversal behaviour of the Co-based Heusler alloy system, showing also stripe domain structures for applied fields away from the HA, made it difficult to achieve a clear identification of the anomalous nature of their effect and its correlation with the observed domain states.

Another and more recent paper[31] presents a fairly complete characterization of the magnetic aspects of the HA anomaly in soft magnetic FeCo layers. In this work, the authors analyse different features of anomaly, such as, angular width and coercive field change. Nevertheless, the work just compares different samples with different thickness and underlayer structure. Thus, no real explanation of the phenomenon is given in terms of a microscopic picture and no correlation of the magnetic anomaly with the crystallographic quality is reported.

So, even though anomalous HA behaviour was observed previously for a number of materials, none of these works correlate the effect with the actual crystalline structure. Given this very limited and incomplete physical picture of the origin of the HA anomaly in previous works and the ability shown in chapter 4 to tune the crystallographic alignment of materials, the origin of the anomalous HA behaviour has been studied in detail here. In addition, the experimental findings have been corroborated with a simple, but effective theoretical model.

5.1. MOKE measurements

Figure 5-1 shows six hysteresis loops measured for the fully epitaxial and one of the partially epitaxial 30 nm thick Co film samples, for which t_{ox} was 0 nm (reference sample) and 0.132 nm, respectively. The hysteresis loops are measured along the HA (figs. 5-1 (b) and (e)) and ±2° away from the HA, i.e. at β = 88° (figs. 5-1 (a) and (d)) and at β = 92° (figs. 5-1 (c) and (f)). The hysteresis loops plotted in figs. 5-1 (a)-(c) correspond to the fully epitaxial sample with no SiO_2 underlayer, while the data plotted in figs. 5-1 (d)-(f) correspond to the partially epitaxial sample (t_{ox} = 0.132 nm).

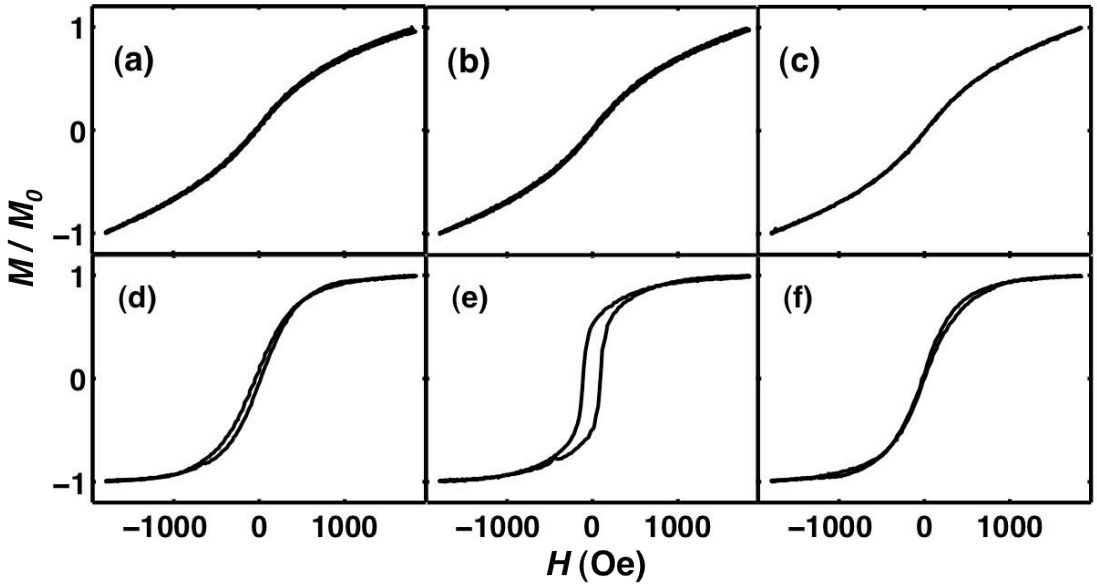

Figure 5-1: Hysteresis loop data for a fully epitaxial sample with t_{ox} = 0 nm (a)-(c) and a partially epitaxial sample with t_{ox} = 0.132 nm (d)-(f), measured for field orientations at β equals to 88° in (a) and (d), 90° in (b) and (e) and 92° in (c) and (f).

From the hysteresis loops at β = 88° (fig. 5-1 (a) and (d)), one can see that the hysteresis effect is almost completely absent for both samples, i.e. the expected behaviour for uniaxial samples in the close vicinity of the HA. However, as the externally applied field direction is oriented exactly along the nominal HA, one observes a substantial difference in between the two samples. While the epitaxial sample shows the expected hysteresis-free HA loop (fig. 5-1 (b)), the partially ordered sample exhibits an unexpected behaviour, namely a loop that shows substantial values of coercive field H_c and remanent magnetization M_r/M_0 (fig. 5-1 (e)). Thus, for the partially ordered sample, the magnetization reversal in the nominal

HA does not show typical HA behaviour anymore. Furthermore when the field is applied along $\beta = 92°$, the nearly hysteresis free conventional hard axis behaviour re-emerges by having almost vanishing values for M_r/M_0 and H_c in both samples (figs. 5-1 (c) and (f)).

Figures 5-2 (a) and (b) show the angular dependence of the normalized remanent magnetization (M_r/M_0) for both samples, i.e. samples with $t_{ox} = 0$ nm and $t_{ox} = 0.132$ nm respectively. This figure is very similar to figs. 4-10 (a) and (c), but here, the vicinity of HA is shown in much more detail. For both samples, M_r/M_0 approaches 0 as the applied field angle approaches the HA. However, in the close vicinity of the HA a sharp increase of the M_r/M_0 value is observed for the partially epitaxial sample, while M_r/M_0 indeed reaches 0 within the experimental error for the fully epitaxial sample. The angular range where this unusual increase of M_r/M_0 occurs is very narrow, specifically it appears in an angular range of only 4.0° total width.

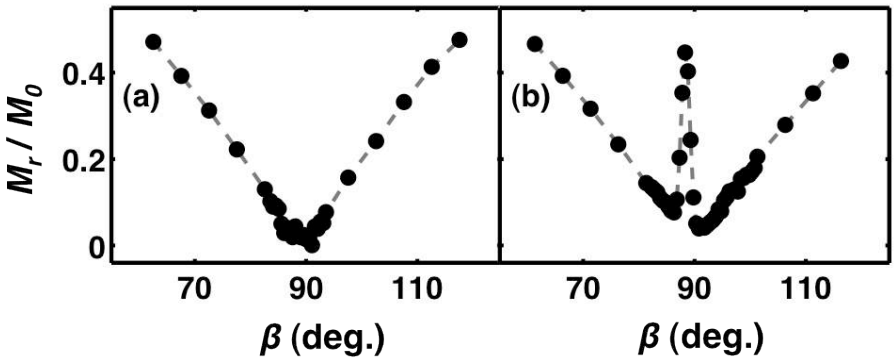

Figure 5-2: Angular dependence of the normalized remanent magnetization M_r/M_0 in the vicinity of the hard axis (HA): (a) shows measured M_r/M_0 – data for the fully epitaxial sample and (b) the corresponding data for the partially epitaxial sample with $t_{ox} = 0.132$ nm. The dashed grey line is a guide to the eye.

In order to analyse how this anomaly behaves as a function of the crystallographic order, the M_r/M_0 values at the HA anomaly peak have been plotted. From M_r/M_0 dependency on t_{ox} (fig. 5-3), one can deduce that a minimum disorder threshold is necessary to have an anomalous reversal, since for the $t_{ox} = 0$ nm and $t_{ox} = 0.11$ nm samples, M_r/M_0 is equal to 0. Above the threshold, M_r/M_0 increases abruptly, with M_r/M_0 being equal to 0.43 for $t_{ox} = 0.132$ nm and reaching already 0.7 for $t_{ox} = 0.154$ nm M_r/M_0. This abrupt increase is followed by more gradual increase for even more disordered samples.

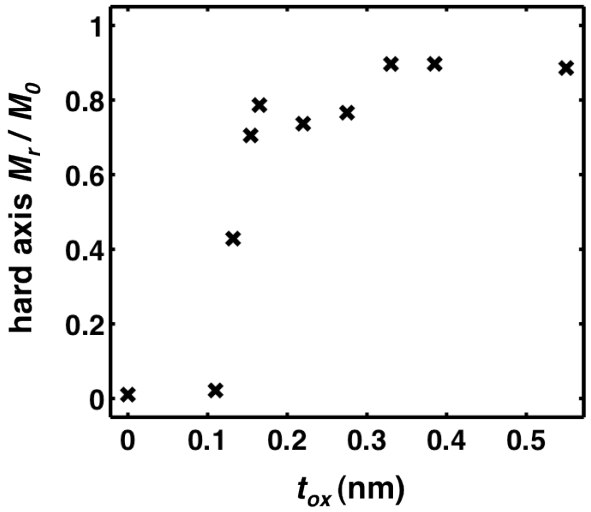

Figure 5-3: t_{ox} dependence of the anomalous hard axis (HA) remanence normalized to the reference magnetization M_0.

5.1.1. Microscopic magnetic states in remanence

For the purpose of identifying the origin of the sharp increase in M_r/M_0 values in the close vicinity of HA in partially epitaxial samples, the microscopic magnetic states at applied field, 88°, 90° and 92° for the t_{ox} = 0.132 nm sample have been measured using MOKE microscopy (sect. 3.3.1.3.) in longitudinal geometry. Figures 5-4 (a)-(c) show the remanent magnetization states taken after saturating the sample for field orientations of β = 88°, β = 90° and β = 92°. The remanent magnetization pictures for applied fields ±2° away from the HA (figs. 5-4 (a) and (c)) show uniform states, that are characterized by a uniform grey colour. This is the expected behaviour for a highly ordered uniaxial sample, because the magnetization reversal is dominated by a coherent rotation near the HA. However, a spatially non-uniform magnetization state, visible as laterally varying areas of different grey colours, appears if the magnetic field is applied exactly along the HA. This microscopic observation demonstrates that the magnetization reversal along the HA is not dominated by a simple uniform magnetization rotation anymore as one would have expected for a simple uniaxial sample with perfect crystallographic alignment. Instead, non-uniform magnetic states appear which are the origin of the hysteretic magnetization reversal behaviour along the HA.

The insets of fig. 5-4 compare the contrast distributions for the different remanent states (blue dashed line) and respective high field states (red solid line).

These distributions have been extracted by summing pixels per grey scale in the Kerr image taken in each magnetic state as described in appendix B (fig. B-1). For the cases, in which the applied field is away from the HA, i.e. figs. 5-4 (a) and (c), the distributions are identical for remanent and saturation states, while there is a clear widening of the contrast distribution in remanence for the HA case in fig. 5-4 (b), which corresponds to 8% ± 0.7% of M_0. Hereby, it is important to notice that all MOKE images have been measured with the same contrast setting. Moreover, one has to keep in mind that the widths of the contrast distribution for the uniform states are due to the noise level of the image detection system only.

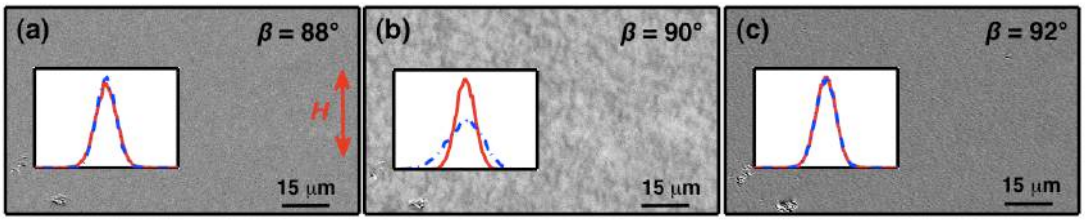

Figure 5-4: MOKE microscopy images of a partially epitaxial sample (t_{ox} = 0.132 nm) after applying a magnetic field: (a) -2° away from, (b) along and (c) +2° away from the HA. The inset figures show the brightness distributions of the MOKE images in saturation (red solid thin lines) and in remanence (blue dashed lines).

As control experiment, the same remanent magnetization measurements have been performed by means of MOKE microscopy for the fully epitaxial reference sample (t_{ox} = 0 nm), and as expected, in this case only the conventional HA uniform remanent magnetization state has been observed for all applied field directions.

5.2. Theoretical model

In order to develop a qualitative understanding of this anomaly a simple theoretical model has been devised, which has been attempted to emulate the main features of the Co samples. The principal requirement for the theoretical model is to take into account that the samples have uniaxial anisotropy, but are not single crystalline and that the crystallographic misalignment varies in a continuous fashion from the completely aligned case to a randomly oriented case. Thus, the description of these samples requires a model that is capable to mimic the crystalline alignment and does so in a tuneable way, while displaying an overall uniaxial magnetic anisotropy. One of the simplest model that includes these characteristics is a two perfect uniaxial grain model with misaligned anisotropy axes. Furthermore, it is clear

that the grains considered in the model should be exchange coupled, because the emulated films contain only Co, so that even in between misaligned Co-grains, the exchange coupling must be strong.

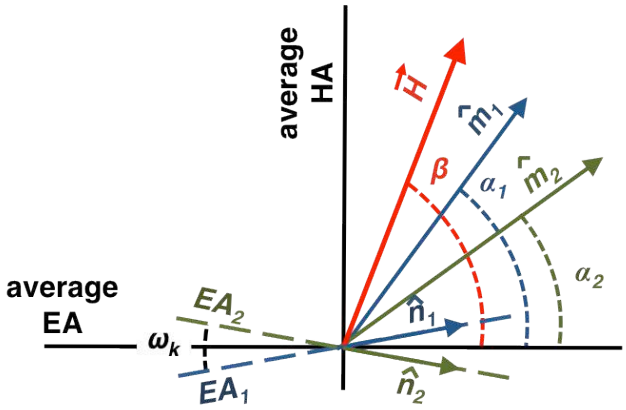

Figure 5-5: Schematic of the two-grain model geometry with ω_k being the misalignment angle between the easy axes of both grains. $\hat{n}_1$ and $\hat{n}_2$ are the unit vectors along the grains´ easy axes. The magnetization vectors are represented by $\hat{m}_1$and $\hat{m}_2$, and α_1 and α_2 are the angles between the magnetization vectors and the average easy axis. $\vec{H}$ is the applied field, which is at an angle of β with respect to the average easy axis.

A schematic of the model geometry can be found in fig. 5-5. The magnetization unit vectors of the two grains are represented by $\hat{m}_1$ and $\hat{m}_2$, while the effective inter-granular exchange coupling constant is given as J_g [nn]. The two uniaxial grains are characterized by their respective first order anisotropy constants K_{1g1} and K_{1g2} as well as by the orientations of their magneto-crystalline easy axes, EA_1 and EA_2 respectively, which are given by the unit vectors $\hat{n}_1$ and $\hat{n}_2$. For simplicity, only the first order magneto-crystalline anisotropy constant (K_1) has been considered. The angle between both EA_1 and EA_2 defines the grain misalignment angle, ω_k. The nominal EA and HA are given by the averaged orientation of the grains' EA and HA vectors. $\vec{H}$ represents the applied field. Identical volume is assumed for the both grains, where the sum of both volumes is given by V. Using this nomenclature the total free energy E_{2g} of the coupled two-grain system is

$$E_{2g} = -J_g \hat{m}_1 \cdot \hat{m}_2 - \vec{H} M_s \, {}^{V}/_{2} \, (\hat{m}_1 + \hat{m}_2) -$$

$$K_{1g1} \, {}^{V}/_{2} \, (\hat{m}_1 \cdot \hat{n}_1)^2 - K_{1g2} \, {}^{V}/_{2} \, (\hat{m}_2 \cdot \hat{n}_2)^2$$

[nn] J_g represents the effective inter-grain exchange coupling that is active in an interface layer only, while the exchange coupling within each grain would be minimized. Thus, J_g should be much smaller than the atomistic exchange coupling.

(5-1),

which is a summation of four different energy terms. The first term refers to the inter-granular exchange coupling energy between two grains. The Zeeman energy is given by the second term, where M_s denotes the total saturation magnetization and the third and fourth terms in the summations describe the anisotropy energy of the first and second grain, respectively. Similar types of models have been used successfully in the past to describe magnetization reversal in films that exhibit a combination of uniaxial and 4-fold magneto-crystalline anisotropy[127].

In order to simplify the mathematical treatment and enhance the transparency of the model a number of additional assumptions and simplifications have been made. First, identical magneto-crystalline anisotropy constants K_1 can be assumed for both grains, given that the thin films presented here only contain one material, namely Co. Furthermore, as mentioned before, the local magnetization can be restricted to in-plane orientations under consideration of the in-plane magneto-crystalline anisotropy present in these samples and the thin film nature of them, which creates a strong demagnetizing effect along the surface normal. Under these simplifying assumptions, the total energy is given by

$$E_{2g} = -J_g cos(\alpha_1 - \alpha_2) - HM_s {}^{V}/_{2} \left[cos(\alpha_1 - \beta) + cos(\alpha_2 - \beta)\right] + K_1 {}^{V}/_{2} \left[sin^2\left(\alpha_1 - \frac{\omega_k}{2}\right) + sin^2\left(\alpha_2 + \frac{\omega_k}{2}\right)\right]$$

(5-2),

where α_1 and α_2 are the in-plane orientation angles of the corresponding magnetization vectors with respect to the averaged anisotropy axis that is shown in fig. 5-5. In eq. 5-2, also a $-K_1V$ term has been omitted from the energy expression because it does not have any orientation dependence, and thus is not relevant in the energy minimization analysis.

From energy expression equation 5-2 it is evident that the magnetization reversal behaviour will depend on the field angle β, the external applied field amplitude H, and the material-specific parameters, namely $2J_g/K_1V$ and ω_k. By calculating the local energy minimum value starting from high-field saturation by means of stepwise field reduction to zero, the magnetization reversal for different ω_k and at fixed $2J_g/K_1V$-ratio has been simulated.

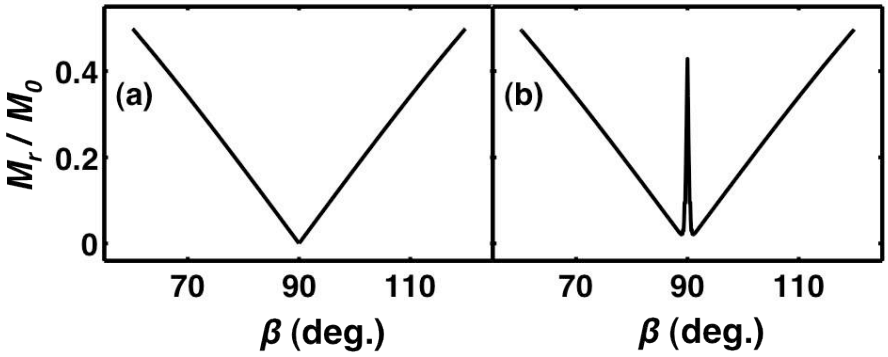

Figure 5-6: remanent magnetization (normalized to the reference magnetization, which indeed is the saturation magnetization) vs. field angle (β), calculated for the two-grain model for aligned anisotropy axes (a) and a Gaussian distribution of misaligned anisotropy axes (b) with a mean misalignment angle of 21.5° and a standard deviation of 1.2°. For these calculations, $2J_g/K_1V$ =0.2 was used.

Figure 5-6 shows simulated M_r/M_0 values in the vicinity of the nominal HA for perfectly aligned grains (ω_k = 0°), in which case the two grain model is identical to the conventional perfect uniaxial one grain model, fig. 5-6 (a), and for misaligned grains in fig. 5-6 (b). Hereby M_0 indeed is the saturation magnetization, M_s. For misaligned grains case (fig. 5-6 (b)) the assumption of a Gaussian distribution of misalignment angles has been made, by first minimizing the energy equation (eq. 5-2) and tracing the nearest local energy minimum starting from saturation for individual misalignment angles in the distribution, and then computing a weighted average of the results with a mean value of ω_k = 21.5° and a distribution width of $\Delta\omega_k$ = 1.2°, using a $2J_g/K_1V$ ratio of 0.2. A clear qualitative agreement is found between the experiments (shown in fig. 5-2) and the simulated curves (fig. 5-6). While the remanent magnetization in the HA vanishes for completely aligned grains (fig. 5-6 (a)), it increases for misaligned anisotropy angles along the HA direction and in its immediate vicinity (fig. 5-6 (b)), just as one observed in the experiments. Even the quantitative agreement is quite good, which is surprising given the simplicity of the two-grain model.

Figure 5-7 shows the remanent magnetization along the nominal HA as a function of the average misalignment angle ω_k for $2J_g/K_1V$ = 0.2 and a fixed alignment angle distribution width of $\Delta\omega_k$ = 1.2° as a solid line, in comparison to the experimental data shown before in figure 5-3. The experimentally obtained M_r/M_0 values are represented by red cross symbols in the plot as a function of t_{ox}. Both, the model and the experiment show a very similar behaviour, with the anomalous

remanent magnetization appearing abruptly at t_{ox} = 0.132 nm and ω_k = 21°, and increasing more slowly for further enhanced disorder levels. This means that the two-grain model does not only predict the anomalous behaviour in general, but it also describes its threshold onset behaviour. For small enough misalignment angles at any given $2J_g/K_1V$ -ratio, there is no anomaly. It takes a non-vanishing critical level of misalignment to be present for the anomaly to occur in the model, in exactly the same way, in which a sufficient level of crystallographic disorder is necessary in uniaxial Co-film samples for the effect to appear.

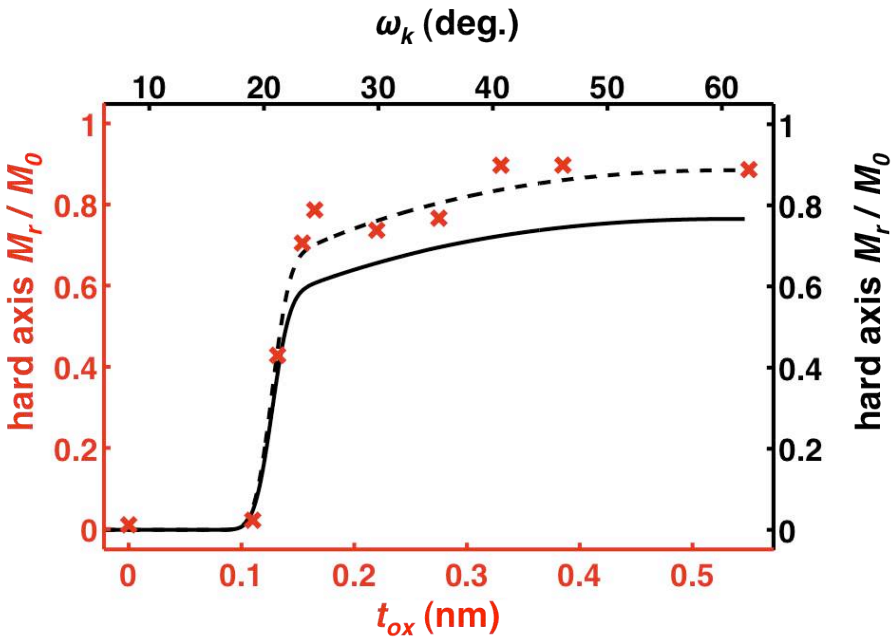

Figure 5-7: Sample dependence of the anomalous hard axis (HA) remanence: The red crosses show the measured HA remanent magnetization values (M_r), normalized to the reference magnetization (M_0), for samples with different t_{ox} (already shown in 5-3). The solid black line shows the calculated HA remanent magnetization, normalized to the saturation magnetization, as a function of the misalignment angle. Consistent with the plots in figure 5-6, the calculations have been done using a Gaussian distribution of misaligned anisotropy axes with a mean misalignment angle of ω_k, a standard deviation of 1.2° and $2J_g/K_1V$ = 0.2. The dashed black line displays the same calculated remanent magnetization curve, but normalized to the reference magnetization, that is achieved at H = 0.3 H_K for each value of ω_k, with H_K being the single particle anisotropy field.

However, the calculated solid line in fig. 5-7 is not an exact match to the experimental data and it shows systematically lower values for large misalignment angles. This may have several reasons. One possibility for this disagreement is that the real samples evidently represent far more complex magnetic systems than a two-grain model or a distribution of two-grain models. Otherwise, one would expect to see a two level magnetization behaviour for the anomalous state in MOKE

microscopy with only two possible magnetization directions (two different grey scales), which one does not observe (fig. 5-4 (b)). Instead one observes a broad distribution of magnetization directions between domains. This aspect is inherently a fundamental limitation of the model. The assumption of a Gaussian misalignment angle distribution is a step to overcome the two level magnetization limitations of the model, but it is only a rudimentary one, because already three particle interactions and correlations are not considered.

Secondly, one would not necessarily expect the misalignment angle ω_k and the SiO_2 interlayer thickness (t_{ox}) to have a linear relationship. In fact, in fig. 4-6 one can see that amplitude of the Ag (220) peak does not decrease in a linear fashion as t_{ox} increases. Given that the crystallographic order of the Co-films depends directly on the crystalline structure of the template layers underneath, one can conclude that the crystallographic misalignment angles in the Co films are not expected to be linearly dependent on t_{ox}.

However, there is an even simpler experimental reason for at least part of the disagreement in fig. 5-7. The simulated M_r data are normalized to the saturation magnetization M_s, which is of course easily accessible in calculations because it is an input parameter. On the other hand as discussed earlier in conjunction with hysteresis loop normalizations in sect. 4.1.2. and as observed in figs. 4-20 and 4-29, this is not easily possible for experimental data due to the lack of M_s actually being reached in nearly all experimental configurations, i.e. field alignments. Thus, the experimental data are normalized to M_0, which is a reference magnetization taken at high fields, but which is also generally smaller than M_s, so that the M_r/M_0-ratio for the experimental data will show larger values than one would see if a true M_s normalization were done. In order to have an indicative comparison of this effect, the calculated data have been normalized to M_0 values, defined as the magnetization values reached at a certain field value. As an example, $H = 0.3H_K$ has been used to recalculate the model results, which is shown as a dashed line in fig. 5-7. This curve shows a surprisingly good quantitative agreement with the experimental data, especially given the fact that the linear compatibility of the two x-axes used here might not be fulfilled. Also, one needs to be aware that the ω_k and $2J_g/K_1V$ parameters used in the model calculations, have been specifically chosen for achieving a good agreement in between the

simulated data and the experimental data and that most probably they do not denote any real structural meaning in terms of the real Co film samples.

These limitations regarding the exact equivalence in between model and experiment aside, it is possible to use this model to analyse the origin of the anomalous effect, given the fact that the two-grain model describes all aspect of the observed experimental HA anomaly and does so with a surprisingly high degree of precision. Hereby, it is particularly helpful to analyse the path that the magnetization vectors follow from saturation to remanence for different misalignment angles and field orientations. In the case of completely aligned anisotropies (ω_k = 0°), both grains behaves like a single grain, emulating the SW model, which is characterized by having a full remanent magnetization in the EA followed by an abrupt switch in the reversal process, while along the HA, no remanent magnetization is observed and the entire magnetization reversal proceeds via to a coherent magnetization rotation. Increasing the misalignment angle above a critical threshold angle ω_c, however, the system stops showing uniform magnetic states in remanence for field orientations along the HA. This effect is shown in fig. 5-8 (a) for ω_k = 21° where the magnetization angle respect to applied field direction, δ, as a function of applied field strength is represented. Upon decreasing the externally applied field, each of the two-grain magnetizations tries to align with their individual EA direction that is closest to the field orientation. This results in the fact that the two magnetization vectors rotate into opposite directions. At the same time, the exchange coupling tries to align both magnetizations, which has the end result that the magnetization vectors get stuck in metastable state rather than the absolute energy minimum at remanence. Specifically, the two grain system gets stuck in a scissor like remanent state with intermediate magnetization orientation angles, for which neither the anisotropy nor the exchange coupling energy is minimized. So, the competition between the exchange coupling energy and anisotropy energy leads to a frustrated state, which also exhibits a high remanent magnetization and correspondingly a significant coercive field. Furthermore, this explains the non-uniform remanent magnetization state that has been observed by MOKE microscopy (fig. 5-4 (b)).

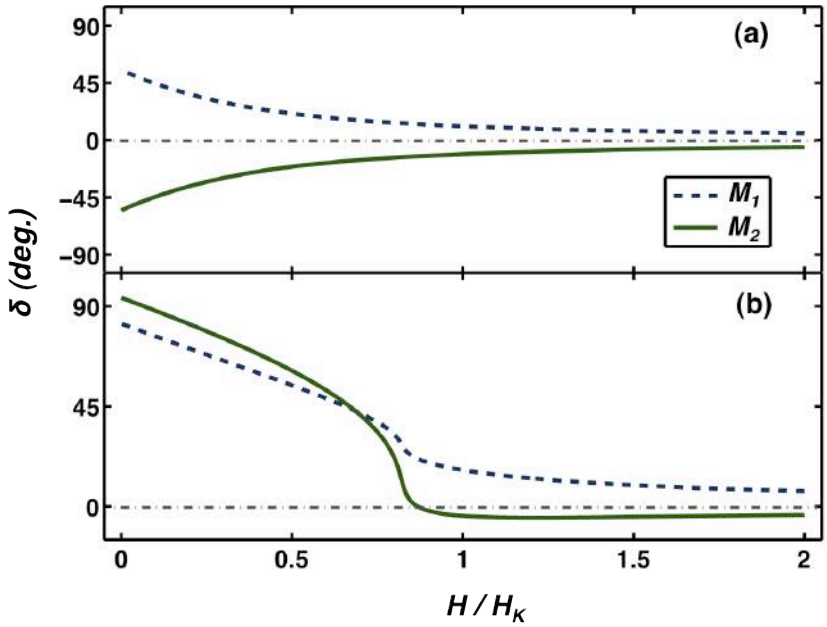

Figure 5-8: Field evolution of the individual magnetization angles in the two-grain SW model. Here, the magnetization angles δ are displayed with respect to the applied field direction, while the applied field strengths are normalized to the single grain anisotropy field H_K. The calculations shown here were done for ω_k =21° and $2J_g/K_1V$ = 0.2, and for a sample alignment of (a) along the HA (β = 90°) and (b) 2° away from the HA (β = 88°). The dashed blue line represents the magnetization angle in the first grain and the solid green line represents the magnetization angle in the second grain. The grey dash-dotted line represents the applied field direction.

Figure 5-8 (b) shows the model behaviour at an applied field angle of $\beta = 88°$ for same level of misalignment, i.e. $\omega_k = 21°$. It is important to notice that for this level of misalignment, also here the respective closest easy axis directions of the two grains define opposite rotations with respect to the field axis. Thus, as one reduces the magnetic field, a scissor state appears initially at intermediate field values. However as the field is decreased further the exchange energy overcomes this initial scissor nucleation and both magnetic moments rotate towards the easy axis that is nearest to the field axis. This also explains why the occurrence of the anomaly is not only dependent of the misalignment angle, ω_k, but also on the inter-granular exchange coupling constant, J_g, and the anisotropic constant, K_1, because the transition between the initial scissor state and the existence/absence of the anomaly at remanence is determined by the strength of the exchange coupling in relation to the anisotropy energy. This behaviour leads to a nearly uniform magnetization state in remanence, as one can see in fig. 5-8 (b). For misalignment angles smaller than ω_c, the exchange coupling energy dominates the behaviour even along the HA and imposes that the magnetic moments rotate together, even though also here a scissor nucleation state is

being formed at intermediate field values. In this case no visible anomaly appears and the overall behaviour is only minimally modified from the case of perfect alignment.

5.3. Spin wave behaviour in the HA anomaly regime

The HA anomaly has been also studied by means of Brillouin light scattering (BLS) spectroscopy. These measurements have been performed at the University of Kaiserslautern in Burkard Hillebrands' group during a two months stay in their laboratories. In particular, the effect that the frustrated magnetic state causing the HA anomaly has onto spin-wave spectra has been studied. The BLS setup at University of Kaiserslautern is equipped with an automated in-plane rotator that allows for a precise variation of the sample orientation with respect to the externally applied in-plane magnetic field, (detailed description of the setup can be found in ref. 128) All measurements have been performed in backward scattering geometry[128,129], i.e. the incident light has been focused onto the sample by an objective lens under an incident angle of 17.5° with respect to the sample normal. The reflected laser light has been collected using the same objective and sent through the Tandem Fabry Perot interferometer, which allows the extraction of the light intensity for different wavelengths. The external field has been applied parallel to the plane of sample and perpendicular to the incidence light wave vector.

In order to analyse the effect that the HA anomaly has on the spin-wave spectra, the dependence of the spin-wave frequencies as a function of β has been measured for the t_{ox} = 0.132 nm sample, for which the anomaly occurs in a very narrow field orientation range as previously seen in figs. 5-1 and 5-2. Figure 5-9 (a) shows colour code maps of the inelastically backscattered intensity as a function of frequency shift, i.e. the excitation frequency of the spin waves, and the externally applied field angle β to generate the remanent state. Figure 5-9 (a) shows measurements in the remanent state after previously applying an external field of 1500 Oe for each β, while figure 5-9 (b) shows the exact same type of measurements, but after saturating the sample only once along the EA. In these BLS intensity maps, the red colour indicates the maximum intensity, i.e. the spin-wave positions, while the blue colour indicates the minimum intensity, i.e. the background noise level. In both figures, two spin-wave modes appear, one belonging to the dipolar type spin-wave

mode at lower absolute values of excitation frequency and one at higher absolute frequency values, which represents the exchange type perpendicular standing spin wave (PSSW) mode[128,129]. While the excitation frequency of the dipolar dominated spin-wave depends, amongst other parameters, on the relative orientation between the spin-wave wave vector and the magnetization direction, the excitation frequency of exchange type mode depends mainly on the film thickness. In fig. 5-9 (a) one can see that due to the anomalous magnetization reversal along the HA, i.e. at β = 90°, the dipolar type spin wave is shifted towards higher absolute excitation frequency values. The origin of this shift arises from the relative orientation between the spin-wave wave vector and the magnetization direction[128,129]. This generally occurring magnetization orientation dependence of dipolar spin wave spectra can be clearly seen in the inset of fig. 5-9 (b), where the full 90° applied field angle dependence of collected light intensity on the excitation frequency is plotted for the same sample after being saturated once along the EA[oo]. So, when a field cycle is applied in the vicinity of the HA, but outside the anomalous reversal range, the magnetization aligns with the EA in remanence, which is nearly 90° away from the applied field direction. However, in the anomalous region, the sample averaged magnetization is forced to stay along the applied field direction (as shown in fig. 5-8 (a)), due to the competition between exchange and misaligned anisotropy energies and this causes the upward shift of the dipolar spin-wave excitation frequency in the regime of HA anomaly. Furthermore, the data in fig. 5-9 (b) corroborate that this effect is induced by the field cycling along the HA, because no such frequency jump is observed for the same sample orientation in the absence of the applied field sequence, because the anomalous state is never populated.

In addition to a substantial frequency shift, the measurements in fig. 5-9 (a) show a broadening of the dipolar spin-wave peak in the HA anomalous state. Such a broadening is to be expected, because the anomalous state is characterized by an inhomogeneous sample magnetization, with a fairly broad distribution of magnetization directions, which was already seen by means of MOKE microscopy in fig. 5-4 (b). Thus, for lateral dimensions larger than the coherence length of the

[oo] Note that the abrupt frequency shift around 50° arises from some imperfection in the sample surface, i.e. a dust particle, that is being illuminated while rotating.

dipolar spin waves, there exists a magnetization orientation distribution, which leads to the observed broadening. The BLS measurements also show that a misalignment of only ±1° away from the HA already causes an almost complete suppression of this anomalous behaviour with a strong reappearances of the 7 GHz low frequency peak. At field orientations of ±2° away from the HA, the usual behaviour of uniaxial samples is fully re-established, a result that is completely consistent with the magnetometry and MOKE microscopy data, i.e. figs. 5-1, 5-2 and 5-4 respectively.

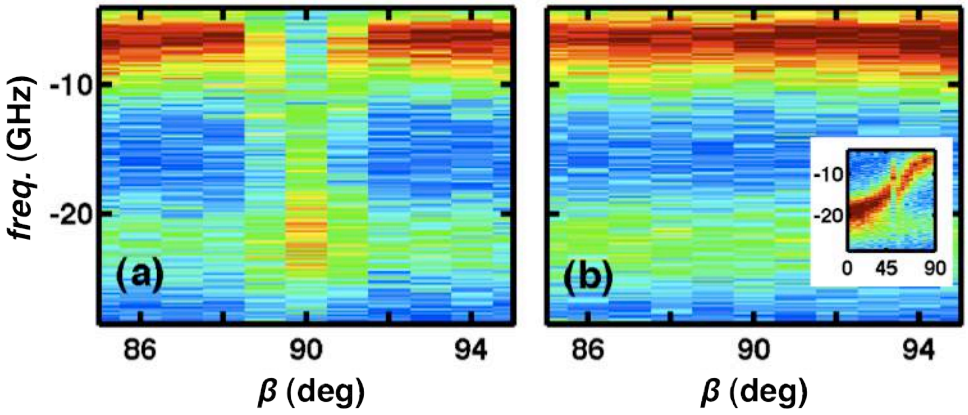

Figure 5-9: Brillouin light scattering data of the partially epitaxial sample with t_{ox} = 0.132 nm. The colour-coded maps show the inelastically backscattered light intensity as a function of the sample orientation β and the excitation frequency. The data were measured in the remanent state (a) after prior saturation at every measured angle and (b) after prior saturation along the easy axis (EA), i.e. β = 0. The inset figure in (b) shows exactly the same as in (b) but for wider angular range of β.

5.4. Conclusions

Thanks to the demonstrated ability to tune the crystallographic order in uniaxial Co films in a well-defined and continuous manner (chapter 4), it has been possible to study the HA anomalous magnetization reversal in a detail. Hereby, it has been found that for the anomaly to appear is necessary to have a crystallographic disorder level above a certain threshold misalignment. Above this threshold, the HA value of M_r/M_0 shows an abrupt increase followed by much more gradual change for larger crystallographic misalignment.

In order to understand the origin of this phenomena, a two grain model has been devised that is able to mimic all key experimental features of the anomaly and from which one is able to conclude that the anomaly is the result of a competition of exchange energy and anisotropy energies in between misaligned grains. The misalignment between the grains causes opposite helicity of the magnetization

rotation near the hard axis, which is opposed by the exchange coupling. However under certain conditions of misalignment angle, exchange coupling constant, anisotropy constant and applied field angle, this opposite helicity causes the existence of a metastable state in remanence, which is being populated in the HA anomalous regime. The nature of this anomalous state is a significantly non-uniform magnetization state, whose existence has been experimentally verified by means of MOKE microscopy and BLS measurements.

6. Dynamic phase transition in ferromagnets

In above experiments the applied magnetic field variations are much slower than the relaxation time of the system, and the magnetization is able to follow the externally applied field. However as described in sect. 2.3. the magnetization reversal is a dynamically ordered process, where the magnetization follows the external applied field with a certain delay, given by its relaxation time. Among different features the dynamically ordered systems may exhibit dynamic phase transition, which consists in the transformation of the system state from one dynamically ordered phase to another at a certain critical point.

The dynamic phase transition phenomenon in ferromagnets was first modelled numerically by Tomé and Oliveira using the kinetic Ising model in mean-field approximation[49]. They found that the averaged magnetization (m) during a full field oscillation cycle, can exhibit a vanishing or non-vanishing value depending on the temperature (T) and the amplitude of the external field for a given field oscillation period (fig. 6-1). They identified the period averaged magnetization, Q, given by

$$Q = \frac{1}{2\pi}\int_0^{2\pi} m(\eta)d\eta \qquad (6\text{-}1),$$

as the dynamic order parameter. Hereby $\eta = \omega_H t$, where ω_H is the frequency of the externally applied field and t denotes the time.

The original work by Tomé and Oliveira subsequently generated substantial scientific interest, in which the DPT phenomenon has been analysed mainly theoretically[32,47,48,130–142], primarily based on the mean field approach[130,137,138] and Monte Carlo simulations[32,47,48,131,132,136,137,139,141,142], using certain models of ferromagnetism and magnetic reversal, such as the Ising[32,47,49,132,136–139,142,143] and the Heisenberg [48,141] models. All theoretical works indicate the existence of the second order DPT in ferromagnetic systems below T_C. As described in sect. 2.3., magnetization states in general do not reach their corresponding equilibrium instantaneously, but instead show a dynamical motion. This dynamics generates a delay for an oscillating field sequence, which depends on the competition between two time scales, namely the period P of the driving oscillatory field and the relaxation time τ of the magnetization itself [140]. For sufficiently large field amplitudes that are capable to reverse the system magnetization in the (quasi-static) DC-mode, the time-dependent magnetization is not able to follow the externally applied field when the period P of the external oscillatory field becomes small in comparison to the ferromagnets' relaxation time τ. At this point, the centre of the resulting hysteresis loop shifts away from the origin of the M vs. H diagram, resulting in an asymmetric loop shape and non-vanishing time-averaged magnetization values Q. For larger period values, the magnetization can follow the external field, even though with a P dependent delay, resulting in a symmetric hysteresis loop around the M vs. H origin. In consequence, the resulting Q is equal to zero. This scenario is referred to as symmetric or paramagnetic phase and the value of the period at which this symmetry is broken is called the critical period P_c.

According to the work of Tomé and Oliveira, there exists a tricritical point (TCP) that separates different types of dynamic phase transitions, i.e. second order phase transitions from the first order phase transitions (fig. 6-1). In the first order phase transition, which appears at low temperatures and high applied field amplitudes, the order parameter goes to zero discontinuously and there is a parameter range, in which Q can exhibit both a finite value or zero value and both solutions are stable or metastable. On the other hand, for small field amplitudes and temperatures near the Curie point, only continuous phase transitions are expected. In this case, the order parameter goes to zero following a power law behaviour, typical for continuous

phase transitions. However, the origin of the discontinuous phase transition and the tricritical point are under controversy[130–135] due to results, which seem to indicate that it may be an artefact of the mean field approximation[132,134], while others show its existence [133,135] even in Monte Carlo simulations [131].

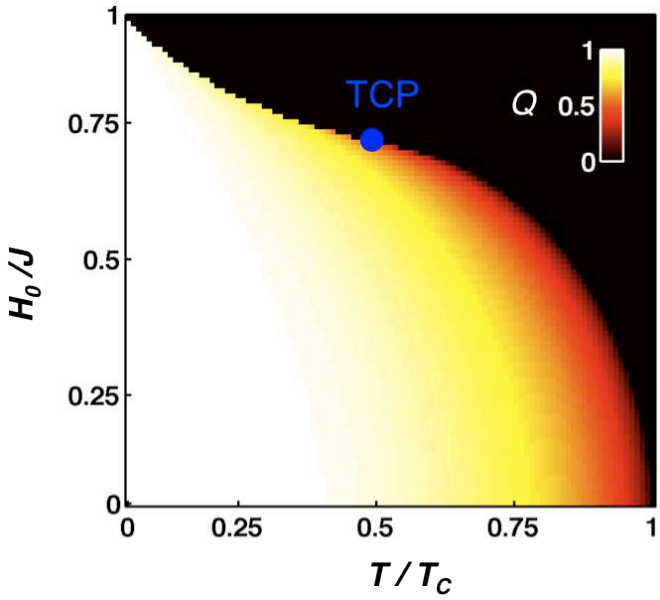

Figure 6-1: Phase diagram for the order parameter *Q* as a function of temperature normalized to Curie temperature (T/T_C) and the externally applied field normalized to the exchange coupling constant (H_0/J). At small fields and high temperatures the order parameter goes to zero continuously while for high fields and low temperatures, it goes to zero discontinuously. The point that joins the two zones is the tricritical point (TCP) shown as a blue dot.

Despite the vast amount of theoretical studies, there are only three experimental observations that are consistent with the theory and indeed suggest the existence of a DPT in real systems[33,144,145]. However, due to experimental limitations, it has not been unambiguously proven up to now that one has a real phase transition in any experimental system.

Moreover, even theoretically the DPT has been investigated in a one-dimensional way, meaning that Q was investigated only as a function of the external oscillatory field period. The question addressing the identity of the conjugate field to the order parameter has only been raised in two recent studies[32,33]. These two works indicate as the result of Monte Carlo numerical simulations[32] and experimental observations in Co/Pt multilayers[33] that an additionally applied time independent field, referred to as bias field H_b is at least a significant part of the conjugate field to the order parameter Q.

In this chapter, the role of this bias field onto the DPT is analysed in detail, both theoretically by means of mean-field calculations and experimentally by using dynamic MOKE measurements for uniaxial Co thin film samples.

6.1. Mean field theory approach

In order to address the effect of H_b onto the DPT, mean-field approximation calculations have been done. Specifically the question addressed has been, whether the $Q(H_b)$-dependence follows the expected behaviour of the conjugate field, i.e. a power law with a critical exponent δ_c that is equal to 3. For this purpose, detailed numerical simulations have been performed and later on, the results have been corroborated analytically in collaboration with the Magnetism Group at the Universidad Técnica Federico Santa María, Valparaiso[146].

The theoretical analysis is based upon the initial work of Tomé and Oliveira[49]. Using the same starting point, an equation of motion for the averaged magnetization in mean field approximation as a function of the external oscillatory field and a time independent field, i.e. bias field, H_b, has been derived. For this purpose, one can consider the mean-field Hamiltonian of the kinetic Ising spin system with N spins under the influence of an oscillating field

$$\widetilde{H} = -\frac{J}{N}\sum_{\substack{i,j \\ i<j}} S_i S_j - H(t)\sum_i S_i$$

(6-2),

where J is the exchange interaction constant (> 0), defined in units of energy per unit volume. In this case, the spins S_i are restricted to values ±1 only. The sum in the exchange interaction extends to all N spins, so that the exchange energy needs to be normalized, i.e. divided by N. The magnetic field H is the sum of a time t dependent periodic field and a continuous bias field H_b, given as

$$H(t) = H_0\, sin(\eta) + H_b$$

(6-3),

with H_0 and H_b given in units of energy per unit volume. Assuming that the system evolves under standard Glauber stochastic dynamics[147], the equation of motion for the average magnetization m normalized to the saturation magnetization is given by

$$\frac{2\pi\tau}{P}\frac{dm(\eta)}{dt} = m(\eta) + tanh\left(\frac{T_C}{T}\left[m(\eta) + \frac{H_b}{J} + \frac{H_0}{J}sin(\eta)\right]\right)$$

(6-4),

where T is the temperature, T_C is the Curie temperature and P is the period of the oscillating external field, i.e. $P = 2\pi/\omega_H$. Eq. (6-4) is the starting point for the numerical simulations. Hereby, eq. (6-4) has been evaluated by means of a finite difference method, from which

$$\begin{aligned} m(k) &= F\big(m(k)\big) \\ &= -\frac{K}{2}\frac{\tau}{P}[m(k+1) - m(k-1)] \\ &+ tanh\left\{\frac{T_C}{T}[m(k)] + \frac{H_b}{J} + \frac{H_0}{J}sin\left(\frac{k}{K}2\pi\right)\right\} \end{aligned}$$

(6-5),

is obtained. The index k goes from 0 to K and one furthermore assumes a periodic boundary condition of $m(0) = m(K)$. K denotes to the total number of discretization steps for each field oscillation cycle within the calculation. Consistent with the continuous case (eq. 6-1) the order parameter Q is given as the magnetization m averaged over all k points, i.e.

$$Q = \frac{1}{K}\sum_{k=1}^{K} m(k)$$

(6-6).

In order to obtain the dynamically stable solutions for the time dependent magnetization at different applied field periods and bias field strengths, the set of equations given in eq. (6-5) has been solved numerically for different values of T/T_C and H_0/J as a function of P and H_b/J. All parameter sets of T/T_C and H_0/J under discussion here have been chosen to restrict the study to the parameter range, in which only second order phase transitions occur, so that one avoids the complications of first order phase transitions that may be an artefact of the mean field approach itself[132,134]. In order to numerically solve eqs. (6-5), the total number of discretization

steps of the periodic field per oscillation cycle, *K*, has been set to 200[pp]. For the first iteration *z*, the magnetization *m(k)* has been initialized to represent a sinusoidal function with the same period as the applied field and in phase with it, plus a continuous magnetization term, namely

$$m_{z=1}(k) = \pm 0.15 + 0.4\, sin\left(\frac{k}{K} 2\pi\right)$$

(6-7)[qq].

Each iteration, i.e. the calculation of *m(k)* for *z*+1 from *m(k)* for *z*, has been done by evaluating

$$m_{z+1}(k) = m_z(k) + l\big(F\big(m_z(k)\big) - m_z(k)\big)$$

(6-8),

whereby eq. (6-5) is being utilized to determine $F\big(m_z(k)\big)$ for every *z*. The quantity *l* represents the fraction of the difference between $F\big(m_z(k)\big)$ and $m_z(k)$ that is added to $m_z(k)$ in order to generate the next iterative set of values. In order to keep the iteration procedure stable in my calculations, *l* = 0.5 has been chosen. As cut off condition for numerical self-consistency,

$$max\left(F\big(m_z(k)\big) - m_z(k)\right) < 10^{-10}$$

(6-9)

has been used, meaning that the maximum error given as the difference between $F\big(m_z(k)\big)$ and $m_z(k)$ should be lower than 10^{-10} for all *k* = 1 to *K*.

[pp] Also simulations for higher *K* values have been performed and although the exact P_c values change slightly with *K*, the critical exponents are identical to the ones obtained for the *K* = 200 case within the error bars.

[qq] The starting condition was chosen in such a way that it was easy for the simulations to achieve stable solutions. To check the validity of the results, simulations with different starting condition were performed and all of them converged to the same solution.

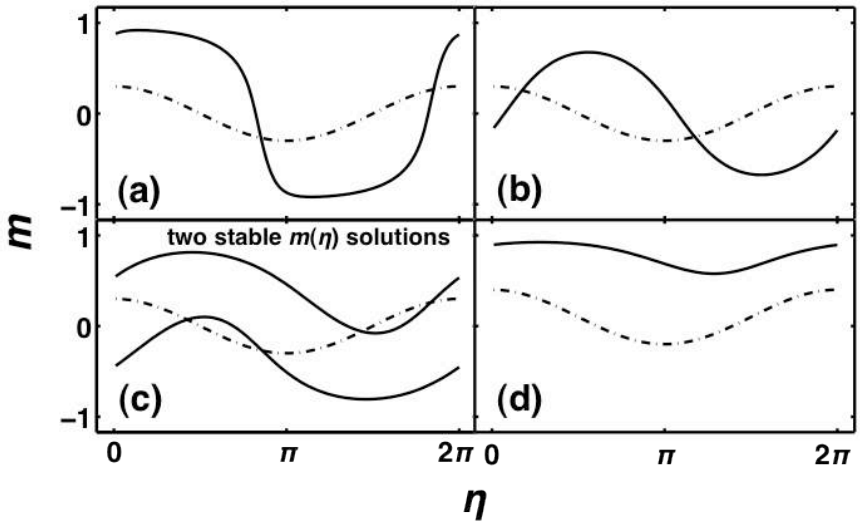

Figure 6-2: Magnetization vs. time behaviour for different P and H_b values at H_0 / J = 0.3 and T/T_C = 0.75 (solid lines). The dashed lines represent the external oscillatory field. In (a) and (b) P is higher than P_c, namely P/P_c = 4.232 and P/P_c = 1.185, respectively, and H_b = 0. In (c) and (d) P is lower than P_c, specifically P/P_c = 0.888 with (c) H_b = 0, and (d) H_b = 0.1. (c) shows two stable magnetization time traces, whose emergence depends on the starting condition chosen in eq. (6-7).

Figure 6-2 shows several examples for the time dependent magnetization m, which have been obtained from the numerical simulations for given values of T/T_C = 0.75 and H_0/J = 0.3 at different periods P and bias fields. While figures 6-2 (a) and (b) show cases, in which the applied field period P is above the critical period, P/P_c = 4.232 and P/P_c = 1.185 respectively, and no bias field being applied, figures 6-2 (c) and (d) show the case of P/P_c = 0.888 for H_b = 0 and H_b = 0.1, respectively. In the symmetric or paramagnetic response (figs. 6-2 (a) and (b)), P is large enough, so that the system can follow the external field with a delay arising from the relaxation time τ. As reported before, the magnetization oscillates around zero, resulting in a vanishing order parameter Q in both cases. The dynamic magnetization delay with respect to the external applied field (fig. 6-2 dashed lines) becomes more pronounced as the P decreases, as can be seen by comparing fig. 6-2 (a) to fig. 6-2 (b). Already in fig. 6-2 (a), the magnetization curve shows a substantial shift to the right if compared to the time-evolution of the applied field in fig. 6-2 (a). This effect is even more pronounced in fig. 6-2 (b). Moreover, for P/P_c = 4.232 the time dependent magnetization appears more square-shaped rather than being a sinusoidal curve, meaning that the magnetization nearly reaches saturation. By decreasing the period, and specifically by going below the critical period, the system can not follow the rapid oscillation of the externally applied field, so that two stable asymmetric or

ferromagnetic solutions are obtained, as can be seen for $P/P_c = 0.888$ in fig. 6-2 (c). It should be mentioned that in this regime, the stable solutions for $m(t)$ depends on the initial parameters chosen in eq. (6-7), i.e. the solution is history dependent just as the static ferromagnetic equilibrium state. If the magnetization is initialized with a positive or negative offset in eq. (6-7), the nearest stable solution will result in a Q with a positive or negative value, respectively, assuming that the time dependent part is the same. This behaviour, however, changes if a sufficiently high H_b is applied as shown in fig. 6-2 (d). In this case, only one possible stable solution exists and it does not matter if the magnetization starting condition is initialized with a positive or negative offset. Instead, the stable solution will depend on the sign of H_b at least for sufficiently large H_b as observed in fig. 6-2 (d), where the H_b is positive and the stable solution results in a positive Q.

In the following, the $Q(P, H_b)$ behaviour has been evaluated in the vicinity of the critical point. In particular, the critical regime has been analysed along two specific directions, namely P approaching P_c for $H_b = 0$ and H_b approaching 0 for $P = P_c$, in order to analyse if Q follows a power law behaviour and if the critical exponents are consistent with the universality class of the equilibrium mean-field theory of ferromagnetism.

In the first part of this study, H_b is set to zero and the $Q(P)$-dependence has been analysed. Fig. 6-3 shows how Q depends on P for two specific examples of the data sets listed in table 6-1, namely for $T/T_C = 0.9$ and $H_0/J = 0.225$ (fig. 6-3 (a)) and $T/T_C = 0.7$ and $H_0/J = 0.325$ (fig. 6-3 (b)). The results of the numerical evaluations of eqs. (6-5) and (6-6) are shown as open circles. For the calculations, equidistant steps for the period P on a logarithmic scale have been used as one approaches P_c. The inset plots in fig. 6-3 show the same data, but as log-log plots of Q vs. p', where p' is the reduced period, i.e. $p' = (P_c - P) / P_c$. The $Q(P)$ power law behaviour is most evident from the log-log plot of the data, as the all data points fall onto a straight line for several orders of magnitude in p'. The green solid lines represent the equilibrium mean field exponent $\beta_c = 0.5$. By simple visual comparison, an excellent agreement is found between the non-equilibrium data shown here and the equilibrium mean field power law in all cases. For the purpose of accomplishing a quantitative analysis, the $Q(P)$-data have been fitted by means of

$$Q(H_b = 0, P \longrightarrow P_C) \propto (P_C - P)^{\beta_c}$$

(6-10),

as P approaches P_c, following the type of analysis one uses for equilibrium systems as T approaches the Curie temperature T_C. The corresponding least-squares fits are shown as solid red lines in figs. 6-3 (a) and (b). From these fits, values for P_c and the critical exponent β_c have been obtained, which are listed in Table 6-1. Overall, one can observe that the numerically determined critical exponents agrees with the equilibrium critical exponent of β_c = 0.5 within the error limits of the analysis or at least with a three significant digit precision, except for T/T_C = 0.6 and H_0/J = 0.375. Specifically, the fits shown in fig. 6-3 correspond to β_c = 0.50093 ± 0.0026 for T/T_C = 0.9 and H_0/J = 0.225 and β_c = 0.50006 ± 0.0008 for T/T_C = 0.7 and H_0/J = 0.325. These fits also allow for the precise determination of P_c, which can then be used to study the role of H_b.

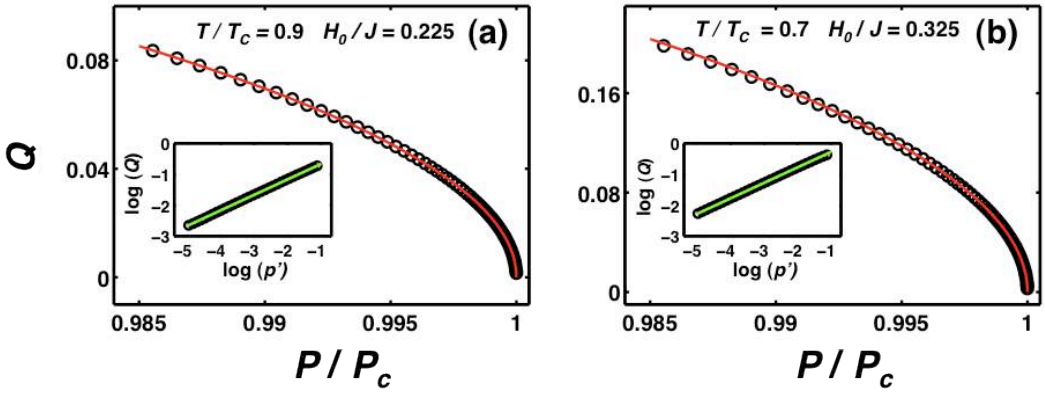

Figure 6-3: Q vs. P at H_b = 0 for (a) T/T_C = 0.9 and H_0/J = 0.225 and (b) T/T_C = 0.7 and H_0/J = 0.325. The open circles are the numerical results of eq. (6-5), while least-squares fits of the data to eq. (6-10) are shown as red solid lines, from which P_c and β_c are extracted. The insets show log-log plots of Q vs. P for the same data sets. Here, the green solid lines represent the equilibrium mean-field critical exponent of β_c = 0.5.

Fig. 6-4 shows some of the resulting Q vs H_b curves for T/T_C = 0.9 and H_0/J = 0.225 (fig. 6-4 (a)) and T/T_C = 0.7 and H_0/J = 0.325 (fig. 6-4 (b)) at their respective P_c values. For these calculations, equidistant H_b steps on the logarithmic scale have been used, hereby changing H_b/J from 10^{-7} to 10^{-3} for a total of 300 points. Also here, the inset figures show the same set of numerical data Q vs H_b, but on a logarithmic scale. In these plots, a clear power law behaviour is evident in both cases, symbolized by the straight line, on which all data fall in the log-log plot. By comparing the numerical data with the known power law for the equilibrium mean field theory,

which has a critical exponent of $\delta_c = 3$ (green solid lines), excellent qualitative agreement is observed, which strongly suggests that H_b is the conjugate field to Q.

In order to corroborate this qualitative observation, the data have been analysed quantitatively by means of a power law fit, namely

$$Q(P = P_C, H_b \longrightarrow 0) \propto (H_b)^{1/\delta_c} \qquad (6\text{-}11).$$

By performing least-squares fits of the simulated Q vs H_b data to eq. (6-11) critical exponents of $\delta_c = 2.9937 \pm 0.0003$ and $\delta_c = 2.9891 \pm 0.0001$ for $T/T_C = 0.9$ and $H_0/J = 0.225$ and $T/T_C = 0.7$ and $H_0/J = 0.325$, have been obtained respectively, both of which are shown in fig. 6-4 as red solid lines. Thus, in both cases the numerical analysis mimics the equilibrium exponent $\delta_c = 3$, however with considerably lower precision than for the case of the exponent β. The lower accuracy here is not surprising because P_c may be already imperfectly defined to start with and this might introduce an extra error in the final values of δ_c, since Q follows $(H_b)^{1/\delta_c}$ for $P = P_c$ only.

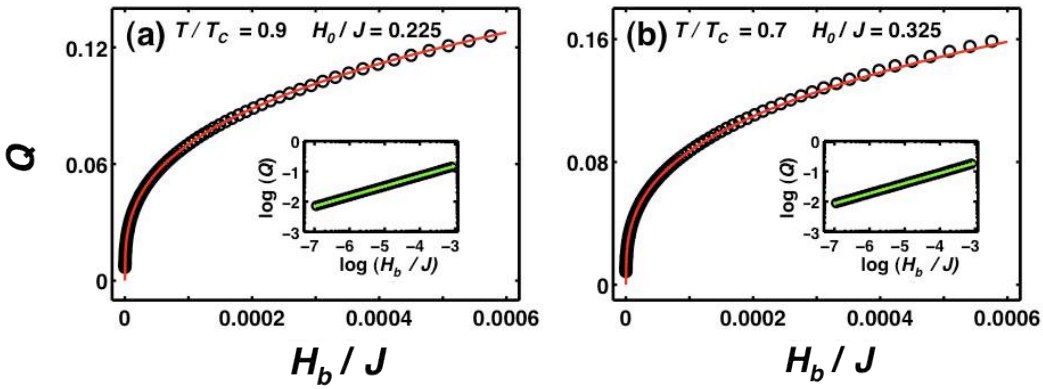

Figure 6-4: Q vs. H_b at $P = P_c$ for (a) $T/T_C = 0.9$ and $H_0/J = 0.225$ and (b) $T/T_C = 0.7$ and $H_0/J = 0.325$. The open circles are the numerical results of eq. (6-5), while least-squares fits of the data to eq. (6-11) are shown as red solid lines, from which δ_c is extracted. The insets show log-log plots of Q vs H_b for the same data sets. Here, the green dashed lines represent the equilibrium mean-field critical exponent of $\delta_c = 3$.

In order to further analyse the numerical precision of the critical exponents β_c and δ_c, their dependence from the Q-value range, from which they are determined, has been studied. Specifically, β_c and δ_c have been analysed as a function of the maximum Q-value, Q_{max}, that is being used. The results for one specific case, $T/T_C = 0.75$ and $H_0/J=0.3$, are shown in fig. 6-5. For both critical exponents one can observe

that the non-equilibrium critical exponents β_c (fig. 6-5 (a)) and δ_c (fig. 6-5 (b)) approach the equilibrium values $\beta_c = 0.5$ and $\delta_c = 3$, shown as blue dashed lines, as one reduces Q_{max}. This is the expected result, because the power laws eqs. (6-10) and (6-11) are only exact in the immediate vicinity of the critical point where Q goes to zero.

However, one notices that the critical exponents actually cross the expected values for both exponents, i.e. β_c and δ_c as Q_{max} is decreased, a fact that might have two different origins. Considering that the number of point used for the data fit decreases as one goes to lower Q_{max}, the uncertainty of the fitted parameter value, i.e. β_c and δ_c, increases as Q_{max} is reduced. The other possible explanation might be related to the so called critical slowdown phenomenon that appears near critical points, which leads to the fact that perturbations having very long lifetimes and that it takes increasingly long to approach the actual stable value. Within the framework of here explain numerical calculations, this can result in the following: as one gets closer to the critical point, the rate of change of the magnetization pattern gets smaller and smaller for each individual iteration ($F(m_z)$-m_z), so that using a constant cut-off condition, (eq. 6-9), means that the calculations in the immediate vicinity of the critical point become less reliable.

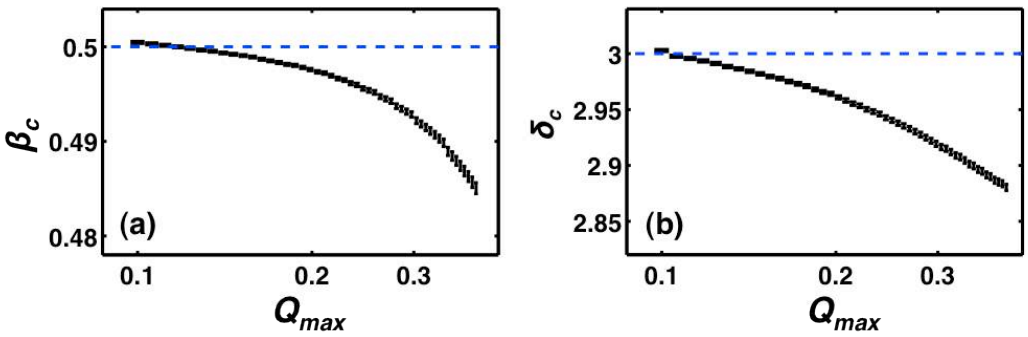

Figure 6-5: Numerically determined critical exponent values for β_c (a) and δ_c (b) as a function of the maximum Q value used in the analysis. The blued dashed lines represent the mean field critical exponents $\beta_c = 0.5$ and $\delta_c = 3$ for the thermodynamic equilibrium system.

The same analysis has been done for different values of T/T_C and H_0/J obtaining similar values of β_c and δ_c. All the results are listed in Table 6-1, and have been derived from numerical fits that were limited to a Q_{max}-value of 0.1[rr].

H_0 / J	T/T_C	P_c	β_c	δ_c
0.2	0.95	1.1577	0.50065 ± 0.00056	2.9905 ± 0.0003
0.225	0.9	1.5920	0.50093 ± 0.00026	2.9937 ± 0.0003
0.25	0.85	1.7696	0.50036 ±0.00019	2.9904 ± 00002
0.275	0.8	1.8478	0.50013 ± 0.00012	2.9897 ± 0.0001
0.3	0.75	1.8800	0.50034 ± 0.00011	3.0001 ± 0.0011
0.325	0.7	1.8914	0.50006 ± 0.00008	2.9891 ± 0.0001
0.35	0.65	1.8967	0.49938 ± 0.00010	2.9866 ± 0.0004
0.375	0.6	1.9071	0.49674 ± 0.00013	2.9941 ± 0.0002

Table 6-1: Numerical values of least-square fits using eqs. (6-10) and (6-11) for P_c, β_c and δ_c for different values of H_0/J and T/T_C. The error is given by the standard deviation. For all P_c values the estimated error is less than 0.0001.

A final proof that H_b is indeed the conjugate field of the order parameter Q has been done by an analytical calculation of the kinetic mean field Ising model based upon a series expansion, which has been performed in collaboration with the Magnetism Group at the Universidad Técnica Federico Santa María (Valparaiso, Chile) and mainly by R. Gallardo[146]. Hereby, it has been found that

$$Q = \frac{T}{T_C}\left(\frac{6\pi}{I_2(P_c)}\right)^{1/3}\left(\frac{H_b}{J}\right)^{1/3} \qquad (6\text{-}12)^{ss}$$

which is formally equivalent to the equilibrium case, and corroborates the bias field as the conjugate field of the order parameter Q, as well as its critical exponent $\delta_c = 3$.

[rr] In addition to the limits of accuracy discussed above, another reason why the standard deviations of β_c and δ_c shown here are in many cases smaller than the deviation from the expected thermodynamic mean field values β_c and δ_c is due to the fact that possible correlations between the free fitting parameters in eqs. (6-10) and (6-11) have not been taken into account. Prefactors have been included in eqs. (6-10) and (6-11) in order to fit the Q ($P \rightarrow P_c$, $H_b = 0$) and Q ($P = P_c$, $H_b \rightarrow 0$) data. These prefactors are also considered as free fitting parameters.

[ss] I_2 is an integral of hyperbolic functions, which contains the time dependent periodic term of the magnetization and external applied field. For a further description, see ref. 146.

6.2. Experimental study of the role of the bias field

After having a theoretical proof that the bias field is indeed the conjugate field of the dynamical order parameter *Q*, at least within the framework of mean-field theory, the non-equilibrium phase diagram of a ferromagnet has been studied experimentally. In order to mimic the theory, it is clear that the sample should be uniaxial and should have negligible magnetostatic effects. Thus, thin film geometry with a single EA of magnetization within the film plane is ideal. Furthermore, the coercive field should be low enough to allow for sufficiently large frequencies of the applied magnetic field to reach stable dynamic states and accumulate good statistics through the measurement of a large number of field cycles.

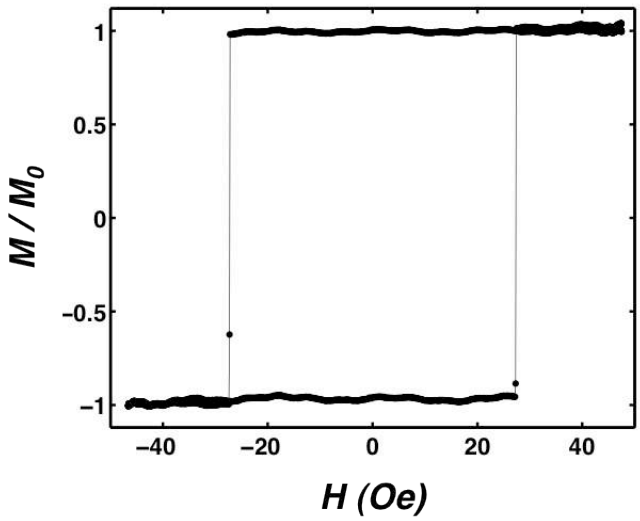

Figure 6-6: Hysteresis loop measured by MOKE along the EA for the uniaxial Co sample used in the DPT studies.

In order to obtain a sample that fulfils these conditions, weakly textured Co thin films have been grown by reducing the Ag-layer thickness in comparison to the previously described epitaxial growth sequence. In this way, Co thin films with low coercive field, but still having uniaxial properties have been obtained. The quasi-static magnetic properties of such a sample are shown in fig. 6-6, where the magnetic hysteresis loop along the EA is displayed, which has been measured by means of the longitudinal MOKE effect. The measurement shows a perfectly square loop with flat branches and an abrupt magnetization transitions at the coercive field of ±27 Oe, highlighting the bimodal Ising model like nature of the sample for magnetic field reversal along the EA, at least in terms of quasi-static magnetic properties. Thus,

these types of samples show the key ingredients needed to experimentally study the dynamically ordered phase, namely a magnetic film system that exhibits only two stable magnetic states in the quasi-static limit while exhibiting a low coercive field and no relevant magnetostatic effects.

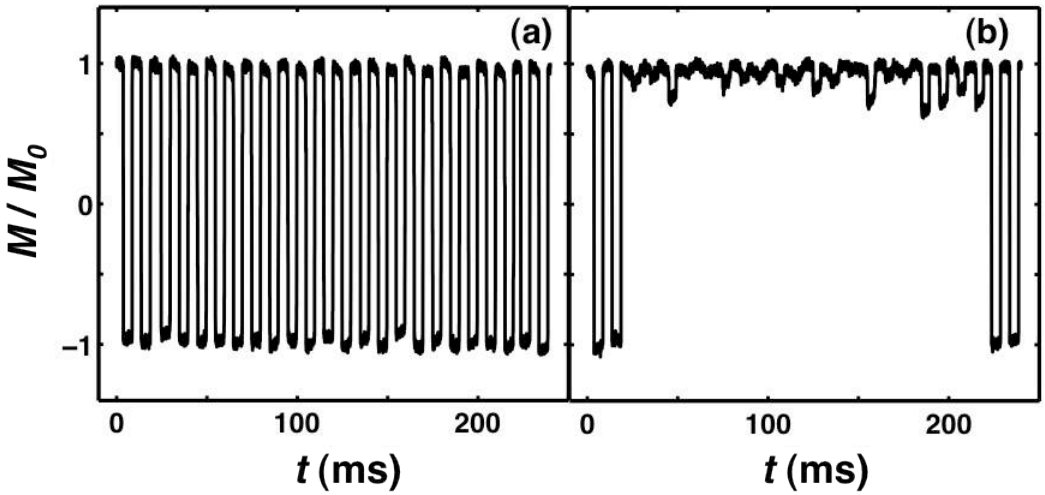

Figure 6-7: Magnetization time-traces upon applying a sinusoidal magnetic field of amplitude H_0 = 30.80 Oe and P = 10 ms along the easy axis of magnetization: (a) measurement without bias field; (b) measurement with a bias field of H_b = 1.40 Oe. The first two and the last two field cycles are done at H_0 = 50.00 Oe to ensure full magnetization reversal for the purpose of generating internal calibration measurements.

Fig. 6-7 shows measured real-time traces of the magneto-optical magnetization signal normalized to the saturation magnetization signal for a Co-film upon applying an oscillatory field amplitude (H_0) of 30.80 Oe at a period of P = 10 ms. The first and the last two field cycles are done at H_0 = 50.00 Oe to ensure a full magnetization reversal for the purpose of generating internal calibration measurements. Hereby, fig. 6-7 (a) shows the signal without an applied bias field, while fig. 6-7 (b) displays a time-trace, in which a relatively large bias field of H_b = 1.40 Oe has been applied. While the biased curve shows only a small magnetization variation, the unbiased curve shows a nearly rectangular shaped time sequence at P = 10 ms. Also, one can see that these data have a very small noise level, and thus make it very easy to accurately determine Q and related quantities.

Figure 6-7 also illustrates the relevance of H_b for the order parameter Q. While the Co-film system clearly exhibits a paramagnetic dynamic state in fig. 6-7 (a) by showing a symmetric $M/M_0(t)$-response with Q = 0 for H_0 = 30.8 Oe and P = 10 ms, the application of H_b = 1.40 Oe is sufficient to induce a very large value of $Q \approx$

0.9 (fig. 6-7 (b)) and thus a bias field induced *Q*-polarization. The fact, that a bias field of only 1.40 Oe can cause such near saturation levels of *Q* underlines the very high sensitivity of the dynamic phase to even small values of the bias field, which in turn highlights the relevance of the excellent field precision and reproducibility needed in this type of experiment.

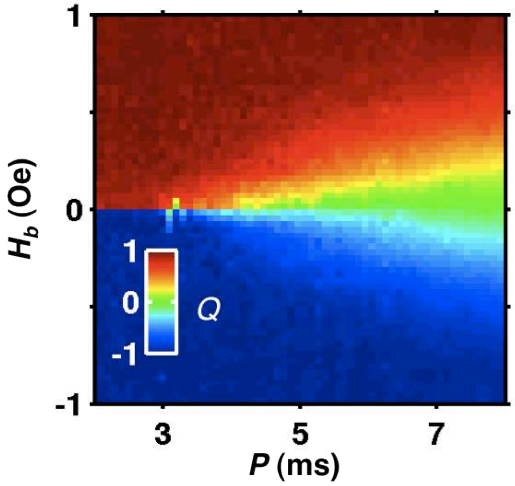

Figure 6-8: Experimentally measured *Q* as a function of the field oscillation period *P* and the applied bias field H_b displayed as a colour coded map for H_0 = 29.8 Oe for an in-plane uniaxial Co film.

Figure 6-8 shows the experimental non-equilibrium phase diagram as a $Q(P, H_b)$ colour coded map, measured for a thin Co-film with H_0 = 29.8 Oe. *Q* has been determined by averaging magnetization traces identical to the two shown in the figs. 6-7 for a range of H_b values at every oscillation period[tt]. While Q =1 and Q = -1 are indicated by the red and blue colour, respectively, green indicates Q = 0, i.e. the paramagnetic or symmetric phase. Below the critical period ($P_c \approx$ 3.5 ms) a sharp transition in between positive (red) and negative (blue)-values is observed. This mimics the existence of a phase boundary just as in the thermodynamic phase diagram (see schematics in fig. 2-8), where the magnetization changes abruptly from positive to negative according to the sign of externally applied field *H* below its Curie temperature. Also consistent with thermodynamic phase diagrams for $T > T_C$, where *M* vanishes upon decreasing the externally applied field, one sees in figure 6-8 that

[tt] The first and last two calibration cycles have been excluded from every *Q* calculation, except for using them as the appropriate normalization at every point. For each measurement point (P, H_b), the system has been initialized in such a way that the final saturation field before the actual measurement sequence start has of the same sign as H_b.

for larger periods, the transition in between positive and negative Q values is gradual with Q actually vanishing at $H_b = 0$. Thus, the phase line separating inverted order states has ended and for $P > 3.5$ ms the system is in the paramagnetic dynamic phase.

6.2.1. Transient behaviour of the dynamically ordered phase

After finding clear equivalences between the non-equilibrium dynamic phase transition and thermodynamic phase transitions in ferromagnetic systems, further experimental measurements have been carried out in order to study in more detail the effect that H_b has on Q.

Figure 6-9 shows measured Q values in the dynamically ordered regime upon a continuous reduction of H_b from +1.2 Oe to -1.2 Oe, shown in red, and subsequently upon increasing the bias field again from -1.2 Oe to +1.2 Oe, shown in blue. In order to calculate Q, magnetization traces (similar to the ones shown in fig. 6-7, but without intermediate calibration cycles) have been averaged over N_c cycles, while the bias field has been kept constant, before changing H_b to the next value in step sizes of 0.025 Oe. The key observation here is the fact that the dynamically ordered state is not simply inverted when H_b crosses 0 as one can observe in fig. 6-9. Instead, the data show a transient behaviour, in which the magnetization cycle dynamics is determined by a delayed approach to the non-equilibrium steady state. This leads to the occurrence of a Q vs. H_b hysteresis behaviour, shown in fig. 6-9, where each Q state depends on the previous state, i.e. the history of the system in the same way the conventional *M(H)* hysteresis loops occur. The comparison of the different curves in fig. 6-9 also shows that this hysteresis effect is reduced upon increasing N_c, which corresponds to an increased number of cycles at every data point, which in turn corresponds to an increase of the measurement time for every Q value. This trend suggests that the $Q(H_b)$ hysteresis loop is a transient behaviour, because longer measurement times will reduce the occurrence or extent of transient dynamics. However, the behaviour is not a simple time argument, since an increase from $N_c = 50$ (fig. 6-9 (a)) to $N_c = 400$ in fig. (6-9 (d)) does not reduce the transient behaviour occurrence or interval by a factor of 8, but to a much lesser degree. Thus, the meta-frequency or $1/N_c$ dependence of the $Q(H_b)$-hysteresis loop is far weaker than linear, showing that a combination of time and H_b-sequence is relevant here.

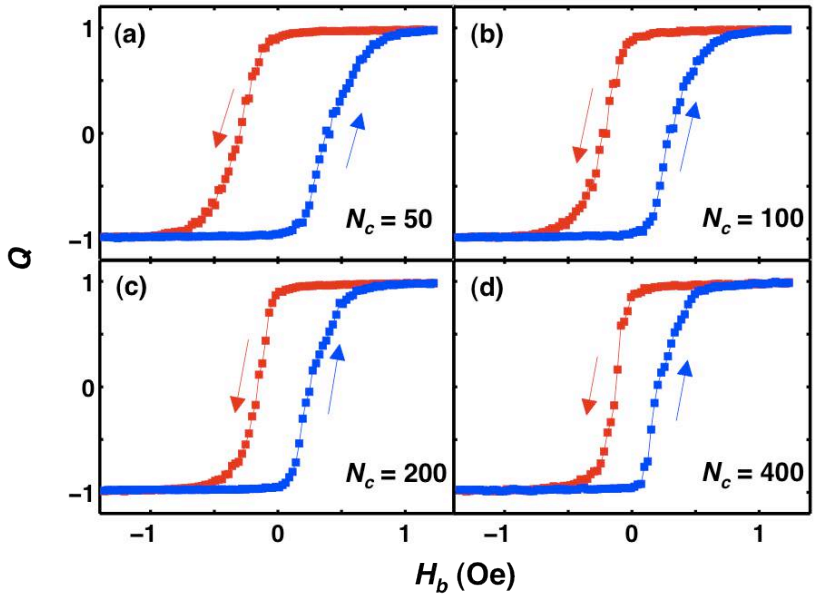

Figure 6-9: H_b-dependence of the dynamic phase order parameter Q measured for a uniaxial Co films with an applied oscillation field amplitude H_0 = 29.8 Oe and period P = 2.5 ms along the easy axis of magnetization. Measurements (a) – (d) differ in the number of the oscillation field cycles N_c that were measured for every bias field step, prior to changing H_b. Data for decreasing and increasing H_b are shown in red and blue, respectively.

Overall the Q vs. H_b behaviour observed here is very reminiscent of the M vs. H behaviour of thermodynamically (meta)stable ferromagnetism, where the inversion of the applied field H causes a first order phase transition due to the crossing of a phase boundary, which in turn produces a hysteretic behaviour as a consequence of metastability and transient magnetization reversal dynamics occurs. Furthermore, this $M(H)$ behaviour is generally found to be only moderately dependent of the applied field frequency in the ferromagnetic phase[148], just as one can observe here a clearly visible, but weak $1/N_c$ meta-frequency dependence for $Q(H_b)$. So, overall the here found $Q(H_b)$-behaviour shows experimentally that H_b is indeed the conjugate field to the order parameter Q and that modifications of H_b cause a transient behaviour that is indicative of a dynamic phase boundary at $H_b = 0$.

To further investigate the occurrence of this transient behaviour and its relation to the dynamically ordered state, its period dependence has been studied for different oscillation field amplitudes H_0. Some representative results are displayed in fig. 6-10. Figures 6-10 (a)-(c) show maps of the quantity $\Delta Q(H_b,P) = Q^d(H_b,P) - Q^i(H_b,P)$, which is the difference of the Q values measured for the decreasing H_b-branch $Q^d(H_b,P)$ and the increasing H_b-branch $Q^i(H_b,P)$ for different periodic applied field amplitudes, namely 29.8 Oe (fig. 6-10 (a)), 30.3 Oe (fig. 6-10 (b)) and 30.8 Oe

(fig. 6-10 (c)). Thus, ΔQ is different from zero only in the hysteretic part of the $Q(H_b)$-loops (fig. 6-10). As one can observe in fig. 6-10 (a), the hysteretic regime is an approximately triangular structure on the left hand side of the figure, which extends in a tip-like fashion to period values of about 3.5 ms. For $P > 3.5$ ms, $\Delta Q \approx 0$ everywhere independent from H_b. This is consistent with the previously mentioned fact that the transient behaviour seen in fig. 6-10 is intimately coupled with the dynamically ordered state and thus, does not appear for the paramagnetic dynamic state, in the same way, in which conventional magnetic hysteresis is a materials property limited to the ferromagnetic phase, because only then one actually crosses a phases boundary upon magnetization reversal. The approximate triangular shape for $P < 3.5$ ms in fig. 6-10 (a) means that there is a certain range of H_b-values, where the lifetime of the metastable dynamically ordered state, for which Q and H_b are oriented antiparallel, is long enough so that it can be observed experimentally. Similar to the conventional ferromagnetic behaviour, this bistability regime increases its size, as one moves away from the critical point, resulting in the here observed triangular shape of dynamic magnetic bi-stability.

Upon applying larger oscillation field amplitudes H_0, one expects the frequency range of the ferromagnetic dynamic state to shift towards higher frequencies or lower P values, since the magnetization can follow the external applied field at higher frequencies, given the shifted energy landscape created by the higher externally applied field. Correspondingly, the bistability regime of $Q(P, H_b)$ should also shift, which is exactly what one observes in figs. 6-10 (b) and (c) with a stepwise shift of the triangular shaped ΔQ structure to the left.

Figures 6-10 (d)–(f) show calculations of the kinetic Ising model by means of the MFT approach (sect. 6.1.), specifically $\Delta Q(H_b,P)$ maps for the purpose of comparison with the experimental data. The existence of two stable dynamic states with opposite Q was already mentioned in the seminal work of Tomé and Oliveira [ref. 49 fig.2 (c)], but the H_b-dependence of this numerical stability has not yet been studied. Here, an H_b-range has been found, in which both dynamic states are numerically stable and its population depends on the system's history, which is defined by the direction H_b is scanned for $P < P_c$. Furthermore, one observes that the bistability range increases with decreasing P in a way that is very similar to the

experiments, producing the same type of triangular shape (fig 6-10 (d)-(f)). Also the H_0/J-dependence of this structure, i.e. the shift of the bistability regime towards lower P for increased H_0/J, resembles the experimental observations very closely.

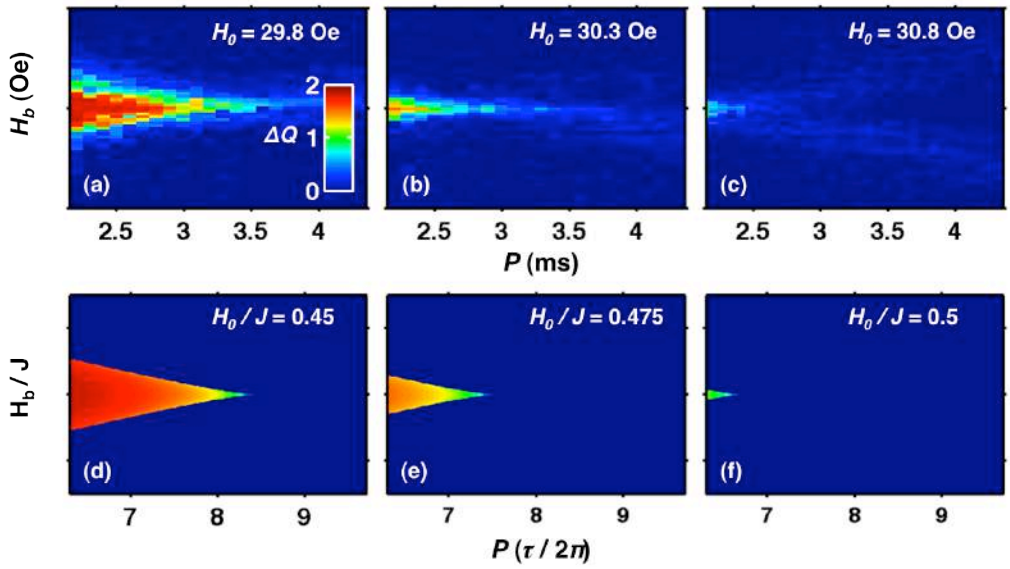

Figure 6-10: $\Delta Q(H_b,P)$ colour coded maps for experimental data measured in in-plane uniaxial Co films (a)-(c) and for numerical simulations based upon the mean-field approximation (d)-(f). The colour code shown in (a) applies to all the figures. (a) – (c) are measured and (d) – (f) are simulated for different oscillation field amplitudes which are identified in each map.

6.3. Conclusions

In this chapter it has been demonstrated theoretically and experimentally that H_b is the conjugate field of the order parameter Q for the dynamically ordered phase in ferromagnets. By using and exploring the H_b dependence of the order parameter Q, one has access to far more aspects of the underlying physics that is driving the dynamically ordered phase, opening up the possibility of much wider investigations and holding the promise of a much better understanding of the dynamically ordered phase and dynamic ordering processes in general.

For the theoretical analysis, the kinetic Ising model in mean field approximation has been analysed, for which it has been demonstrated that Q vs. H_b follows a power law behaviour with the same critical exponent that is being found for M vs. H in the equilibrium phase transition, namely $\delta_c = 3$.

Experimentally it has been confirmed that H_b does indeed define a phase line at $H_b = 0$ for $P < P_c$, causing a first order phase transition in between two anti-parallel

but otherwise equivalent dynamic order states, that upon crossing also generate hysteresis like phenomena. All this seems to indicate that the similarities of the dynamic phase transition and the conventional thermodynamic ferromagnetic phase transition are much broader than has been assumed so far.

An experimental determination of the critical exponents of the DPT has been attempted, but was not achieved. Here, the extremely small critical field range and the corresponding requirements on field stability made the resulting data insufficient to reliably determine experimental values for β_c and δ_c.

7. Magnetic properties of individual Co nanostructures

The previously mentioned reduction of lateral sizes in ferromagnetic systems is a key research area in the field of magnetism and of crucial importance for a wide range of technological applications[4,5]. In order to understand the magnetization reversal of nanostructures in detail, it is advantage to study individual nanostructures independently.

On the other hand, even though structuring of nanoscale systems can be achieved by different lithography techniques, such as the mostly used electron beam and optical lithography techniques for instance, FEBID[56,57] (sect. 3.1.2.2.) and FIB[55] (sect. 3.1.2.1.) have recently attracted a substantial amount of interest, due to the simplicity of the fabrication process. However, in the case of FIB the aggressive nature of the ions may lead to undesired modifications of the magnetic properties.

This chapter is focused on studying two different aspects related to the ferromagnetic nanostructures. In one part of the work, the ability of MOKE microscopy (sect. 3.3.1.3.) to measure the magnetic properties of sub wavelength structures is analysed, for which Co-nanowires with down to 30 nm width have been fabricated by the FEBID. In the second part, the chapter reports an efficient method to fabricate nanostructures in ferromagnetic multilayers using FIB.

7.1. Achieving high MOKE sensitivity for signals from sub-wavelength nanostructures

In a MOKE detection system, the magnetization reversal signal is given as $\Delta I/I_0$, where $\Delta I = I(M) - I(-M)$ is the intensity variation proportional to MOKE signal variation upon magnetization reversal and $I_0 = [I(M)+I(-M)]/2$ is the average light intensity. A commonly accepted condition to be able to measure the magnetization reversal is the requirement that the minimum signal to noise ratio (S/N) needs to be equal or larger than 2. When measuring continuous thin films the fractional MOKE signal, namely $\Delta I/I_0$, does not depend on the illuminated area. However, in the case of individual magnetic nanostructures, the MOKE signal amplitude $\Delta I/I_0$ is diluted according to the area ratio AR given as

$$AR = \frac{A_{mag}}{A_{mag} + A_{nomag}}$$

(7-1),

where A_{mag} is the illuminated magnetic area and A_{nomag} is the illuminated non-magnetic area, assuming identical reflectivities in both areas. Correspondingly, $\Delta I/I_0$ for sub-wavelength magnetic structures $(\Delta I/I_0)_{sw}$ is given by,

$$\left(\frac{\Delta I}{I_0}\right)_{sw} = \frac{\Delta I A_{mag} + 0 A_{nomag}}{I_0\left(A_{mag} + A_{nomag}\right)}$$

(7-2).

Thus, in order to increase $(\Delta I/I_0)_{sw}$ it is necessary to make AR as large as possible. Previous studies, in which MOKE systems have been used to characterize individual sub-wavelength wires, were based on focused cw laser beams[149,150]. Focused laser beams are commonly utilized in order to increase AR, and thus $(\Delta I/I_0)_{sw}$, as much as

possible. Using this approach, the smallest nanostructure measured in a single sweep hysteresis loop with S/N = 2 that is reported in the literature, is an individual 200 nm wide and 5 nm thick Permalloy nanowire[149]. Considering that the length of the illuminated structure was approximately 5 μm, this measurement indicates a single sweep sensitivity of ~ 6 x 10^{-12} emu. Moreover, this work showed that by using the focused laser approach for a material like Permalloy (Kerr rotation angle θ_k ~ 3 μrad), the maximum S/N that is theoretically achievable in a single shot measurement is $(S/N)_{max}$ ~ 2, using the highest laser power that does not cause any significant heating of the sample. Even if the focused laser approach could be improved slightly by reducing the experimental noise, for instance by using a differential photo detector or averaging multiple hysteresis loops[150], its main limitation comes from the large total focus area and thus low AR values for structures that are sub-wavelength.

In order to push beyond this limitation of MOKE nano-magnetometry performance in focused laser systems, a different approach has been pursued here, for which the aforementioned MOKE microscope has been used (sect. 3.3.1.3.). The key feature of this approach is that one can maximize AR well beyond what is achievable by using a focused laser technique. This is feasible due to the possibility to select an arbitrary (shape, size, and position in the field of view) region of interest (ROI) (fig. 7-1), by means of a reduced number of pixels[uu] within the CCD camera array, and use only these selected pixels jointly as a conventional light intensity detector.

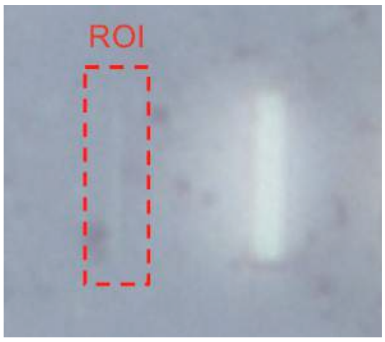

Figure 7-1: Optical image of two nano-magnetic structures as they appear in the Kerr microscope. The red dashed line represents the possibility of selecting a specific measurement area, i.e. the "region of interest" (ROI).

[uu] Each pixel corresponds to nominal 15 x 15 nm^2, however one needs to take into account that the light captured by each pixel is given by the optical resolution, which is approximately 500 nm. Thus each pixel captures the light arising from a 500 x 500 nm^2 area.

Thanks to this feature, one can select the desired area to measure the field dependent local intensity variation, i.e. a local hysteresis loop. This approach is especially relevant for high aspect ratio nanostructures, like wires, for which one can keep relatively high values of AR, far larger than with a focused laser approach.

7.2. Co nanowires deposited by FEBID

In order to verify the sensitivity of MOKE microscopy to magneto-optical signals arising from sub-wavelength structures, Co nanostructures with high aspect ratio have been fabricated, specifically high purity FEBID Co nanowires. This work has been possible due to a collaboration with "Electron Microscopy" group at CIC nanoGUNE who fabricated the Co nanowires by FEBID (sect. 3.1.2.2.). Dr. E. Nikulina was the main responsible for this fabrication process.

The FEBID of cobalt nanostructures has been done by using the previously described Helios NanoLab^{TM} DualBeam^{TM} (sect. 3.1.2.3.). For the fabrication process of the nanowires, the following parameters have been used: electron beam current = 2.7 nA, dwell time = 1 μs, pitch size = 5 nm and a base pressure of 2 x 10^{-4} Pa in the chamber. As mentioned in the experimental techniques chapter, deposits with high purity, good lateral resolution and uniform thickness are achieved by using these values for electron beam current, dwell time and pitch size. On the other hand, a base pressure of 2.10^{-4} Pa in the chamber is enough to ensure stable and good deposition conditions. Using these parameters and tuning the electron beam energy and the deposition time, Co wires of 5 μm length and different width and thicknesses have been fabricated. The corresponding magnetization reversal study is focused on three of these wires, whose deposition conditions, SEM verified dimensions and atomic compositions measured by energy-dispersive x-ray spectrometry (EDX) are reported in table 7-1[vv]. For all beam conditions used here, the Co purity was determined to be equal to 82 ± 4 at.%. Specifically, Table 7-1 shows that the final deposits are composed by Co, C and O, whose percentages are comparable to values obtained by other groups[59].

[vv] The composition analysis has been performed on test structures grown under identical beam conditions but during longer deposition times, in order to avoid an excessive signal contribution from the substrate.

With respect to the dimensions listed in Table 7-1, one observes that by using the appropriate deposition conditions, Co-wires with different width and height can be fabricated. As E. Nikulina found previously in her parameter optimization process[58], an increase of the width or decrease of the lateral resolution occurs by decreasing the electron beam energy. Moreover, for identical electron beam conditions but higher deposition time, wires become thicker and wider. This effect, has been previously reported and arises as a results of the SE emission from the deposit itself. [56]

	Deposition conditions	**Content in at.%**	**Dimensions (L_w×T_w×W_w)**
Wire 1	30 kV, 2.7 nA, 60 min	Co:C:O = 82:12:6	5 µm × 20 nm × 30 nm
Wire 2	2 kV, 2.7 nA, 3 min	Co:C:O = 82:13:5	5 µm × 7.5 nm × 55 nm
Wire 3	2 kV, 2.7 nA, 30 min	Co:C:O = 82:13:5	5 µm × 75 nm × 115 nm

Table 7-1: Deposition conditions, corresponding compositions, and dimensions (where L_w represents the length, T_w represents the thickness and W_w is the width) of FEBID grown cobalt wires.

The SEM images of these wires are shown in fig. 7-2, where the labels show the width of each corresponding wire. While for thicker wires, namely 30 nm thick (a) and 115 nm thick (c) wires, nicely defined edge structures are visible, the wire with 7.5 nm thickness has a more diffuse shape due to its ultrasmall thickness.

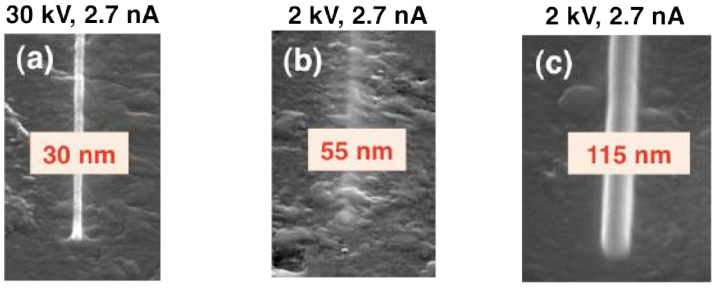

Figure 7-2: Scanning electron microscopy images showing FEBID cobalt wires, deposited at beam energy, beam current and deposition time of: 30 kV, 2.7 nA and 60 min (a), 2 kV, 2.7 nA and 3 min (b) and 2 kV, 2.7 nA and 30 min (c).

7.2.1. Demonstration of magnetization reversal characterization in sub-wavelength nanostructures

In order to measure the magnetization reversal in these sub-wavelength wires, the highest possible magnification of the MOKE microscope has been used, which corresponds to a 100 x objective lens and auxiliary microscope magnification of 4 x,

so that a final magnification of 400 x is achieved. The measurements have been performed in longitudinal geometry and the magnetic field has been applied in the plane of the sample, parallel to the long axis of the wires, which is the EA due to shape anisotropy. The ROI had a rectangular shape utilizing 340 x 8 pixels.

The advantage of keeping AR as high as possible is evident from the measurement reported in fig. 7-3, where a single cycle hysteresis loop[ww] for the 30 nm wide wire (fig. 7-3 (a)) and the 55 nm wide wire (fig. 7-3 (b)) are shown. The S/N ratios for these hysteresis loops are 4.1 and 4.4 for 30 nm wide and 55 nm wide wires, respectively. These values demonstrate the ability of being sufficiently sensible to MOKE signals arising from nanostructures, which are sub-wavelength, allowing even for single cycle hysteresis loop measurements.

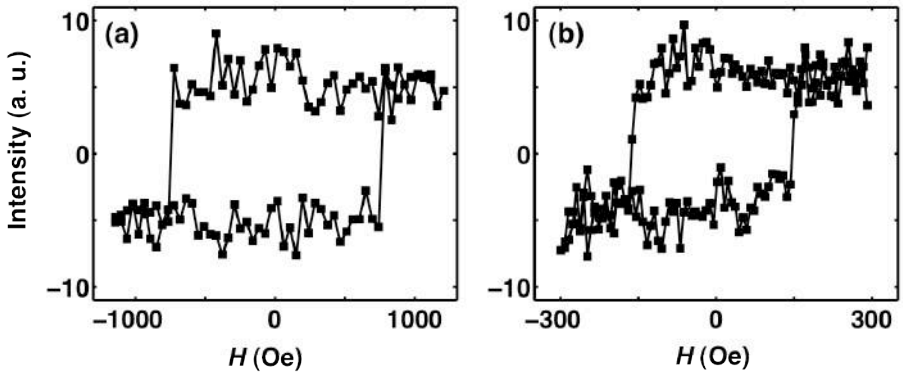

Figure 7-3: Single shot MOKE hysteresis loop signal using a ROI of 340 x 8 pixels (a) for the 30 nm wide wire and (b) for 55 nm wide wire.

If one renormalizes the obtained S/N values to the S/N = 2 criterion mentioned before, and considering that the measurements have been done by measuring the entire wire length, a single sweep measurement sensitivity of up to 1.0 x 10^{-12} emu is obtained. This sensitivity corresponds to a 6-fold improvement compared to the previously reported sensitivity using focused laser based MOKE magnetometry. Also, this value compares very favourably with the sensitivity of 10^{-8}-10^{-9} emu for the latest generation of commercial SQUID magnetometers. Moreover, it is worth to point out that the fundamental limit of the MOKE microscopy approach here has not been reached yet. For example, one way of increasing the sensitivity is by increasing the light intensity. To a good approximation, the S/N scales with the

[ww] Single cycle hysteresis loop refers to only one individual full period magnetization versus applied field measurement.

square root of the light intensity I_{light} per unit area that is used to illuminate the sample, which in the present study is 1μW/μm^2. This value is about 100 times smaller than the typically used intensity in focused beams systems, therefore, by simply increasing I_{light} 100 times, which is technically feasible, one can gain an additional order of magnitude in the sensitivity, thus extrapolating the sensitivity potential of this approach to 1 x 10^{-13} emu without causing significant heating of the sample.

Another approach to improve the sensitivity is to average multiple loops. In fig. 7-4, averaged hysteresis loops are compared that have been also measured on the three Co nanowires described in Table 7-1. Each hysteresis loop shown in this figure is the average of 9 individual reversal cycle measurements. For the cases displayed in figs. 7-4 (a) and (b), namely the 30 nm and 55 nm wide Co wires, an increase of the S/N ratio by a factor of 2.1 for 30 nm wide wire and an improvement of 2.5 for the 55 nm wide wire have been found. This confirms that a wire of less than 10 nm width and 7.5 nm thickness could be studied by means of the magneto-optical approach described here. Moreover assuming the possibility to use 100 times larger light intensity and that the signal reduces with the volume, one can extrapolate the smallest detectable size to be around 3 nm wide and 2.5 nm thick wires for this type of magnetometry.

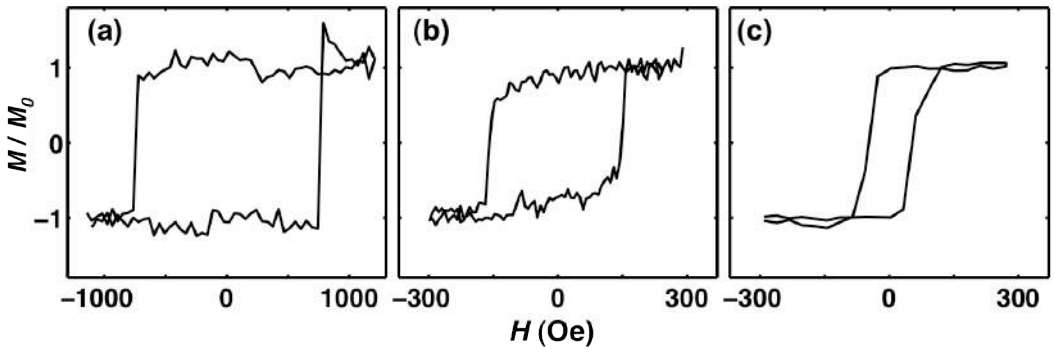

Figure 7-4: Average of 9 single shot hysteresis loops, measured in the MOKE microscope using a ROI of 340 x 8 pixels for FEBID Co wires of 30 nm (a), 55 nm (b) and 115 nm (c) widths.

Concerning the hysteresis loops shape one can observed a remarkably square loop shape for the 30 nm wide wire (fig. 7-4 (a)), which is expected given that the shape anisotropy is very strong here and the wire ends allow only very little non-uniformity. In contrast, the averaged hysteresis loop of the 55 nm wide wire exhibits a small bending before the reversal, a fact that may arise from the less well defined

edges observed in SEM micrograph for this wire (fig. 7-2 (b)). Comparing hysteresis loops for differently sized wires, one also finds a considerable reduction in the coercive fields as the wire width increases. Specifically, the coercive field values are 750, 155, and 55 Oe for 30, 55, and 115 nm wire widths, respectively. The reduction of the field values triggering the magnetization reversal with increasing wire width is consistent with the magnetization reversal being induced by the nucleation of domain walls at wire ends and their subsequent abrupt displacement along the wire.

7.3. Pt/Co/Pt magnetic nanostructures fabricated by FIB

Multilayers show great potential for tuning magnetic properties, such as the magnetic anisotropy[42], for instance. This is also the case for Co/Pt multilayers, which have large perpendicular anisotropy and recently have been recognized to be a good candidate for current induced domain wall displacement devices due to the possibility of controlling domain wall pinning by ion irradiation.[151,152] However, such multilayers whose magnetic properties depend crucially on the layered geometry are particularity susceptible to ion irradiation, because the geometry can easily be perturbed by the ions. Correspondingly, any ion that is not well focused may contribute to modifications of the magnetic properties, so that even the low intensity surrounding areas of highly focused beams, called halos, have to be considered.[153] Consequently, these ions can cause a considerable washing out or damage of the surroundings of milled structured when structuring very sensitive materials systems.

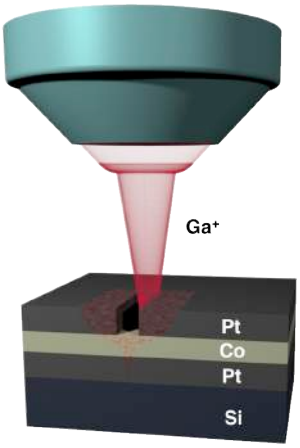

Figure 7-5: Schematic of the fabrication process of nanostructures in Pt/Co/Pt samples via the focused ion beam methodology.

The dependence of the magnetic properties on different ion irradiation doses has been widely analysed by several groups [154–160] and even though this dependency opens new pathways of precise tuning of Co/Pt magnetic properties for different applications, it also limits the fabrication of nano-scale structures as a consequence of the previously mention imperfectly shaped ion beam profiles (fig. 7-5). The area dose that is needed to remove one nanometre of Co/Pt is 2.5 x 10^{15} $Ga^{+}cm^{-2}$ (at 30kV ion beam acceleration voltage) while for suppressing the perpendicular magnetic anisotropy in $Pt_{2.8\ nm}$ $(Pt_{0.6\ nm}/Co_{\ 0.3\ nm})_6$ one needs only 0.5% of this dose.[154,158] As shown schematically in fig. 7-5, such a percent level ion intensity in the beam halo or tail would cause considerable damage in the surroundings of irradiated areas, and most probably it would destroy the magnetic properties of the very nanostructures, one intends to fabricate.

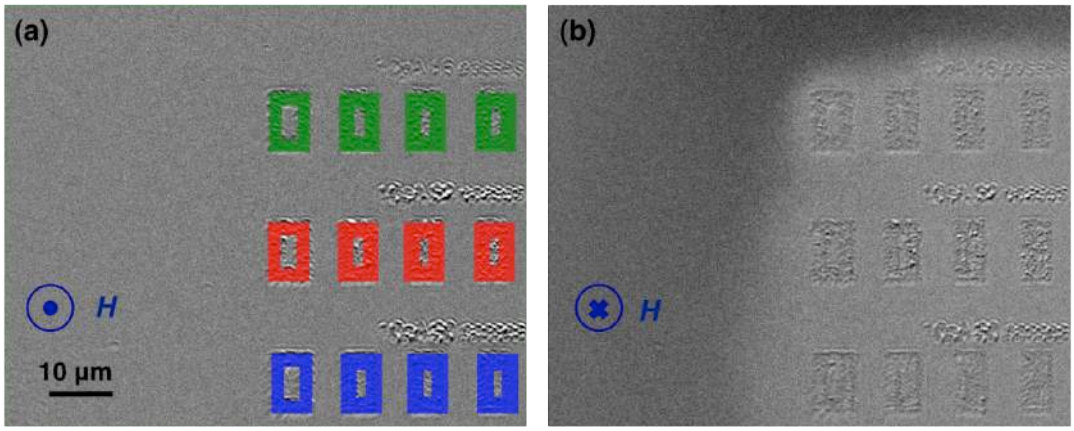

Figure 7-6: MOKE microscope images taken for a Co/Pt multilayer sample at high positive applied field (a) and at high negative applied field (b). The green, red and blue areas in (a) show the irradiated areas of the sample by means of FIB at 30 kV and 10 pA. Each colour indicates different ion doses: green 4 x 10^{15} Ga^{+} ions/cm^2, red 8 x 10^{15} Ga^{+} ions/cm^2 and blue 2 x 10^{16} Ga^{+} ions/cm^2

This effect is clearly visible in MOKE microscope images taken for Co/Pt multilayers, shown in fig. 7-6, at high positive perpendicular applied field (fig. 7-6 (a)) and at high negative perpendicular applied field (fig. 7-6 (b)). In fig. 7-6 (a) the green, red and blue areas show the intended irradiated areas of the sample by the focused ion beam. Specifically the green colour shows the irradiated area using an ion dose of 4 x 10^{15} Ga^{+} ions/cm^2, red shows an irradiated area with 8 x 10^{15} Ga^{+} ions/cm^2 ion dose and blue using an ion dose of 2 x 10^{16} Ga^{+} ions/cm^2. In these MOKE images, upon magnetization reversal there should be a grey scale difference between both images in areas that are magnetic. Indeed, this grey scale difference or

magnetization reversal is visible at the edges of both images, i.e. far away from the irradiated part. However, the surroundings of the irradiated areas exhibit clear damage visualized by the complete lack of a magnetic response. Therefore, one can conclude from this experiment that it is impractical if not impossible to directly fabricate magnetic structures by means of FIB irradiation of Co/Pt multilayers, since a complete destruction of the magnetic signal in the surroundings of the irradiated part is observed.

Up to now, there have been several attempts to pattern Co/Pt nanoscale structures without destroying the magnetic properties. In these attempts an electron beam pre-patterned hard mask[161–163] such as silica[162,163] or stencil masks were used[164,165]. Even though by using these techniques it is possible to pattern nanoscale magnetic structures, the main advantage of the FIB is lost, since it is no longer a two steps process, in which one can directly pattern a previously deposited thin film. A route out of this dilemma is the use of protective coatings that absorb the ions up to a certain level. Streit-Nierobish et al. have recently demonstrated the ability of fabricating 75 nm diameters holes in $Pt_{2.8\ nm}(Co_{0.3}\ nm/Pt_{0.6}\ nm)_6$ multilayers deposited onto 200 nm Si_3N_4 membranes by irradiating through the membrane.[158] But even though this experiment shows a viable way of milling Co/Pt multilayers, it has the very severe drawback that it is limited to systems grown onto membranes.

In this section, a very efficient manner to fabricate magnetic nanoscale structures by means of FIB in Co/Pt multilayers systems through protective coatings is shown. It is clear that the removal of the Co/Pt structure to define a magnetic nanostructure is incompatible with the extremely high sensitivity of the multilayer structure to the ion irradiation. This is especially true for the trilayer structure used here, which contains very little Co, so that it can be fairly easily dissolved into the Pt-layers by ion intermixing. Thus, ions have been used here for intermixing rather than material removal. In this case, even though the halo is still a problem, one can sufficiently suppress its effect by means of a hard mask layer. Specifically as hard mask or coating layer, TiN thin films deposited directly on the Co/Pt multilayers have been used. As a result, the ability of fabricating 100 nm wide lateral magnetic structures in Co/Pt multilayers has been demonstrated, whose magnetic properties have been measured by means of MOKE microscopy using the previously described approach.

7.3.1. Nanostructure fabrication utilizing a TiN hard layer mask

Pt (5.0 nm)/Co (0.8 nm)/Pt (3.0 nm) multilayer films were grown by Prof. Oepen's group at the University of Hamburg onto thermally oxidized Si wafers by means of sputter deposition. X-ray diffraction measurements showed that the films are polycrystalline with (111) crystallographic Pt texture and (0001) Co texture[166]. Prof. Oepen's group found that up to about 1.1 nm thickness of Co, the multilayer geometry results in a perpendicular anisotropy[167].

As hard mask or sacrificial layer, 40 nm of reactive magnetron sputtered TiN layer has been used[xx]. The TiN has been deposited by means of the ATC series UHV sputter systems (sect. 3.1.1.1.) at CIC nanoGUNE using a pure Ti target sputtered at 200 W in 85% Ar and 15% Nitrogen atmosphere at a pressure of 3 mTorr. It has been previously shown that TiN presents excellent properties as a mechanically hard coating[168]. X-ray diffraction spectra confirmed that the deposited TiN thin film is indeed chemically TiN and not some other or stoichiometry deficient compound.

A scanning electron microscope (SEM) image (fig. 7-7) displays a series of fabricated magnetic structures whose length is 5 μm and whose width has been varied from 2 μm down to 100 nm, namely 2 μm, 1 μm, 500 nm, 200 nm and 100 nm. The dark areas are the irradiated regions while the non-irradiated parts appear brighter. The main purpose of fabricating nanostructures with high length, namely 5 μm, is to measure their magnetization easily by MOKE microscopy. On the other hand, structures of different width have been fabricated in order to estimate the influence of the ion beam tail onto the magnetic properties of the structures. Three sets of wires have been fabricated with above described dimensions and each of them with different ion doses, namely: $D_{i1} = 4 \times 10^{15}$ Ga^+ ions/cm^2 (16 passes), $D_{i2} = 8 \times 10^{15}$ Ga^+ ions/cm^2 (32 passes) and $D_{i3} = 2 \times 10^{16}$ Ga^+ ions/cm^2 (80 passes). These ion doses have been used in order to cover a broad range of ion dose values and to investigate how different ion doses may influence the magnetic properties. Ion beam energy and current have been kept constant for all three doses, namely at 30 kV and 10 pA and the ion dose has been varied simply by adjusting the amount of ion beam passes over the structure. Patterns have been created in raster mode with a pitch size of 5 nm.

[xx] The main reason of considering a thickness of 40 nm as a starting value, is that the penetration depth of ions at 30 kV is approximately this value[171].

These structures have been fabricated with the support of the Electron Microscopy group, mainly Dr. Andrey Chuvilin.

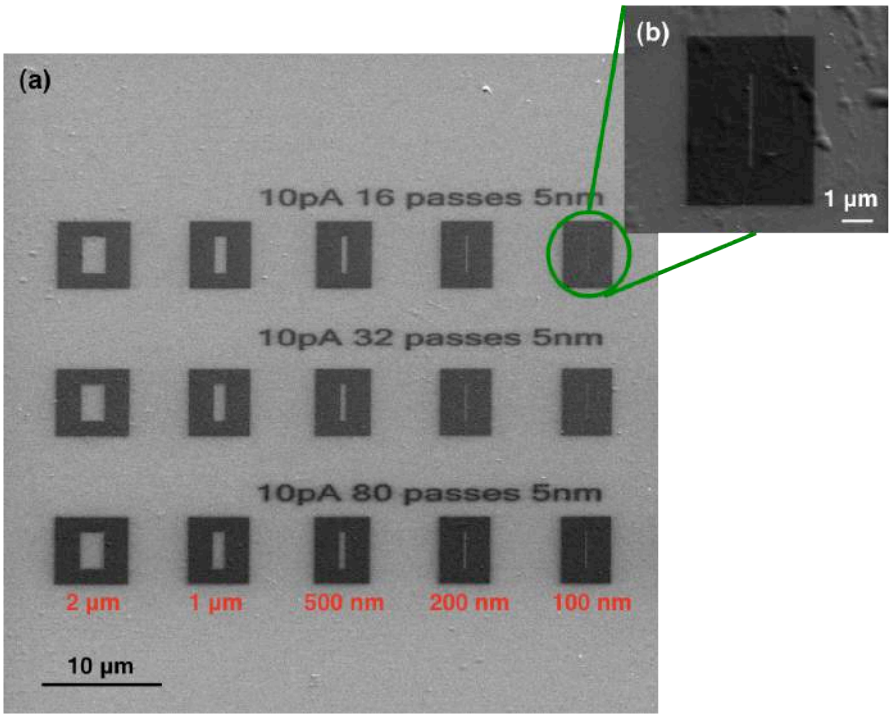

Figure 7-7: (a) Scanning electron microscope images of nano-structures fabricated in Pt/Co/Pt layers, specifically 5 µm long and 2 µm, 1 µm, 500 nm, 200 nm, 100 nm and 50 nm wide wires. The same set of wires have been fabricated using different ion doses D_{i1} = 4 x 10^{15} Ga^+ ions/cm^2, D_{i2} = 8 x 10^{15} Ga^+ ions/cm^2 and D_{i3} = 2 x 10^{16} Ga^+ ions/cm^2, by using a ion energy of 30 kV and 10 pA beam current and adapting the number of ion passes for each ion dose. (b) SEM micrograph of a 100 nm wide wire that was fabricated using the lowest dose D_{i1}.

Even if the SEM images allow one to see the structure and enables an initial check of the successful milling process, one cannot estimate the actual depth of the very shallow topography in a quantitative manner from them. Therefore, one needs the AFM in order to determine precisely the topographical influence of the ion radiation (fig. 7-9 (a)). Figures 7-8 (b) and (c) show topographic cross section profiles of AFM measurements in Pt/Co/Pt structures capped by a TiN hard layer (fig. 7-8 (b)) in comparison to uncovered structures (fig. 7-8 (c)). Different colours on figs. 7-8 (b) and (c) indicate different ion doses, where green represents structures fabricated using D_{i1} ion dose, red using D_{i2} ion dose and blue using D_{i3} ion dose.

A substantial decrease of the sputtering yield is found in the case of Pt/Co/Pt structures covered by TiN (fig. 7-8 (b)) compared to uncovered structures (fig. 7-8 (c)). In the case of the widest structures, no apparent milling of the real structures by the hallo can be observed, which together with previously observed MOKE images

(fig. 7-6 (b)), indicates that in the case of the uncovered Pt/Co/Pt structures, it is enough to simply cause structural damage through the ion implantation to annihilated the magnetic properties.

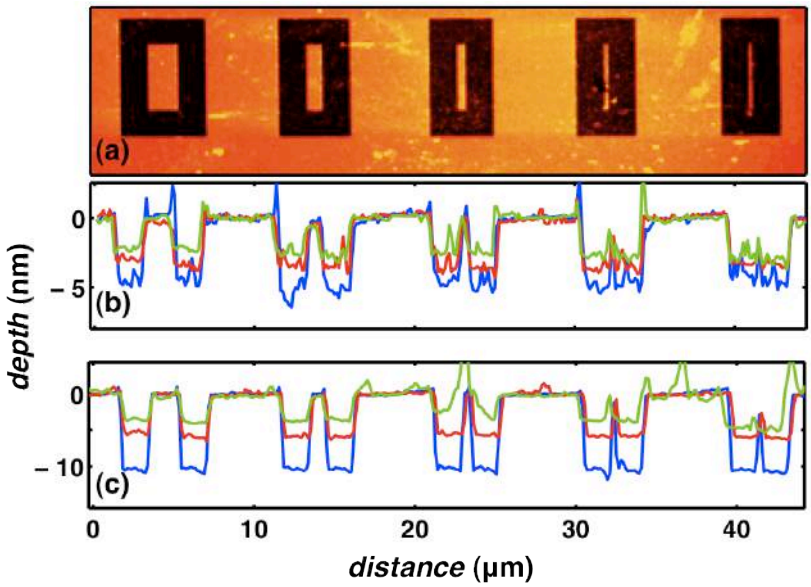

Figure 7-8: (a) atomic force microscopy image of structures fabricated in Pt/Co/Pt layers without TiN protection layer with D_{i1} dose. (b) and (c), atomic force microscopy profiles of the structures with TiN protective layer (b) and without TiN protective layer (c). Different colours represent different ion doses: green 4 x 10^{15} Ga^+ ions/cm^2, red 8 x 10^{15} Ga^+ ions/cm^2 and blue 2 x 10^{16} Ga^+ ions/cm^2.

In structures capped by TiN, the FIB depth of milling varies between 7 nm and 2.5 nm depending on the dose. So, considering that the TiN layer is 40 nm thick it is clear that one is not milling through the actual Pt/Co/Pt multilayer. However, as magnetization reversal measurements will show later, magnetism is suppressed in irradiated areas through local sub-surface intermixing of Co and Pt.

7.3.2. Magnetization reversal

The magnetization reversals of the magnetic nanostructures fabricated by FIB in Pt/Co/Pt multilayer with TiN overcoat have been measured by MOKE microscopy. These measurements have been carried out with polar MOKE geometry using an applied field out-of-plane. In this case also the highest possible magnification, which the MOKE microscope allows, has been used, namely a magnification of 400x. The selected ROI of interest vary from structure to structure, but always the minimum selected area has been slightly bigger than the actual structure, so that one avoids any noise or signal drift that could arise from mechanical motions.

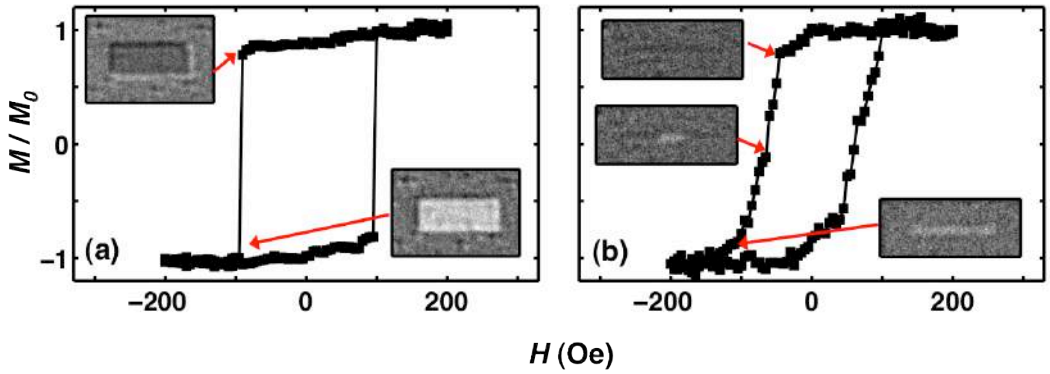

Figure 7-9: (a) and (b) show hysteresis loops measured in a 2 µm wide wire and a 100 nm wide wire by magneto-optical Kerr effect, respectively. The inset figures show domain images measured along the hysteresis loops, right before, during, and after the reversal.

Figures 7-9 (a) shows a hysteresis loop measured for a 2 µm wide wire and figure 7-9 (b) shows a hysteresis loop for a 100 nm wide magnetic structure. Both structures have been patterned using the D_{i1} ion dose. For the 2 µm wide structure, one can see a squared hysteresis loop, with an abrupt magnetization switch at the reversal point. This behaviour is very similar to the Pt/Co/Pt extended film magnetization reversal. On the other hand, for narrower structures, namely the 100 nm wide structure, the magnetization reversal is not anymore a single abrupt switch and intermediate states appear. As insets, MOKE microscope images of the various magnetic states at different applied field amplitudes during the reversal are shown. For the 2 µm wide structure two domain images are shown (fig. 7-9 (a) insets), where one corresponds to the domain state before magnetization reversal and the second one to the domain state right after the full reversal. Both images evidence uniform magnetic states as expected from the observed abrupt magnetization switch on the hysteresis loop. Thus, the magnetic moments of the entire structure reverse together, showing only uniform stable or metastable magnetic states. In the case of the 100 nm wide structure (fig. 7-9 (b) insets), while the magnetic state image before the reversal shows a uniform state, an intermediate reversal state is observed, for which a magnetic domain occurs in the central area of the wire, where the magnetization has already switched while the magnetization at the edges remains still in the original direction. Upon applying higher fields, the wire shows again a uniform magnetic state, but of opposite polarity. Therefore, one can conclude that the reversal proceeds by nucleation of a domain in the central part of the structure. Most probably the domain nucleation in the central part of the wire is driven by magneto-static energy

minimization. As the magnetic domain images indicate, it is energetically favourable for the reversal domain to nucleate in the central part in narrow wires. This is not surprising since even though the nucleation of this central domain will create an energy cost due to the formation of two domain walls, the magnetostatic energy reduction overcomes this cost favouring the domain to nucleate in the centre part (fig. 7-10 (a)). Moreover this particular domain state is (meta)stable and persists until the external applied field is large enough to move the domain walls out. On the other hand, one can not be sure if a reversal domain is nucleated in the centre part of the wire or on the edges for the wider structure, since there is no domain state that one could observe within the time resolution of the MOKE experiment presented hereby (fig. 7-10 (b)).

Besides the nano-structure magnetic reversal itself, it is important to notice that the surrounding areas, which have been ion-irradiated, do not show any polar magneto-optical signal and neither any longitudinal magneto-optical signal, confirming that the ferromagnetic state has been completely suppressed in areas, which have been directly irradiated by ions, at least to the degree that one cannot detect it anymore by the here used MOKE microscope. Moreover, the observed reversal in the nano-structures themselves is fully consistent with an isolated magnetic particle, which switches completely independent from its surrounding material.

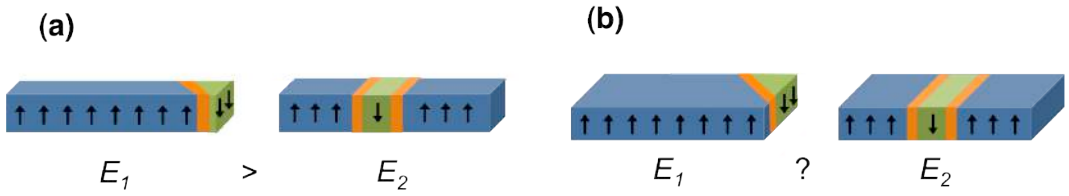

Figure 7-10: Schematic of domain nucleation in a narrow structure (a) and in a wide structure (b). While for narrow structures it is energetically favourable for the domain to nucleate in the central part of the structure as one can observe in the MOKE microscopy images (fig. 7-9 (a)), for wide structures it is not possible to determine if the domain nucleates in the centre part or on the edge.

Furthermore, from these measurements one can extract again the magnetic moment sensitivity of the MOKE microscope in the same manner as for the FEBID Co wire measurements. The single cycle hysteresis loop measurements for the 100 nm wide wire show a S/N ratio of 11.5, which is far better than the S/N value obtained for the FEBID Co wires. If one renormalizes the obtained S/N value to the

S/N = 2 criterion, and considering the dimensions of the Co structure, namely a height of 0.8 nm, width of 100 nm and length of 5 µm, a sensitivity of 1.0×10^{-13} emu is obtained for a single cycle measurement. This shows an about one order of magnitude higher sensitivity than in the case of FEBID Co nanowires single sweep hysteresis loop measurements, which is not unexpected, because polar MOKE measurements have approximately one order of magnitude higher signals than longitudinal MOKE. Also here, the achieved sensitivity might be further improved by using larger light intensities or averaging more than one hysteresis loop.

7.3.3. TEM structural analysis

In order to study the structural modifications created by ion irradiation, transmission electron microscope (TEM) studies have been done on a cross section of the 2 µm wide wire[yy]. These measurements have been carried out in the Electron Microscopy group at CIC nanoGUNE by Dr. Andrey Chuvilin.

Figure 7-11 (a) shows a cross sectional scanning-TEM image of the D_{i3} dose prepared structure using the high angle detector. In this image, one can clearly distinguish three different areas, namely the intended ion irradiated area where a clear intermixing between Pt and Co is visible, the non-irradiated area where a clear separation between Pt and Co layer can be observed, and in between these two areas a transition region. In the intended irradiated part (shown by orange arrows in fig. 7-11 (a)), the TiN becomes denser and results in a reduction of thickness from the originally deposited 40 nm to 35 nm, which is consistent with previously observed AFM data. In this intended irradiated area also an accumulation of Ga^+ ion is visible above the Pt layer. Concerning the Pt/Co/Pt layers themselves, it is not possible to distinguish them clearly, which is a consequence of the intermixing due to the ion irradiation.

In the non-irradiated area, one can observe a more porous TiN, whose thickness corresponds to the deposited TiN thickness and a clear distinction between Pt and Co layers can be observed. The Pt layers are represented by an almost white

[yy] Lamellae for TEM analysis have been fabricated by standard FIB method. Prior to the ion beam induced Pt deposition of a protection layer, 300 nm of Pt have been deposited by electron beam induced deposition in order to protect the surface. For the image acquisition, the TEM has been operated at 300 kV acceleration voltage in TEM and STEM modes.

colour, while a clearly darker grey layer is visible in between both Pt layers, which is the Co layer.

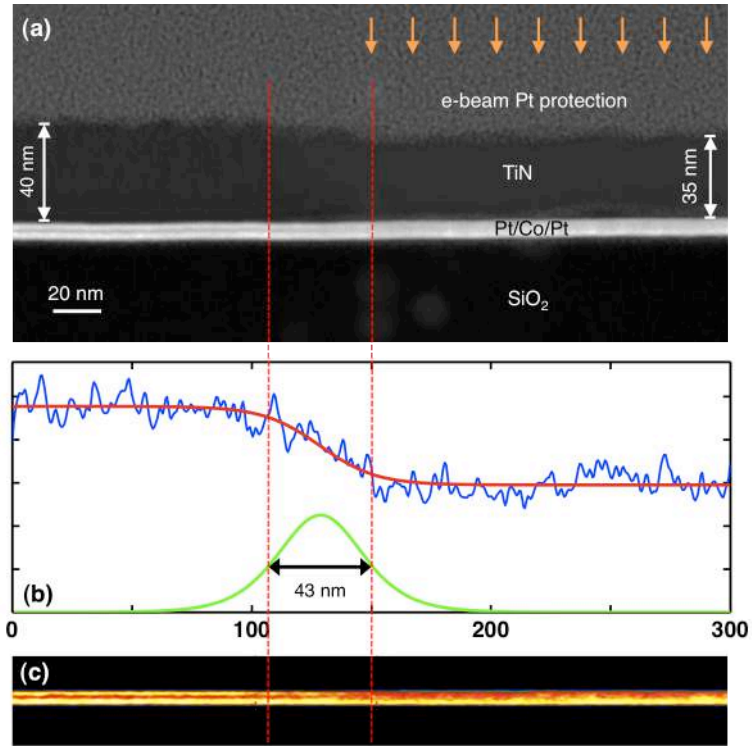

Figure 7-11: Scanning transmission electron microscope cross section image of a Pt/Co/Pt thin film sample structured by means of a focused ion beam with a dose of 2 x 10^{16} ions/cm^2. (a) and (c) show the same area but in the case of (c), the contrast has been change in order to better visualize the Co layer between the two Pt layers. (b) The blue line represents the intensity analysis given by the subtraction of the Co layer intensity from the sum of both Pt layers intensities, for which a least squares fit to the hyperbolic tangent function is represented by a red line. (c) The green line shows the slope of the fit function, from which the unintended damage width is estimated to 43 ± 8 nm.

In between both areas, namely the intended irradiated area and the non-irradiated area, there is a non-intended irradiated area, which is caused by the overall ion beam shape at the target depth. These ions cause a non-intended partial intermixing of the Pt/Co/Pt layers, which one can analyse by means of the image intensity along the multilayers in order to quantify its dimensions. Specifically, the Co layer intensity profile integrated along the thickness has been subtracted from the sum of both Pt layers intensity profiles, which are also integrated along their thickness. This gives the intensity profile shown as a blue line in fig. 7-11 (b), which has been fitted to a hyperbolic tangent function (fig. 7-11 (b) red line). The full width at half maximum of the differential of this least-squares fit (fig. 7-11 (b) green line) gives the lateral size of the non-intended intermixing of the Pt/Co/Pt layers. The

intermixed area within the nanostructure is highlighted by the red dashed lines and it has been estimated to be 43 ± 8 nm wide.

Figure 7-11 (c) shows the same area as figure 7-11 (a) but with increased gain of the detector to highlight the Pt/Co/Pt layers. Furthermore a colour scheme has been use to increase the contrast between the different layers. Here, one can even more clearly see a difference between, the non-irradiated area, intended irradiated area, and the non-intended irradiated area in the Pt/Co/Pt layers. While the Co layer (yellow colour) is visible in between both Pt layers (red colour) in the non-irradiated part, a clear intermixing of the Co layer with the Pt layers can be observed in the intended irradiation area. On the other hand, in the non-intended irradiated area, a gradual transition between non-intermixed Pt/Co/Pt layers to intermixed Pt/Co/Pt layers can be seen. From this structural analysis one can conclude that by using a TiN overcoat, a clear suppression of the wide ranging halo region and a reduction of the unintended intermixing area to only 43 ± 8 nm has been achieved for ion dose D_{i3}.

Figure 7-12 shows high resolution-TEM images of the 2 μm wide structure for ion dose D_{i1}. While fig. 7-12 (a) corresponds to a micrograph of the non-irradiated area, the image in fig. 7-12 (b) shows the irradiated area. In both cases the central Co-layer can be clearly identified as a separate intermediate layer between both Pt layers. However, while in the non-irradiated area (fig. 7-12 (a)) a clear and well-defined Co layer can be seen, the Co-film in the irradiated area (fig. 7-12 (b)) is more diffuse. Thus, from these images one can conclude that to suppress ferromagnetism in the Co-film, it is not necessary to dissolve this film completely. This result also indicates that rather small modification to the layering will result in dramatic changes of the magnetic properties, consistent with the premise of the work and the already mentioned results obtained by other groups.

Figure 7-12 (c) shows a lateral profile of the normalized average intensity along the whole image as a red dashed line for the irradiated case and as a blue solid line for the non-irradiated structure. Even though both cases show a relative intensity modulation along the layers, it is significantly decreased in the irradiated case due to the intermixing.

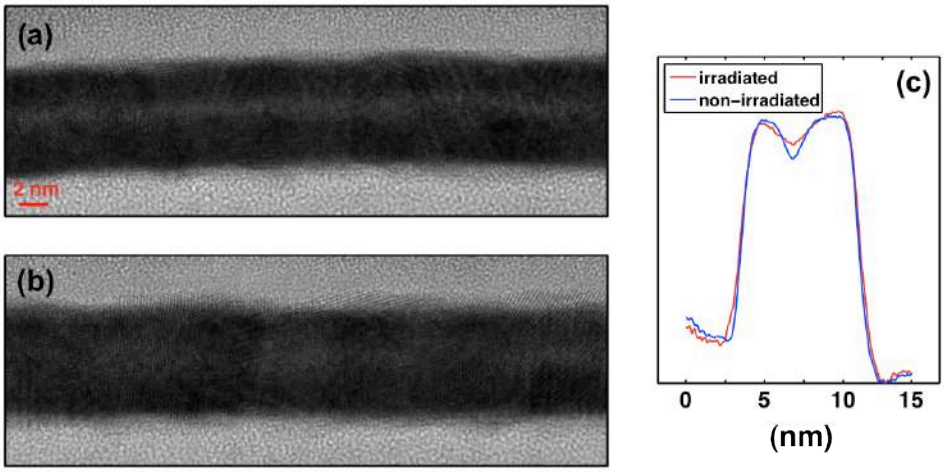

Figure 7-12: High resolution transmission electron microscopy images of Pt/Co/Pt structures: (a) shows an area, which has not been irradiated by ions and which has been taken from the central part of a 2 μm wide wire structure, (b) shows an area that has been directly irradiated by ions, using the D_{i1} dose. (c) Integrated intensity contrast over entire cross section image: the red line represents the irradiated case and the blue line the non-irradiated case.

7.4. Conclusions

In this chapter, the benefits that MOKE microscopy offers for the study of individual structures and their magnetization reversal has been successfully applied. Specifically, the ability of the Kerr microscope to measure magnetization reversal in ultrasmall individual nanostructures has been analysed using a high sensitive CCD camera. As a result of this high sensitivity, single cycle hysteresis loop measurements of 30 nm wide FEBID Co wires have been demonstrated and furthermore, the possibility to measure averaged hysteresis loop of only 3 nm wide and 2.5 nm thick wires has been extrapolated by using a light intensity of 100 $\mu W/\mu m^2$ in longitudinal MOKE geometry. Moreover around one order of magnitude better signal levels have been found for polar MOKE geometry.

Also, it has been demonstrated that by using an adequate hard mask, which acts as a sacrificial layer, such as TiN, for instance, a new and promising pathway is opened for directly nano-structuring multilayered materials by means of focused ion beam exposure. Hereby, Co/Pt nanostructures with dimensions down to 100 nm were successfully fabricated, maintaining their original perpendicular anisotropy, which has been measured by MOKE microscopy. Future work on this topic should focus on the combined optimization of the hard mask material and geometry, such as thickness, as well as the specific ion dose, to explore if the unintended intermixing

can be further limited[zz]. Also, the behaviour of more complex structures, such as edges, etc. would need to be explored to achieve a structure adjusted dose optimum, similar to the proximity effect in e-beam lithography.

Considering the strength of FEBID and FIB to fabricate and MOKE microscopy to characterize magnetic nanostructures, one can envision future studies of more complex and functional magnetic nanostructures, such as, magnetic logic gates[1], for instance.

[zz] J.-P. Adam et al. claim that by decreasing the ion dose down to 3 x 10^{13} Ga^{+} ions/cm^2, they are able to fabricate Pt/$Co_{0.5\ nm}$/Pt dots with a nominal diameter down to 50 nm[159]. However, their MOKE microscope images suggest much bigger magnetic structures.

8. Conclusion and outlook

Overall, the work of this thesis is intended to achieve a better understanding of magnetization reversal processes in thin films and nanostructures.

For this purpose, the work contains amongst other topics, a detailed analysis of the influence of crystallographic order, composition and thickness onto the magnetization reversal of Co and CoRu alloy films. Hereby, a well-defined, controlled and reproducible process for the tuning of crystallographic order was demonstrated based upon the partial interruption of epitaxy and its net effect onto magnetization reversal was explored. Special attention was given to the occurrence of (meta-)stable domain states during the reversal in these samples, because this domain stability is a qualitatively distinct feature for samples with sufficiently high levels of disorder. As future work on this subject, one can envision to extend this study to variable temperatures. This should be interesting and relevant, because the presumed meta-stable nature of the disorder induced domain states should produce a strong and non-trivial temperature dependence. One can hereby envision to pursue two experimental pathways, namely an actual temperature dependent study or a study at room temperature for a series of materials with varying Curie temperature, which is experimentally easier. Also, the analysis itself could be further refined, such as by studying in detail how the domain size correlates with the crystallographic disorder.

Concerning the study on the Ru concentration effects in CoRu alloys, one can conclude that this alloy can be grown with well controlled crystallographic orientations in a process similar to Co and other Co-alloy growth, so that it could be possibly combined with other such materials for technological device applications, such as hard disk drive media. Such an application could be interesting since these CoRu alloys allow for the fabrication of materials with low Curie temperature and

high magneto-crystalline anisotropy. Materials with these types of properties are certainly useful for hard disk drive applications and might be even more relevant in the future once the technological shift towards heat assisted magnetic recording has been made, for which materials or multilayers with graded anisotropy and Curie temperature profiles are needed.

This work also reports on an anomalous magnetization reversal near the HA orientation of the magnetic field in partially disordered samples, which arises from the partial misalignment of the anisotropy axes in exchange coupled systems. Even though anomalous magnetization curves near the hard axis orientation have been observed previously, none of these works had studied this phenomenon in detail or was able to explain its origin. With the work presented in this thesis, the origin of this hard axis anomaly has been well characterized and fully explained by means of a theoretical model, which in itself is furthermore corroborated by all of the different experimental findings.

Another aspect of this work is related to the dynamic phase transition. In regard to this subject, it has been demonstrated theoretically and experimentally that the conjugate field of the already established order parameter Q of the dynamically ordered phase is a constant bias field H_b. By exploring the H_b dependence, far-reaching similarities of the dynamic phase transition and the conventional thermodynamic ferromagnetic phase transition were found that appear to be much broader than what has been assumed so far in the primarily theoretical literature. I hope that this work will open up a promising pathway for future studies in this field, both theoretical and experimental, which should contribute to the development of a better or even far better understanding of dynamically ordered phenomena.

Another important aspect of this work has been the investigation of magnetization reversal in individual nanostructures. Hereby, my studies have demonstrated that a MOKE microscope can measure the magnetization reversal of structures, whose size is far below the wavelength of the light used for these observations. Specifically, it was shown that MOKE microscopy is able to measure individual magnetization switches in 30 nm wide wires and that one can push this limit to even smaller structures. As part of this overall study, it has been shown that FEBID and FIB are promising techniques for the fabrication of nanostructures. Hereby, a new pathway was utilized for the fabrication of nanostructures from

sensitive magnetic layers by means of FIB induced intermixing using a sacrificial hard mask. Extensions of this work should lead in the near future to more complex functional magnetic nanostructures by FIB, by FEBID or even by using a combination of both techniques.

A. Polarization analysis of the MOKE magnetometry setup

The path that the light follows in the MOKE magnetometry setup can be described mathematically by using the Jones calculus method[169]. Hereby, the electric field (E_f) of an electromagnetic plane wave is described by a two component vector

$$E_f = \begin{pmatrix} E_{0x}e^{i\delta x} \\ E_{0y}e^{i\delta y} \end{pmatrix}$$

(A-1),

where E_{0x} and E_{0y} are the amplitudes in *x* (here *p* polarized) and *y* (here *s* polarized) axes and δ_x and δ_y are their respective phases.

If the incident light of the experimental setup is linearly *p* polarized light after passing the linear polarizer on the incoming side of the light path, then the Jones vector is given by

$$p = \begin{pmatrix} 1 \\ 0 \end{pmatrix}$$

(A-2).

As described in sect. 3.3.1., the reflective matrix of the sample is given by eq. 3-4 and the reflection from the sample can be expressed by the multiplication of the incident light vector with the reflective matrix,

$$E_R = \begin{pmatrix} r_{pp} \\ r_{sp} \end{pmatrix} = \begin{pmatrix} r_{pp} & r_{ps} \\ r_{sp} & r_{ss} \end{pmatrix} \begin{pmatrix} 1 \\ 0 \end{pmatrix}$$

(A-3).

For a $\lambda/4$ retarder or waveplate with a fast axis oriented at 45º away from the *x* axis[aaa], the corresponding Jones matrix is given by

$$J_{m\left(\lambda/4,45^\circ\right)} = \begin{pmatrix} i & 1 \\ 1 & i \end{pmatrix}$$

(A-4).

Thus, after the λ/4 retarder the Jones vector of the light will be given by

$$E_{\lambda/4} = \begin{pmatrix} ir_{pp} + r_{sp} \\ r_{pp} + ir_{sp} \end{pmatrix} = \begin{pmatrix} i & 1 \\ 1 & i \end{pmatrix} \begin{pmatrix} r_{pp} \\ r_{sp} \end{pmatrix}$$

(A-5).

Subsequently, the Wollaston prism will separate the two orthogonal components that lie along the horizontal (*x*) and transversal (*y*) axes, so that one will be ir_{pp} + r_{sp} and the other r_{pp} + ir_{sp}. Given that the corresponding light intensities of these two beams are detected, they need to be evaluated.

The intensity of the horizontal component is

$$I_x = \left(ir_{pp} + r_{sp}\right)\left(-ir_{pp}^* + r_{sp}^*\right) = \left|r_{pp}\right|^2 + 2Im\left[r_{pp}r_{sp}^*\right] + \left|r_{sp}\right|^2$$

(A-6).

The intensity of the vertical component is

$$I_y = \left(r_{pp} + ir_{sp}\right)\left(r_{pp}^* - ir_{sp}^*\right) = \left|r_{pp}\right|^2 - 2Im\left[r_{pp}r_{sp}^*\right] + \left|r_{sp}\right|^2$$

(A-7),

so that the measured difference signal will be given by

$$I_x - I_y = 4Im\left[r_{pp}r_{sp}^*\right]$$

(A-8),

which is proportional to the magneto-optically induced ellipticity according to eq. (3-5) and thus to the magnetization component along the applied field axis.

[aaa] This is the configuration that was used in the experiment.

B. Method that represents existence of multidomain states

In perfect uniaxial samples, static multidomain states should not occur. Therefore, in uniaxial Co thin film samples, static domain states are associated with deviations from perfect behaviour due to the introduction of defects. A detailed study of the magnetic domains formation will allow for a correlation of this phenomena with the crystalline quality of the samples. In order to study the multidomain states in uniaxial Co thin films with different crystalline quality, MOKE microscopy (sect. 3.3.1.3.) measurements have been performed.

The corresponding study of the existence of multidomain states is not only challenging in terms of the large number of required measurements by means of MOKE microscopy, but also in terms of an appropriate representation of this vast amount of data. So, a new representation methodology has been developed, which allows for the comprehensive and automated analysis of domain structure images to analyse the existence of magnetic multidomains states.

In general terms, the methodology consists in a pixel-by-pixel grey scale evaluation for every MOKE microscopy image. By quantifying the pixels per grey

scale one generates a magnetization projection or orientation histogram that allows a characterization of the magnetization state at every field value, which goes beyond the simple average of a conventional magnetic hysteresis loop.

Figures B-1 (a)-(c) show 3 MOKE microscopy images that have been taken during a magnetization reversal sequence for one of the Co thin film samples. While figs. B-1 (a) and (c) show magnetization states for large positive and negative applied fields with uniform positive and negative magnetization values, fig. B-1 (b) displays an intermediate magnetic state, where magnetic domains are formed. As explained earlier, due to the polarizing optics of the MOKE microscope, different magnetization states appear with different grey-scale levels and given the linear relation in between the locally measured light intensity in the MOKE microscope, the corresponding grey-scales of images figs. B-1 (a)-(c) and the magnetization, one can determine the magnetization distribution in every MOKE image by assembling the corresponding histogram of the grey-scales in the picture. This is shown in figs. B-1 (d)-(f), where magnetization distribution $D(M,H)$ histograms that correspond to each MOKE image shown in figs. B-1 (a)-(c) are displayed. For uniform magnetic states (figs. B-1 (d) and (f)), a single peak histogram appears where the position of the peak corresponds to positive (fig. B-1 (d)) and negative reference magnetization values (fig. B-1 (f)). A clear separation of both magnetization states in terms of their representative histogram is achieved. However, one can also see that the histograms $D(M)$ are not perfectly sharp, even though the magnetization is in a uniform state in either case due to the application of a large magnetic field. Fundamentally, the width of the histogram is given by the finite signal to noise ratio in every pixel as well as the imperfect uniformity of the sample illumination and polarization sensitivity. Thus, this analysis method has a limited resolution that it can achieve. However, the resolution is clearly sufficient to determine various aspects of the magnetization behaviour, and especially the existence of domain states, which is its purpose. For instance, figure B-1 (e) shows a $D(M)$ histogram for an intermediate domain state (fig. B-1 (b)), where bi-modal magnetic domains are visible. In this histogram one can observe two peaks corresponding to the two magnetization orientations. The intensity of each peak is given by the magnetization probability for each orientation.

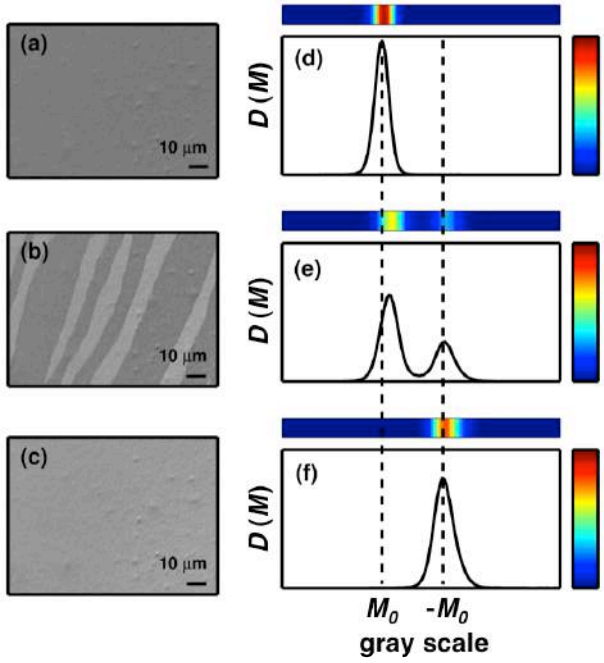

Figure B- 1: Histogram representation method of magnetization distributions: MOKE microscopy images are shown for the positive saturation state (a), an intermediate domain state (b) and the negative saturation state (c). The graphs (d)-(f) display the magnetization distribution histograms *D*(M) that are obtained from images (a)-(c). In addition, the right-hand side of (d)-(f) shows the colour code scheme that is being used to represent the *D*(*M*) histogram data in a single line each. The corresponding color-coded representations of magnetization distributions are shown above each of the histograms (d)-(f).

On top of the different figs. in B-1 (d)-(f), one can see how these histograms can be displayed by means of an appropriate colour code (as defined on the right-hand side in figs. B-1 (d)-(f)) as individual colour-coded lines. While for the uniform states at positive and negative saturation magnetization (top of figs. B-1 (d) and (f)) only one peak appears corresponding to a red coloured line segment, for the intermediate non-uniform state (top of fig. B-1 (e)) two peaks and thus two yellow-coloured segments appear that represent the bimodal magnetization state. Therefore, by using a histogram method, i.e. analysing MOKE images by summing pixels per grey scale and assigning an appropriate colour code to the histogram levels, one is able to display all crucial information about the magnetization distribution *D*(*M*) in a single, color-coded line.

This initial data extraction step, now allows for the display of the field dependent magnetization distribution *D*(*M*,*H*), corresponding to a full video sequence measured via Kerr microscopy, as a colour-coded picture map by combining the individual lines (top figs. B-1 (d)-(f)) for every applied field value. Figure B-2 (a) shows such a magnetization reversal sequence as a function of the applied field

strength for the upper branch of a hysteresis loop (starting from positive saturation and moving towards negative saturation) by using a full sequence of histograms extracted from the corresponding MOKE microscopy images. In contrast to conventional hysteresis loop measurements, this histogram representation is able to illustrate the entire magnetization distribution as a function of field and not just its average. Correspondingly, one can distinguish in fig. B-2 (a) the coherent rotation of the magnetization in between -30 Oe and -80 Oe from a non-uniform state formation starting at about -80 Oe and extending to approximately -115 Oe. While a coherent rotation or any uniform magnetization reversal process is represented here by a histogram peak shift, domains or any other non-uniform state formations are shown by a peak splitting or peak broadening. It is therefore possible to formalize and automate the non-uniformity or domain state analysis further by subtracting the uniform magnetization state histogram $D_0(M,H)$ for every magnetic field value, i.e. calculate

$$\Delta D(M,H) = |D(M,H) - D_0(M,H)|$$

(B-1).

Hereby, the uniform magnetization histogram, i.e. $D_0(M,H)$, was determined at large applied fields and then subtracted from the magnetization distribution $D(M,H)$ for every field value after adjusting for possible peak position shifts. Thus, the magnetization distribution difference, $\Delta D(M,H)$, deviates from zero only if non-uniform magnetization states exist. In this way, one obtains a representation of non-uniform magnetization states only, which is shown in fig. B-2 (b). Figure B-2 (b) clearly displays the occurrence of these non-uniform states during the magnetization reversal in bright blue colour, while the rotation processes that occur exclusively until about -80 Oe (coming from positive field values), do not show up in this representation.

In order to further formalized the multi-domain state analysis, one can quantify the non-uniform magnetization by integrating the non-uniformity indicator $\Delta D(M)$ as a function of M, i.e. calculating

$$ID(H) = \int_M \Delta D\,(M,H)dM$$

(B-2),

hereby obtaining a new histogram that quantifies the occurrence of magnetic non uniformity as a function of the applied field strength (fig. B-2 (c)). By assigning the colour code that is indicated on the right hand side of fig. B-2 (c) to this histogram, one is now in a position to obtain a single line representation of the multi-domain state existence range as a function of the externally applied field strength, which is shown at the bottom of fig. B-2 (c)[bbb]. The analysis methodology described here allows for the determination of domain existence and at the same time does so in a very efficient way, so that an entire video sequence of MOKE microscopy pictures can be condensed to a single colour coded line, representing exactly all the crucial information that one tries to extract in a completely automated way.

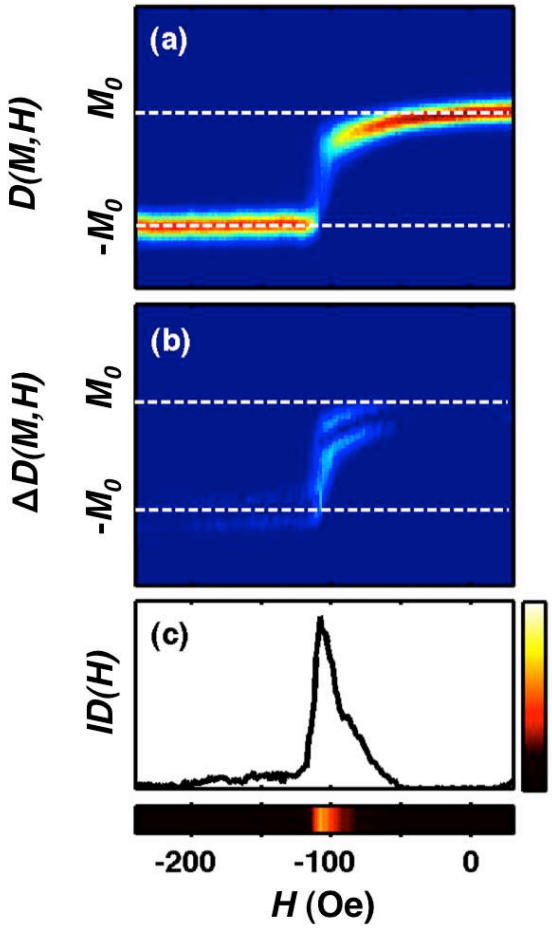

Figure B- 2: Quantitative domain existence analysis method: (a) shows a magnetization reversal sequence for a partially epitaxial sample, which has been analysed by means of the histogram representation method, leading to a *D*(*M*,*H*)-map representation of the experimental data. (b) displays the same set of data after removing the uniform

[bbb] When choosing the colour code scheme one has to find a compromise between the sensitivity of multidomain states and suppression of noise due to the natural fluctuations of the *D*(*M*)-width even in uniform states, which would otherwise produce many false positives of multi-domain existence.

magnetization histogram for every field value, leading to the difference map $\Delta D(M,H)$ (eq. B-1). (c) shows a histogram representation of $ID(H)$, which is derived, according to eq. B-2, by means of a magnetization axis integration of the $\Delta D(M,H)$-map, shown in (b). In addition, the right-hand side of (c) shows the colour code scheme that is being used to represent the $ID(H)$ histogram data in a single line. The corresponding colour-coded quantitative representation of domain state existence is shown below the histogram (c).

Furthermore, it is possible to analyse the magnetization reversal as a function of field strength and field orientation (β) and display the existence of multi-domain (MD) states in a single picture. An example of this $ID(H,\beta)$ map can be seen in fig. B-3, where SD denotes to single domain state and MD multi-domain state.

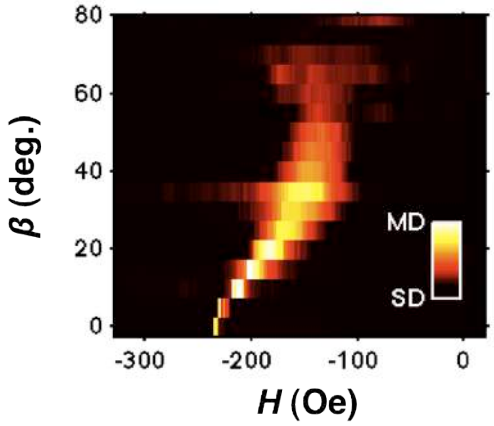

Figure B- 3: $ID(H,\beta)$ map of domain existence for the sample with t_{ox} = 0.275 nm; here, the black colour corresponds to magnetic uniformity or single domain (SD) states, while other colours correspond to the existence of multi domain states (MD).

List of publications

Work related to this thesis has also resulted in the following publications:

- O. Idigoras, P. Vavassori, J. M. Porro, and A. Berger, "Kerr microscopy study of magnetization reversal in uniaxial Co-films", J. Magn. Magn. Mater. **322**, L57-L60 (2010)
- O. Idigoras, A. K. Suszka, P. Vavassori, P. Landeros, J. M. Porro, and A. Berger, "Collapse of hard-axis behavior in uniaxial Co films", Phys. Rev. B **84**, 132403 (2011)
- O. Idigoras, P. Vavassori, and A. Berger, "Mean field theory of dynamic phase transitions in ferromagnets", Physica B **407**, 1377 (2012)
- E. Nikulina, O. Idigoras, P. Vavassori, A. Chuvilin, and A. Berger, "Magneto-optical magnetometry of individual 30 nm cobalt nanowires grown by electron beam induced deposition", Appl. Phys. Lett. **100**, 142401 (2012)
- O. Idigoras, U. Palomares, A. K. Suszka, L. Fallarino and A. Berger, "Magnetic properties of room temperature grown epitaxial $Co_{1-x}Ru_x$-alloy films" submitted to Appl. Phys. Lett. (01/06/2013)
- A. Berger, O. Idigoras, P. Vavassori, "Transient behavior of the dynamically ordered phase in uniaxial Co-films" submitted to Phys. Rev. Lett. (14/06/2013)

Other publications:

- J. A. Arregi, J. B. Gonzalez-Diaz, E. Bergaretxe, O. Idigoras, T. Unsal, and A. Berger, "Study of generalized magneto-optical ellipsometry measurement reliability", J. Appl. Phys. **111**, 103912 (2012)
- A. Rosales-Rivera, N. A. Salazar, O. Hovorka, O. Idigoras, and A. Berger, "Determination of critical exponents of inhomogeneous Gd films", Physica B **407**, 3141 (2012)
- J. A. Arregi, O. Idigoras, P. Vavassori, and A. Berger, "Field orientation dependent decorrelation of magnetization reversal in uniaxial Co-films ", Appl. Phys. Lett. **100**, 262403 (2012)
- J. M. Stiegler, R. Tena-Zaera, O. Idigoras, A. Chuvilin, and R. Hillenbrand "Correlative infrared–electron nanoscopy reveals the local structure–conductivity relationship in zinc oxide nanowires" Nat. Commun. **3**, 1131 (2012)
- A. K. Suszka, O. Idigoras, E. Nikulina. A. Chuvilin, and A. Berger, "Crystallography-driven positive exchange bias in Co/CoO-bilayers", Phys. Rev. Lett. **109**, 177205 (2012)
- R. A. Gallardo, O. Idigoras, P. Landeros, and A. Berger, "Analytical derivation of critical exponents of the dynamic phase transition in the mean-field approximation", Phys. Rev. E **86**, 051101 (2012)
- J. B. Gonzalez-Diaz, J. A. Arregi, E. Bergaretxe, M. J. Fertin, O. Idigoras, and A. Berger, "Anomalous magneto-optical behavior of uniaxial Co/CoO bilayer films", J. Magn. Magn. Mater. **325**, 147 (2013)

Acknowledgments

I would like to express my gratitude to my advisor, Dr. Andreas Berger for giving me the opportunity to work with him, for educating me and for encouraging me in difficult moments. I own to him all that I know about magnetism. Especially I want to thank him for looking always the best for me and for being so supportive and encouraging with all my decisions, particularly during this last year.

I am grateful also to Prof. Paolo Vavassori, for being always so helpful, with all the doubts that I had and for rescuing so many times with the MOKE setup and especially with the microscope. I enjoyed very much working with him in the lab and almost all that I know about the MOKE setup and microscope comes from his side.

I could not imagine this thesis without the support of all the nanomag people, they have been the constant emotional support that I was lacking during the hard times. Especially I would like to acknowledge Ania for being always there helping both with scientific and personal issues, for teaching so many things in the lab and outside from the lab. Thanks Suszkita for all the good advices. To Jon Ander for all the scientific doubts that he clarified me, all the times that he cheered me up, all the moments that we spent in the lab and all the super plannings that we did but never worked out. I was lucky when he decided to come back again to CIC nanoGUNE for his PhD. Eskerrik asko benetan jarregi. I want to thanks also to Ondrej for showing me looking the world from the pink glasses; definitely I could not manage the first year without his sense of humour. Thanks also to our technician, Cesar Antonio, for helping me thousand of times doing HF and opening the sputter chamber, even sometimes on Friday afternoons. I would not want to forget neither thanking to Juan who is always ready to help, to Txema for avoiding me for killing so many AFM tips, Lorenzo for bringing fresh air to the group, Usue, Marco Donolato, Nicolo, Ananda, Telem and all the actual and former members of the group.

I would like to thanks also all the collaborations that have made this thesis possible, specially the Electron Microscopy group at CIC nanoGUNE, Dr. Andrey Chuvilin and Dr. Elizaveta Nikulina. I could not forget neither with Prof. Hans Peter Oepen; thank you for these nice afternoons in the MOKE microscope together with Ania, looking for signal in Co/Pt multilayer structures and in the meantime betting for pintxos.

Thanks to Dr. Christian Binek and Dr. Pedro Landeros for agreeing to read the thesis and giving their feedbacks for international doctoral mention. I would like to express my greetings also to Dr. Neil Mathur and Dr. Burkard Hillerbrands for hosting me in their laboratories, in Cambridge and Kaiserslautern universities respectively and to Björn and Sam for helping during my stays there.

I would like to thank Prof. Txema Pitarke for the opportunity to work and carry out my experiments at CIC nanoGUNE Consolider.

Greetings also to all the rest people in CIC nanoGUNE, particularly to nanodevices group members for the nice hours in the lab, to Marco for sharing with me his nice tweezers and Roger for all the technical support. Thanks also to Gorka Pazos and Ralph Gay for all their help with experimental instruments. I also want to thank the administration of CIC nanoGUNE Consolider for their assistance.

I acknowledge the financial support of my PhD studies from the “Programa de Formación de Personal Investigador” promoted by the Department of Education, Universities and Research of the Basque Government. I also acknowledge the financing from CIC nanoGUNE Consolider during the first years of my PhD studies.

Eta zelanik ez, nire eskerrik beruenak zeuentzat diz, Ama, Aita, Dorleta eta Andoni. Dakaten dana zeuei zor dotzuet, beti egon zaze neure ondun hartu doten erabaki guztixetan laguntzen eta tesi hau esan ixango posible zeuen laguntza baik. Bixitxa honetan dakaten helburu guztik ez diz ixe lortuz gero zeuekin konpartiuten ez badotxuaz.

Bibliography

[1] D.A. Allwood, G. Xiong, C.C. Faulkner, D. Atkinson, D. Petit, and R.P. Cowburn, Science **309**, 1688 (2005).
[2] C. Sun, J.S.H. Lee, and M. Zhang, Adv. Drug Delivery Rev. **60**, 1252 (2008).
[3] H. Song, M.A. Reed, and T. Lee, Adv. Mater. **23**, 1583 (2011).
[4] S.N. Piramanayagam and K. Srinivasan, J. Mag. Mag. Mat. **321**, 485 (2009).
[5] D.D. Awschalom, L.C. Bassett, A.S. Dzurak, E.L. Hu, and J.R. Petta, Science **339**, 1174 (2013).
[6] S.N. Piramanayagam, J. Appl. Phys. **102**, 011301 (2007).
[7] B.N. Engel, J. Akerman, B. Butcher, R.W. Dave, M. DeHerrera, M. Durlam, G. Grynkewich, J. Janesky, S.V. Pietambaram, N.D. Rizzo, J.M. Slaughter, K. Smith, J.J. Sun, and S. Tehrani, IEEE Trans. Mag. **41**, 132 (2005).
[8] H.J. Richter, J. Phys. D: Appl. Phys. **32**, R147 (1999).
[9] R. Skomski, J. Phys.: Condens. Matter **15**, R841 (2003).
[10] S. Bader, Rev. Mod. Phys. **78**, 1 (2006).
[11] O. Hellwig, A. Berger, J.B. Kortright, and E.E. Fullerton, J. Mag. Mag. Mat. **319**, 13 (2007).
[12] C.A.F. Vaz, J.A.C. Bland, and G. Lauhoff, Rep. Prog. Phys. **71**, 056501 (2008).
[13] A. Khapikov and L. Uspenskaya, Phys. Rev. B **57**, 14990 (1998).
[14] A. Berger, Physica B **407**, 1322 (2012).
[15] M. Grimsditch, E.E. Fullerton, and R. Stamps, Phys. Rev. B **56**, 2617 (1997).
[16] R. Loloee, J. Appl. Phys. **112**, 023902 (2012).
[17] D. Weller, H. Brändle, G. Gorman, C.-J. Lin, and H. Notarys, Appl. Phys. Lett. **61**, 2726 (1992).
[18] M. Maret, M.C. Cadeville, R. Poinsot, A. Herr, E. Beaurepaire, and C. Monier, J. Appl. Phys. **166**, 45 (1997).
[19] D. Paudyal, T. Saha-Dasgupta, and A. Mookerjee, J. Phys.: Condens. Matter **16**, 2317 (2004).
[20] F. Aguilera-Granja, R.C. Longo, L.J. Gallego, and A. Vega, J. Ch. Phys. **132**, 184507 (2010).
[21] A. Berger, N. Supper, Y. Ikeda, B. Lengsfield, A. Moser, and E.E. Fullerton, Appl. Phys. Lett. **93**, 122502 (2008).
[22] A. Berger, H. Do, E.E. Fullerton, Y. Ikeda, B. Lengsfield, and N. Supper, U.S. Patent No. 7550210B2 (2009).
[23] A. Berger, H. Do, B. Lengsfield, and N. Supper, U.S. Patent No. 7582368B2 (2009).
[24] A. Berger, E.E. Fullerton, and H. Do, U.S. Patent No. 0166371A1 (2004).
[25] W.R. Beam and K.Y. Ahn, J. Appl. Phys. **34**, 1561 (1963).
[26] E.J. Torok, J. Appl. Phys. **36**, 952 (1965).
[27] F. Scheurer, R. Allenspach, P. Xhonneux, and E. Courtens, Phys. Rev. B **48**, 9890 (1993).
[28] X. Liu and G. Zangari, J. Appl. Phys. **90**, 5247 (2001).
[29] G.S. Chang, A. Moewes, S.H. Kim, J. Lee, K. Jeong, C.N. Whang, D.H. Kim, and S.-C. Shin, Appl. Phys. Lett. **88**, 092504 (2006).

[30] J. Hamrle, S. Blomeier, O. Gaier, B. Hillebrands, R. Schäfer, and M. Jourdan, J. Appl. Phys. **100**, 103904 (2006).
[31] C. Mathieu, V.R. Inturi, and M.J. Hadley, IEEE Trans. Mag. **44**, 431 (2008).
[32] D. Robb, P. Rikvold, A. Berger, and M. Novotny, Phys. Rev. E **76**, 021124 (2007).
[33] D. Robb, Y. Xu, O. Hellwig, J. McCord, A. Berger, M. Novotny, and P. Rikvold, Phys. Rev. B **78**, 134422 (2008).
[34] J.M.D. Coey, *Magnetism and Magnetic Materials* (Cambridge University Press, Cambridge, U.K., 2010).
[35] S. Blundell, *Magnetism in Condesed Matter* (Oxford University Press, Oxford, U.K., 2006).
[36] G. Bertotti, *Hysteresis in Magnetism, for Physicists, Materials Scientists, and Engineers* (Academic Press, Inc, San Diego, California, 1998).
[37] C. Kittel, Rev. Mod. Phys. **21**, 541 (1949).
[38] P. Poulopoulos and K. Baerschke, J. Phys.: Condens. Matter **11**, 945 (1999).
[39] R. Zhang and R. Willis, Phys. Rev. Lett. **86**, 2665 (2001).
[40] A. Aldea and V. Bârsan, *Trends in Nanophysics: Theory, Experiment and Technology* (Springer Verlag Berlin Heidelberg, 2010).
[41] E.C. Stoner and E.P. Wohlfarth, Philosophical Transactions of the Royal Society A: Mathematical, Physical and Engineering Sciences **240**, 599 (1948).
[42] M.T. Johnson, P.J.H. Bloemen, F.J. den Broeder, and J.J. de Vries, Rep. Prog. Phys. **59**, 1409 (1996).
[43] P.F. Carcia, J. Appl. Phys. **63**, 5066 (1988).
[44] M. Kisielewski, A. Maziewski, and V. Zablotskii, J. Mag. Mag. Mat. **316**, 277 (2007).
[45] K. Binder, D.P. Landau, and A.M. Ferrenberg, Phys. Rev. Lett. **74**, 298 (1995).
[46] P. Peczak, A.M. Ferrenberg, and D.P. Landau, Phys. Rev. B **43**, 6087 (1991).
[47] G. Korniss, C. White, P. Rikvold, and M. Novotny, Phys. Rev. E **63**, 016120 (2000).
[48] M. Acharyya, Phys. Rev. E **69**, 027105 (2004).
[49] T. Tomé and M.J. Oliveira, Phys. Rev. A **41**, 4251 (1990).
[50] D.L. Smith, *Thin-films Deposition: Principles and Practice* (McGraw-Hill, Inc, North America, 1995).
[51] K. Wasa and S. Haykawa, *Handbook of Sputter Deposition Technology: Principles, Technology and Applications* (Noyes Publication, New Yersey, U.S.A., 1992).
[52] P.J. Kelly and R.. Arnell, Vacuum **56**, 159 (2000).
[53] F. Adibi, I. Petrov, J.E. Greene, L. Hultman, and J.-E. Sundgren, J. Appl. Phys. **73**, 8580 (1993).
[54] L.A. Giannuzi and F.A. Stevie, *Introduction to Focused Ion Beam-Instrumentation, Theory, Techniques and Practice* (Springer Science + Bussiness Media, Inc, New York, U.S.A., 2005).
[55] C.-S. Kim, S.-H. Ahn, and D.-Y. Jang, Vacuum **86**, 1014 (2012).
[56] W.F. van Dorp and C.W. Hagen, J. Appl. Phys. **104**, 081301 (2008).
[57] M. Huth, F. Porrati, C. Schwalb, M. Winhold, R. Sachser, M. Dukic, J. Adams, and G. Fantner, Beilstein J. Nanotechnol. **3**, 597 (2012).
[58] E. Nikulina, O. Idigoras, E. Villamor, F. Casanova, P. Vavassori, A. Berger, and A. Chuvilin, In Preparation. (n.d.).
[59] L. Serrano-Ramón, R. Córdoba, L.A. Rodríguez, C. Magén, E. Snoeck, C. Gatel, I. Serrano, M.R. Ibarra, and J.M. De Teresa, ACS Nano **5**, 7781 (2011).

[60] Y.M. Lau, P.C. Chee, J.T.L. Thong, and V. Ng, J. Vac. Sci. Technol., A **20**, 1295 (2002).
[61] W.F. van Dorp, B. van Someren, C.W. Hagen, P. Kruit, and P. a Crozier, Nano Lett. **5**, 1303 (2005).
[62] R. Lavrijsen, R. Córdoba, F.J. Schoenaker, T.H. Ellis, B. Barcones, J.T. Kohlhepp, H.J.M. Swagten, B. Koopmans, J.M. De Teresa, C. Magén, M.R. Ibarra, P. Trompenaars, and J.J.L. Mulders, Nanotechnology **22**, 025302 (2011).
[63] M. Takeguchi, M. Shimojo, K. Mitsuishi, M. Tanaka, R. Che, and K. Furuya, J. Mater. Sci. **41**, 4532 (2006).
[64] A. Perentes, G. Sinicco, G. Boero, B. Dwir, and P. Hoffmann, J. Vac. Sci. Technol., B **25**, 2228 (2007).
[65] L.M. Belova, E.D. Dahlberg, A. Riazanova, J.J.L. Mulders, C. Christophersen, and J. Eckert, Nanotechnology **22**, 145305 (2011).
[66] L. Serrano-Ramón, A. Fernández-Pacheco, M.R. Ibarra, D. Petit, R.P. Cowburn, T. Tyliszeczak, and J.M. De Teresa, Eur. Phys. J. B **86**, 97 (2013).
[67] A. Fernández-Pacheco, L. Serrano-Ramón, J.M. Michalik, M.R. Ibarra, J.M. De Teresa, L. O'Brien, D. Petit, J. Lee, and R.P. Cowburn, Scientific Reports **3**, 1492 (2013).
[68] B.D. Cullity and S. Stock, *Elements of X-ray Diffraction* (Pretice-Hall, Inc., New Yersey, U.S.A., 2001).
[69] M. Birkholz, *Thin Film by X-ray Scattering* (Wiley-VCH Veralg GmbH & Co., Weinheim, Germany, 2006).
[70] G. Haugstad, *Atomic Force Microscopy Understanding Basic Modes and Advanced Applications* (John Wiley & Sons, Ltd, New Yersey, U.S.A., n.d.).
[71] M.J. Freiser, IEEE Trans. Mag. **4**, 152 (1968).
[72] S. Visnovsky, Czech. J. Phys. B **36**, 625 (1986).
[73] Z.Q. Qiu and S.D. Bader, Rev. Sci. Instrum. **71**, 1243 (2000).
[74] C.-Y. You and S.-C. Shin, J. Appl. Phys. **84**, 541 (1998).
[75] Z.Q. Qiu, J. Pearson, and S.D. Bader, Phys. Rev. B **46**, 8195 (1992).
[76] R. Schäfer, *Handbook of Magnetism and Advanced Magnetic Materials. Vol. 3: Novel Techniques for Characterizaing and Preparing Samples. Part 5.* (John Wiley & Sons, Ltd, 2007).
[77] A. Hubert and S. R, *Magnetic Domains: The Analysis of Microstructures* (Springer Verlag, Berlin, Germany, 1998).
[78] F. Fiorillo, Metrologia **47**, S114 (2010).
[79] http://www.lot-qd.de/files/downloads/qd/eu/MPMS_SQUID_VSM_eu.pdf, (n.d.).
[80] B.D. Cullity and C.D. Graham, *Introduction to Magnetic Materials* (John Wiley & Sons, Inc., New Yersey, U.S.A., 2009).
[81] O. Blaschko, G. Krescner, J. Pleschiutschnig, G. Ernst, C. Hitzenberger, H.P. Karnthaler, and A. Korner, Phys. Rev. Lett. **60**, 2800 (1988).
[82] S. Yuasa and D.D. Djayaprawira, J. Phys. D: Appl. Phys. **40**, R337 (2007).
[83] N. Patel, R. Fernandes, G. Guella, A. Kale, A. Miotello, B. Patton, and C. Zanchetta, J. Phys. Chem. **112**, 6968 (2008).
[84] J.-T. Li, J. Swiatowska, A. Seyeux, L. Huang, V. Maurice, S.-G. Sun, and P. Marcus, J. Power Sources **195**, 8251 (2010).
[85] D. McGrouther, J. Appl. Phys. **95**, 7772 (2004).
[86] L. Sun, Y. Wang, M. Yang, Z. Huang, Y. Zhai, Y. Xu, J. Du, and H. Zhai, J. Appl. Phys. **111**, 07A328 (2012).
[87] J.S. Chen, Y. Xu, and J.P. Wang, J. Appl. Phys. **93**, 1661 (2003).

[88] A. Khapikov, L. Uspenskaya, I. Bdikin, Y. Mukovskii, S. Karabashev, D. Shulyaev, and A. Arsenov, Appl. Phys. Lett. **77**, 2376 (2000).
[89] O. Hovorka, Y. Liu, K. a. Dahmen, and A. Berger, Appl. Phys. Lett. **95**, 192504 (2009).
[90] F. Virot, L. Favre, R. Hayn, and M.D. Kuz'min, J. Phys. D: Appl. Phys. **45**, 405003 (2012).
[91] W. Yang, D.N. Lambeth, and D.E. Laughlin, J. Appl. Phys. **85**, 4723 (1999).
[92] M. Hacke, H.L. Bay, and S. Mantl, Thin Solid Films **280**, 107 (1996).
[93] L. Verlag, Philosophical Magazine **31**, 83 (1916).
[94] H. Gong, M. Rao, D.E. Laughlin, and D.N. Lambeth, J. Appl. Phys. **85**, 4699 (1999).
[95] M.F. Toney, E.E. Marinero, and J. a. Hedstrom, J. Appl. Phys. **99**, 033907 (2006).
[96] K.E. Johnson, M. Mirzamaani, and M.F. Doerner, IEEE Trans. Mag. **31**, 2721 (1995).
[97] X.D. Liu, Z. Xu, R.X. Gao, Z.F. Chen, T.S. Lai, J. Du, and S.M. Zhou, J. Appl. Phys. **106**, 053907 (2009).
[98] M. Mathews, E.P. Houwman, H. Boschker, G. Rijnders, and D.H.A. Blank, J. Appl. Phys. **107**, 013904 (2010).
[99] J.A. Arregi, O. Idigoras, P. Vavassori, and A. Berger, Appl. Phys. Lett. **100**, 262403 (2012).
[100] J.B. Staunton, S.S.A. Razee, M.F. Ling, D.D. Johnson, and F.J. Pinski, J. Phys. D: Appl. Phys. **31**, 2355 (1998).
[101] T.R. Albrecht, D. Bedau, E. Dobisz, H. Gao, M. Grobis, O. Hellwig, D. Kercher, J. Lille, E. Marinero, K. Patel, R. Ruiz, M.E. Schabes, L. Wan, D. Weller, and T.-W. Wu, IEEE Trans. Mag. **49**, 773 (2013).
[102] S.S.P. Parkin, N. More, and K.P. Roche, Phys. Rev. Lett. **64**, 2304 (1990).
[103] J. Sort, B. Rodmacq, S. Auffret, and B. Dieny, Appl. Phys. Lett. **83**, 1800 (2003).
[104] E.E. Fullerton, D.T. Margulies, M.E. Schabes, M. Carey, B. Gurney, A. Moser, M. Best, G. Zeltzer, K. Rubin, H. Rosen, and M. Doerner, Appl. Phys. Lett. **77**, 3806 (2000).
[105] A. Dinia and K. Ounadjela, J. Mag. Mag. Mat. **146**, 66 (1995).
[106] K. Himi, K. Takanashi, S. Mitani, M. Yamaguchi, D.H. Ping, K. Hono, and H. Fujimori, Appl. Phys. Lett. **78**, 1436 (2001).
[107] C. Song, X. Wei, K. Geng, F. Zeng, and F. Pan, Phys. Rev. B **72**, 184412 (2005).
[108] V. Pierron-bohnes, N. Ringelstein, A. Michel, S. Boukari, L. Bouzidi, N. Persat, E. Beaurepaire, M. Hehn, D. Muller, and M.C. Cadeville, J. Mag. Mag. Mat. **165**, 176 (1997).
[109] L. Bouzidi, O. Haemmerle, C. Bouillet-Ulhaq, and M.C. Cadeville, Thin Solid Films **318**, 215 (1998).
[110] O. Ersen, L. Bouzidi, V. Pierron-Bohnes, and M.C. Cadeville, Mat. Res. Soc. Symp. Proc. **528**, 11 (1998).
[111] K. Rahmouni, A. Dinia, D. Stoeffler, K. Ounadjela, H.A.M. Van den Berg, and H. Rakoto, Phys. Rev. B **59**, 9475 (1999).
[112] D. Zitoun, C. Amiens, B. Chaudret, M.-C. Fromen, P. Lecante, M.-J. Casanove, and M. Respaud, Journal of Physical Chemistry B **107**, 6997 (2003).
[113] H. Hashizume, K. Ishiji, J. Lang, D. Haskel, G. Srajer, J. Minár, and H. Ebert, Phys. Rev. B **73**, 224416 (2006).
[114] S.B. Qadri, T.M. Keller, M. Laskoski, C.A. Little, M.S. Osofsky, and H.R. Khan, Appl. Phys. Lett. **91**, 214101 (2007).

[115] W.C. Wang, Y. Dai, T.L. Wang, J.H. Li, X. He, and B.X. Liu, Appl. Phys. Lett. **94**, 131903 (2012).
[116] C. Eyrich, W. Huttema, M. Arora, E. Montoya, F. Rashidi, C. Burrowes, B. Kardasz, E. Girt, B. Heinrich, O.N. Mryasov, M. From, and O. Karis, J. Appl. Phys. **111**, 07C919 (2012).
[117] A.-C. Sun, J.-H. Hsu, C.H. Sheng, P.C. Kuo, and H.L. Huang, IEEE Trans. Mag. **43**, 882 (2007).
[118] M.D. Kuz'min, Phys. Rev. Lett. **94**, 107204 (2005).
[119] A. V. Vannikov and A.D. Grishina, Russian Chemical Reviews **62**, 35 (1993).
[120] V. Sharma, P. Manchanda, R. Skomski, D.J. Sellmyer, and A. Kashyap, J. Appl. Phys. **109**, 07A727 (2011).
[121] J.M. MacLaren, S.D. Willoughby, M.E. McHenry, B. Ramalingam, and S.G. Sankar, IEEE Trans. Mag. **37**, 1277 (2001).
[122] S.D. Willoughby, J.M. MacLaren, T. Ohkubo, S. Jeong, M. McHenry, D.E. Laughlin, S.-J. Choi, and S.-J. Kwon, J. Appl. Phys. **91**, 8822 (2002).
[123] E.R. Callen and H.B. Callen, J. Phys. Solids **16**, 319 (1960).
[124] E. Du Trémolet de Lacheisserie, D. Gignoux, and M. Schlenker, *Magnetism Fundamentals* (Springer Science + Bussiness Media, Inc, New York, U.S.A., 2005).
[125] R. Skomski, O.N. Mryasov, J. Zhou, and D.J. Sellmyer, J. Appl. Phys. **99**, 08E916 (2006).
[126] F. Aldinger and S. Jonsson, Z. Metallkd. **68**, 362 (1977).
[127] M. Cougo dos Santos, J. Geshev, L. Pereira, M. Alves, J. Schmidt, and P. Allongue, Phys. Rev. B **70**, 104420 (2004).
[128] O. Gaier, A Study of Exchange Interaction, Magnetic Anisotropies, and Ion Beam Induced Effects in Thin Films of Co2-based Heusler Compounds, University of Kaiserslautern, 2009.
[129] B. Hillebrands, in *Light Scattering in Solids VII*, edited by M. Cardona and G. Güntherodt (Springer Verlag, Heidelberg, Germany, 1999).
[130] M.F. Zimmer, Phys. Rev. E **47**, 3950 (1993).
[131] M. Acharyya, Phys. Rev. E **59**, 218 (1999).
[132] G. Korniss, P. Rikvold, and M. Novotny, Phys. Rev. E **66**, 056127 (2002).
[133] G. Berkolaiko and M. Grinfeld, Phys. Rev. E **76**, 061110 (2007).
[134] X. Shi and G. Wei, Phys. Lett. A **374**, 1885 (2010).
[135] B. Deviren and M. Keskin, J. Mag. Mag. Mat. **324**, 1051 (2012).
[136] W.S. Lo and R.A. Pelcovits, Phys. Rev. A **42**, 7471 (1990).
[137] M. Acharyya and B.K. Chakrabarti, Phys. Rev. B **52**, 6550 (1995).
[138] G.M. Buendía and E. Machado, Phys. Rev. E **58**, 1260 (1998).
[139] S. Sides, P. Rikvold, and M. Novotny, Phys. Rev. Lett. **81**, 834 (1998).
[140] B.K. Chakrabarti and M. Acharyya, Rev. Mod. Phys. **71**, 847 (1999).
[141] H. Jang, M. Grimson, and C. Hall, Phys. Rev. B **67**, 094411 (2003).
[142] G. Buendía and P. Rikvold, Phys. Rev. E **78**, 051108 (2008).
[143] M. Acharyya, Phys. Rev. E **58**, 179 (1998).
[144] Q. Jiang, H.N. Yang, and G.C. Wang, Phys. Rev. B **52**, 14911 (1995).
[145] J. Suen and J.L. Erskine, Phys. Rev. Lett. **78**, 3567 (1997).
[146] R.A. Gallardo, O. Idigoras, P. Landeros, and A. Berger, Physical Review E **86**, 051101 (2012).
[147] R.J. Glauber, J. Math. Phys. **4**, 294 (1963).
[148] M.P. Sharrock, J. Appl. Phys. **76**, 6413 (1994).

[149] D.A. Allwood, G. Xiong, M.D. Cooke, and R.P. Cowburn, J. Phys. D: Appl. Phys. **36**, 2175 (2003).
[150] H.T. Zeng, D. Read, L. O'Brien, J. Sampaio, E.R. Lewis, D. Petit, and R.P. Cowburn, Appl. Phys. Lett. **96**, 262510 (2010).
[151] M. Cormier, A. Mougin, J. Ferré, J.-P. Jamet, R. Weil, J. Fassbender, V. Baltz, and B. Rodmacq, J. Phys. D: Appl. Phys. **44**, 215002 (2011).
[152] J.H. Franken, M. Hoeijmakers, H.J.M. Swagten, and B. Koopmans, Phys. Rev. Lett. **108**, 037205 (2012).
[153] R.L. Kubena and J.W. Ward, Appl. Phys. Lett. **51**, 1960 (1987).
[154] R. Hyndman, P. Warin, J. Gierak, J. Ferré, J.N. Chapman, J.P. Jamet, V. Mathet, and C. Chappert, J. Appl. Phys. **90**, 3843 (2001).
[155] P. Warin, R. Hyndman, J. Glerak, J.N. Chapman, J. Ferré, J.P. Jamet, V. Mathet, and C. Chappert, J. Appl. Phys. **90**, 3850 (2001).
[156] C. Vieu, J. Gierak, H. Launois, T. Aign, P. Meyer, J.P. Jamet, J. Ferré, C. Chappert, T. Devolder, V. Mathet, and H. Bernas, Journal of Applied Physics **91**, 3103 (2002).
[157] J. Jaworowicz, A. Maziewski, P. Mazalski, M. Kisielewski, I. Sveklo, M. Tekielak, V. Zablotskii, J. Ferré, N. Vernier, A. Mougin, A. Henschke, and J. Fassbender, Appl. Phys. Lett. **95**, 022502 (2009).
[158] S. Streit-Nierobisch, D. Stickler, C. Gutt, L.-M. Stadler, H. Stillrich, C. Menk, R. Frömter, C. Tieg, O. Leupold, H.P. Oepen, and G. Grübel, J. Appl. Phys. **106**, 083909 (2009).
[159] J.-P. Adam, J.-P. Jamet, J. Ferré, A. Mougin, S. Rohart, R. Weil, E. Bourhis, and J. Gierak, Nanotechnology **21**, 445302 (2010).
[160] S. Breitkreutz, J. Kiermaier, S. Vijay Karthik, G. Csaba, D. Schmitt-Landsiedel, and M. Becherer, J. Appl. Phys. **111**, 07A715 (2012).
[161] C. Chappert, H. Bernas, J. Ferré, V. Kottler, J.-P. Jamet, Y. Chen, E. Cambril, T. Devolver, F. Rousseaux, V. Mathet, and H. Launois, Science **280**, 1919 (1998).
[162] T. Devolder, C. Chappert, Y. Chen, E. Cambril, H. Bernas, J.P. Jamet, and J. Ferré, Appl. Phys. Lett. **74**, 3383 (1999).
[163] T. Devolder, C. Chappert, V. Mathet, H. Bernas, Y. Chen, J.P. Jamet, and J. Ferré, J. Appl. Phys. **87**, 8671 (2000).
[164] B.D. Terris, L. Folks, D. Weller, J.E.E. Baglin, a. J. Kellock, H. Rothuizen, and P. Vettiger, Appl. Phys. Lett. **75**, 403 (1999).
[165] N.D. Telling, S. Langridge, R.M. Dalgliesh, P.J. Grundy, and V.M. Vishnyakov, J. Appl. Phys. **93**, 7420 (2003).
[166] A. Kobs, S. Heße, W. Kreuzpaintner, G. Winkler, D. Lott, P. Weinberger, A. Schreyer, and H.P. Oepen, Phys. Rev. Lett. **106**, 217207 (2011).
[167] H. Stillrich, C. Menk, R. Frömter, and H.P. Oepen, J. Appl. Phys. **105**, 07C308 (2009).
[168] J. Takadoum and H.H. Bennani, Surf. Coat. Tech. **96**, 272 (1997).
[169] G.R. Fowles, *Introduction to Modern Optics* (Dover publications, Inc., New York, U.S.A., 1975).
[170] A. Berger and E.E. Fullerton, J. Mag. Mag. Mat. **165**, 471 (1997).
[171] D. Cohen-Tanugi and N. Yao, J. Appl. Phys. **104**, 063504 (2008).